Dissertation

Unravelling the Energy Flow

Probing Vibrational Dynamics in Non-Equilibrium Alkyl Chain Monolayers Using Sum-Frequency Spectroscopy

From the Faculty of Chemistry
the University of Duisburg-Essen
approved dissertation
to obtain the degree
Dr. rer. nat.
from

Marvin Marquardt

Advisor:
Prof. Dr. Eckart Hasselbrink
Co-advisor:
Prof. Dr. Christian Mayer

Mülheim, Germany
2023

DOI: 10.17185/duepublico/81498
URN: urn:nbn:de:hbz:465-20240301-075632-0

Gutachter:
Prof. Dr. Eckart Hasselbrink
Prof. Dr. Christian Mayer

Vorsitz:
Prof. Dr. Alexander Probst

Datum der Disputation:
01. Februar 2024

Danksagung

Der erste Dank geht an meinen Doktorvater Eckart, dessen wirklich leidenschaftliche Betreuung seiner Doktoranden stehts als Anker in herausfordernden Zeiten diente. Die Momente in denen Eckart kurzfristig mal keine Zeit für mich hatte, in den letzten 5 Jahren, kann ich vermutlich an einer Hand abzählen. Weiterhin hat Eckart stehts die richtige Balance gefunden um fachspezifisch zu beraten ohne den Doktoranden die nötige Freiheit zum selbstständigen Arbeiten zu nehmen. Dabei kam Humor natürlich auch nicht zu kurz. Also, Eckart: Vielen Dank für die letzten Jahre! Ich habe diese Zeit als sehr angenehme empfunden und es nie bereut den Weg der Promotion eingeschlagen zu haben.

Der zweite Dank geht an Prof. Dr. Christian Mayer für die Übernahme des Zweitgutachtens.

Weiterhin danke ich dem gesamten Arbeitskreis Hasselbrink. Ohne euch wäre die Zeit nicht annähernd so schön geworden! Damian mit seiner offenen Art, Matthias mit einer Antwort auf jede Frage, Denise mit der stets gefüllten Süßigkeiten-Schublade, Daniel mit täglichen Gesprächen über Physik und das Leben, Nelli mit ihrem trockenen Humor und Elke mit einer helfenden Hand in jeder Situation. Besonderer Dank geht auch an Tim, in dem ich einen Freund fürs Leben und einen hingabevollen Patenonkel für Malou gefunden habe. Der letzte Dank im AK Hasselbrinks geht an Michael, mit dem ich die Arbeiten im Laserlabor zusammen bewältigt habe. Auch wenn ich Micha anfangs mit meinen etlichen Fragen an den Rand der Verzweiflung getrieben habe, haben wir uns zu einem äußerst effektiven Team entwickelt und eine Freundschaft gefunden, die über die Grenzen der Universität reicht. Danke Micha, für deine ausdauernde Geduld, deine schlauen Ideen und deine motivierende Zusammenarbeit.

In meinem privaten Umfeld muss ich insbesondere meiner eigenen Familie danken, die sich in den letzten Jahren drastisch erweitert hat. Gleich zu Beginn der Promotion habe ich meine jetzige Frau Phillis kennengelernt, die einen erheblichen Anteil dazu beigetragen hat warum ich die letzten Jahre als die besten meines Lebens bezeichne. Philli, deine charmante Art wärmt mir stets das Herz und zaubert mir immer ein Lächeln ins Gesicht. Dazu kommen unsere 2-jährige Malou und unser 3-monatige Tamo, die für mich den Sinn des Lebens neu definiert haben. Auch wenn ihr beide mir einiges an Zeit und Nerven beim Schreiben der Dissertation gekostet habt, liebe ich euch über alles. Ihr seid das Beste was ich in diesem Leben erreicht habe und je erreichen werde. Großer Dank gilt auch meiner restlichen Familie, die mich stets unterstützt hat und immer ein offenes Ohr für meine spontanen Ausschweifungen über aktuelle Probleme im Laserlabor fand.

Hiermit versichere ich, die vorliegende Dissertation selbstständig, ohne fremde Hilfe und ohne Benutzung anderer als den angegebenen Quellen angefertigt zu haben. Alle aus fremden Werken direkt oder indirekt übernommenen Stellen sind als solche gekennzeichnet. Die vorliegende Dissertation wurde in keinem anderen Promotionsverfahren eingereicht. Mit dieser Arbeit strebe ich die Erlangung des akademischen Grades Doktor der Naturwissenschaften (Dr. rer. nat.) an.

Mülheim an der Ruhr, 31.10.2023

Ort, Datum

Marvin Marquardt

Abstract

Vibrational spectroscopy is a powerful tool for investigating the dynamics of molecular systems in non-equilibrium states. In this thesis, we employ a time-resolved two-colour IR sum-frequency pump-probe setup to delve into the transient energy redistribution in calcium arachidate (CaAra) Langmuir-Blodgett monolayers. Our novel experimental design involves a broadband IR pulse and a narrowband visible pulse generating a sum-frequency signal for probing the sample, while an independent narrowband IR pulse serves as the pump, populating specific vibrational levels.

We were led by several fundamental questions in our research:

1. How does the system react or evolve in time after it has been brought into a non-equilibrium state?

2. How does the coupling to different degrees of freedom work?

3. How long does a 'hot' adsorbate exist on the surface after an initial chemical reaction step?

Our investigation encompasses a range of techniques, including simple sum-frequency spectra in *ssp* and *ppp* polarisation, wavelength scans to explore resonant pumping and delay scans to investigate the transient bleach of different vibrational modes. We focus our attention on the CH_3 symmetric (r^+) and antisymmetric (r^-) stretch vibrations, as these are the most prominent modes in our sum-frequency spectra.

Our main findings include:

1. Strong resonant pumping observed at $2920\,\mathrm{cm}^{-1}$ (CH_2 antisymmetric stretching, d^-) and $2962\,\mathrm{cm}^{-1}$ (r^-).

2. The dynamics differ when pumping r^- vs d^-, with r^- showing a very slow decay with a time constant of a few nanoseconds and d^- displaying multiple decay components, including the very slow component but also a ≈ 100 ps component.

3. To explain these findings, we propose a three-temperature model accounting for different heat baths for the CH_2, the CH_3 and the lower deformation modes. Coupling parameters between these baths are estimated, shedding light on the energy redistribution pathways.

We further explore the system by altering sample conditions:

1. Reducing the surface pressure during deployment of the Langmuir-Blodgett films results in less dense monolayers. This impacts the dynamics, particularly the r^+ mode when pumping d^- shows a smaller bleach for decreasing density. Surprisingly, this is only observable in *ssp* polarisation.

2. Deuterating specific CH_2 groups aims to disrupt anharmonic coupling between the CH_2 and CH_3 modes. This reveals interesting behaviour in the deuterated samples, such as a delayed lift-off point in the bleach when pumping d^-.

Our findings provide valuable insights into the complex dynamics of CaAra Langmuir-Blodgett films and highlight the importance of film density and isotopic substitutions in controlling energy redistribution processes.

This research advances our understanding of vibrational dynamics in molecular monolayers and paves the way for future investigations into non-equilibrium states of condensed matter.

Zusammenfassung

Vibrationsspektroskopie ist ein leistungsfähiges Werkzeug zur Untersuchung der Dynamik von molekularen Systemen im Nichtgleichgewichtszustand. In dieser Arbeit verwenden wir einen zeitauflösenden Zweifarben Infrarot Summenfrequenz Pump-Probe Aufbau, um die zeitliche Energieumverteilungen in Calciumarachidat (CaAra) Langmuir-Blodgett Monolagen aufzulösen. Unser neuartiges experimentelles Design umfasst einen breitbandigen Infrarot Puls und einen schmalbandigen sichtbaren Puls, die ein Summenfrequenzsignal zur Untersuchung der Probe erzeugen, während ein unabhängiger schmalbandiger Infrarot Puls als Pumppuls dient und bestimmte Schwingungsniveaus anregt.

Unsere Forschung wurde von mehreren grundlegenden Fragen geleitet:

1. Wie reagiert oder entwickelt sich das System im Laufe der Zeit, nachdem es in einen Nichtgleichgewichtszustand versetzt wurde?

2. Wie funktioniert die Kopplung zu verschiedenen Freiheitsgraden?

3. Wie lange existiert ein 'heißes' Adsorbat auf der Oberfläche nach einem ersten chemischen Reaktionsschritt?

Unsere Untersuchung umfasst eine Reihe von Techniken, darunter die Analyse einfacher Summenfrequenzspektren in der *ssp* und *ppp* Polarisation, Wellenlängen-Scans zur Erkundung von resonanten Pump-Anregungen und Verzögerungs-Scans zur Untersuchung des transienten Bleicheffekts verschiedener Schwingungsmoden. Unser Hauptaugenmerk liegt auf den symmetrischen (r^+) und antisymmetrischen (r^-) Streckschwingungen der CH_3-Gruppen, da diese die prominentesten Moden in unseren Summenfrequenzspektren sind.

Unsere wichtigsten Ergebnisse umfassen:

1. Starke resonante Anregung bei $2920\,\mathrm{cm}^{-1}$ (CH_2-antisymmetrische Streckung, d^-) und $2962\,\mathrm{cm}^{-1}$ (r^-).

2. Die Dynamik unterscheidet sich, wenn r^- im Vergleich zu d^- angeregt wird. Bei r^- zeigt sich ein sehr langsamer Abbau mit einer Zeitkonstanten von einigen Nanosekunden, während bei d^- mehrere Komponenten sichtbar werden, einschließlich der sehr langsamen Komponente, aber auch einer ≈ 100 ps-Komponente.

3. Zur Erklärung dieser Ergebnisse schlagen wir ein Drei-Temperatur-Modell vor, das verschiedene Wärmebäder für die CH_2-, die CH_3- und die niedrigeren Deformationsmoden berücksichtigt. Kopplungsparameter zwischen diesen Bädern werden abgeschätzt und offenbaren die Energieumverteilungswege.

Wir erforschen das System weiter, indem wir die Probenkonditionen verändern:

1. Die Reduzierung des Oberflächendrucks während der Herstellung der Langmuir-Blodgett-Filme führt zu weniger dichten Monolagen. Dies wirkt sich auf die Dynamik aus, insbesondere die r^+-Mode, wenn d^- angeregt wird, zeigt eine geringere Bleiche bei abnehmender Dichte. Überraschenderweise ist dies nur in der *ssp*-Polarisation zu beobachten.

2. Die Deuterierung bestimmter CH_2-Gruppen zielt darauf ab, die anharmonische Kopplung zwischen den CH_2- und CH_3-Moden zu stören. Dies enthüllt interessantes Verhalten in den deuterierten Proben, wie einen verzögerten Abhebepunkt in der Bleiche, wenn d^- angeregt wird.

Unsere Ergebnisse liefern wertvolle Einblicke in die komplexe Dynamik von CaAra Langmuir-Blodgett-Filmen und betonen die Bedeutung von Film-Dichte und isotopischen Substitutionen zur Kontrolle von Energieumverteilungsprozessen.

Diese Forschung trägt dazu bei, unser Verständnis der Schwingungsdynamik in molekularen Monolagen zu vertiefen und ebnet den Weg für zukünftige Untersuchungen im Bereich der Nichtgleichgewichtszustände von kondensierter Materie.

Contents

Chapter 1

Introduction

This chapter is intended to put the research that is presented in this thesis in a broader context. The main topic of this thesis is the tracking of the vibrational energy flow through adsorbate monolayers. For this reason, we decided to briefly talk about time scales and the orders of magnitude that can be observed with our setup. This will be covered in the first section. The second section gives more context to the scope of the project and emphasises the motivation of our research.

1.1 Time Scales

What is time? This seemingly simple question has been the topic of many philosophical theories and debates. Despite this fact, or maybe because of it, there is no universally agreed-upon definition of time. Physicists often define time as a coordinate that allows us to order events and measure the duration between them. Further, this coordinate is influenced by the relative motion and gravitational field of the observers, according to the theory of relativity.[1] Ultimately, the most intuitive and simple definition might just be, as Feynman puts it: "it is how long we wait!".[2]

Regardless of the actual definition of the concept, the more relevant question (for us at least) is how to measure time. Galileo supposedly used his heartbeat to count equal intervals of time for his first experiments on motion. Later, the use of sand running through an hourglass and the swinging of a pendulum became common tools to measure time. But the basic idea is always the same: measure a certain event by counting the periods of another recurring event.

Needless to say, the tracking of faster events became problematic at some point because of the practical limitations of the mechanical pendulum. This gave rise to electrical pendulums, in which it is an electric current that now swings back and forth. With these electronic oscillators, it suddenly became very easy to cut recurring events into even smaller fractions. Today, there are resonant tunnelling diodes, called RTDs that

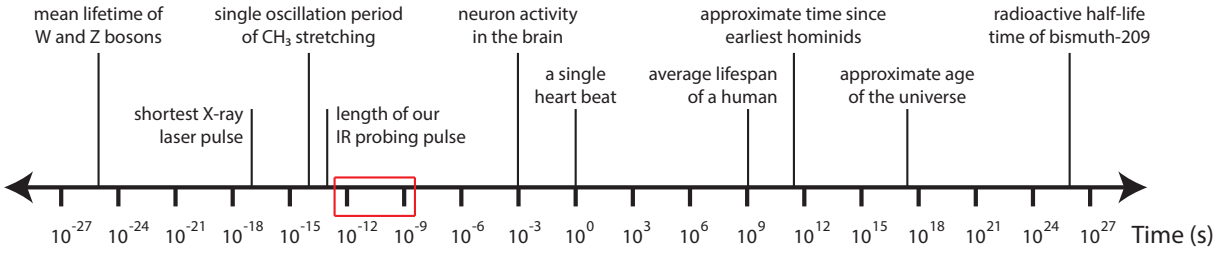

Figure **1-1**: Shown are different orders of magnitude of seconds and corresponding events. The red box indicates the orders of magnitude that we will investigate in the scope of this thesis.

are synthetically manufactured solid-state electronic oscillators, which reach fundamental frequencies into the THz regime, corresponding to periods of 10^{-12} s.[3]

This is, however, not the limit of what has been measured up till today but the method of measurement has changed. Instead of cutting a recurring event into smaller fractions, we can also measure the *distance* that something travelled. If we then also know the speed of the traveller, we can simply calculate the time it took to get from point A to point B. By this method, the shortest event that was ever experimentally measured is 247 zeptoseconds ($247 \cdot 10^{-21}$ s) long, which is the time it takes for a photon to cross a hydrogen molecule.[4]

Figure **1-1** shows a time scale in seconds that encompasses different orders of magnitude. It is quite fascinating that almost all of the known processes in our universe occur on this scale. In this work, we will investigate core vibrations in CH_3 molecules, which are oscillating at a frequency of roughly 10^{14} Hz. So a single of these oscillations has a period of about 10 fs. Unfortunately, our experiment is not able to resolve such short events because the periodicity of our 'hourglass' is limited by the width of our IR probing pulse, which has a width of about 300 fs. We can, therefore, only resolve dynamics that occur on a longer timescale. Most of the interesting vibrational dynamics in adsorbate systems occur on the picosecond scale, as we will see in the next subsection. Therefore, in the scope of this thesis, we will investigate how vibrational energy flows through our molecules on the timescale of pico- to nanoseconds, as indicated by the red box in figure **1-1**.

1.2 Vibrational Energy Redistribution

The research presented in this thesis is a subproject in a collaborative research centre (CRC 1242), which is funded by the *Deutsche Forschungsgemeinschft* (DFG). The title of the CRC 1242 reads: 'Non-Equilibrium Dynamics of Condensed Matter in the Time Domain' and tackles fundamental questions about ultrafast processes in systems that are pushed out of equilibrium.

Our subproject is titled: 'Time-Resolved 2D-IR-Spectroscopy on Adsorbate Layers' even though we decided to drop the 'two-dimensional' attribute later. Usually, this term is reserved for pump-probe setups that derive both lasers from the same source. In our case, however, the pump and probe beams are completely independent and non-coherent, which we now refer to as 'two-colour' spectroscopy.

In this thesis, we will investigate how the vibrational energy in an excited mode 'travels' through the molecular system. By doing this, we hope to reveal the fundamental intra- but also intermolecular vibrational energy redistribution mechanism. The motivation for this research can be expressed by these questions:

1. How does the system react or evolve in time after it has been brought into a non-equilibrium state?
2. How does the coupling to different degrees of freedom work?
3. How long does a 'hot' adsorbate exist on the surface after an initial chemical reaction step?

By tackling these questions we hope to gain more insights into the energy redistribution mechanism. Specifically, knowledge about 'hot' adsorbates that have enough energy to overcome the activation barriers for subsequent reactions is crucial for chemical engineering. The power to manipulate reactions and tailor a specific reaction outcome has become an increasingly attractive subject.

Relaxation Mechanisms

In 1989, Harris et al. conducted pump-probe experiments on cadmium stearate adsorbed on a silver film to investigate vibrational energy relaxation.[5,6] They observed a bi-exponential decay in the symmetric methyl stretching vibration, with a fast component (2.5 ps) convoluted with the pump pulse and a second component (165 ps). They achieved a 15% excited state population with pump pulse energies of 10 to 30 μJ. At specific wavenumbers (2940 cm^{-1} and 2965 cm^{-1}), corresponding to the Fermi resonance and the antisymmetric stretching vibration of the methyl group, they only achieved lower excited state populations of 2% to 3%, with just a fast recovery time constant and no slow component.

Further, in 1991, Harris et al. conducted similar pump-probe experiments on methylthiolate ($S-CH_3$) on an Ag(111) surface, finding a bi-exponential decay in the CH3 symmetric stretching mode.[7] The fast component had a lifetime of 2.5 to 3.0 ps, and the slow component showed temperature-dependent behaviour, decreasing from 90 ps at 110 K to 55 ps at 380 K. They proposed that the antisymmetric CH_3 stretching modes and the overtone of the CH_3 antisymmetric bending modes played a role in vibrational energy relaxation.

Coupling Between Vibrational Modes

Two-dimensional vibrational spectroscopy can be realized in both the frequency and time domains. In the frequency domain, recent advancements, particularly by the Zanni group, have driven investigations into the dynamics of molecular excitations.[8] This involves generating a sequence of three pulses from a single fs-laser pulse through pulse shaping. Spatially overlapping all three pulses, they were able to detect the free induction decay with a heterodyne setup. When combined with sum-frequency generation, this yields a selectively surface-sensitive spectroscopy method.[9] Its application to a surface system, such as CO on polycrystalline Pt, has been demonstrated, offering access to studying ultrafast processes at a level of detail previously unattainable for surface processes.[10,11]

Bonn et al. utilized frequency-domain 2D spectroscopy to investigate the coupling between different vibrational modes in the OD stretch vibration region ($2600 \pm 250\,\mathrm{cm}^{-1}$) at water surfaces.[12] Nibbering and Elsässer employed a two-colour experiment to excite the H-O-H bending vibration ($1650\,\mathrm{cm}^{-1}$) and subsequently probe this mode as well as librations in water with a spectrally broad pulse.[13] This model suggests that, after exciting high-frequency internal vibrations, a transient population of overtones of low-frequency bending and external vibrations is generated, based on the anharmonicity of vibrations. However, this transient population has never been directly observed for surface systems.

Internal Vibrational Energy Redistribution

Internal Vibrational Energy Redistribution (IVR) has been extensively studied for isolated molecules in the gas phase. One fundamental insight is that internal rotations are crucial for dynamics. In adsorbate layers, these rotations are hindered by interactions with neighbouring molecules. Thus, it is presumed that, in addition to substrate coupling, these intermolecular interactions play a significant role in adsorbate dynamics compared to the gas phase. Adsorbate layers are also distinct from molecular crystals, with one end of the molecule firmly anchored and the other end loose, which must be considered in dynamics. Dlott and colleagues demonstrated that in alkyl-SAMs, vibrational excitation propagates along the methylene chain from the headgroup to the endgroup within a few 10 ps when the substrate is rapidly heated by laser excitation.[14] The time constants scaled with chain length, approximately 5 ps/nm, depending on the number of CH2 groups in the chain.

Dipole-Dipole Coupling Effects

Since Ryberg's work in the 1980s, it has been known that in adsorbate systems with strong dipole-dipole-(Förster)-coupling, such as CO on Cu(100), one cannot consider individual, separate oscillators during vibrational excitation.[15] For example, in isotope mixtures, the line positions shift significantly with changes in the mixing ratio, and the intensities do

not faithfully represent the mixture ratio. There exists a classical theory by B. Persson to explain this phenomenon. Line positions also shift during strong excitation, i.e., in non-equilibrium situations, and this affects the dynamics of overtone excitations.[16–18]

Chapter 2

Principles

The goal of the second chapter is the presentation and interpretation of the various physical principles upon which our experimental approach is based. Since the main tool for probing our systems of interest is the use and manipulation of light, the first section aims to provide a broad, fundamental understanding of this phenomenon. Building up on that knowledge, the second section details the interaction of light with matter. This leads the reader to the final section, which introduces simple and advanced experimental methods, using light as a high-precision tool to probe molecular systems.

2.1 Theory of Light

This first section of the theory chapter is intended for a general audience because it addresses historical aspects and tackles very fundamental questions about the physical character of light. It is, therefore, not necessary to read this section in order to understand the ideas of this thesis but should rather be seen as a treat for the curious mind.

The outline of this section is as follows: The first part briefly introduces the scientific history up to the formulation of Fermat's *principle of least time*, which ultimately led to the first law about the behaviour of light. After that, the duality of wave and particle characteristics is discussed and further investigated quantum-mechanically in the third subsection. This leads to *Maxwell's equations* and his great unification of electricity, magnetism and light. Finally, we conclude the first section with the presentation of *Schrödinger's equation*, which is essential to fully describe any interaction of light with matter.

2.1.1 Principle of Least Time

Light has been a subject of study since the first civilisations emerged. However, the first known mathematical exposition of vision was given by Euclid in his *Optica* around 300

B.C.E. Contradictory to the modern view, Euclid was convinced that the process of seeing involved light rays that travel in straight lines from the eyes onto objects. Furthermore, he deduce the relation between the incident θ_i and the reflected angle θ_f of a light ray hitting a surface as[19]

$$\theta_i = \theta_f, \tag{2.1}$$

with a lack of a deeper explanation for the cause of this phenomenon.

It is widely believed that Heron of Alexandria (alive between 100 B.C.E and 100 C.E.) was the first to think of an optimum principle, which gave cause to the behaviour of light. After studying Euclid's *Optica*, Heron concluded that light always takes the shortest distance, thus explaining the reflection off a mirror.[20,21]

This, however, did not explain the refraction of light in different media and it was not until the 2nd century C.E. that Claudius Ptolemy tackled this problem. Ptolemy was supposedly the first experimentalist, as he, based on his knowledge from Euclid's *Optica*, experimentally tried to find a law of refraction with light rays that traversed from air to water. In his *Optics*, Ptolemy wrote about a certain proportionality between the incident θ_i and the refracted angle θ_r, which approximates the real parabola remarkably well for small angles, but he could not derive the full equation.[22]

Only many years later, around 984 C.E., it was the Persian Ibn Sahl who finally succeeded in developing an equation mathematically equivalent to the modern refraction law of Snellius:

$$\sin(\theta_i) = n \sin(\theta_r), \tag{2.2}$$

with the proportionality factor $n = \frac{n_r}{n_i}$ depending on the media. Sahl's findings were never published because his manuscript was eventually disassembled and partly lost. However, recent historical research suggests that Sahl was the original inventor of the law of refraction.[23–25]

The theory of optics gained a lot of attention again in the early 17th century, when Thomas Harriot rediscovered the law of refraction in 1602, without publishing his results.[25] Independently, Willebrodt Snellius discovered in 1621 the formula that was later named after him, although he also never published his findings. It was René Descartes that published the first law of refraction in 1637, without citing Harriot or Snellius. It remains, however, a topic of controversy if Descartes knew about the discoveries that were made before him or not.[26] Finally a publication made by Isaac Vossius in 1662 proved Snell's priority over Descartes in discovering the law of refraction and ultimately led to its naming.[27]

Following this enthusiasm of the 17th century, the development of science took another step. Since the observed data were now predictable with laws the next question that puzzled the human mind was the nature of this behaviour or as Feynman put it: "*can we*

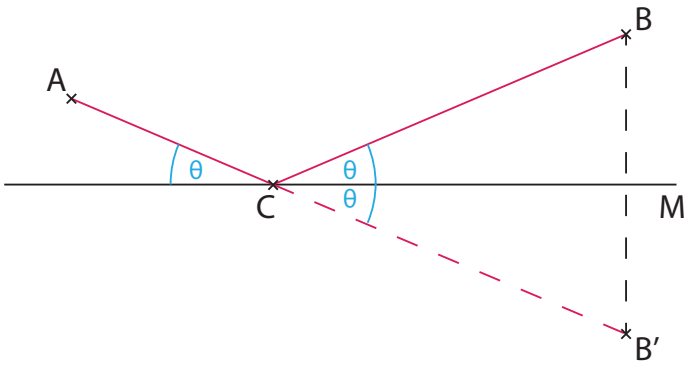

Figure **2-1**: Schematic of a light ray that is reflected at a mirror to illustrate Fermat's *principle of least time*.

find a way of thinking such that the law is evident"?[2] In 1657, Pierre de Fermat, inspired by Heron's principle of least distance thought of a way to explain the refraction of light, which could not be explained by Heron's principle. He then enunciated the *principle of least time*, stating that light always takes the path with the shortest travel time. This principle worked extremely well in explaining most of nature's behaviour. It did, however, raise a great deal of controversy as it seemed to ascribe intent to light and nature in checking for multiple paths and taking the fastest one.[28] Although the controversy has died down over the years and the theory was generally accepted, the behaviour of light is still a puzzling phenomenon, as we will see in the next subsection.

Even though Fermat's principle comes very close to explaining all of the different, complex facets of light, there are a few exceptions where we need to refine the principle a little to still be accurate. We will get to these exceptions later. First, let us see how Fermat's principle applies to mirrors and refracting media.

In figure **2-1** we see a mirror M and a light ray travelling from point A to point B. The *fastest* path from A to B is evidently the path AB, but what if we arrange the experiment in a way so that the light has to hit the mirror once? Then there is a simple geometrical trick to quickly find the solution here as well. If we mirror point B to a fictive point B' behind the mirror and look for the *fastest* path from A to B' the answer is simply the path AB'. But since B' is symmetrical to B the paths CB' and CB are the same and the path the light takes is therefore ACB. Furthermore, we can directly see that the incident angle θ is the same as the reflected angle, thus proving the law of reflection. This was already deduced by Heron with his principle of least distance, which, however, failed to explain the refraction in different media.

The law of refraction is not quite as easy to draw from qualitative arguments. It is, however, still rather simple to derive quantitatively with Fermat's principle as long as we permit the assumption that light travels slower in dense media by a factor n. In figure **2-2** we see a light ray refracting at the boundary of two arbitrary media. To apply the

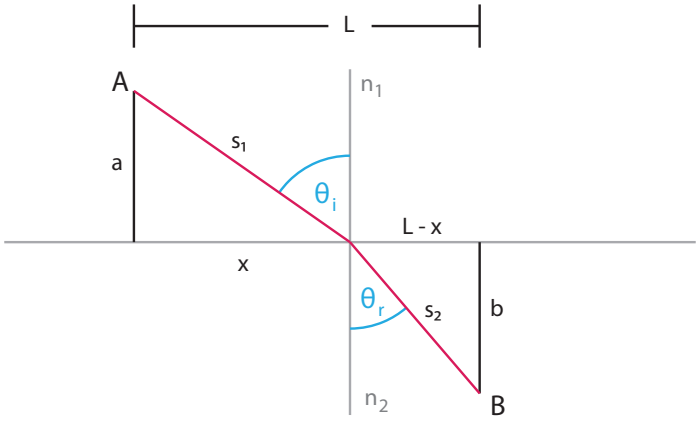

Figure **2-2**: Illustration of a light ray that is refracted at the boundary of two different media to derive Snell's law.

principle of least time to this problem we need to calculate the time t it takes to travel from point A to point B as

$$\begin{aligned} t &= \frac{s_1}{v_1} + \frac{s_2}{v_2} = \frac{s_1 n_1}{c} + \frac{s_2 n_2}{c} \\ &= \frac{n_1\sqrt{a^2+x^2}}{c} + \frac{n_2\sqrt{b^2+(L-x)^2}}{c}, \end{aligned} \tag{2.3}$$

with c, the speed of light and x as the variation parameter. Now we can optimize this quantity and directly derive the law of refraction:

$$\frac{\mathrm{d}t}{\mathrm{d}x} = \frac{n_1}{c}\underbrace{\frac{x}{\sqrt{a^2+x^2}}}_{\sin(\theta_i)} - \frac{n_2}{c}\underbrace{\frac{(L-x)}{\sqrt{b^2+(L-x)^2}}}_{\sin(\theta_r)} \stackrel{!}{=} 0 \tag{2.4}$$

$$\Rightarrow \quad \sin(\theta_i) = \frac{n_2}{n_1}\sin(\theta_r). \tag{2.5}$$

Therefore this simple principle seemed to explain the behaviour of light very accurately and one could deduce a lot of interesting phenomena from it. One curious example is the sunset. Since light always takes the *fastest* path through the atmosphere of the earth and the outer layers are a lot less dense, the actual path of the light looks something like in figure **2-3**. This is because the rays are trying to avoid the denser atmosphere for as long as possible. Consequently, when we see the sun setting on the horizon our eyes cannot distinguish where the bent light rays actually originated from and the sun is already below the horizon by a few degrees when we just see it fading.[29]

Fermat's principle in its original form, however, is not the complete "truth" as it fails to describe a certain aspect of the nature of light, which is illustrated in the following experiment. In figure **2-4** we see a source producing electromagnetic radiation that is

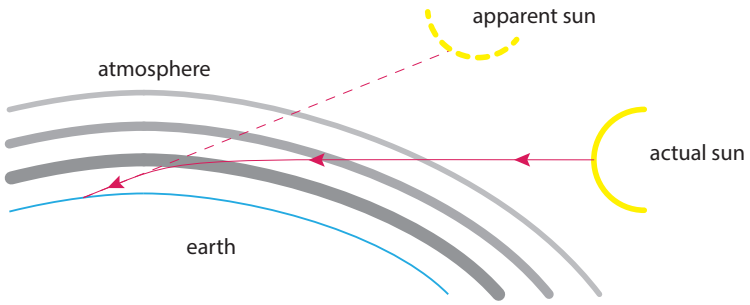

Figure **2-3**: Oversimplified sketch of a light ray travelling through the outer atmosphere. Inspired by lecture 26, volume I of the Feynman lectures.[2]

directed onto a variable slit. The opened slit is roughly in the same order of magnitude as the wavelength of the radiation. Now, the detector at point D observes the light that comes in a straight line from S and if we narrow down the slit then the light still goes through and hits the detector, although somewhat less. The detector at point D', however, only detects very small amounts of radiation with a wide slit but increasingly more when we make the slit more narrow.[2] This experimental fact cannot be explained by the original *principle of least time*, because if the detectors at points D and D' are arranged on a circular front, the paths from the middle of the slit to each detector should correspond to the same time. Therefore there should be no distinction between the two detectors and also the width of the slit should not influence the relative intensity detected by each one.

To make Fermat's principle true for all cases we need to add a locality argument to the statement. The full "truth", as far as we know, is that light checks in a certain area if similar paths correspond to the same travelling time. Or to formulate this phenomenon more precisely: light always looks for a path that lies in the vicinity of other paths where a slight deviation does not lead to a first-order change in the travelling time. This is basically what we did already when deriving the law of refraction in 2.5, we set the first-order derivative of the travelling time to zero.

So how can we explain the experiment in **2-4** with the addition of Fermat's principle? If we look at the wide slit and compare the travelling time of a path from the top part of the slit to D with a path going from the bottom part to D it turns out they are close to equal and, therefore, most of the radiation goes to D. If we look at detector D', on the other hand, the paths from the top and bottom of the slit correspond to very different times, so here we get a lot less intensity. Now, by narrowing down the slit we prohibit the light to check the outer paths and more radiation reaches D' the narrower the slit gets. Also, we learn from this experiment that the distance in which light compares the different travelling times is approximately the wavelength of the light since we set the width of the open slit close to that.

This is difficult to set up experimentally with visible light since we need a slit on the

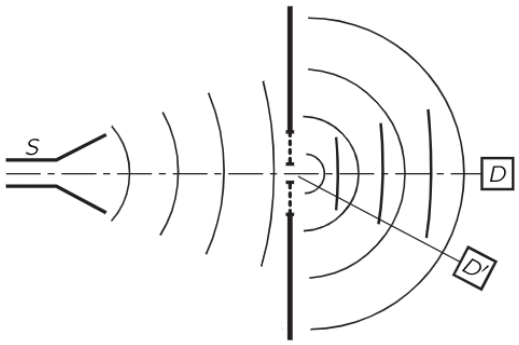

Figure **2-4**: Illustration of an experiment proving that Fermat's principle is not complete in its original form. The source S produces electromagnetic radiation that is hitting a variable slit. Depending on the width of the slit the detectors D and D' observe different amounts of radiation. Taken with permission from lecture 26, volume I of the Feynman lectures.[30]

nano-scale, but there is a very intuitive way to do this experiment qualitatively. One can look for a bright point source far away and look at it with one eye through a slit made by two fingers. When squeezing the fingers together slowly one can observe elongated lines coming from the point source. This is the same phenomenon that occurs in our experiment in **2-4** and shows that light bends behind narrow slits.

2.1.2 Wave and Particle Approximation

The curious behaviour of light has triggered a lot of speculation in history about its character. The first experiments indicated that light is a wave while others hinted more toward a particle phenomenon. The most important experiment for the latter was the *photoelectric effect*, which was first discovered by Heinrich Hertz in 1887.[31] With the prominent wave picture at the time, the expectations of this experiment were the following: when light hits a metal plate, the electromagnetic wave interacts with all the electrons in the metal simultaneously and drives them to oscillate until they have enough energy to break free of the surrounding potential. Therefore, physicists made the following predictions:

1. Increasing the amplitude of the light wave should increase the kinetic energy of the emitted electrons because the amplitude is proportional to the energy of the wave.

2. Increasing the frequency of the light wave should increase the rate of electron emission because more wavefronts per time necessarily release more electrons per time.

On the contrary, the observation was entirely different and impossible to explain with the wave picture. In figure **2-5** we can see the essence of the experiment. When red light,

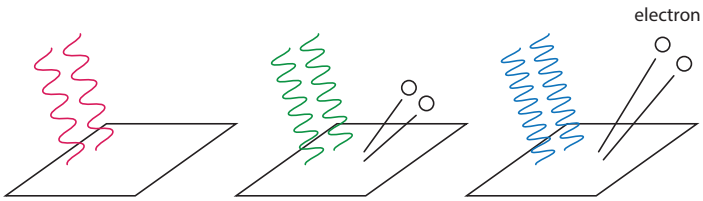

Figure **2-5**: Visible light of different frequencies hits a metal surface. The red light does not release electrons and the green and blue light release the same amount of electrons, but with different kinetic energies.

with a lower frequency, hits a metal surface, no electrons are emitted at all. But if we increase the frequency and pass a certain threshold, let's say green light, then we always detect the same amount of released electrons. Only an increase in the amplitude of the light wave resulted in a higher rate of electron emission.

This phenomenon was first completely explained by Albert Einstein in 1905 when he, based on Planck's theories, proposed that the energy of light is not continuously distributed like a wave but instead localised in discreet energy quanta, later called photons. This photon energy is given by the product of Planck's constant and the frequency of the electromagnetic radiation $E_p = hf$ and one of these quanta can only ever release one photoelectron, thereby verifying the particle character of light.[32]

The wave picture of light, on the other hand, was established a century before Einstein, in 1803, when Thomas Young devised a setup that was later known as the original double-slit experiment.[33] In figure **2-6** is a sketch of Young's experiment. Here we have a source of radiation that is directed at a barrier with two slits and a screen behind the barrier observes the projected radiation. Young did his experiment with sunlight and demonstrated the resulting interference pattern, which is typical for overlapping waves.

To understand this pattern we need to understand how waves interfere with each other. Let us define two arbitrary, oscillating functions with amplitudes A_i, frequencies ω_i and phases ϕ_i, representing the waves that are forming in the slits and make a superposition S of the two

$$S = A_1 \cos(\omega_1 t + \phi_1) + A_2 \cos(\omega_2 t + \phi_2). \tag{2.6}$$

In our particular case, we have a single source producing the radiation in the two slits, so we can approximate the amplitudes and frequencies to be equal. Furthermore, if we make use of a trigonometric identity we can see what the resulting wave is composed of,

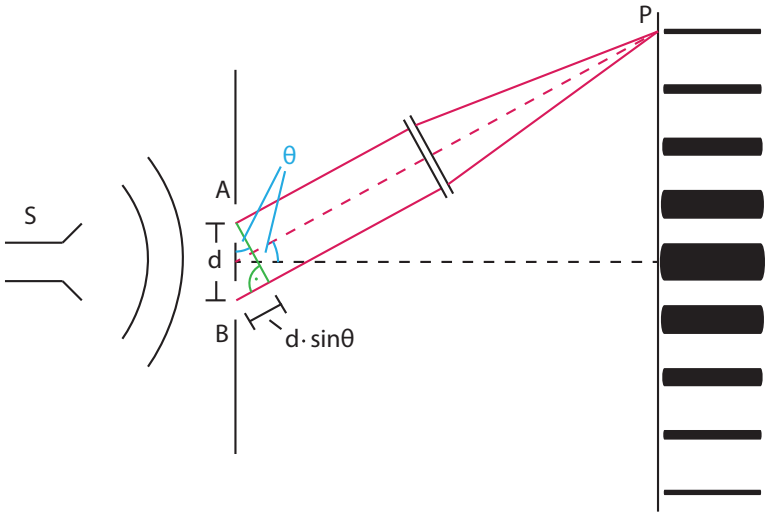

Figure **2-6**: The double-slit experiment. A source S produces radiation that is directed onto a barrier with two slits. Behind the barrier is a screen with an interference pattern.

directly:

$$\left[\cos(A) + \cos(B) = 2\cos\left(\frac{A+B}{2}\right)\cos\left(\frac{A-B}{2}\right)\right] \tag{2.7}$$

$$\Rightarrow \quad S = \underbrace{2A\cos\left(\frac{\phi_1 - \phi_2}{2}\right)}_{A_S}\cos\left(\omega t + \frac{\phi_1 + \phi_2}{2}\right). \tag{2.8}$$

This equation reveals some interesting characteristics of the resulting wave: it oscillates with the same frequency as the original waves, has a phase shift that is the average of the two initial phases and the superposed amplitude A_S is only dependent on the difference of the two initial phases $\Delta\phi = \phi_1 - \phi_2$, for a fixed amplitude.

In order to understand the pattern in figure **2-6** we first need to clarify what it is that we see. The bright spots (illustrated as black lines) are bright because there is a lot of *energy* per *area* per *time* and, naturally, there is much less energy in the darker areas in between. That is what we call intensity. Now we need to figure out how energy is transmitted by an electromagnetic wave to get a relationship between our wave in equation 2.8 and the interference pattern in figure **2-6**. Qualitatively speaking, when electromagnetic radiation hits a surface, the force that every charge in the material experiences is proportional to the field strength of the radiation if the field is sufficiently weak. So the displacements and velocities are all proportional to the field and the kinetic energy that is developed in the charges is proportional to the square of the field.

Following this qualitative analysis, we now know that the intensity of the interference pattern is proportional to the square of the amplitude of our resulting wave A_S, which, in turn, is only dependent on the phase difference $\Delta\phi$. Looking back at equation 2.8 we

can now deduce how the bright spot in our intensity correlates to a phase difference of $\Delta\phi = 2\pi n$, with an integer $n \geq 0$ and, consequently, there are dark spots for $\Delta\phi = 2\pi n + \pi$. Since the waves travel at the same velocity c, the only relevant factor to determine the phase difference then becomes the distance by which two wavefronts are delayed and the wavelength λ of the wave. If we take a look at figure **2-6** again we see a sketch of wavefronts coming from slit A to P and from B to P and the delay between these wavefronts is given by $d\sin(\theta)$, with d being the spacing between the slits and θ representing the angle at which the wavefronts are travelling to the screen.

The final step to derive the general formula is then to recall how waves interfere constructively when two crests are overlapping and how they cancel each other if a crest hits a trough. So if the delay distance is exactly a wavelength or a multiple of the wavelength we will observe constructive interference on the screen at that angle and dark spots in between. That gives us the following general formula for the phase difference between two interfering waves

$$\Delta\phi = \phi_1 - \phi_2 = 2\pi\frac{d\sin(\theta)}{\lambda}. \tag{2.9}$$

The demonstration and explanation of the double-slit experiment by Young in 1803 led the scientific world to believe that light is indeed a wave and it was generally accepted for a century until Einstein published his analysis of the photoelectric effect. Hence, the character of light remained a topic of controversy and to many it still is. The most accurate statement one can make about light is probably that it is neither a particle nor wave but behaves in a "typical" quantum-mechanical manner. This, of course, is a very unintuitive statement but it is the only one we can make because human intuition and logic apply to our experience with large objects in a macroscopic world and things on the atomic scale do not behave the same way. Therefore, we have to learn about this behaviour abstractly, using different tools and methods but we cannot connect our findings to anything we have a direct experience with, which makes it so hard to understand.

On the upside, however, all things on the atomic scale seem to behave the same way. What we know about electrons, protons and the like also applies to photons and they all behave like "particle-waves" or in a quantum-mechanical fashion as we will see in the next subsection.

2.1.3 Principles of Quantum Mechanics

To illustrate all of the peculiar behaviour of things on a small scale it is enough to present one key experiment, which is taken from lecture 37, volume I of the Feynman lectures.[2] This key experiment is the double-slit experiment, which we have already presented in the last section, but this time we are using macroscopic bullets and think of them as indestructible for reasons of simplicity. In figure **2-7** we can see the experimental setup:

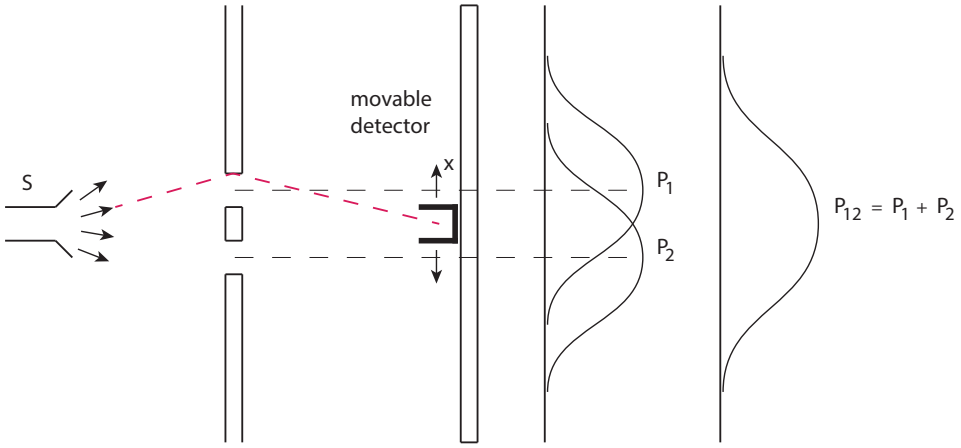

Figure **2-7**: The double-slit experiment with bullets. A gun shoots bullets over a large angular spread onto a wall with two holes and behind the wall is a detector to count the bullets that arrive. On the right side are plots of the probability of arrival if hole 2 is blocked (P_1), hole 1 is blocked (P_2) or both holes are open (P_{12}).

an imperfect gun shoots bullets randomly over a large angular spread onto a wall with two holes. Behind this wall is another wall with a moveable detector to count the bullets at an arbitrary position x and since the bullets are indestructible the detector always counts whole bullets, not fractions.

By measuring the lumps of bullets at every position in a certain time interval we can find the probability of their arrival as a function of x. If hole 2 is blocked then we get the probability P_1 and vice versa, which is sketched in figure **2-7**. When both holes are open then the probability function is the sum of the single hole probabilities $P_{12} = P_1 + P_2$. This is the classical expectation of a double-slit experiment with macroscopic bullets.

The interesting part occurs when the experiment is done with electrons, which was hard to realise at the time due to experimental limitations. However, the effect has been shown in many experiments of different scales and proportions in the past. In 1961, Jönsson was able to show interference patterns with electrons but was unable to observe single-electron diffraction.[35] With the advancement in technology on the nano-scale, however, the original double-slit experiment, with electrons instead of light, was finally realised by Bach et al. in 2013 and is illustrated in figure **2-8**. Apart from experimental difficulties, the setup is the same with the only exception that our bullets are now on an atomic scale. Surprisingly, this results in a probability function that is not the superposition of the single hole probabilities $P_{12} \neq P_1 + P_2$, but rather looks like the interference pattern that we already saw in figure **2-6**. Furthermore, if the rate at which the electrons come out of the gun is greatly reduced so that there is only one electron detected at a time, the probability distribution will also eventually look like the interference pattern again. This suggests that the electrons not only interfere with each other but with themselves, which

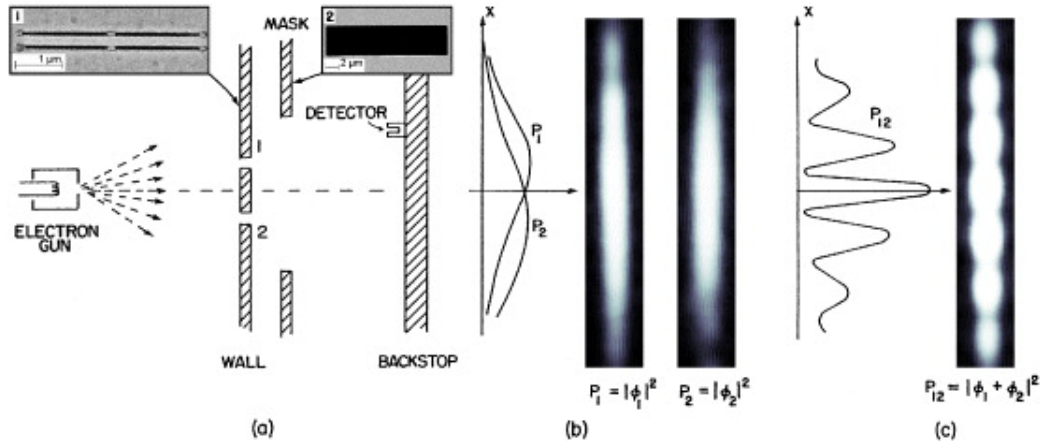

Figure **2-8**: The double-slit experiment with electrons. (a) An electron gun shoots electrons onto a wall with two holes. Behind the wall is a moveable mask to temporarily block the holes and a detector to count the electrons that arrive. (b) The probability of arrival P_1 if hole 2 is closed and P_2 if hole 1 is closed, respectively. (c) The probability of arrival P_{12} when both holes are open. Taken from Bach et al. (2013).[34]

cannot be explained in any classical way.

There were a lot of creative ideas to find ways of explaining this peculiar behaviour and the most prominent was putting a light source behind the holes so one could observe the scattered light when an electron passes to determine what hole it went through. Although the observation worked, it resulted in an even more confusing phenomenon. When the light was scattered from the electrons and one could tell which hole the electron went through, the probability distribution came out to be the one from the macroscopic bullets in figure **2-7**. Moreover, the intensity of the light was made very dim and the frequency of the radiation was reduced so that the light could not disturb the electrons as much as to destroy the interference pattern. But it all resulted in the same phenomenon: if one could tell through which hole the electrons went then one would get the superposition of the two single-hole probabilities and if the method of detection was too weak to accurately tell which hole the electron took then one would get the interference pattern of waves as a result.

This led Heisenberg to suggest in 1927 that there had to be a general limitation to the experimental capabilities in order for the laws of nature to be consistent on the atomic scale.[36] He stated with his *uncertainty principle* that the x-component of the momentum p_x of a particle cannot be measured precisely without taking the position x of the particle into account, at any instant. Three years earlier, in 1924, de Broglie had studied the interference of electrons and proposed that particles also exhibit wave characteristics with a wavelength that is inversely proportional to their momentum $\lambda = \frac{h}{p}$. Therefore, Heisenberg assumed the uncertainty in position x_1 is proportional to the wavelength and

the uncertainty in the momentum p_1 is given by de Broglie:[37]

$$\begin{aligned} x_1 &\propto \lambda, \\ p_1 &\propto \frac{h}{\lambda} \\ \rightarrow x_1 p_1 &\propto h. \end{aligned} \tag{2.10}$$

Thus assuming that the product of uncertainties for position and momentum had to be proportional to Planck's constant h. This was the original statement of Heisenberg's *uncertainty principle*, although he did not give a precise definition for the uncertainties x_1 and p_1. Later in the same year 1927, Earle Kennard proved the general case and derived the modern inequality[38]

$$\sigma_x \sigma_p \geq \frac{\hbar}{2}, \tag{2.11}$$

with the standard deviations of position σ_x and momentum σ_p and the reduced Planck constant $\hbar = \frac{h}{2\pi}$. This general form reads: "If one makes a measurement on any object and determines the x-component of the momentum with a standard deviation of σ_p, one cannot, at the same time, measure the x-position more accurately than $\sigma_x \geq \frac{\hbar}{2\sigma_p}$." This is a fundamental rule of nature to protect quantum mechanics and, since nobody has found a way to measure anything more precisely than 2.11 yet, we assume the *uncertainty principle* to be true. On a side note, this principle also solves one of the greatest mysteries of the atomic theory in explaining why atoms are stable and electrons do not crush into the nucleus, which is predicted by classical physics. When an electron comes close to the centre, its position becomes increasingly sharper and according to the *uncertainty principle*, the average momentum rises in turn. For this reason, there is always an equilibrium between localisation around the nucleus and the momentum of the electron.

Going back to the double-slit experiment, we will now derive the first principles of quantum mechanics. According to the interference pattern of the electrons, it seems reasonable to describe their behaviour with a wave function, similar to the ones we have used in the previous subsection. On the other hand, the detector counts single hits and not arbitrary values, so we have to assume there is also a probability of arrival for each electron. Combining these ideas, we can think of the probability as an intensity, which, recalling the last subsection again, is given by the square of the amplitude of the wave function. So ultimately, the electrons are described by a wave function with a probability amplitude ϕ and the square of this amplitude gives us the probability of arrival at the screen $P = \phi^2$.

With that, we can finally summarise the main conclusions from the double-slit experiment for a general case:[2]

1. The probability of an event in an ideal experiment is given by the square of ϕ, which

is called the probability amplitude:

$$\begin{aligned} P &= \text{probability}, \\ \phi &= \text{probability amplitude}, \\ P &= \phi^2. \end{aligned} \tag{2.12}$$

2. When an event can occur in several alternative ways, the probability amplitude for the event is the sum of the probability amplitudes for each way considered separately. There is interference:

$$\begin{aligned} \phi &= \phi_1 + \phi_2 \quad , \\ P &= (\phi_1 + \phi_2)^2 \end{aligned} \tag{2.13}$$

3. If an experiment is performed which is capable of determining whether one or another alternative is taken, the probability of the event is the sum of the probabilities for each alternative. The interference is lost:

$$P = P_1 + P_2 \tag{2.14}$$

Therefore, at the core of quantum mechanics lies the inability to predict exactly what is going to happen with a given set of initial conditions, since we can only predict the odds. This is a very important difference between classical and quantum mechanics and has given rise to a lot of speculation about the determinism of the world. No one knows what kind of machinery could produce such curious laws and maybe this is as far as we can go in trying to understand nature, but if we accept this fact then the whole theory of quantum mechanics gives us a very effective tool to predict nature, nonetheless. In order to appreciate this theory, however, we first need to define and interpret the previously mentioned wave function, which will be done in subsection 2.1.5.

2.1.4 Maxwell's Equations

To approach the topic of wave functions and wave equations, we are going to briefly cover the history of scientific advances in electricity and magnetism that led to the present view of calling light an electromagnetic wave.

At the beginning of the 19th century, there have been a lot of accomplishments in the understanding of electromagnetics. Coulomb published the law to describe the force between two stationary charged particles in 1785,[39] around 1820 Ampére laid the foundations for electromagnetism after Hans Ørsted discovered the magnetic effects of an electric current flowing through a wire[40] and electromagnetic induction was discovered independently by Faraday and Henry in 1831 and 1832, respectively.[41]

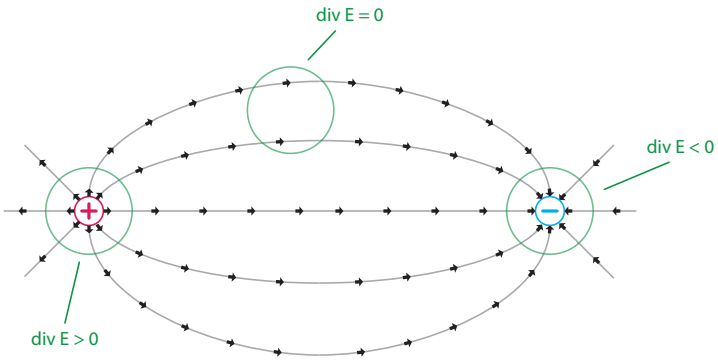

Figure **2-9**: Possible visualisation of the resulting electric field **E** of a positive and negative charge in 2 dimensions. Every point in space is associated with a vector that represents the electric force on a unit charge at this point. The divergence of **E** vanishes everywhere, except in the regions where there is charge present.

These experimental results and laws, however, were not written down and organised properly, so they were widely seen as independent phenomena. It was not until the 1860s that one of the greatest unifications in the history of physics took place when James Maxwell combined the laws of electricity, magnetism and light in a series of papers. In 1873, he finally published the summary of his findings with more than 20 equations governing the behaviour of electromagnetism.[42] These equations were later synthesized into the 4 known *Maxwell's equations* using vector calculus by Oliver Heaviside:[43]

$$\boldsymbol{\nabla} \cdot \mathbf{E} = \frac{\rho}{\epsilon_0} \tag{2.15}$$

$$\boldsymbol{\nabla} \cdot \mathbf{B} = 0 \tag{2.16}$$

$$\boldsymbol{\nabla} \times \mathbf{E} = -\frac{\partial \mathbf{B}}{\partial t} \tag{2.17}$$

$$\boldsymbol{\nabla} \times \mathbf{B} = \mu_0 \mathbf{j} + \mu_0 \epsilon_0 \frac{\partial \mathbf{E}}{\partial t} \tag{2.18}$$

The variables **E** and **B** represent the electric and the magnetic field, respectively and the universal constants μ_0 and ϵ_0 are the permeability and the permittivity of free space. Furthermore, we have the charge density ρ and the current density **j** and all variables that are printed in bold denote three-dimensional vectors.

The first of *Maxwell's equations*, which is also called Gauss's law, states that the scalar product of the differential operator nabla and the electric field is proportional to the charge density, which reads as: "divergence of **E** is equal to $\frac{\rho}{\epsilon_0}$". The divergence is, essentially, a mathematical tool but in physics, we can find a deeper interpretation of this derivative operator. To get a better understanding of the divergence we need to recall that the electric field is a vector field, which is illustrated in figure **2-9**. We can, for example, compare the electric field with a gas flow in the sense that every point in space has a

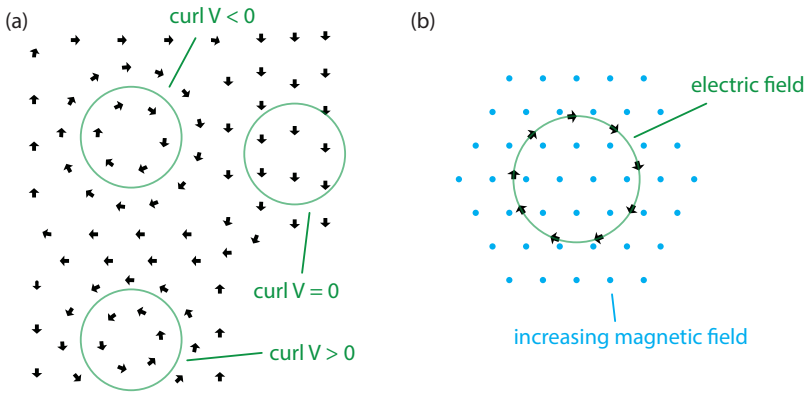

Figure **2-10**: Illustration of the curl of a vector field. (a) The curl of a vector field $\mathbf{V}$, representing the flow of gas molecules, indicates if there is rotational movement in the vicinity of any point in space. (b) An axially symmetric magnetic field that increases in time produces a non-conservative, rotational electric field.

vector of magnitude and direction, representing the velocity of the gas molecules at that point. Naturally, the electric field is no gas and the vectors represent the electric force on a unit charge at a certain point in space. However, this concept illustrates how divergence can be interpreted physically as it indicates how much is flowing in and out of a region. As we can see in figure **2-9**, the flux through any closed volume, which is the definition of the divergence, is zero everywhere, except in the regions where the gas is contracting and expanding. Therefore, the first of *Maxwell's equations* predicts that the electric field has sources and sinks, which are the electric charges in our universe.

Going to the second equation, we can already see the strong statement that the magnetic field $\mathbf{B}$ has no such sinks and sources, meaning there are no magnetic monopoles and the magnetic field lines always form loops. Since nobody has ever found something that resembles a magnetic analogue to an electric charge, Maxwell's predictions are believed to be true.

The third of *Maxwell's equations*, which is also called Faraday's law of induction states that the vector product of nabla and $\mathbf{E}$ is equal to the change of $\mathbf{B}$ in time, which reads as: "the curl of $\mathbf{E}$ is $-\frac{\partial \mathbf{B}}{\partial t}$". To get an intuition about the curl of a vector field, it again helps to think about the vector field as a representation of the flow of gas molecules. In figure **2-10** we can see how the curl at any point in space is an indicator of rotational movement in the vicinity of that point. Therefore, Faraday's law implies that a changing magnetic field forces charges on a circular motion perpendicular to the field. This seemingly simple law laid the foundation for electric motor technology and drastically changed the modern way of life.

The fourth and last equation is based on Ampére's law, which states that the flux of the magnetic field is only dependent on a flowing electric current. In general, this is true for static fields, but when Maxwell tried to combine the known laws for the dynamic

case he found inconsistencies. He found that adding the second term on the right side of equation 2.18 made the equations mutually consistent without changing the other laws.[44] This addition ultimately led to the naming of *Maxwell's equations* and predicts another beautiful phenomenon. Not only do changing magnetic fields generate perpendicular electric fields, but these electric fields themselves are producing new magnetic fields as well so that there is a constant perpetual interplay that extends through space, completely disconnected from the source. Surprisingly, this propagation does not rely on any medium, but the fields rather maintain themselves in accordance to *Maxwell's equations*, which was difficult to accept by the scientific world at the time and eventually came to be known as electromagnetic radiation.

The connection to light, however, was not immediately apparent and came to Maxwell after further analysis of his newfound phenomenon. With the vector identity for an arbitrary vector function of space $\mathbf{V}$

$$\boldsymbol{\nabla} \times (\boldsymbol{\nabla} \times \mathbf{V}) = \boldsymbol{\nabla} \cdot (\boldsymbol{\nabla} \cdot \mathbf{V}) - \nabla^2 \mathbf{V}, \tag{2.19}$$

one can quickly deduce from *Maxwell's equations* the equation that governs the propagation of the electric and magnetic field in a vacuum, respectively. In the case of the electric field $\mathbf{E}$ we need to take the curl of the third equation

$$\begin{aligned} \boldsymbol{\nabla} \times (\boldsymbol{\nabla} \times \mathbf{E}) &= \boldsymbol{\nabla} \times \left(-\frac{\partial \mathbf{B}}{\partial t} \right) \\ \Leftrightarrow \quad \boldsymbol{\nabla} \cdot \underbrace{(\boldsymbol{\nabla} \cdot \mathbf{E})}_{=0} - \nabla^2 \mathbf{E} &= -\frac{\partial}{\partial t} \underbrace{(\boldsymbol{\nabla} \times \mathbf{B})}_{\mu_0 \epsilon_0 \frac{\partial \mathbf{E}}{\partial t}} \\ \Leftrightarrow \qquad \nabla^2 \mathbf{E} - \mu_0 \epsilon_0 \frac{\partial^2}{\partial t^2} \mathbf{E} &= 0. \end{aligned} \tag{2.20}$$

On the right side of the first equation, we made use of the interchangeability of time and space derivatives in Euclidean space and, since we are looking for solutions in a vacuum we set ρ and $\mathbf{j}$ to zero.

The resulting equation is a second-order linear partial differential equation for the description of three-dimensional waves. Even though we have no charges and no currents in a vacuum, the solution for the electric field is not necessarily zero, although that is one possible solution. Other solutions for this kind of differential equation are the periodic sin and cos functions, which we already used earlier to describe waves. The general approach to solving periodic problems like this is to make use of *Euler's formula*

$$\mathrm{e}^{ix} = \cos(x) + i \sin(x), \tag{2.21}$$

with the imaginary unit i. This equation is praised by Feynman as "the most remarkable formula in mathematics" because it ultimately describes a connection between algebra

and geometry.[2] In physics, we can exploit this by approaching oscillating problems with complex exponential functions, which are a lot easier to handle than their geometric counterparts sin and cos. It is, however, necessary to think carefully about what it is that the complex number describes and how real and imaginary parts correlate to physical observables because nothing that we can measure is complex in nature and *Euler's formula* is only a tool to make the mathematics easier.

Utilizing this formula, one possible solution for the three-dimensional wave equation 2.20 is

$$\mathbf{E}(\mathbf{r}, t) = \mathbf{E}_0 \mathrm{e}^{i(\mathbf{kr}-\omega t)}, \tag{2.22}$$

with an euclidean vector $\mathbf{r} = (x, y, z)$, an oscillating frequency ω and a wavevector $\mathbf{k} = (k_x, k_y, k_z)$. The magnitude of the wavevector $|\mathbf{k}| = k = \frac{2\pi}{\lambda}$ is the spacial angular frequency of the wave, describing the number of completed oscillations per unit of space. The orientation of the wavevector is in the direction of the phase velocity $v_p = \frac{\omega}{k}$, which means it is normal to the surfaces of constant phase, called wavefronts. Solutions like 2.22 are called *plane waves* because at any given time they look the same as one moves along any plane $\mathbf{k} \cdot \mathbf{r} =$ constant.

When we solve the wave equation for a plane wave

$$\begin{aligned} \left(\nabla^2 - \mu_0\epsilon_0 \frac{\partial^2}{\partial t^2}\right) \mathbf{E}_0 \mathrm{e}^{i(\mathbf{kr}-\omega t)} &= 0 \\ \left(-k^2 + \mu_0\epsilon_0\omega^2\right) \mathbf{E}_0 \mathrm{e}^{i(\mathbf{kr}-\omega t)} &= 0, \end{aligned} \tag{2.23}$$

we get a very interesting result for the relation between the phase velocity and the product of $\mu_0\epsilon_0$. For the non-trivial case of $\mathbf{E}_0 \neq 0$ we have

$$\begin{aligned} -k^2 + \mu_0\epsilon_0\omega^2 &= 0 \\ \Rightarrow v_p = \frac{\omega}{k} &= \frac{1}{\sqrt{\mu_0\epsilon_0}} = c_0. \end{aligned} \tag{2.24}$$

The permeability of free space μ_0 and the permittivity of free space ϵ_0 are quantities that can be determined by various electromagnetic experiments. In the relation of 2.24, however, they equate to another important constant, which was already determined from optical experiments during Maxwell's time to be $c_0 = 299792458\frac{\mathrm{m}}{\mathrm{s}}$ and is known as the speed of light in vacuum. This means that the wavefronts of the electric and magnetic fields travel through space with the speed of light and it strongly implies a connection between electromagnetism and light, which drove Maxwell to propose that light is not a different phenomenon but indeed the radiation of these fields. And, although his proposition was not accepted immediately, Maxwell has been proven right in countless experiments ever since.

2.1.5 Schrödinger's Equation

Coming back to quantum mechanics, we are wrapping up the introductory section with the moment when the theory of quantum mechanics was essentially born.

In 1926, Erwin Schrödinger wrote down the first-ever quantum-mechanical equation to explain the behaviour of atomic particles.[45] This equation, however, is impossible to derive from anything because there are no known fundamental laws governing quantum mechanics and we only have the observations we acquired in section 2.1.3 from experimentation. *Schrödinger's equation*, therefore, is a construct that originated in his mind as an attempt to describe the curious behaviour of interfering electrons and probability amplitudes. Nonetheless, the reason it is still relevant almost a century later is the fact that it manages to explain chemical binding, the energy level of an atom and in general all atomic phenomena except those involving relativity, at least in theory. In reality, only the simplest systems can be calculated analytically because the solutions to the equations quickly become too complicated. To approach more complex systems one needs to find reasonable approximations and use numerical calculus, but even then Schrödinger's equation prevails.

Although we cannot deduce the Schrödinger equation from a higher governing law like we did the wave equation from *Maxwell's equations* in the last subsection, we will try to give the reader some sort of motivation to at least make the idea reasonable. Schrödinger knew that in order to describe interference phenomena and the fact that particles are no longer localised but distributed probabilistically he would need some sort of wave as the plane wave in equation 2.22. This wave function had to predict the probability of the particle's location in space and the change of this probability in time. Further, it may seem reasonable to find a relation that connects ω and $\mathbf{k}$ in 2.22 to physical properties of particles like kinetic and potential energy. Taking into account de Broglie's wavelength $\lambda = \frac{h}{p}$ and recalling the spatial angular frequency $|\mathbf{k}| = k = \frac{2\pi}{\lambda} = \frac{p}{\hbar}$ we can express the energy of a particle as

$$E_{\text{particle}} = E_{\text{kinetic}} + E_{\text{potential}} = \frac{p^2}{2m} + V(\mathbf{r}) = \frac{(\hbar k)^2}{2m} + V(\mathbf{r}), \tag{2.25}$$

with the mass m of the particle and an arbitrary potential $V(\mathbf{r})$. Combining this with Einstein's formula for the photon energy

$$E_{\text{photon}} = hf = \hbar\omega \tag{2.26}$$

we get the important relation

$$\hbar\omega = \frac{(\hbar k)^2}{2m} + V(\mathbf{r}). \tag{2.27}$$

We know that our probability function is some kind of wave, so we need a differential equation, not unlike the wave equation in 2.20 to derive the evolution of our function in

time. Therefore, the idea is to look for derivates that satisfy 2.27. Specifically, we have the ansatz of a plane wave and take derivates to find ω and k:

$$\Psi(\mathbf{r},t) = \Psi_0 \mathrm{e}^{i(\mathbf{kr}-\omega t)}, \tag{2.28}$$

$$\frac{\partial \Psi(\mathbf{r},t)}{\partial t} = -i\omega\Psi(\mathbf{r},t), \tag{2.29}$$

$$\nabla^2\Psi(\mathbf{r},t) = -k^2\Psi(\mathbf{r},t). \tag{2.30}$$

Incorporating this into our relation 2.27, we finally get

$$i\hbar\frac{\partial}{\partial t}\Psi(\mathbf{r},t) = \underbrace{\left(-\frac{\hbar^2}{2m}\nabla^2 + V(\mathbf{r})\right)}_{\hat{H}}\Psi(\mathbf{r},t), \tag{2.31}$$

with the energy operator $\hat{H}$ usually called the *Hamiltonian* or *Hamilton operator*.

This is Schrödinger's famous equation and arguably marks the birth of the quantum-mechanical description of matter. It describes the form of the probability wave that governs the non-relativistic motion of atomic particles in an arbitrary potential $V(\mathbf{r},t)$. One can take relativistic effects into account and this was done by Dirac in 1928 after Schrödinger published his findings, but we will not get into that in this thesis.[46]

With the discovery of an equation to precisely calculate the wave function of atomic particles came the topic of debate of how to interpret the wave function physically. Schrödinger himself struggled quite a bit with the complex nature of his equation and even tried to avoid the explicit appearance of the imaginary unit i.[47] When we introduced the complex function of *Euler's formula* in 2.21, we specifically mentioned carefully defining what parts of the function correlate to physical quantities since nothing that we can measure can be complex. In the same sense, Schrödinger only attached physical meaning to the real component of his wave function at first, but the fact that his equation itself already features the imaginary unit might imply how the complex nature of the wave function is more than a mathematical tool, but an intrinsic part of quantum mechanics.

The discussions of Niels Bohr and Werner Heisenberg mostly contributed to what is now known as the *Copenhagen interpretation* of quantum mechanics.[48] It is a collection of views about the meaning of the wave function and quantum mechanics altogether and the one that is most commonly taught. The physical interpretation of the wave function, however, goes back to the statistical calculations of Max Born who interpreted the square of the wave function, which is a real number, as the probability density of the particle's location at a given time.[49] Thereby, Born circumvented the conflict of a complex wave function because only its square is observable as a physical quantity and in time this view was generally accepted.

This concludes the section about some of the fundamental ideas of light and the quantum-mechanical theory and hopefully paved the way for the next topic of how light interacts with matter.

2.2 Interaction of Light and Matter

This section tackles the phenomena that arise when light interacts with matter. The appreciation of these phenomena is essential for any kind of spectroscopic experimental approach, as it builds the basis for most spectroscopic methods. At first, we introduce the model of the harmonic oscillator, which is a linear approximation to many spectroscopic problems and usually acts as a decent starting point. This knowledge, in turn, is then used to explain the scattering of light at atoms and molecules, which leads us to the polarisation of the electromagnetic wave and its effect on materials. In conclusion, we synthesise the previously mentioned topics in an attempt to clarify the origin of the refractive index, which we defined in the last section as the attenuation factor of the speed of light in different media.

2.2.1 The Harmonic Oscillator

The oscillation of the electric field vector in an electromagnetic wave is the driving force for most optical phenomena. This type of fluctuation, however, is not limited to light. In fact, there are a plethora of phenomena in our world that can be described by an oscillating motion, like the flow of electrons in an AC circuit, a mass on a spring, but also the growth of bacteria in interaction with the food supply and the population of foxes and rabbits as hunter and prey. All of these phenomena are described by linear differential equations with constant coefficients:[2]

$$a_n \frac{\partial^n y}{\partial t^n} + a_{n-1} \frac{\partial^{n-1} y}{\partial t^{n-1}} + \cdots + a_1 \frac{\partial^1 y}{\partial t^1} + a_0 y = f(t), \tag{2.32}$$

where the integer n indicates the order of the differential equation.

In our case, we are interested in the motion of the electrons in an atom, which are bound to a certain region around the nucleus by the interplay of the electric force and the uncertainty principle, as described in subsection 2.1.3. An external force can push the electrons out of their equilibrium position, which starts an oscillating motion as soon as the external force disappears because the electrons are compelled to get back to their initial equilibrium. As mentioned before, this motion is the same as that of a mass attached to a spring and can be approximated by

$$F_s = m \frac{\partial^2 \mathbf{x}}{\partial t^2} = -k\mathbf{x}. \tag{2.33}$$

Here, F_s is the restoring force exerted by the spring, m is the mass that oscillates, $\mathbf{x}$ is the displacement vector from the equilibrium position and k is not to be confused with the wavevector, but represents a material constant of the spring or in our case the atom. Equation 2.33 is called *Hooke's law* and it approximates oscillatory motion with the idea

of a linear restoring force, proportional to the displacement $\mathbf{x}$.[50] This approximation is only valid for weak external forces such that the displacement of the mass is small in comparison to the total possible deformation of the system but this simple approach often gives a decent insight into the problem at hand.

We can solve this equation with a general oscillating function, utilising *Euler's formula* in 2.21 to obtain

$$\mathbf{x}(t) = \mathbf{x_0} \mathrm{e}^{-i\omega_0 t} \tag{2.34}$$

$$\Rightarrow m\omega_0^2 = k, \tag{2.35}$$

which gives us an important relation for the frequency of the oscillation $\omega_0 = \sqrt{\frac{k}{m}}$. Note that this frequency is in no way dependent on the force that was applied to start the motion, it is only determined by the mass and k, which makes ω_0 a characteristic frequency of the system, called a *resonance*.

To approach a more realistic case, one can refine *Hooke's law* to describe the response of the system when the external force is constantly applied in the form of an oscillating function $\mathbf{F}(t)$, like the electric field vector of radiation. Furthermore, we should introduce some sort of damping parameter γ, which forces the oscillation to die out at some point, to better represent a real situation. In general, such a problem is very difficult to solve because of the complexity of this frictional term. There is, however, an often-used approximation of a frictional force that is proportional to the speed of the motion, which, more often than not, gives good results for many problems. With that, we can formulate our differential equation for a forced oscillator with damping as

$$m\frac{\partial^2 \mathbf{x}}{\partial t^2} + m\gamma\frac{\partial \mathbf{x}}{\partial t} + m\omega_0^2 \mathbf{x} = \mathbf{F}(t). \tag{2.36}$$

If we solve this equation for an oscillating external force $\mathbf{F}(t) = \mathbf{F_0}\mathrm{e}^{-i\omega t}$ and expect the system to respond with the same frequency $\mathbf{x}(t) = \mathbf{x_0}\mathrm{e}^{-i\omega t}$ we can derive the amplitude of the resulting oscillation as

$$\left(-\omega^2 - i\omega\gamma + \omega_0^2\right)\mathbf{x_0}\mathrm{e}^{-i\omega t} = \frac{\mathbf{F_0}}{m}\mathrm{e}^{-i\omega t} \tag{2.37}$$

$$\Rightarrow \mathbf{x_0}(\omega) = \frac{\mathbf{F_0}}{m}\frac{1}{\omega_0^2 - \omega^2 - i\omega\gamma}. \tag{2.38}$$

Equation 2.38 describes the amplitude of an oscillating electron bound to a nucleus in dependence on the driving frequency of an external fluctuating field. The energy that is generated in this motion is proportional to the square of the (complex) amplitude

$$|x_0(\omega)|^2 = \frac{F_0^2}{m^2}\frac{1}{((\omega_0^2 - \omega^2)^2 + \omega^2\gamma^2)}, \tag{2.39}$$

which also dictates the intensity of the fields that are re-radiated by this oscillating electron. Equation 2.39 is called the *Cauchy distribution* after Augustin Cauchy, which he defined as a continuous probability distribution in the field of mathematics.[51] In spectroscopy, it is usually called *Lorentz distribution* or the *Lorentzian*, named after Hendrik Lorentz, who was arguably the first to find this function to be the solution of forced oscillators that describe resonances and lineshapes.[52]

In many cases, however, equation 2.39 is not the function that is used to fit resonances in a spectrum because there is a good approximation to simplify the equation. In general, the damping term is very small $\gamma \ll \omega_0$ and the most interesting part of the curve is near the resonance $\omega \approx \omega_0$, which simplifies equation 2.38 to be

$$\begin{aligned} &\omega_0^2 - \omega^2 = (\omega_0 + \omega)(\omega_0 - \omega) \approx 2\omega_0(\omega_0 - \omega) \\ &\text{and} \quad \gamma\omega \approx \gamma\omega_0 \qquad (2.40) \\ \Rightarrow &\omega_0^2 - \omega^2 + i\gamma\omega \approx 2\omega_0(\omega_0 - \omega + i\frac{\gamma}{2}) \qquad (2.41) \\ \Rightarrow &\mathbf{x_0}(\omega) \approx \frac{\mathbf{F_0}}{2m\omega_0}\frac{1}{\omega_0 - \omega + i\Gamma}. \qquad (2.42) \end{aligned}$$

The square of this equation is frequently used to model the Lorentzian shape of a singular resonance in a molecular spectrum. In reality, even a single atom exhibits multiple resonance frequencies and we can include this quantum-mechanical effect by adding up all the contributions from the different oscillations to get

$$\mathbf{x_0}(\omega) \approx \frac{\mathbf{F_0}}{2m\omega_0}\sum_k \frac{f_k}{\omega_{0,k} - \omega + i\Gamma_k}. \qquad (2.43)$$

Here f_k represents the relative strength of a resonant mode k, usually called the oscillator strength and $\Gamma_k = \frac{\gamma_k}{2}$ is the damping constant.[53]

In figure **2-11** we see a plot of the square of equation 2.42, which represents a common intensity spectrum of a system that features a singular resonance. One should note that the peak is not infinitely sharp at the resonance frequency but broadened. This *full width at half maximum* (FWHM) is given by the damping term and equals 2Γ, which is called the natural line width of the system. Various aspects can define the shape of resonant lines in a spectrum, like the Doppler effect, collisions and proximity to other systems, just to name a few. But even in an almost ideal experiment with a gaseous sample at low temperature, the spectrum will still exhibit a natural *homogeneous broadening*. When many oscillators in an ensemble experience different degrees of these broadening effects, the resulting lineshape is a superposition of slightly displaced curves, resulting in a broader line width than the natural one, which is called *inhomogeneous broadening*.[54]

The natural line width, however, cannot be reduced by any means because it represents an intrinsic characteristic of every atomic system and its roots lie in Heisenberg's

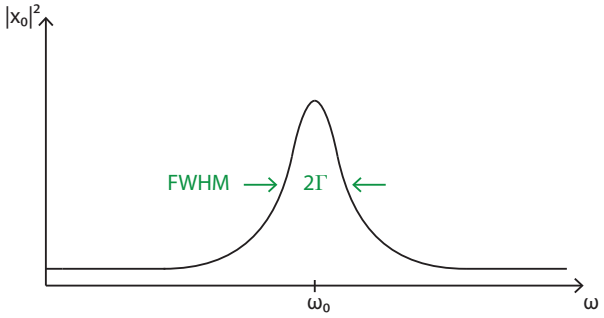

Figure **2-11**: Plot of the squared amplitude $|x_0(\omega)|^2$ of a forced oscillation vs the external driving frequency ω.

uncertainty principle. Analogue to the relation of space and momentum uncertainties, one can derive a similar inequality formalism for energy and time as

$$\delta t \delta E \geq \frac{\hbar}{2}. \tag{2.44}$$

In this formalism, however, the uncertainties do not necessarily represent the standard deviations but rather $\delta t = \tau$ is a measure of the lifetime of a resonant excitation and $\delta E = 2\Gamma$ is the energy spread, governing the natural width of the spectral line.[55] In other words, independent of the precision of the optical tool, atomic systems with a long lifetime excitation exhibit sharper peaks than those with shorter ones.

To conclude, we now have a powerful tool to approximate how matter reacts to incident radiation with the model of the harmonic oscillator, which is one of the key models for most spectroscopic problems.

2.2.2 Light Scattering

When light hits charged particles they are forced to follow the oscillation of the electric field vector, which can be described by the model of the harmonic oscillator that we introduced in the last subsection. According to *Maxwell's equations*, this accelerated motion, in turn, generates new electromagnetic radiation, perpendicular to the oscillating motion. This new wave is called *scattered* radiation and the process is what we call the *scattering of light*.

When there are multiple oscillators, close together in a periodic pattern, the scattered waves can interfere with each other and one can observe a diffraction pattern, as we have seen in Young's double-slit experiment in subsection 2.1.2. This interference is governed by the phase difference of the various oscillators and in the case of two waves, it is given by equation 2.8. If, however, we are looking at thin gas with random spacing between moving molecules then the interference of two radiated waves oscillates very rapidly because the phase relation between these moving generators also changes rapidly. In this case, the

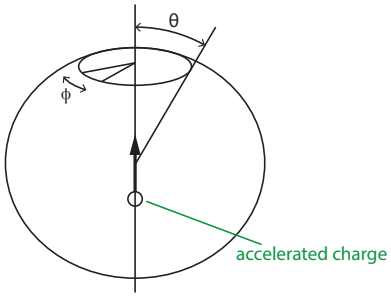

Figure **2-12**: Spherical geometry around a charge that is accelerated along one axis.

cosine in equation 2.8 averages to zero and the interference is seemingly lost, which makes the intensity I only dependent on the amplitudes $\mathbf{A}_i$ of the two waves, such that

$$I \propto A_r^2 = A_1^2 + A_2^2. \tag{2.45}$$

In reality, however, the interference is not lost but rather hard to detect, because two oscillators are only in-phase on a very short timescale. In that sense, a precise tool can detect the oscillation of the cosine but most equipment like our eyes, for example, are too insensitive and only observe the macroscopic time average of this rapid oscillation.

Important quantities for experimental setups are the amount and direction of the scattered energy. The intensity is independent of the angle ϕ around the oscillating axis and only depends on the angle θ, which is measured from the axis of motion. This spherical geometry is illustrated in **2-12**. The derivation of the intensity's angular dependence is done in detail in lecture 32, volume I of the Feynman lectures and it comes out to be proportional to $\sin^2(\theta)$.[2] Consequently, most of the energy is scattered perpendicular to the motion and there is no radiation scattered along the axis. If one averages over all spatial coordinates, the total power that is radiated by the oscillator is given by

$$P = \frac{q^2\omega^4 x_0^2}{12\pi\epsilon_0 c^3}, \tag{2.46}$$

with the charge q, frequency ω and amplitude $\mathbf{x_0}$ of the oscillating particle that generates the radiation. We already calculated the amplitude of such a particle with the approximation of the harmonic oscillator in equation 2.39 of the last subsection, which we can now incorporate into equation 2.46. The force on the charged particle is $\mathbf{F_0} = q\mathbf{E_0}$ and for simplicity, we disregard the frictional term γ to get the total energy that is scattered in all directions per second as

$$\begin{aligned} P &= \frac{q^2\omega^4}{12\pi\epsilon_0 c^3}\frac{q^2 E_0^2}{m^2(\omega^2-\omega_0^2)} \\ &= \left(\frac{1}{2}\epsilon_0 c E_0^2\right)\frac{8\pi}{3}\left(\frac{q^2}{4\pi\epsilon_0 mc^2}\right)^2\frac{\omega^4}{(\omega^2-\omega_0^2)^2}. \end{aligned} \tag{2.47}$$

This equation is written out like that for a reason. First of all, the factor $\frac{1}{2}\epsilon_0 c E_0^2$ is precisely the energy per square meter per second that is carried by the incident wave, which is driving the oscillation. Accordingly, the total energy scattered is proportional to the energy per square meter that is going in. Secondly, the proportionality factor has the dimension of an area and is known as the *cross section for scattering*.[56] This area, however, does not have a physical meaning in the sense that it can be attributed to the oscillator but rather describes the size of the area that would be irradiated if the total scattered radiation was directed onto it. This cross-section σ_s is a quantity often used to describe the amount of scattered radiation and in our case is defined as

$$\sigma_s = \frac{8\pi}{3} \underbrace{\left(\frac{q^2}{4\pi\epsilon_0 m c^2} \right)^2}_{r_0^2} \frac{\omega^4}{(\omega^2 - \omega_0^2)^2}. \tag{2.48}$$

The quantity $r_0 = \frac{q^2}{4\pi\epsilon_0 m c^2} = 2.82 \cdot 10^{-15}$ m is called the *classical electron radius* because it is the solution to a simplistic calculation of a sphere of charge that ignores quantum-mechanical effects.[57,58] Modern research suggests, however, that this quantity does not represent the radius of the electron but can rather be seen as an interaction length on atomic scales. According to experimental data, the actual radius is much smaller or even non-existent such that the electron can be seen as a point particle with no spatial extent.[59]

From the cross-section in 2.48 we can deduce some interesting phenomena in terms of the scattering of light in different situations. Firstly, if the light is scattered at weakly bound or free particles ($\omega_0 = 0$), the scattering cross-section becomes a constant

$$\sigma_T = \frac{8\pi}{3} \left(\frac{q^2}{4\pi\epsilon_0 m c^2} \right)^2 \tag{2.49}$$

and in the case of free electrons is known as the *Thomson scattering cross section*.[60] On the other hand, if we go to the limit of very large natural frequencies, we can disregard ω^2 in the denominator, such that

$$\sigma_R \approx \sigma_T \frac{\omega^4}{\omega_0^4}, \tag{2.50}$$

which is an approximation for the *Rayleigh scattering cross-section*.[61] One rather obvious example of Rayleigh scattering is the interaction of visible light with particles in our atmosphere. The electronic excitation energies of most gases, like nitrogen, for example, are generally located in the ultraviolet region of the electromagnetic spectrum such that the frequencies of visible light are small in comparison.[62] This makes the cross-section in 2.50 a good approximation for the scattering of sunlight in air and from the powerful ω^4 dependency it becomes apparent how the blue end of the visible spectrum with the highest frequency is scattered most in our atmosphere, which is the reason why we perceive the sky as blue.

When we transition from gas to a more condensed phase like a cloud of water molecules, we can observe yet another phenomenon. Up until now, we ignored the effects of interference because the oscillators were too far apart to keep their phase relations stable for long. In a condensed phase, however, the oscillators can be quite close together in comparison to the wavelength of the light. In that case, the electric field acts on all oscillators simultaneously and they necessarily scatter in-phase. The intensity of scattered light of N oscillators close together, therefore, scales with a factor of N^2 because the amplitudes add up when they are in-phase and this effect is much stronger than that for randomly spaced oscillators, which only goes with a factor of N. This is the reason why clouds are so opaque since all the microscopic water droplets scatter such a tremendous amount of sunlight.

There is, however, a limit to the increase in scattered intensity, which is closely tied to the wavelength of the light. When the drops become bigger and their sizes are of the same magnitude as the wavelength, the oscillators are not all in-phase anymore and the intensity does not increase nearly as fast as before, which is described by the *Mie theory for scattering*.[63] Thus, there is an equilibrium of two processes that occur in the clouds. On the one hand, according to Lord Rayleigh, the blue end of the visible spectrum is scattered more intensely per oscillator and on the other hand, the Mie theory predicts that the scattering in water drops is much stronger for the red end of the spectrum because the drops can become bigger for longer wavelengths. On average then, all the wavelengths of the visible spectrum are scattered almost equally, which gives the clouds their white colour.

If the size of the scattering volume is increased even more the Mie theory usually becomes too complex to calculate but converges quite well to the limit of geometrical optics for sizes comparable to 10λ.[63] Indeed when we arrange a macroscopic surface to have evenly spaced oscillators that are not closer spaced than a wavelength, the scattered waves will strongly interfere with each other. This results in multiple strong-intensity reflections at different angles because the beams cancel out in every other direction, which we already discussed in subsection 2.1.2. For normal incidence, the angles of strong intensities are given by equation 2.9 as

$$\begin{aligned} \Delta\phi &= m2\pi \\ \Rightarrow m\lambda &= d\sin(\theta), \end{aligned} \tag{2.51}$$

with the nonzero integer m representing the diffraction order of the reflection. These surfaces are called *diffraction gratings* and are widely used in almost all spectroscopic setups to spatially split up a laser pulse in its respective wavelength components.[28] Note that the spacing between oscillators has to be bigger than a wavelength to observe this effect because the only solution for $d < \lambda$ is the 0th diffraction order, which does not contain any wavelength information.

With that, we conclude our introduction of the fundamental scattering processes of light and continue in the next subsection with the topic of the polarisation of the light wave and its effect on irradiated materials.

2.2.3 Polarisation

When we talk about polarisation in the scope of this thesis we will contextually refer to one of two things: the oscillatory motion of the tip of the electric field vector of a light wave or the microscopic distortion of the electron distribution around the nucleus in matter. In the first part of this subsection, we will tackle the former concept and the latter is discussed in the second part, which is based on lecture 33, volume I and lectures 10-11, volume II of the Feynman lectures, respectively.[2,64]

As we mentioned before, the electric field component of electromagnetic radiation drives most optical processes and until now we only considered an oscillating **E** vector in one dimension. This oscillation can, however, have arbitrary x and y components in the plane of incidence and the phase relation between these components can also vary, which gives rise to very different possible motions of the vector. The most common case can be observed in radiation emitted from a heat source like the sun, for example. When there are a lot of atomic oscillators that are randomly oriented and they emit their radiation only very briefly until the next oscillator takes over, the phase relation between two oscillating fields can also only be constant on these short timescales. If the equipment we are using to detect the radiation is too insensitive to pick up these brief moments of constant phase, we will only observe an average that we call *unpolarised light*.

In a laser, we can circumvent this effect by forcing all the atoms to emit together in time, such that their phases are kept constant on much longer timescales, which allows the generation of different polarisations. Figure **2-13** (a) is an illustration of two oscillators in the x and y dimension that are in-phase but have different amplitudes, which results in *linearly polarised* light. If the oscillators are out of phase like in figure **2-13** (b) the resulting electric field vector usually oscillates in an elliptic motion, which is called *elliptically polarised* light. The special case of an elliptic motion for equal amplitudes and a phase shift of $\frac{\pi}{2}$ is called *circularly polarised* light since the electric field vector follows the motion of a circle.

Although the radiation of the sun is unpolarised, we can still detect polarised light in nature. In fact, most of the sunlight that is scattered in the sky is linearly polarised, which is an intrinsic trait of all scattered radiation in a direction perpendicular to the incident beam. When the unpolarised sunlight acts on the atoms in the air, the electrons follow the random oscillating motion of the **E** vector in the plane of incidence and radiate, in turn, their waves in every direction perpendicular to their motion. If we now observe this scattered light from the side, that is to say, perpendicular to the incident sunlight, we will only see the projected motion of the electrons in one dimension, which radiates

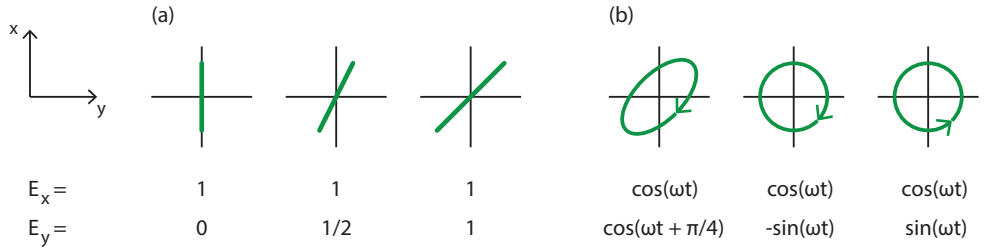

Figure **2-13**: Illustration of different polarisations of the electric field vector **E**. In (a) the oscillations are in-phase and only the amplitudes change, which results in linear polarisation and in (b) the amplitudes are kept constant but the phase relation changes, which results in elliptical and circular polarisation. Adapted from lecture 33, volume I of the Feynman lectures.[2]

linearly polarised light. In this sense, a possibility of creating linearly polarised light is through the use of scattered radiation.

Another interesting effect of polarisation can be observed in anisotropic media because they exhibit something that is called an optical axis. For every material that is made out of long molecules, which are aligned parallel to each other, the refractive index is usually different when light is polarised along the molecular axis than it is perpendicular to it. Such materials are called *birefringent* because they have two indexes of refraction. If linearly polarised light is oriented parallel or perpendicular to the optical axis it just goes through the medium with different velocities but if the polarisation is oriented at a 45° angle to the optical axis something interesting happens. The component of the electric field vector that is parallel to the optical axis now travels at a different speed through the medium than the component perpendicular to it, which results in a phase shift between these two that increases with the distance travelled through the material. In other words, if the thickness of the birefringent material is made just so that the two components of the incident light have a phase difference of π when they leave the material, the incident linearly polarised light is still linearly polarised but perpendicular to the original axis. Such an object is called a *half-wave plate* and it rotates linearly polarised light by 90°. There is also a *quarter-wave plate*, which fixes the phase delay to $\frac{\pi}{2}$, resulting in a transformation of linearly polarised light to circularly polarised light and vice versa.

Birefringent wave plates are a special example of how polarised light can interact with matter. In general, any non-conducting material that experiences an external electric field responds with a macroscopic polarisation, which is the average of a microscopic polarisation of all the atoms inside the material. When an external electric field acts, the electron cloud of every atom inside the dielectric is pushed in the opposite direction than the nucleus, which results in a very small dipole. For sufficiently weak electric fields this displacement is approximately proportional to the field strength and is given by the

amplitude of a harmonic oscillator that we already derived in equation 2.38. Following this analysis, we can define a dipole moment per atom $\mathbf{p}$ as the charges q that are separated multiplied by the separation distance $\mathbf{x}$, such that

$$\mathbf{p} = q\mathbf{x} \tag{2.52}$$

$$= \frac{q^2}{m(\omega_0^2 - \omega^2 - i\omega\gamma)}\mathbf{E} \tag{2.53}$$

$$= \alpha\mathbf{E}. \tag{2.54}$$

Here we substituted the electric force on a charged particle as $\mathbf{F}_0 = q\mathbf{E}$ and rearranged the equation to match the usual depiction in most textbooks. The material-specific proportionality constant $\alpha = \frac{q^2}{m(\omega_0^2 - \omega^2 - i\omega\gamma)}$ is called the *atomic polarisability* because it represents a measure of how easy it is to induce a dipole moment in an atom with an electric field. Strictly speaking, equation 2.54 is only valid if the variation in the electric field amplitude does not change across the atomic diameter and can be seen as constant. This is, however, usually the case in most spectroscopic setups with wavelengths in the visible spectrum and is known as the *electric dipole approximation*.[52]

In general, the polarisability α is not the same in every direction because there might be charges in the medium that are quite easy to move along one axis but stiffer for motion perpendicular to this axis. Therefore, we need to express the polarisability as a second-rank tensor with 9 coefficients α_{ij} to fully describe the polarisation of the medium. We will, however, postpone this detail to a later section and assume for reasons of simplicity that the polarisation is the same in every direction. In this case, the microscopic dipoles are all oriented the same way, that is, parallel to the electric field vector and therefore add up to constitute a macroscopic dipole moment per unit volume $\mathbf{P}$ of the material

$$\mathbf{P} = N\mathbf{p} \tag{2.55}$$

$$= \chi\epsilon_0\mathbf{E}, \tag{2.56}$$

with N atoms in a unit volume. This macroscopic polarisation is governed by the material-specific constant

$$\chi = \frac{Nq^2}{\epsilon_0 m(\omega_0^2 - \omega^2 - i\omega\gamma)}, \tag{2.57}$$

which is known as the *electric susceptibility* of dielectrics. One can derive from *Maxwell's equations* how the susceptibility is directly related to the relative permittivity κ with

$$\kappa = \frac{\epsilon}{\epsilon_0} = \chi + 1. \tag{2.58}$$

The constants ϵ and ϵ_0 are the material-specific absolute permittivity and the permittivity of free space. From equation 2.58 follows that a material, which is easily polarised has

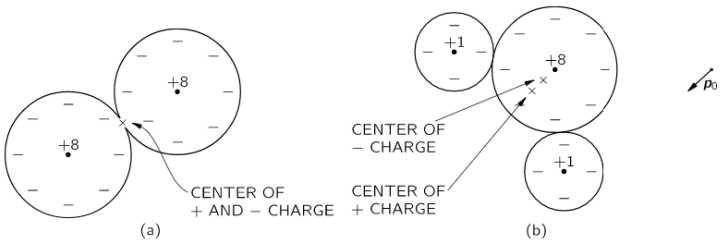

Figure **2-14**: Representation of an oxygen molecule (a) with no permanent dipole moment and a water molecule (b) with a net permanent dipole moment $\mathbf{p}_0$. Taken with permission from lecture 11, volume II of the Feynman lectures.[66]

a large susceptibility and in the limit of vacuum ($\epsilon = \epsilon_0$) the susceptibility vanishes. In general, the electric susceptibility is very important for spectroscopic setups because it greatly influences the form and intensity of the optical response of a system, which is something that we will cover in detail in later sections.

For conducting materials with very weakly bound electrons, the electric susceptibility is usually zero because the electrons move through the material, according to the external field, until the field inside of the material cancels out. That is, however, only true for static fields. If we apply a time-varying oscillating electric field to a conductor or any material with a huge electron density, for that matter, we can induce rapid oscillations of this density known as *plasma oscillations* or *Langmuir waves* after Irving Langmuir. This phenomenon, however, will not be covered in this thesis and the reader is referred to the book of José Bittencourt instead.[65]

Coming back to dielectrics, there are two more important aspects we need to cover on the topic of polarisation. The first one is that molecular samples can have an inherent dipole moment due to their electron distribution. If the centres of positive and negative charges in the molecule do not coincide, there is a permanent net dipole moment even without an external electric field. These molecules are called *polar*, while those without a permanent dipole are called *nonpolar*. Figure **2-14** is a representation of a nonpolar oxygen molecule and a polar water molecule to illustrate this phenomenon.

When dealing with polar molecules one has to carefully think about how the permanent dipole moment affects the polarisation of the system. In gases, for example, polar molecules tend to align in the direction of the applied field, which increases the electric susceptibility. This alignment, however, is closely tied to the temperature of the system, as there are more collisions at higher temperatures, resulting in a $\frac{1}{T}$ dependence of the susceptibility that is known as *Curie's law*. For denser materials, there is no alignment due to the external field because the molecules are usually stuck in place. This, on the other hand, leads to interesting possibilities like determining the orientation of molecules at a surface, as the susceptibility becomes greater the more the polarisation of the incident light and the permanent dipole of the molecules are aligned.

The second aspect we want to cover is mostly relevant in condensed phases, where the single atoms can be close together. Until now, we only considered external radiation to be responsible for the field that is felt by the electrons. When the oscillators are close together, however, there can be a considerable contribution from the fields of neighbouring atoms that influences the local field, depending on the strength of the polarisation. For isotropic material with small spacing between atoms in comparison to the wavelength of the light, one can approximate this contribution to be

$$\mathbf{E}_{\text{local}} = \mathbf{E}_{\text{external}} + \frac{\mathbf{P}}{3\epsilon_0}, \tag{2.59}$$

which is derived in detail in lecture 11, volume II of the Feynman lectures.[64] This contribution, however, is usually small and omitted in most theoretical works in favour of a more accessible explanation of the underlying principle.[67]

This concludes the introduction of the concept of polarisation of light and matter and with this knowledge, we now have the tools to dive even deeper into the principles of spectroscopy to understand how the refractive index of materials comes about and what it entails.

2.2.4 Origin of the Refractive Index

In the earlier sections, we defined the refractive index of matter as the factor by which the speed of light is reduced when travelling through a medium. We did, however, not elaborate on this phenomenon until now because there are certain topics that we preferred to introduce beforehand. This subsection now aims to give a deeper understanding of the origin of the refractive index through the knowledge we accumulated so far.

In general, the total electric field at an arbitrary point P in space can be calculated by the sum of the fields from all the charges in the universe. And these fields are, in turn, generated by the accelerated motion of these charges, retarded by the speed of light c. Retarded because they first need to travel to P to affect the field at this point. Naturally, this is also true inside of materials, which begs the question of why light *appears* to travel at reduced speed through a medium when all of the charges inside of the material radiate their waves at the speed c.

In section 2.2.2 we learned about the scattering of light such that the atoms in an irradiated material become little oscillating dipoles that produce their own waves. The superposition of these new waves then is the scattered radiation. Consequently, when we look at the process of refraction, we observe a superposition of the original source wave and the scattered waves inside of the material. This superposition constitutes a new wave with a different phase velocity than c, namely $v_p = \frac{c}{n}$, which is, qualitatively speaking, the origin of the refractive index.

The bending of light at the interface of different refractive media is just a consequence of this new phase velocity, which is illustrated in figure **2-15** as the refraction of wave

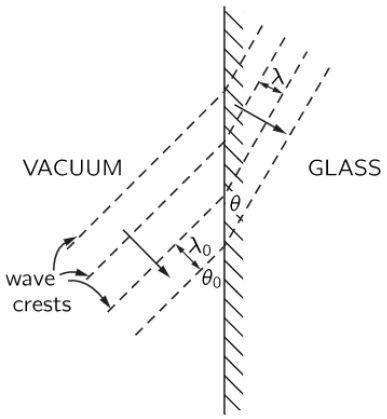

Figure **2-15**: Illustration of a wave that is refracted at a glass surface because of the different wavelengths in the two media. Taken with permission from lecture 31, volume I of the Feynman lectures.[30]

crests at the interface of vacuum and glass. When the incident wave fronts interact with the atoms in the material, the electrons are compelled to start oscillating with the same frequency as the incoming wave. The reduced phase speed inside the glass, however, results in a smaller spacing between the crests of the wave $\lambda = \frac{2\pi v_p}{\omega} = \frac{2\pi c}{n\omega} = \frac{\lambda_0}{n}$. The consequence of this smaller wavelength is a change in the direction of the wave to make the crests geometrically "fit" at the interface, which is the reason for the refraction angle. In fact, one can directly get the relation $\frac{\lambda_0}{\sin(\theta_0)} = \frac{\lambda}{\sin(\theta)}$ or $\frac{\sin(\theta_0)}{\sin(\theta)} = n$ from the geometry in figure **2-15**, which is Snell's law for refraction that we already derived in equation 2.2.

In the next part, we will give a brief derivation of the refractive index of dense materials, which is going to cover the most important aspects that motivated our qualitative approach. For the full story, the reader is referred to lecture 32, volume II of the Feynman lectures on which this subsection is based.

To understand how waves travel through a dielectric material, we need to solve *Maxwell's equations* for this kind of material. As we learned in the last subsection, the incident light induces small oscillating dipoles that constitute a macroscopic polarisation per unit volume $\mathbf{P}$ of the material. A spatial change in this polarisation is equivalent to a charge density and in particular one can show that the charge density due to polarisation of the material ρ_{pol} is given as

$$\rho_{\text{pol}} = -\boldsymbol{\nabla} \cdot \mathbf{P}. \tag{2.60}$$

For time-varying fields, such as light, the induced polarisation also changes quickly in time, which results in a polarisation *current* $\mathbf{j}_{\text{pol}}$ that is defined as

$$\mathbf{j}_{\text{pol}} = \frac{\partial \mathbf{P}}{\partial t}. \tag{2.61}$$

With the assumption that there are no charges other than those bound in atoms and these definitions for $\rho = \rho_{\text{pol}}$ and $\mathbf{j} = \mathbf{j}_{\text{pol}}$, we can now formulate *Maxwell's equations* for a dielectric, according to 2.15-2.18:

$$\boldsymbol{\nabla} \cdot \mathbf{E} = \frac{-\boldsymbol{\nabla} \cdot \mathbf{P}}{\epsilon_0} \tag{2.62}$$

$$\boldsymbol{\nabla} \cdot \mathbf{B} = 0 \tag{2.63}$$

$$\boldsymbol{\nabla} \times \mathbf{E} = -\frac{\partial \mathbf{B}}{\partial t} \tag{2.64}$$

$$\boldsymbol{\nabla} \times \mathbf{B} = \mu_0 \frac{\partial \mathbf{P}}{\partial \mathbf{t}} + \mu_0 \epsilon_0 \frac{\partial \mathbf{E}}{\partial t} \tag{2.65}$$

We now apply the trick of taking the curl of equation 2.64 that we already used in section 2.1.4 to calculate the behaviour in a vacuum. This yields

$$\boldsymbol{\nabla}(\boldsymbol{\nabla} \cdot \mathbf{E}) - \nabla^2 \mathbf{E} = -\frac{\partial}{\partial t} (\boldsymbol{\nabla} \times \mathbf{B}) \tag{2.66}$$

$$\Rightarrow \nabla^2 \mathbf{E} - \frac{1}{c^2} \frac{\partial^2 \mathbf{E}}{\partial t^2} = -\frac{1}{\epsilon_0} \boldsymbol{\nabla}(\boldsymbol{\nabla} \cdot \mathbf{P}) + \mu_0 \frac{\partial^2 \mathbf{P}}{\partial t^2}. \tag{2.67}$$

The left side of this equation is already familiar to us from section 2.1.4 as it represents a wave equation for the electric field vector $\mathbf{E}$. In a vacuum, this wave equation equals zero but in a dielectric, the field depends on two terms that involve the polarisation $\mathbf{P}$.

To keep this example simple, we make two more assumptions. First of all, we restrict our approach to isotropic media, which results in $\mathbf{P}$ and $\mathbf{E}$ having the same direction. Secondly, our waves travel in the z-direction and are linearly polarised in the x-dimension. Therefore, we can represent $\mathbf{E}$ as $E_x = E_0 \mathrm{e}^{i(\omega t - kz)}$ and consequently the polarisation vector $\mathbf{P}$ only has an x-component as well. Furthermore, there is no spatial change of P_x in the x-dimension and the time evolution is given by the driving field, in the case of a linear dielectric, such that $P_x \propto \mathrm{e}^{i\omega t}$. This allows us to simplify equation 2.67 accordingly:

$$\boldsymbol{\nabla} \cdot \mathbf{P} = 0, \tag{2.68}$$

$$\frac{\partial^2 P_x}{\partial t^2} = -\omega^2 P_x \tag{2.69}$$

$$\Rightarrow -k^2 E_x + \frac{\omega^2}{c^2} E_x = -\mu_0 \omega^2 P_x, \tag{2.70}$$

which is now a one-dimensional wave equation that couples E_x and P_x. We already derived this connection in the last subsection in equation 2.56 and, including the local field effects

that are described in equation 2.59, we can express the polarisation as

$$P_x = \chi\epsilon_0 E_{\text{local}} \tag{2.71}$$
$$= \chi\epsilon_0 \left(E_x + \frac{P_x}{3\epsilon_0}\right) \tag{2.72}$$
$$= \frac{\chi}{1-\frac{\chi}{3}}\epsilon_0 E_x. \tag{2.73}$$

Incorporating this into equation 2.70 lets us eliminate E_x and yields the important relation

$$k^2 - \frac{\omega^2}{c^2} = \frac{\chi}{1-\frac{\chi}{3}}\frac{\omega^2}{c^2} \tag{2.74}$$
$$\Rightarrow \frac{k^2c^2}{\omega^2} = 1 + \frac{\chi}{1-\frac{\chi}{3}}. \tag{2.75}$$

Finally, we can include our definition of the refractive index as the reduced phase velocity inside the material $v_p = \frac{\omega}{k} = \frac{c}{n}$ to get

$$n^2 = 1 + \frac{\chi}{1-\frac{\chi}{3}}, \tag{2.76}$$

which is usually rewritten as

$$3\frac{n^2-1}{n^2+2} = \chi \tag{2.77}$$
$$= \frac{Nq^2}{\epsilon_0 m}\sum_k \frac{f_k}{\omega_{0,k}^2 - \omega^2 - i\omega\gamma_k}. \tag{2.78}$$

This equation is known as the *Clausius-Mossotti relation* and it describes the refractive index of dense materials.[68] Note, however, that with the local field approximation of equation 2.59 this relation is only strictly true for isotropic materials with small spacing between atoms in comparison to the wavelength of the light. Furthermore, we made some adjustments to the susceptibility from equation 2.57. Specifically, we included quantum-mechanical effects like we did in equation 2.43 such that one atom can exhibit multiple resonances k and the relative strength of each resonance is given by f_k. The internal modes of oscillation $\omega_{0,k}$ and their damping γ_k are usually quite different from those of free atoms because of the strong interaction of neighbouring atoms. Nevertheless, equation 2.78 is a decent approximation for the refractive index of matter. Finding the correct values for f_k, $\omega_{0,k}$ and γ_k, however, is a difficult problem of quantum mechanics but one that can be tackled with a spectroscopic approach as we will see in future sections.

In the next part, we want to emphasise some important aspects of the formula for the refractive index of matter. First of all, we can see a dependence on the frequency of the incident light such that light of different frequencies has a different refractive index

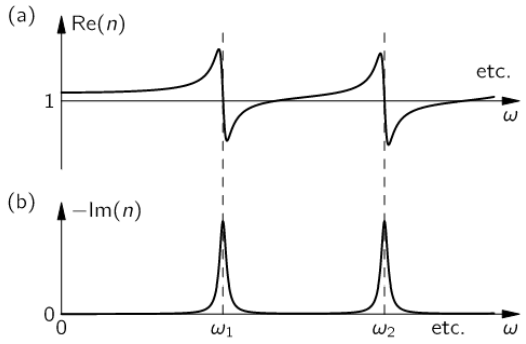

Figure **2-16**: Real and imaginary part of the index of refraction as a function of frequency. Taken with permission from lecture 31, volume I of the Feynman lectures.[30]

and also a different angle of refraction. This phenomenon is called *dispersion* because light of different colours is spatially dispersed into a spectrum when travelling through a refractive medium.

Secondly, the index of refraction is a complex quantity because we included the damping term $i\gamma$, which has some interesting consequences. In figure **2-16** we can see a plot of the real (a) and the imaginary (b) part of n as a function of the irradiated light frequency. Most of the real part has a positive slope, which only becomes very steep and negative, close to the resonance frequency. This behaviour is sometimes called "normal" and "abnormal" dispersion because when it was first discovered a long time ago it seemed very unusual. Apart from this historical aspect though we can describe both slopes as quite normal because they stem from the same equation that we derived.

Furthermore, the index of refraction can be smaller than one and even become negative. The latter, however, just means that the phase shift due to the scattered radiation is negative such that the transmitted wave has an advance of phase and not a delay. More interesting is the fact that $|n|$ can be smaller than one, which corresponds to a phase velocity greater than the speed of light. This is, in fact, true and also reasonable because a wave with a single frequency does not carry information so it can travel at a speed greater than c. To transmit information there has to be some sort of modulation such that the wave is composed of different frequencies. For such a modulated wave it can be shown that the speed of sending a *signal*, which is called the *group velocity* is not only dependent on the index at one frequency but also how the index changes with frequency and this speed cannot exceed c.[69]

According to figure **2-16** (b) the imaginary part vanishes everywhere except in the region close to resonance. To understand this phenomenon, we should take a look at how the complex refractive index influences our wave. We express n as

$$n = n_R - in_I, \tag{2.79}$$

with n_R and n_I as the real and imaginary parts of n, respectively. If we now incorporate

this representation into our plane wave from earlier, we get

$$E_x = E_0 \mathrm{e}^{i(\omega t - kz)} \tag{2.80}$$

$$= E_0 \mathrm{e}^{i\omega\left(t - \frac{nz}{c}\right)} \tag{2.81}$$

$$= \underbrace{E_0 \mathrm{e}^{-\frac{\omega n_I z}{c}}}_{E_0'} \mathrm{e}^{i\omega\left(t - \frac{n_R z}{c}\right)}. \tag{2.82}$$

The part $\mathrm{e}^{i\omega\left(t-\frac{n_R z}{c}\right)}$ is a wave that travels with the phase velocity $\frac{c}{n}$, which means that the real part of the refractive index n_R is responsible for the behaviour that we expect. The imaginary part n_I, however, results in an enveloping exponential function E_0' as the new amplitude, which is decaying with the travel distance z. For the same reason, the intensity, which is proportional to the square of the amplitude

$$I \propto \mathrm{e}^{-\frac{2\omega n_I z}{c}} = \mathrm{e}^{-\beta z}, \tag{2.83}$$

is also decaying inside the material. The factor $\beta = \frac{2\omega n_I}{c}$ is called the absorption coefficient because it is a measure of how much energy the material is absorbing from the wave due to the frictional term $i\gamma$ we introduced in the beginning. Comparing this result with the plot in figure **2-16** (b) again, we now understand why n_I peaks around the resonances of the material. The imaginary part of n is directly related to the absorption of the material and, naturally, the atoms can only absorb a decent amount of energy if the frequency of the light corresponds to a resonance frequency of the system. If there is not much absorption and the length $\frac{c}{\omega n_I}$ is quite large in comparison to the thickness of the material, we usually refer to this material as transparent.

This concludes not only the subsection about the refractive index and the absorption of electromagnetic radiation in matter but also the second section of the theory of light chapter. In summary, we introduced the important model of the harmonic oscillator and learned about the scattering of light in different scattering volumes. Furthermore, we explained how polarisation comes about and gave a deeper insight into one of the most important quantities in spectroscopy, the refractive index. We feel that all of these topics are essential to appreciating and understanding most of the modern spectroscopic approaches, which we are going to describe in the next section.

2.3 Light as a Tool

The third section of the theory chapter intends to convince the reader of the versatility and precision of light when used as a tool to investigate atoms and molecules. The use of sum-frequency generation is a powerful method to reveal vibrational information of an interfacial monolayer and is utilised in many modern setups. However, we start this section by introducing a model to describe molecular systems in a quantum-mechanical

manner. Subsequently, we tackle vibrational excitations and take a closer look at the vibrational dynamics inside a molecule and a monolayer of molecules. After that, we present how to reveal this vibrational information by the use of light and transition to more advanced non-linear techniques in the following subsection. Lastly, we are going to introduce vibrational sum-frequency spectroscopy, which is the method that we use to probe our molecular systems.

2.3.1 Quantum Model of Molecules

This subsection introduces a quantum-mechanical view of molecules and models to approximate their behaviour, which is for the most part adapted from the book by Hertel and Schulz.[70]

When we talk about the probing of molecules we usually refer to the approach of putting a certain amount of energy into the system and watching the response. From section 2.2.1 we know that this input energy has to correspond to a resonance of the system to observe a strong response. Furthermore, the order of magnitude of the input energy dictates what kind of excitation we will induce in the molecule. The excited states of each system can be categorised into three parts: electronic, vibrational and rotational levels. Strictly speaking, there are also translational energies, which, however, are not only extremely small and hard to detect but also only quantised for particles that are confined to a fixed volume. For these reasons, translational excitation levels are usually neglected and will not be covered in this thesis. Despite these distinct categories, it is possible to have a superposition of two or more different kinds of excitations simultaneously if the circumstances are right. We do, however, want to emphasise the important fact that the excitation energies of each category are magnitudes apart, as we will see in the following.

The electronic excitations occur at very high energies and usually, the outermost electron of a system is forced into a bound state further away from the core. To give an example, the electronic excitation energies E_e are of the order of the electron's binding energy and in the case of a hydrogen molecule it can be shown that this energy is approximated by the average kinetic energy, which is

$$|E_e| \approx \frac{p^2}{2m_e} = \frac{\hbar^2}{2m_e r_0^2} \approx 7\,\mathrm{eV}. \tag{2.84}$$

Here, we estimated the momentum $p = \frac{\hbar}{r_0}$ with the *uncertainty principle* and approximated the expansion of the electron cloud with the bond length of the molecule $r_0 \approx 0.074\,\mathrm{nm}$. The order of magnitude of $1 - 10\,\mathrm{eV}$ corresponds to photon energies in the ultraviolet and visible regions and this is also where we expect the spectrum to show resonant peaks.

The second category consists of energies that correspond to vibrations of the core structure and are therefore restricted to molecules, whereas the previously discussed electronic

excitations are observable for molecules as well as single atoms. The vibrational excitation energies are much smaller than the electronic excitations and can be approximated by the harmonic oscillator model. In section 2.2.1 we learned that the frequency of such a model comes out as $\omega = \sqrt{\frac{k}{m}}$ and the generated energy is $\hbar\omega$. The harmonic restoring force on the electron is, however, the same as for the core only in the opposite direction and we can use this equality to find a relation between the electronic excitation energy E_e and the vibrational energy that is generated in the cores E_v. Accordingly, we can write

$$\frac{E_v}{E_e} \approx \frac{\sqrt{\frac{k}{m_c}}}{\sqrt{\frac{k}{m_e}}} \approx \sqrt{\frac{m_e}{m_c}} \lessapprox 10^{-2}, \tag{2.85}$$

where we approximated the force constants to be of the same order of magnitude. Comparing this result to the electronic case, we find the vibrational excitations for energies of about 0.1 eV, which corresponds to photons in the infrared region. The vibrational spectra of molecules are quite vast and usually categorised even further into the high energetic stretching modes and the lower deformation modes, consisting of bending, rocking, wagging and twisting motions.[53] For the most part we are going to be interested in vibrational spectra in this thesis.

The rotational levels are very close together, resulting in much smaller energies for rotational excitations. These rotational energies E_r are of the same order of magnitude as the rotational constant, which is defined as

$$E_r \approx B = \frac{\hbar^2}{2I} = \frac{\hbar^2}{2m_c r_0^2}. \tag{2.86}$$

And if we take the example of a hydrogen molecule again, we can approximate this value to be

$$E_r \approx \frac{m_e}{m_c} E_e \approx 10^{-4} E_e. \tag{2.87}$$

From this, we can see how the rotational excitation energies are 4 and 2 orders of magnitude smaller than the electronic and the vibrational ones, respectively. Rotational transitions are, therefore, common around 0.001 eV and can be spectrally observed in the far-infrared region.

The huge gap between electronic and core excitations, i.e. vibration and rotation, comes about because the nucleus is much heavier than the electrons and this fact is the foundation of molecular physics. Generally speaking, a three-body problem with mutual interaction cannot be solved analytically and, therefore, the Schrödinger equation of any molecular system can also only be solved numerically. However, since the nuclei are that much heavier than the electrons they also move a lot slower, such that on the timescales of the core movement the electrons respond almost instantaneously. This motivates the

approach of separating core and electronic wave functions, effectively cancelling their interaction in the sense that the electrons become independent of the rate of change of the nuclei coordinates. Qualitatively speaking, one can then solve the electronic Schrödinger equation for every fixed set of nuclei coordinates to calculate the electronic energies. With the electronic energies, the Schrödinger equation for the nuclei can be calculated accordingly. This approach was proposed in 1927 by Born and Oppenheimer and is called the *Born-Oppenheimer* approximation.[71] The Born-Oppenheimer approximation is essential for molecular physics because it simplifies the numerical calculations for larger systems immensely and even allows for analytical solutions of systems with a single electron.[72]

In the case of a diatomic molecule, the Hamiltonian for the motion of the nuclei in the Born-Oppenheimer approximation becomes

$$\hat{H}_n = -\frac{\hbar^2}{2\mu}\nabla_R^2 + \underbrace{\hat{T}_e + V(\mathbf{r};R)}_{V_n}, \tag{2.88}$$

which is derived in detail in the book by Hertel and Schulz.[70] Since the two atoms in our molecule exert the same force on each other, it is common practice to work with relative coordinates such that the two-body problem is simplified to a single reduced mass $\mu = \frac{m_1 m_2}{m_1+m_2}$ and the relative position of the two objects $\mathbf{R} = \mathbf{R_2} - \mathbf{R_1}$. Furthermore, as mentioned before, the potential energy of the electrons $V(\mathbf{r};R)$ is only dependent on the distance of the two nuclei $R = |\mathbf{R}|$ as a parameter in the Born-Oppenheimer approximation, which is denoted with a semicolon in 2.88. Therefore, the kinetic and potential energy of the electrons $\hat{T}_e + V(\mathbf{r};R) = V_n$ act as the potential energy for the nuclei and we can calculate this energy for every R. The resulting function is called a *potential curve* or, in multiple dimensions, a *potential hypersurface*.

Our goal is now to find a suitable potential to understand and model the motion of the nuclei in a molecule. One usually approaches such a problem with a Taylor expansion about the equilibrium length R_0. For small disturbances, we can take the Taylor expansion up to the first non-vanishing order, such that

$$V_n(R) \approx V_n(R_0) + (R-R_0)\left.\frac{\mathrm{d}V_n}{\mathrm{d}R}\right|_{R=R_0} + \frac{1}{2}(R-R_0)^2\left.\frac{\mathrm{d}^2V_n}{\mathrm{d}R^2}\right|_{R=R_0}. \tag{2.89}$$

The second term vanishes because we expect our potential to have a minimum at the equilibrium length. Therefore, in the first approximation, we have the harmonic potential

$$V_n(R) \approx V_n(R_0) + \frac{1}{2}k(R-R_0)^2 \tag{2.90}$$

that describes the motion of the nuclei. The classical harmonic oscillator was already discussed in section 2.2.1 and we know that such a system has a specific resonance frequency of $\omega = \sqrt{\frac{k}{\mu}}$. In our quantum-mechanical description, however, we have to solve

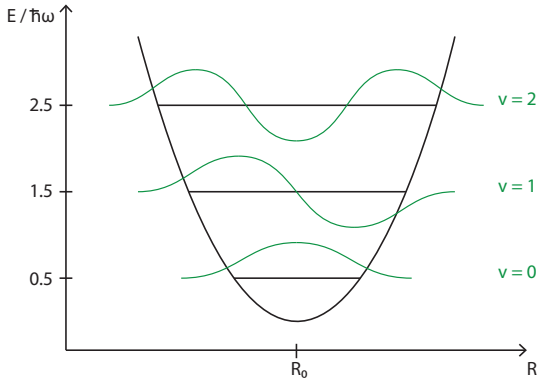

Figure **2-17**: Plot of the potential energy of a harmonic oscillator in dependence of the core distance R and an illustration of the first three vibrational wave functions.

the time-independent Schrödinger equation with the harmonic potential, which leads to the wave functions of the nuclei and their respective energies. The quantum-mechanical harmonic oscillator is a well-discussed topic in various textbooks and one can find a thorough description there, as we will only state the results here.[70,73] The energy eigenvalues for a vibrational level ν are given by

$$E_\nu = \hbar\omega \left(v + \frac{1}{2} \right) \tag{2.91}$$

and their respective eigenfunctions are products of Hermite polynomials and a Gaussian function. These eigenfunctions can be calculated, for instance, with

$$\phi_\nu(x) = \frac{(-1)^\nu}{\sqrt{2^\nu \nu! \sqrt{\pi}}} \mathrm{e}^{\left(\frac{x^2}{2}\right)} \frac{\mathrm{d}^\nu}{\mathrm{d}x^\nu} \mathrm{e}^{(-x^2)}. \tag{2.92}$$

The harmonic potential and the wavefunctions for the first three levels ($\nu = 0, 1, 2$) are plotted for an arbitrary system in fig **2-17**.

This harmonic approach, however, not only fails rather quickly for stronger deviations from the equilibrium position but also ignores the fact that molecules dissociate when their cores are pushed apart far enough. For these reasons, Philip Morse proposed in 1929 an asymmetric potential of the form

$$V_m(R) = D_e \left[1 - \mathrm{e}^{-a(R-R_0)} \right]^2, \tag{2.93}$$

with the depth of the potential well D_e and the stiffness of the potential a. This Morse potential is extensively used as an empirical description of atomic interaction because it describes experimental data extremely well. In figure **2-18** we can see the experimental data of the potential energy of the electronic ground state of CO and a Morse potential that is fitted to these data points. Evidently, we can see how the Morse potential is a lot

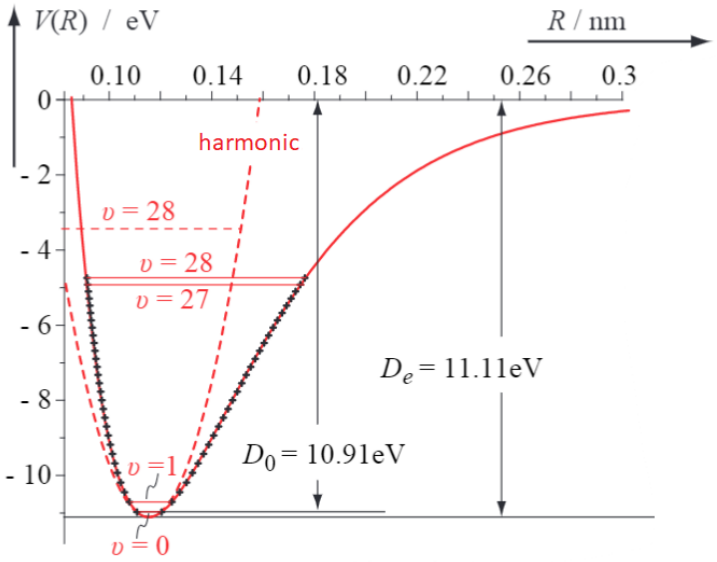

Figure **2-18**: Potential energy of the ground state of CO. The crosses indicate the experimental data points according to Fleming and Rao, to which a Morse potential was fitted with $D_e = 11.108\,\text{eV}$ and $R_0 = 0.1128\,\text{nm}$.[74] The dashed line is a ground state harmonic potential of the same frequency. This figure is taken with permission from Hertel and Schulz.[70]

more accurate than the harmonic oscillator for most of the vibrational energy levels and usually only begins to fail close to the dissociation level.

In this qualitative derivation, we have completely neglected the rotational motion of the molecule, which, although small, does influence the vibrational motion due to centrifugal deformation. This, however, is only truly relevant for molecules in a gas that can rotate freely. The densely packed adsorbed monolayers that we investigate in the context of this thesis, on the other hand, are restricted in their rotational motion, which makes this approach reasonable.

In conclusion, we now have a better understanding of excitation levels in molecular systems and tools to model their behaviour. In the next step, we are tackling the main topic of interest of this thesis, which are the vibrational modes and the energy flow of the system through these modes, called *vibrational dynamics*.

2.3.2 Vibrational Dynamics

All vibrational modes of a molecule can be expressed in a set of normal coordinates by transforming the local coordinates of a system in a specific way. This is demonstrated in the first part of this subsection. In the second part, we take a closer look at these fundamental vibrational modes and see how they influence each other in the anharmonic

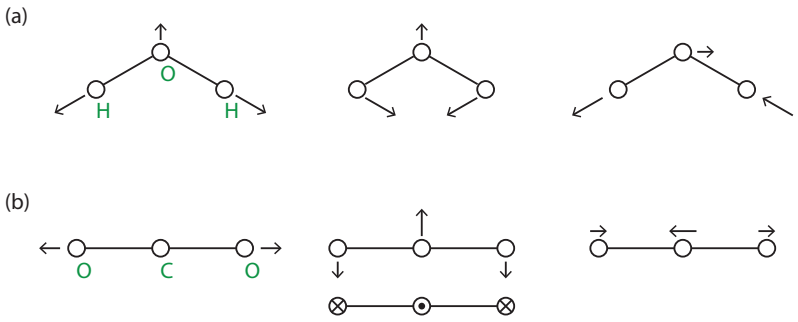

Figure **2-19**: Normal vibrational modes of a non-linear (a) and linear (b) molecule. In the linear case, the mode ν_2 is degenerated. Adapted from Demtröder.[73]

approximation. The first part is adapted from the books by Hertel/Schulz and Demtröder and the second part is based on different scientific articles.[70,73]

In general, every N-atomic molecule in free space has $3N$ degrees of freedom because every single atom can move in 3 dimensions. Of these $3N$ degrees of freedom, 3 are reserved for the translational motion of the centre of mass of the molecule and another 3 for the rotation about the three main axes of inertia that cross in the centre of mass. For linear molecules, only 2 degrees of freedom are reserved for rotation because the rotation about the molecular axis is not considered a rotation of the core frame. This results in $3N-5$ and $3N-6$ degrees of freedom for linear and non-linear molecules, respectively, that correspond to vibrations of the nuclei. For that reason, the vibrational spectra of larger molecules are quite vast and further categorised in the high-energy stretching vibrations and the lower-energy deformation modes, i.e. bending, rocking, wagging and twisting. The latter usually features a significant change in the bond angle, while the former mainly changes the bond length.

For sufficiently small displacements from equilibrium, the atoms in a molecule experience a linear restoring force, resulting in a harmonic oscillation. In this case, every of the $3N-6$ vibrational modes can be expressed as a linear combination of fundamental oscillations, called *normal modes*. A normal mode is a vibration of the core structure in which every nucleus passes its equilibrium position at the same time. In figure **2-19** we can see an illustration of the 3 normal modes of the non-linear H_2O (a) and the 4 normal modes of the linear CO_2 (b) molecule. The ν_2 mode of CO_2 is degenerated because the oscillation in the drawing plane and the one orthogonal to it have the same energy.

In the following, we are going to quantitatively describe these fundamental vibrational modes and we start by defining the displacement of a single nucleus from its equilibrium position in one dimension as ξ, such that the whole system is characterised by $3N$ parameters $\xi_1 \dots \xi_{3N}$. If we now focus only on the vibrational modes of a non-linear molecule and approximate the potential of the cores with a Taylor expansion about the equilibrium

position, we get

$$V(\xi) \approx V_0(0) + \sum_{i=1}^{3N-6} \left.\frac{\partial V}{\partial \xi_i}\right|_{\xi_i=0} \xi_i + \frac{1}{2} \sum_{i,j=1}^{3N-6} \left.\frac{\partial^2 V}{\partial \xi_i \partial \xi_j}\right|_0 \xi_i \xi_j. \tag{2.94}$$

We can now shift the potential, such that $V(0) = 0$ and since we expect the potential to have a minimum at equilibrium $\xi = 0$ the second term also vanishes, leaving us with the harmonic potential

$$V_h = \frac{1}{2} \sum_{i,j=1}^{3N-6} \left.\frac{\partial^2 V}{\partial \xi_i \partial \xi_j}\right|_0 \xi_i \xi_j. \tag{2.95}$$

The restoring force on the nuclei is the derivative of this potential energy, therefore

$$F_i = -\frac{\partial V_h}{\partial \xi_i} = -\sum_{j=1}^{3N-6} \left.\frac{\partial^2 V}{\partial \xi_i \partial \xi_j}\right|_0 \xi_j, \tag{2.96}$$

which gives us the classical equations for the motion of the cores as

$$F_i = m_i \frac{\partial^2 \xi_i}{\partial t^2} \tag{2.97}$$

$$\Rightarrow \sum_{j=1}^{3N-6} \left.\frac{\partial^2 V}{\partial \xi_i \partial \xi_j}\right|_0 \xi_j + m_i \ddot{\xi}_i = 0, \tag{2.98}$$

with the mass of the nuclei m_i. Further, we now define new mass-weighted coordinates $q_i = \sqrt{m_i}\xi_i$ that simplify our set of equations to

$$\ddot{q}_i + \sum_{j=1}^{3N-6} V_{ij} q_j = 0 \quad (i = 1, \ldots, 3N-6), \tag{2.99}$$

where $V_{ij} = \left.\frac{\partial^2 V}{\partial q_i \partial q_j}\right|_0$ are the elements of the *Hessian matrix* $\tilde{\mathbf{V}}$, which is real, symmetric ($V_{ij} = V_{ji}$) and positiv definit. The terms in 2.99 describe a set of differential equations that are coupled because the off-diagonal elements $V_{ij}(i \neq j)$ are typically nonzero. That said, it now becomes obvious how the fundamental modes come about. If we find a specific set of initial conditions, such that the off-diagonal elements of $\tilde{\mathbf{V}}$ are all zero, the nuclei will all oscillate with the same frequency and phase. These oscillations are what we call *normal modes*.

First, we begin by rewriting equation 2.99 with vectors $\mathbf{q} = q_1, \ldots, q_{3N-6}$, such that

$$\ddot{\mathbf{q}} + \tilde{\mathbf{V}} \cdot \mathbf{q} = 0. \tag{2.100}$$

We can then use some simple methods of linear algebra to find an orthogonal transformation matrix $\tilde{\mathbf{T}}$ that diagonalises $\tilde{\mathbf{V}}$ with

$$\tilde{\mathbf{T}}^{-1}\tilde{\mathbf{V}}\tilde{\mathbf{T}} = \tilde{\mathbf{D}}. \tag{2.101}$$

Here, $\tilde{\mathbf{D}}$ is a diagonal matrix with $3N-6$ elements λ_i. Now, we just need to transform our coordinates q_i accordingly

$$\mathbf{Q} = \tilde{\mathbf{T}}^{-1} \cdot \mathbf{q}, \tag{2.102}$$

to end up with a set of differential equations in the new coordinate system that is now uncoupled:

$$\ddot{\mathbf{Q}} + \tilde{\mathbf{D}} \cdot \mathbf{Q} = 0. \tag{2.103}$$

The solutions to equation 2.103 are harmonic oscillators and their displacement from equilibrium in the new coordinates Q_i is given by

$$Q_i(t) = A_i \cos(\omega_i t + \phi_i), \tag{2.104}$$

with amplitudes A_i, phases ϕ_i and frequencies $\omega_i = \sqrt{\lambda_i}$.

In conclusion, we have transformed the system to new coordinates Q_i that are superpositions of the mass-weighted displacement of the nuclei in the original cartesian coordinates q_j, according to equation 2.102. In these new coordinates, called *normal coordinates*, the system can be solved by uncoupled harmonic oscillators. Therefore, the oscillations in these normal coordinates correspond to a simultaneous vibration of the whole core structure with a single frequency ω_i, such that all nuclei pass their equilibrium position at the same time. These fundamental vibrational modes are called *delocalised* because they span over the whole molecule. On the other hand, a careful superposition of normal modes can lead to a predominant stretching of a certain bond, effectively creating a *local mode*.

In the harmonic approximation, an unperturbed, isolated molecule in free space would stay in an excited normal mode forever because the energy is trapped in this state. This, however, does not agree with experimental observation. In fact, most excited vibrational states are only stable on a timescale of picoseconds until their energy is transferred to other degrees of freedom. In equation 2.94 we approximated the nuclei potential by a second-order Taylor expansion, which is a good approximation in most cases but not generally true. If we take terms of higher order into account as well, we necessarily end up with an anharmonic potential that ultimately leads to *anharmonic coupling* because the interaction matrix $\tilde{\mathbf{V}}$ does not have a completely diagonalised representation anymore. For this reason, the vibrational modes can now exchange energy, which is called *internal vibrational energy redistribution* (IVR) for an isolated system or *energy relaxation* in general when the system is connected to external reservoirs as well.[75]

IVR can also be understood from a quantum-mechanical perspective in which we describe the system with the Schrödinger equation, whose solutions are the true molecular eigenstates of the system. These are, by definition, orthogonal, i.e. uncoupled, and time-independent. However, when we push the system into an excited state with our experimental setup we usually invoke a superposition of these molecular eigenstates with a particular phase relationship. The differing phase dependencies of each eigenstate then cause the superposition to become time-dependent and the initial phase relationship is lost after some time, which gives rise to the finite lifetime of a vibrational mode.[75,76] However because the true eigenstates are often unknown and generally hard to resolve, most authors prefer to introduce normal coordinates and anharmonic coupling as the cause for IVR. Either picture can be adopted and in this thesis, we are following the norm with classical anharmonic oscillators rather than the loss of phase information.

The precise mechanism of how an excited mode transfers its energy to other degrees of freedom is highly non-trivial and not yet completely understood. Some experiments suggest proportionality between the density of states of a molecular system and the excitation lifetime, such that a slow decay rate corresponds to a single excitation in a sparse region.[75,77] Another theory proclaims the necessity of certain vibrational modes to act as 'doorways' for strong anharmonic coupling to occur.[75,78] In addition, for free molecules in the gas phase, the internal rotation plays a significant role for IVR, which is known as *Coriolis coupling*.[75] The samples that we are going to investigate, however, are adsorbed on a substrate, such that the rotations are frustrated and strongly coupled to the surface atoms. Furthermore, the adsorbed monolayer is squeezed tightly together to the point that intermolecular coupling might also become relevant for the energy transfer.[79]

Since our molecules are long organic chains, these densely packed monolayers resemble, in good approximation, a form of two-dimensional molecular crystal. The vibrational dynamics of such crystals were investigated by Dlott et al. and can be roughly categorised into three frequency regimes.[80] The low-frequency modes usually distribute their energy by emission of two phonons, which are vibrations of the crystal layer. In the intermediate frequency regime, the vibrational relaxation mostly occurs by emission of one phonon and a lower energy vibration and the high-frequency modes behave similarly to isolated molecules, as they transfer their energy to a bath of lower vibrational levels.

Even though the mechanism of energy relaxation is still vigorously investigated, the theory regarding the excitation lifetime of adsorbed monolayers is generally understood. Two important time constants determine the decay rate of an excited state: the so-called *longitudinal relaxation time* T_1 and the *transversal relaxation time* T_2^* in analogy to the terminology used in magnetic resonance.[81] The relaxation time T_1 represents the loss of population due to energy relaxation into different degrees of freedom. As we mentioned before, this relaxation is due to intra- and intermolecular vibrational energy transfer, multiphonon emission in the monolayer and the coupling to substrate phonons. In addition, the excitation of electron-hole pairs in the substrate also plays an important

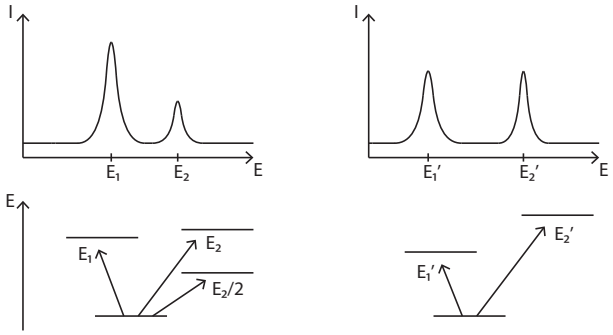

Figure **2-20**: Schematic illustration of a Fermi resonance. On the left side are the theoretically calculated intensities for a fundamental transition at E_1 and an overtone at E_2 in an arbitrary system. On the right side is the actual spectrum, in which the intensities are averaged and the energy levels are pushed apart due to anharmonic coupling.

role in energy relaxation, which, however, is only truly relevant for metallic surfaces and our samples are adsorbed on glass.[79] The relaxation time T_2^*, on the other hand, comes about due to the loss of coherence in the monolayer. This phase decay is either caused by elastic collisions with surface phonons or anharmonic coupling to low-frequency modes, which causes a random modulation of the observed excitation.[82]

In section 2.2.1 we talked about lineshapes and how the FWHM of a Lorentzian, defined in equation 2.42, is inversely proportional to the lifetime of an excitation. Similarly, one can show that in the case of a monolayer, the lineshape of a resonant excitation is given by a superposition of T_1 and T_2^* terms as

$$2\Gamma = \frac{2}{T_2} = \frac{1}{T_1} + \frac{2}{T_2^*}, \tag{2.105}$$

which is derived in detail by Ueba.[83] Here, 2Γ is the FWHM of a Lorentzian lineshape, according to equation 2.42 and T_2 is the overall relaxation time. There are two commonly deployed methods to obtain information about these relaxation times, namely time-resolved and frequency-resolved spectroscopy. The latter extracts the information from lineshape analysis, while the former has the advantage of separately probing the population decay T_1 and the overall relaxation time T_2. In this thesis, we are using the time-resolved method and mostly investigate the population decay of our samples to track the vibrational dynamics.

Before we wrap this section up, we want to address one last phenomenon because it is relevant to our molecular systems. When two vibrational modes are very close in energy, the anharmonic coupling between these levels becomes very strong if the symmetry of the vibrations is identical. In that case, the energy levels are pushed apart due to a mixing of the two wave functions, which is essentially an avoided crossing of vibrational levels that is known as a *Fermi resonance*. This mixing increases the coupling strengths between

modes and can act as a 'doorway' for the energy flow in the molecule, as we mentioned earlier.[53,75] Also, when we look at the spectrum of a Fermi resonance, the otherwise weaker mode is usually more intense, effectively becoming more 'allowed' and borrowing intensity from the stronger mode, which is illustrated schematically in figure **2-20**.

An example of such a Fermi resonance can be observed in the Raman spectrum of CO_2, in which the fundamental symmetric stretching and the much weaker first overtone of the bending mode are theoretically calculated to $\nu_s = 1337\,\mathrm{cm}^{-1}$ and $2\nu_b \approx 1334\,\mathrm{cm}^{-1}$, respectively. In the spectrum, however, there are two almost equally strong lines at $1388\,\mathrm{cm}^{-1}$ and $1286\,\mathrm{cm}^{-1}$, which is a strong indicator for a Fermi resonance.[84] On a side note, the quantity with unit cm^{-1} is called the *wavenumber*, which is usually preferred in spectroscopy because the fundamental frequencies are uncomfortably large in atomic systems. Therefore, the norm was established to divide the frequency by c and calling this quantity the wavenumber $\nu = \frac{f}{c} = \frac{1}{\lambda}$ in analogy to the angular wavenumber $k = \frac{2\pi}{\lambda}$ that we introduced in section 2.1.4. With the equation for the photon energy $E = hf$, we can calculate the energy in Joule from the wavenumber in cm^{-1} accordingly: $E = hc\nu 10^2$.

This concludes the section about vibrational dynamics and in the following, we are going to address the spectroscopic techniques by which we can observe these vibrational modes.

2.3.3 Vibrational Spectroscopy

The fact that all molecules vibrate with inherent characteristic frequencies, due to their structure, allows us to study molecular compounds with light. This field of science is called vibrational spectroscopy and it is one of the least invasive and least destructive methods of analysing a sample for its molecular structure.

In a prior subsection, we learned about the potential energy of the nuclei and their quantised motion in this potential, called vibrational levels. If we arrange for a light source to produce radiation of just the right frequency and direct it onto the system, we can observe a transition from one vibrational level to another, effectively changing its motion. Conceptually speaking, there are two mainly used techniques to realise such a transition of vibrational states: infrared absorption and Raman scattering. As the name implies, infrared absorption forces a system to transition to a higher state by absorption of a photon that usually correlates to energies in the infrared region. Raman scattering, on the other hand, induces the vibrational transition by an inelastic scattering process that was first discovered by C.V. Raman in 1928.[85] We will take a closer look at both of these techniques in the following paragraphs, which are, for the most part, adapted from the books by Hertel/Schulz and Demtröder.[70,73]

In general, the most important quantity for the interaction of light with matter is the dipole moment, which we already discussed in section 2.2.3. For a quantum-mechanical description of this interaction, however, we need to refine this statement slightly. We start

with a system in an arbitrary vibrational state $|i\rangle$ and want to transition this system to the vibrational state $|k\rangle$ by absorption of a photon. According to quantum mechanics, we can only find the probability of triggering such a transition and this probability is proportional to the square of

$$\mathbf{M}_{ik} = \int \Psi_k^* \hat{p} \Psi_i \, \mathrm{d}\mathbf{r} \, \mathrm{d}\mathbf{R} \,, \tag{2.106}$$

which is the quantity that the electromagnetic field interacts with, called the transition dipole moment. The $\mathbf{M}_{ik}$ can be seen as elements of a matrix that couples all the different states of a system, denoted by their respective wave functions Ψ. The operator $\hat{p}$ is the dipole operator

$$\hat{p} = -\sum_m e\mathbf{r}_m + \sum_n Z_n e\mathbf{R}_n \tag{2.107}$$

$$= \hat{p}_e + \hat{p}_n, \tag{2.108}$$

with the elementary charge e, the atomic number Z and the sums running over all electron $\mathbf{r}$ and nuclei $\mathbf{R}$ coordinates in the molecule. Furthermore, we split the operator into an electron $\hat{p}_\mathrm{el}$ and a nucleus $\hat{p}_\mathrm{n}$ part for convenience.

According to subsection 2.3.1, we can separate the motion of electrons and cores in the Born-Oppenheimer approximation such that the wave functions can also be split up into an electronic and a nuclei part

$$\Psi = \Psi_e \cdot \Psi_n. \tag{2.109}$$

If we now incorporate equations 2.108 and 2.109 into the transition dipole moment 2.106 we get, with some rearranging,

$$\mathbf{M}_{ik} = \int \Psi_{e,k}^* \Psi_{n,k}^* \left(\hat{p}_e + \hat{p}_n\right) \Psi_{e,i} \Psi_{n,i} \, \mathrm{d}\mathbf{r} \, \mathrm{d}\mathbf{R} \tag{2.110}$$

$$= \int \Psi_{n,k}^* \underbrace{\left[\int \Psi_{e,k}^* \hat{p}_e \Psi_{e,i} \, \mathrm{d}\mathbf{r}\right]}_{=0 \quad \text{for} \quad i=k} \Psi_{n,i} \, \mathrm{d}\mathbf{R}$$

$$+ \int \Psi_{n,k}^* \hat{p}_n \underbrace{\left[\int \Psi_{e,k}^* \Psi_{e,i} \, \mathrm{d}\mathbf{r}\right]}_{=1 \quad \text{for} \quad i=k} \Psi_{n,i} \, \mathrm{d}\mathbf{R} \,. \tag{2.111}$$

Since we are only interested in vibrational transitions in the scope of this thesis, we can disregard a change in the electronic level, such that

$$\Psi_{e,k} = \Psi_{e,i}. \tag{2.112}$$

Due to $\hat{p}_e$ being an odd function of $\mathbf{r}$, the integral over $\mathbf{r}$ in the first term in equation 2.111 equals zero if $\Psi_{e,k}^*$ and $\Psi_{e,i}^*$ are both even or odd functions, which is the case when

the electronic level does not change. Furthermore, the integral over $\mathbf{r}$ in the second term comes out as 1 because of the orthogonality of the wave functions. With that, we can write the transition dipole moment elements as

$$\mathbf{M}_{ik} = \int \Psi^*_{n,k} \hat{p}_n \Psi_{n,i} \, \mathrm{d}\mathbf{R} \,. \tag{2.113}$$

In theory, we have all the tools now to calculate these elements for a given system. We do, however, want to derive some more general principles from this formula, regarding IR absorption spectroscopy. As we have done before, we can approximate the dipole moment $p_n(R)$ with a Taylor expansion around the equilibrium distance R_0 as

$$p_n(R) \approx p_n(R_0) + \left.\frac{\partial p_n}{\partial R}\right|_{R=R_0} (R - R_0) \tag{2.114}$$

because the oscillation amplitudes $R - R_0 = |\mathbf{R_2} - \mathbf{R_1}| - R_0$ are usually sufficiently small. Seemingly, this representation is now restricted to diatomic molecules. One can, however, transform the local coordinates of any N-atomic system into the normal coordinates that we introduced in the last subsection, which describes the motion of the whole structure. In these normal coordinates, the Taylor expansion comes out the same as equation 2.114 and we can, therefore, stay with our simplified view of a diatomic molecule as a representation of the general case.

If we plug equation 2.114 into our transition dipole moment 2.113 we finally get

$$\mathbf{M}_{ik} = \underbrace{\int \Psi^*_{n,k} \hat{p}_n(R_0) \Psi_{n,i} \, \mathrm{d}R}_{=0 \quad \text{for} \quad i \neq k} + \left.\frac{\partial \hat{p}_n}{\partial R}\right|_{R=R_0} \int \Psi^*_{n,k} (R - R_0) \Psi_{n,i} \, \mathrm{d}R \,. \tag{2.115}$$

Here, the first term equals zero because $\hat{p}_n(R_0)$ is just a constant and the wave functions of different vibrational levels are orthogonal to one another. Furthermore, we can extract some very interesting facts about IR absorption spectroscopy from equation 2.115. First of all, for a molecular vibration to be susceptible to infrared radiation, the dipole moment has to change during the oscillation. This is one of the most important aspects of IR absorption spectroscopy and one can often find if a potential transition is IR active or not just by looking at the symmetry of the molecule. Secondly, in the harmonic approximation, the vibrational wave functions Ψ_n consist of the Hermite polynomials that we already discussed briefly in equation 2.92. Due to the special form of these polynomials, one can show how the second integral in equation 2.115 equals zero in all cases that are not $k = i \pm 1$. Therefore, the only allowed transitions are the ones that excite or de-excite the system to adjacent vibrational levels. Nevertheless, this is only strictly true for the harmonic oscillator and if we allow the potential to have anharmonicity, transitions of $k = i \pm 2$ and higher become possible solutions as well. These transitions are called

overtones and they occur with significantly less intensity. This concludes the part about IR absorption spectroscopy and we will now discuss Raman scattering.

For an accessible introduction to Raman scattering, most textbooks prefer to give a classical view of this phenomenon. We will follow this example but refer the reader to the book by Hertel and Schulz for a quantum-mechanical approach.[70] As before, the important quantity to look at is the dipole moment. The Raman effect, however, comes about not because of the permanent dipole of a system but the induced dipole due to the electric field of the light. It is, therefore, a time-dependent quantity that is proportional to the applied electric field, which we already discussed in section 2.2.3. Whenever a molecule is exposed to an electric field, the positive and negative charges are pushed in opposite directions, effectively polarising the system. This polarisation then oscillates with the same frequency as the light $\mathbf{E}(t) = \mathbf{E}_0 \cos(\omega t)$ and overlaps with any inherent permanent dipoles of the system. Therefore, the dipole operator from equation 2.108 becomes

$$\hat{p} = \hat{p}_e + \hat{p}_n + \hat{p}_{ind}. \tag{2.116}$$

According to equation 2.54, this induced dipole moment $\hat{p}_{ind}$ depends on the polarisability of the system α and the electric field of the light $\mathbf{E}(t)$, such that

$$\hat{p}_{ind} = \alpha \mathbf{E}(t) \tag{2.117}$$

$$= \alpha \mathbf{E}_0 \cos(\omega t). \tag{2.118}$$

Again, we take α as a scalar in favour of a more simplified explanation but we want to emphasise that α usually does depend significantly on direction and should be expressed as a second-rank tensor.

In the Born-Oppenheimer approximation, the polarisability becomes essentially dependent on the nuclei distance, which usually only changes slightly from the equilibrium distance R_0. For this reason, we can express α in a Taylor series around R_0, similarly to how we developed the permanent dipole moment in equation 2.114. Therefore, we write

$$\alpha(R) \approx \alpha(R_0) + \left.\frac{\partial \alpha}{\partial R}\right|_{R=R_0} (R - R_0). \tag{2.119}$$

As we mentioned before, although this equation represents a diatomic system, the principle is true for any N-atomic molecule and can be represented in the same way, using normal coordinates. Without the driving field, the molecule will oscillate harmonically with a characteristic frequency ω_0 about the equilibrium position R_0, which can be expressed as

$$R(t) - R_0 = R_1 \cos(\omega_0 t). \tag{2.120}$$

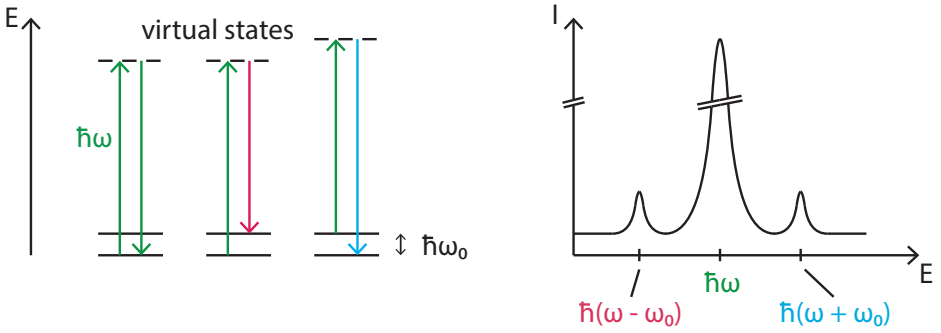

Figure **2-21**: Illustration of different scattering processes of photons. On the left, we see a potential energy diagram and multiple vibrational states of a system. The first transition is the elastic Rayleigh scattering that does not change the energy of the scattered photon and the other two transitions depict the Stokes (energy loss) and Anti-Stokes scattering (energy gain), respectively. The dotted lines indicate virtual states. On the right side, the corresponding spectrum is illustrated.

If we incorporate this into equation 2.118, the induced dipole moment becomes

$$\hat{p}_{ind} = \alpha E(t) \approx \left[\alpha(R_0) + \left.\frac{\partial\alpha}{\partial R}\right|_{R=R_0} R_1 \cos(\omega_0 t)\right] E_0 \cos(\omega t) \tag{2.121}$$

$$= \alpha(R_0) E_0 \cos(\omega t) + \left.\frac{\partial\alpha}{\partial R}\right|_{R=R_0} \frac{R_1 E_0}{2} \left[\cos\left((\omega+\omega_0)t\right) + \cos\left((\omega-\omega_0)t\right)\right]. \tag{2.122}$$

We can learn two very important aspects of Raman spectroscopy from this classical description. Firstly, the induced dipole oscillates at three different frequencies: the unmodulated frequency ω of the light and two modulated bands with $\omega+\omega_0$ and $\omega-\omega_0$. The unmodulated frequency is just the elastic Rayleigh scattering that we already discussed in section 2.2.2 but the two modulated bands arise from inelastic Raman scattering. The process in which the molecule gains energy $\omega - \omega_0$ is called a *Stokes* transition and the opposite band in which an excited molecule loses energy $\omega + \omega_0$ is called an *Anti-Stokes* transition. These transitions and their respective spectra are illustrated in figure **2-21**. The Raman effect is usually very weak, which is why the Raman lines are that much smaller than their Rayleigh counterpart in the spectrum. Additionally, the scattering process is usually illustrated with a dotted line to indicate a transition to a *virtual state*. Such a virtual state is not an eigenstate of the free atom but rather a level with the combined energy of an eigenstate and one or more photons of the irradiating field.[86]

The second important aspect we can extract from equation 2.122 is the fact that Raman lines can only be observed in molecules that change their polarisability during the nuclei oscillation ($\left.\frac{\partial\alpha}{\partial R}\right|_{R=R_0} \neq 0$). This makes Raman spectroscopy a very powerful technique because it can identify structures that are transparent for IR absorption. There

are, however, also vibrational modes that change neither their dipole moment nor their polarisability during the oscillation, which are called *silent modes* because they cannot be observed spectroscopically.[87]

Concludingly, we introduced the two most applied techniques to induce vibrational transitions in molecules, which are IR absorption and Raman scattering. Moreover, we learned that for a vibrational mode to be IR or Raman active, the dipole moment or the polarisability of the system has to change during the vibration of the cores, respectively. Building up on that, we are going to take a look at more advanced spectroscopic methods that make use of non-linear effects, in the following subsection.

2.3.4 Non-Linear Optics

When we introduced optical phenomena in the previous sections, we always assumed the response of the system to be linear in regard to the electric field of the light. In other words, light that interacts with a medium will get reflected or refracted but never changes its frequency. This, however, is only a good approximation for weak fields and in the following subsection, we will address phenomena that arise in the presence of strong electric fields. For the most part, this subsection is adapted from the first chapter of '*Nonlinear Optics*' by Robert Boyd.[86]

In equation 2.56 of section 2.2.3 we defined the macroscopic polarisation $\mathbf{P}$ of a medium due to the irradiation of light as

$$\mathbf{P} = \chi^{(1)}\epsilon_0\mathbf{E}. \tag{2.123}$$

Here, we denoted the proportionality constant χ with a superscript to indicate the *linear susceptibility*. In general, this equation is a good approximation for most optical effects that can be observed in nature. However, with the advent of lasers that generate highly intense and coherent radiation came the observation of phenomena that could not be explained by this linear polarisation. Specifically, the discovery of second-harmonic generation by Franken et al. in 1961 is often referred to as the beginning of the field of non-linear optics.[88]

To accurately describe these new phenomena, it became necessary to include non-linear terms in the optical response. Therefore, one often expresses the polarisation in a power series, such that

$$\begin{aligned} P &= \epsilon_0 \left(\chi^{(1)}E + \chi^{(2)}E^2 + \chi^{(3)}E^3 + \dots\right) \\ &= P^{(1)} + P^{(2)} + P^{(3)} + \dots, \end{aligned} \tag{2.124}$$

where $\chi^{(2)}$ and $\chi^{(3)}$ are called the second- and third-order non-linear susceptibilities, respectively. We now have taken the quantities to be scalar in favour of a more simplistic approach when in reality, the susceptibilities are tensors of rank $(1, 2, 3, \dots)$ and $\mathbf{P}$ and

E are three-dimensional vectors. We will take a closer look at the nature of these tensors in the next subsection.

Usually, all of the contributions to the polarisation $P^{(n)}$ are several orders of magnitudes apart, which is the reason why enormous field strengths are necessary to observe these non-linear effects. The second-order non-linear susceptibility becomes significant for electric fields that are comparable in strength to these inside of the atom E_{at}. If we take the hydrogen atom as an example, we can approximate the strength of this electric field by

$$E_{at} = \frac{e}{4\pi\epsilon_0 a_0^2} \approx 5.14 \cdot 10^{11} \frac{\mathrm{V}}{\mathrm{m}}, \tag{2.125}$$

with the Bohr radius of the hydrogen atom a_0. Furthermore, one can show how the second- and third-order susceptibilities are of the order of $\frac{\chi^{(1)}}{E_{at}}$ and $\frac{\chi^{(1)}}{{E_{at}}^2}$, respectively in the case of significant non-linear effects.[89] Empirically, it was found that for condensed matter $\chi^{(1)}$ is of the order of unity, which lets us predict the strength of the non-linear contributions accordingly. We find

$$\chi^{(2)} \approx \frac{1}{E_{at}} = 1.94 \cdot 10^{-12} \frac{\mathrm{m}}{\mathrm{V}} \quad \text{and} \tag{2.126}$$

$$\chi^{(3)} \approx \frac{1}{E_{at}^2} = 3.78 \cdot 10^{-24} \frac{\mathrm{m}^2}{\mathrm{V}^2}, \tag{2.127}$$

which does indeed agree with the experimental data of various experiments and shows quite well how significantly different these contributions are in strength.[86] We should also note, however, that the approximations in equations 2.126 and 2.127 are only good for optical frequencies away from resonance. Near resonances, χ_2 and χ_3 can become quite large such that the non-linear effects are observable with much weaker light.[90]

The non-linear contributions to the polarisation give rise to a multitude of new phenomena. If we take the second-order contribution for example and have our irradiating light be a superposition of two different frequencies

$$E(t) = E_1 \cos(\omega_1 t) + E_2 \cos(\omega_2 t) = E_1 \mathrm{e}^{-i\omega_1 t} + E_2 \mathrm{e}^{-i\omega_2 t} + \mathrm{c.c.}, \tag{2.128}$$

we find that

$$\begin{aligned} P^{(2)}(t) =& \epsilon_0 \chi^{(2)} E(t)^2 \\ =& 2\epsilon_0 \chi^{(2)} \left(E_1^2 E_2^2\right) + \epsilon_0 \chi^{(2)} (E_1^2 \mathrm{e}^{-i2\omega_1 t} + E_2^2 \mathrm{e}^{-i2\omega_2 t} \\ &+ 2E_1 E_2 \mathrm{e}^{-i(\omega_1+\omega_2)t} + 2E_1 E_2 \mathrm{e}^{-i(\omega_1-\omega_2)t} + \mathrm{c.c.}). \end{aligned} \tag{2.129}$$

Here, we can see how the non-linear contribution results in multiple mixing processes, such that the induced polarisation now oscillates with not just the original frequencies but new ones. In most textbooks, $P^{(2)}(t)$ is often expressed as

$$P^{(2)}(t) = \sum_n P(\omega_n) \mathrm{e}^{-i\omega_n t}, \tag{2.130}$$

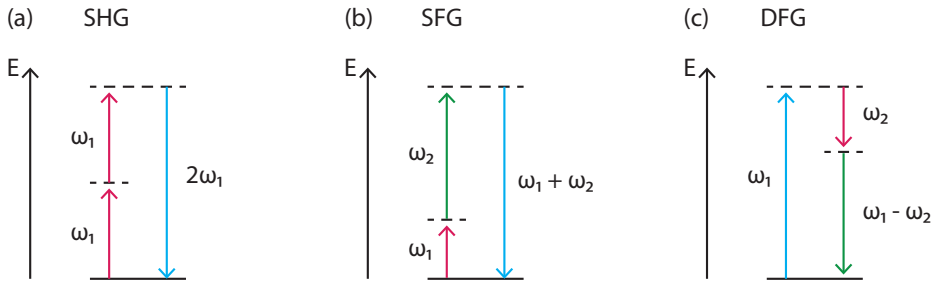

Figure **2-22**: Energy level description of (a) second-harmonic generation (SHG), (b) sum-frequency generation (SFG), and (c) difference-frequency generation (DFG).

where the sum extends over all positive frequencies ω_n. In this notation, we can conveniently take a closer look at each individual oscillating term, which for $n = 2$ are

$$\begin{aligned} P(2\omega_1) &= \epsilon_0 \chi^{(2)} E_1^2 \quad \text{(SHG)}, \\ P(2\omega_2) &= \epsilon_0 \chi^{(2)} E_2^2 \quad \text{(SHG)}, \\ P(\omega_1 + \omega_2) &= 2\epsilon_0 \chi^{(2)} E_1 E_2 \quad \text{(SFG)}, \\ P(\omega_1 - \omega_2) &= 2\epsilon_0 \chi^{(2)} E_1 E_2 \quad \text{(DFG)}, \\ P(0) &= 2\epsilon_0 \chi^{(2)} (E_1^2 + E_2^2) \quad \text{(OR)}. \end{aligned} \tag{2.131}$$

(2.132)

As mentioned previously, the second-harmonic generation (SHG) was the first observed non-linear effect and it induces a polarisation in the medium that oscillates with twice the original frequency. The process of SHG is schematically illustrated in figure **2-22** (a) with an energy level diagram. Here, two photons at frequency ω_1 are annihilated and a photon at frequency $2\omega_1$ is created simultaneously in a single quantum-mechanical process. In this figure, the solid lines indicate the ground state and the dashed lines are virtual states that we already mentioned in the previous subsection.

The energy level diagrams of sum- and difference-frequency generation (SFG) and (DFG), respectively are illustrated in figure **2-22** (b) and (c). These processes are more general in the sense that they can generate a wide array of different photons and specifically in this thesis we are using two laser pulses to induce a sum-frequency photon that probes our molecular systems. Although SFG and DFG are seemingly very similar processes, there is an important difference between them. If we look at the energy level diagram in figure **2-22** (c), we see that to create a photon at $\omega = \omega_1 - \omega_2$, a photon at higher energy ω_1 must be annihilated and a photon at lower energy ω_2 is created. Consequently, the lower-frequency field is amplified in this process, which is known as *optical parametric amplification* and most infrared lasers feature such an amplifier. In this sense, we are utilising SFG, DFG and SHG in our setup to generate all the photons we need to investigate our molecules.

The last equation in 2.132 features terms with zero frequency. This contribution to the polarisation does not lead to the generation of electromagnetic radiation because its second derivative vanishes. It does, however, induce a static electric field across the non-linear medium and this process is known as *optical rectification* (OR).

Although all of the contributions in 2.132 are theoretically possible, usually only one will be significant in an experiment. The reason for that is the necessity for a certain phase-matching condition to be satisfied, which can only really be done for a single frequency component. The phase-matching condition for our sum-frequency setup is discussed in more detail in the next subsection. Naturally, this derivation can be extended to the third-order polarisation as well, yielding even more different frequencies. We will, however, omit this approach since our main interest lies in the second-order contribution and the reader is instead referred to the book by Robert Boyd.[86]

The last point we want to emphasise is the fact that due to the tensor nature of the susceptibility, the non-linear contributions are strongly dependent on the symmetry of the medium. Furthermore, one can specifically show how the second-order contribution to the polarisation vanishes completely in media that have inversion symmetry, which is also known as *centrosymmetry*. Although it is true in general that $\chi^{(2)}$ vanishes in centrosymmetric media, one can easily demonstrate this fact for the special case of second harmonic generation. We assume the second-order polarisation to be

$$P^{(2)}(t) = \epsilon_0 \chi^{(2)} E(t)^2, \tag{2.133}$$

with $E(t) = E_0 \cos(\omega t)$. Now, if we change the sign of the applied electric field, the inversion symmetry forces the polarisation to change signs as well and we get

$$-P^{(2)}(t) = \epsilon_0 \chi^{(2)} (-E(t))^2. \tag{2.134}$$

Comparing this result to equation 2.133, we find that $-P^{(2)}(t) = P^{(2)}(t)$, which is only true for $P^{(2)}(t) = 0$. Accordingly, if the polarisation vanishes for an arbitrary applied electric field, the non-linear susceptibility has to vanish as well, namely

$$\chi^{(2)} = 0. \tag{2.135}$$

As an alternative perspective, we can also look at the potential energy functions of non- and centrosymmetric media. The potential energy depends on the restoring force on the electrons, which is given by Hook's law in equation 2.33 for the harmonic case. The actual potential, however, is given by a Taylor expansion of Hook's law and if we just take the lowest order, we find for the non-centrosymmetric case that

$$F_{restore} = -m\omega_0^2 x - max^2, \tag{2.136}$$

with the strength of the non-linearity denoted by a. The associated potential energy is the integral of this force, which is

$$V_{ncs}(x) = -\int F_{restore}\, \mathrm{d}x = \frac{1}{2} m\omega_0^2 x^2 + \frac{1}{3} max^3. \tag{2.137}$$

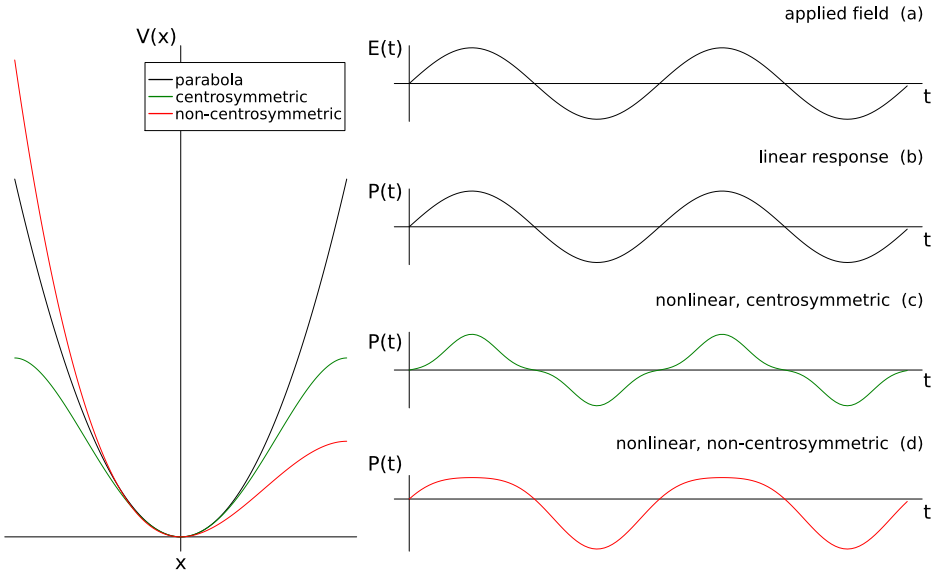

Figure **2-23**: On the left side are the potential energy functions for centrosymmetric and non-centrosymmetric media and a parabola for comparison. On the right side is the plot of a sinusoidal applied electric field (a). The polarisation response due to this field is sketched for the linear contribution (b) and the non-linear contributions in a centrosymmetric (c) and non-centrosymmetric (d) medium. Adapted from Boyd.[86]

In centrosymmetric media, on the other hand, the first-order Taylor contribution vanishes because it does not satisfy the symmetry of the $x \to -x$ operation. Therefore, we need to expand the series to the second order in the centrosymmetric case, such that

$$V_{cs} = -\int -m\omega_0^2 x + mbx^3 \,\mathrm{d}x = \frac{1}{2}m\omega_0^2 x^2 - \frac{1}{4}mbx^4. \tag{2.138}$$

The centrosymmetric $V_{cs}(x)$ and non-centrosymmetric $V_{ncs}(x)$ potential energy functions are plotted on the left side of figure **2-23** along with a simple parabola for comparison. On the right side of this figure, we can see the polarisation in response to an applied electric field. Part (a) is the sinusoidal waveform of an arbitrary incident electromagnetic wave of a single frequency ω. The linear response mirrors the applied field such that there is no distortion of the waveform, which is illustrated in part (b). For centrosymmetric media that feature a potential like V_{cs}, we find strong waveform distortion in the non-linear polarisation, as we can see in part (c) of figure **2-23**. Although the distortion is significant, we only find odd overtones of the fundamental frequency because of the symmetry of the potential energy. For the anharmonic potential of a non-centrosymmetric medium V_{ncs}, however, we find strong distortion of polarisation waveform because both even and odd overtones of the fundamental frequency are present. This case is depicted in part (d).

We also want to point out that the time-average of the waveforms in parts (c) and (d) of figure **2-23** are different. In the centrosymmetric case, the time average of the

non-linear polarisation comes out as zero, whereas for non-centrosymmetric media it is nonzero. The reason for that is the strong dependence of the non-linear susceptibility on direction, such that the polarisation of the incident electric field dictates the polarisation of the medium. This direction dependence is very important for the structural analysis of molecular monolayers and will be further discussed in the following subsection. Furthermore, we are taking a closer look at the sum-frequency contribution to $\chi^{(2)}$ specifically, since we are mainly utilising this process in our vibrational sum-frequency spectroscopy (vSFS) setup.

2.3.5 Sum-Frequency Generation

In the previous section, we introduced non-linear contributions to the induced polarisation of dense materials that become significant when the irradiating fields are very intense. We also found that the second-order and more generally all even-order contributions vanish in centrosymmetric media. For that reason, the second-order polarisation is an effective tool to investigate interfaces because the layer at which two different centrosymmetric media come together, necessarily features a break in symmetry. Especially the sum-frequency contribution became a major player in molecular interface analysis, ultimately establishing the field of science known as *vibrational sum-frequency spectroscopy* (vSFS). This subsection aims to provide a deeper understanding of sum-frequency generation and is partly based on the second chapter of '*Nonlinear Optics*' by Robert Boyd and the tutorial review by Lambert, Davies, and Neivandt.[67,86]

We begin with a qualitative view of the sum-frequency generation process. When an atomic system is irradiated with an electric field of frequencies ω_1 and ω_2, this system develops a dipole moment, according to equation 2.118. This dipole moment will oscillate with many frequencies, including a component at $\omega_1 + \omega_2$ and radiate its energy like a typical dipole that we already described in section 2.2.2. This quantum-mechanical process is sketched in part (a) of figure **2-24**. In dense materials, there are numerous of these oscillators close together and if their phase relationship is just right, their radiated fields interfere constructively, forming a strong beam in a single direction, which is illustrated in part (b) of figure **2-24**. When we talked about the scattering of light in section 2.2.2, we already described how the intensity of such an interference field is proportional to N^2, if all N oscillators are in-phase. So even though the $\chi^{(2)}$ contribution is fairly small, we can still generate a decent signal with an appropriate laser setup, which is known as the *phase-matching condition*.

To find this phase-matching condition, we need to solve *Maxwell's equations* while allowing for non-linearities in the polarisation. With equation 2.67 in section 2.2.4 we already derived the wave equation for a linear polarisation, which we are going to take as

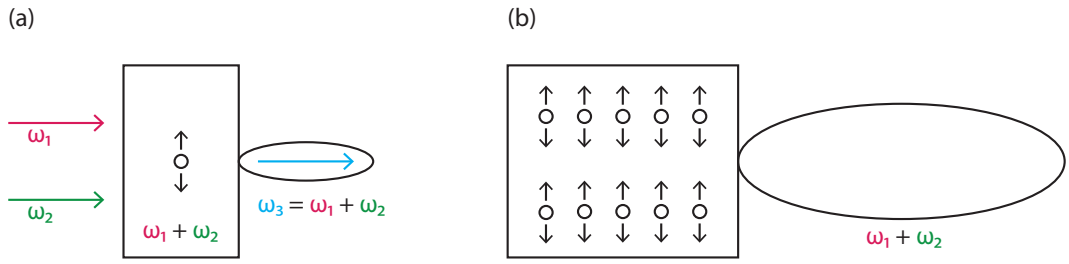

Figure **2-24**: Schematic illustration of the sum-frequency generation process. The atomic response of a single oscillator is shown in part (a) and the enhanced radiation for multiple oscillators in-phase is illustrated in part (b). Adapted from Boyd.[86]

our starting point:

$$\nabla^2\mathbf{E} - \frac{1}{c^2}\frac{\partial^2\mathbf{E}}{\partial t^2} = -\frac{1}{\epsilon_0}\boldsymbol{\nabla}(\boldsymbol{\nabla}\cdot\mathbf{P}) + \mu_0\frac{\partial^2\mathbf{P}}{\partial t^2}. \tag{2.139}$$

Previously, we discussed how the first term on the right-hand side of this equation vanishes for a linear polarisation response. In the case of non-linearities, this contribution is usually non-vanishing but can still be neglected for most cases of interest. Specifically, in the *slowly varying amplitude approximation*, which is valid as long as the amplitude of the sum-frequency component does not change much in a distance of the order of an optical wavelength, $\boldsymbol{\nabla}(\boldsymbol{\nabla}\cdot\mathbf{P})$ is negligibly small. That leaves us with

$$\nabla^2\mathbf{E} - \frac{1}{c^2}\frac{\partial^2\mathbf{E}}{\partial t^2} = \mu_0\frac{\partial^2\mathbf{P}}{\partial t^2}. \tag{2.140}$$

For further convenience, we express the polarisation as

$$\mathbf{P} = \mathbf{P}^{(1)} + \mathbf{P}^{(\mathrm{NL})}, \tag{2.141}$$

such that $\mathbf{P}^{(1)}$ is the part that goes linearly with $\mathbf{E}$ and $\mathbf{P}^{(\mathrm{NL})}$ describes the non-linear contributions. With that, our equation becomes

$$\nabla^2\mathbf{E} - \frac{1}{c^2}\frac{\partial^2\mathbf{E}}{\partial t^2} = \mu_0\frac{\partial^2}{\partial t^2}\left(\mathbf{P}^{(1)} + \mathbf{P}^{(\mathrm{NL})}\right) \tag{2.142}$$

$$\Leftrightarrow \quad \nabla^2\mathbf{E} - \mu_0\frac{\partial^2}{\partial t^2}\underbrace{\left(\epsilon_0\mathbf{E} + \mathbf{P}^{(1)}\right)}_{\mathbf{D}^{(1)}} = \mu_0\frac{\partial^2\mathbf{P}^{(\mathrm{NL})}}{\partial t^2}. \tag{2.143}$$

Historically, the quantity $\mathbf{D}^{(1)} = \epsilon_0\mathbf{E} + \mathbf{P}^{(1)}$ was defined as part of a new vector $\mathbf{D} = \mathbf{D}^{(1)} + \mathbf{P}^{(\mathrm{NL})}$ to express *Maxwell's equations* in a simpler form. With equation 2.56 we find that

$$\mathbf{D}^{(1)} = \epsilon_0\mathbf{E} + \chi^{(1)}\epsilon_0\mathbf{E} = \epsilon_0\underbrace{\left(1 + \chi^{(1)}\right)}_{\kappa^{(1)}}\mathbf{E}, \tag{2.144}$$

where $\kappa^{(1)}$ is a real, frequency-dependent dielectric tensor, called the relative permittivity. This is analogous to the definition we gave in equation 2.58 of section 2.2.3 because the permittivity becomes a scalar in isotropic media. In general, however, the permittivity is dependent on direction and expressed as a tensor, such that

$$\nabla^2\mathbf{E} - \frac{\kappa^{(1)}}{c^2} \cdot \frac{\partial^2\mathbf{E}}{\partial t^2} = \mu_0 \frac{\partial^2\mathbf{P}^{(\mathrm{NL})}}{\partial t^2}, \tag{2.145}$$

which has the form of an inhomogeneous wave equation with $\mathbf{P}^{(\mathrm{NL})}$ appearing as the source term that is driving the radiation.

In the case of a dispersive medium, we need to consider each frequency component separately. Therefore, we express $\mathbf{E}$ and $\mathbf{P}^{(\mathrm{NL})}$ as

$$\mathbf{E}(\mathbf{r},t) = \sum_n \mathbf{E}_n(\mathbf{r})\mathrm{e}^{-i\omega_n t} + \mathrm{c.c} \quad \text{and} \tag{2.146}$$

$$\mathbf{P}^{(\mathrm{NL})}(\mathbf{r},t) = \sum_n \mathbf{P}_n^{(\mathrm{NL})}(\mathbf{r})\mathrm{e}^{-i\omega_n t} + \mathrm{c.c}, \tag{2.147}$$

with the summation running over all positive frequencies. Incorporating this into equation 2.145, we get a wave equation for each frequency component of the field

$$\nabla^2\mathbf{E}_n(\mathbf{r}) + \frac{\omega_n^2}{c^2}\kappa^{(1)}(\omega_n) \cdot \mathbf{E}_n(\mathbf{r}) = -\frac{\omega_n^2}{\epsilon_0 c^2}\mathbf{P}_n^{(\mathrm{NL})}. \tag{2.148}$$

This frequency-domain wave equation is also known as a *Helmholtz* equation.

We first consider the simple homogeneous case of an absent source term. Here, we find the solution to the Helmholtz equation for a plane wave that travels in the z-direction and oscillates with the sum-frequency component ω_3 as

$$E_3(z,t) = E_3(z)\mathrm{e}^{-i(\omega_3 t)} + \mathrm{c.c.} = A_3\mathrm{e}^{i(k_3 z - \omega_3 t)} + \mathrm{c.c.}, \tag{2.149}$$

with

$$k_3 = \frac{n_3\omega_3}{c} \quad \text{and} \quad n_3^2 = \kappa^{(1)}(\omega_3). \tag{2.150}$$

The last relation comes about due to equation 2.76 and we also disregarded local field effects as well as the tensor character of $\kappa^{(1)}$, for reasons of simplicity. In this homogeneous solution, the amplitude A_3 is a constant. This is no longer the case, however, when we include the non-linear source term. In good approximation, we can expect the solution to be of the same form as 2.149 but with a slowly varying amplitude $A_3(z)$ if the source term is not too large. Further, we represent the source term as

$$P_3(z,t) = P_3(z)\mathrm{e}^{-i\omega_3 t}, \tag{2.151}$$

where the amplitude P_3 can be expressed in terms of the amplitudes of the incident fields as

$$P_3(z) = 2\epsilon_0 \chi^{(2)} E_1(z) E_2(z), \tag{2.152}$$

which is derived in detail by Boyd.[86] The applied fields ($i = 1, 2$) are given by

$$E_i(z,t) = E_i(z) \mathrm{e}^{-i\omega_i t} + \text{c.c.} = A_i \mathrm{e}^{i(k_i z - i\omega_i z)}. \tag{2.153}$$

Incorporating equation 2.149 with a varying amplitude $A_3(z)$ and the source term 2.152 into the Helmholtz equation 2.148, we end up with

$$\begin{aligned} &\left[\frac{\partial^2}{\partial z^2} A_3(z) + 2ik_3 \frac{\partial}{\partial z} A_3(z) - k_3^2 A_3(z) + \frac{\omega_3^2 \kappa^{(1)}(\omega_3)}{c^2}\right] \mathrm{e}^{ik_3 z} + \text{c.c.} \\ &\quad = -\frac{2\omega_3^2}{c^2} \chi^{(2)} A_1 A_2 \mathrm{e}^{i(k_1+k_2)z} + \text{c.c.}. \end{aligned} \tag{2.154}$$

With $k_3^2 = \frac{\omega_3^2 \kappa^{(1)(\omega_3)}}{c^2}$ the third and fourth term cancel. Furthermore, we do not lose the equality if we drop the complex conjugate forms on either side, which simplifies the equation to

$$\frac{\partial^2}{\partial z^2} A_3(z) + 2ik_3 \frac{\partial}{\partial z} A_3(z) = -\frac{2\omega_3^2}{c^2} \chi^{(2)} A_1 A_2 \mathrm{e}^{i(k_1+k_2-k_3)z}. \tag{2.155}$$

This form is usually simplified even further by saying that the first term on the left side is much smaller than the second, which is the slowly varying amplitude approximation that we mentioned earlier. We can, therefore, drop the first term and get

$$\frac{\partial A_3(z)}{\partial z} = \frac{i\omega_3}{n_3 c} \chi^{(2)} A_1 A_2 \mathrm{e}^{i\Delta k z}, \tag{2.156}$$

where we introduced the wavevector mismatch $\Delta k = k_1 + k_2 - k_3$.

We solve equation 2.156 by integrating over the interaction length L of the non-linear medium, such that

$$A_3(L) = \frac{i\omega_3 \chi^{(2)} A_1 A_2}{n_3 c} \int_0^L \mathrm{e}^{i\Delta k z} dz = \frac{i\omega_3 \chi^{(2)} A_1 A_2}{n_3 c} \left(\frac{\mathrm{e}^{i\Delta k L} - 1}{i\Delta k}\right). \tag{2.157}$$

The intensity of the sum-frequency contribution is proportional to the square of this amplitude. More specifically, the intensity is equal to the time average of the Poynting vector, which is, according to Boyd,[86]

$$I_i = 2n_i \epsilon_0 c |A_i|^2, \quad i = 1, 2, 3. \tag{2.158}$$

With that, we find the intensity of the generated wave as

$$I_3 = \frac{2\epsilon_0 \omega_3^2 {\chi^{(2)}}^2 |A_1|^2 |A_2|^2}{n_3 c} \left|\frac{\mathrm{e}^{i\Delta k L} - 1}{\Delta k}\right|^2, \tag{2.159}$$

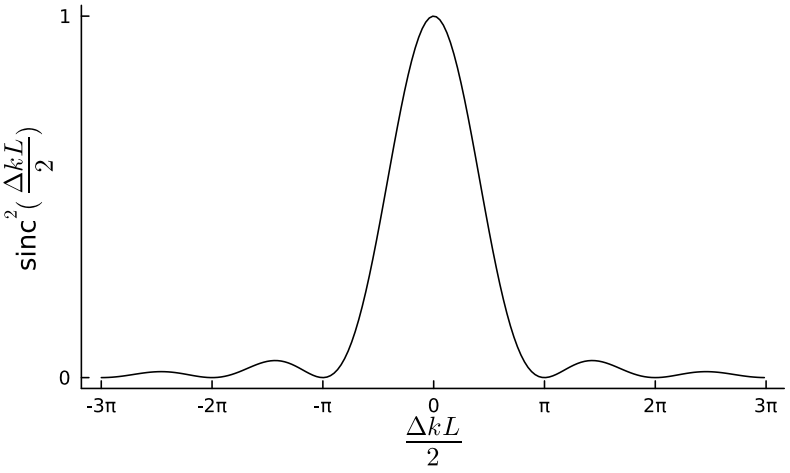

Figure **2-25**: Plot of the intensity of the sum-frequency signal in dependence of the wavevector mismatch Δk

which can be simplified even further with

$$\left|\frac{\mathrm{e}^{i\Delta kL}-1}{\Delta k}\right|^2 = L^2\left(\frac{\mathrm{e}^{i\Delta kL}-1}{\Delta kL}\right)\left(\frac{\mathrm{e}^{-i\Delta kL}-1}{\Delta kL}\right) = 2L^2\frac{(1-\cos(\Delta kL))}{(\Delta kL)^2}$$
$$= L^2\frac{\sin^2\left(\frac{\Delta kL}{2}\right)}{\left(\frac{\Delta kL}{2}\right)^2} \equiv L^2\mathrm{sinc}^2\left(\frac{\Delta kL}{2}\right). \tag{2.160}$$

As the last step, we express I_3 in terms of the intensities of the incident fields I_1 and I_2 with equation 2.158, which yields the final equation for the intensity of the sum-frequency field as

$$I_3 = \frac{\omega_3^2{\chi^{(2)}}^2 I_1 I_2}{2n_1n_2n_3\epsilon_0c^3}L^2\mathrm{sinc}^2\left(\frac{\Delta kL}{2}\right). \tag{2.161}$$

By taking a closer look at equation 2.161, we can learn some very interesting aspects about the sum-frequency signal. First of all, the intensity of SFG is proportional to the intensity of each of the incident waves I_1 and I_2. Secondly, the strong quadratic dependence indicates how the non-linear susceptibility plays a huge part in the strength of the signal. Furthermore, we can finally see the strong influence of the wavevector mismatch Δk on the intensity of the sum-frequency wave, which is plotted in figure **2-25**.

The condition

$$\Delta k = 0 \tag{2.162}$$

is the phase-matching that we were looking for and we can see now, how the efficiency of SFG is maximal at perfect phase-matching. Moreover, the intensity of the signal decreases drastically, with some oscillations occurring, when the condition 2.162 is not met. On a

microscopic scale, one can assume that all atomic dipoles are in-phase and add coherently to the emitted signal when perfect phase-matching is achieved. Consequently, in such a case the total power of the sum-frequency signal scales as the square of the number of atomic oscillators that participate, as we have stated in the beginning. Furthermore, the results we presented here are for the one-dimensional case but the three-dimensional case leads to the same equations. However, there is one important aspect that we want to mention. When the k_i are represented by vectors, the wavevector mismatch in three dimensions necessarily leads to a directed beam in space, which is an inherent characteristic of sum-frequency generation.

It should be noted that in equation 2.157 we specifically restricted our derivation to the case where the amplitudes of the incident waves A_1 and A_2 are taken as constants. This approximation is valid as long as the conversion of the input fields into the sum-frequency field is not too large. In our experimental setup, we have a weaker field at a lower frequency that corresponds to infrared radiation and a stronger field at a frequency in the visible region. This process is known as *upconversion* because the weaker, information-carrying wave is enhanced and shifted to higher frequencies, which usually makes it much easier to detect. In this case, usually, only the amplitude of the stronger field A_2 can be taken as constant in equation 2.157 and the weaker field amplitude A_1 becomes a function of z. This situation leads to a somewhat more complicated formula than equation 2.161 due to the more intricate dependence on the amplitude $A_1(z)$. However, the efficiency of the sum-frequency generation near $\Delta k = 0$ still roughly follows the curve in figure **2-25** and is mainly dependent on the above-mentioned quantities. Therefore, we are not getting into details about the so-called *undepleted-pump approximation* here but instead, refer the interested reader to the thorough derivation by Boyd.[86]

Second-Order Non-Linear susceptibility

Now that we understand the impact of the phase-matching condition on the sum-frequency signal, we are going to take a closer look at the influence of the second-order non-linear susceptibility. As mentioned above, we utilise an upconversion setup with a weaker infrared beam and a beam in the visible region that converts the vibrational information of the IR beam to a higher frequency. The susceptibility in equation 2.161 is the only quantity that changes significantly with the IR frequency and is therefore solely responsible for the vibrational information in our sum-frequency spectrum.[67]

In section 2.2.3 we introduced the atomic polarisability α and the (linear) susceptibility as the proportionality factors that govern the microscopic and the macroscopic polarisation of a system, respectively. In this sense, we can regard the susceptibility as the macroscopic average of the atomic polarisability α. In equation 2.124 we expanded the polarisation of a system into a power series to include non-linear terms and accordingly,

we can also expand the microscopic polarisation in the same manner, such that

$$p = \alpha E + \beta E^2 + \gamma E^3 + \dots . \tag{2.163}$$

The quantities β and γ are called second- and third-order *hyperpolarisabilities* and we can, in analogy to the linear case, define the non-linear susceptibility $\chi^{(2)}$ as the macroscopic average of the second-order hyperpolarisability β. The complete formula for β requires a lengthy quantum-mechanical derivation, using perturbation theory, which is why we are only giving the results here.[91] Specifically, one can show that

$$\beta \propto M_{\nu,k}\alpha_{\nu,i,j}. \tag{2.164}$$

The $M_{\nu,k}$ are the components of the IR transition dipole moment that we defined in equation 2.106 and $\alpha_{\nu,i,j}$ are the components of the Raman transition dipole moment, which we did not specifically derive in this thesis.[92] The exact form of the Raman components is, however, not that important. The more crucial consequence of equation 2.164 is the strong selection rule of vSFS, such that a resonance has to be both IR and Raman active to be visible in a vSF spectrum.

The lineshape of such a resonance can be modelled with a Lorentzian that we already derived in equation 2.43 because we can express the second-order susceptibility, similarly to the linear case in equation 2.57, as

$$\chi^{(2)} = \left|\chi^{(2)}_{\mathrm{nr}}\right| e^{i\xi} + \sum_k \frac{A_k}{\omega_{0,k} - \omega_{\mathrm{IR}} + i\Gamma_k}, \tag{2.165}$$

with k running over all vibrational modes of the system. Accordingly, we find the intensity as

$$I_{\mathrm{sf}} \propto \left| \left|\chi^{(2)}_{\mathrm{nr}}\right| e^{i\xi} + \sum_k \frac{A_k}{\omega_{0,k} - \omega_{\mathrm{IR}} + i\Gamma_k} \right|^2 . \tag{2.166}$$

Here, we included all of the contributions from β in the oscillator strength A_k, and ω_{IR} and Γ_k are the frequency of the IR beam and the damping constant, respectively. Furthermore, in addition to the resonant contributions that we model with the Lorentzian part in 2.165 we also need to include any possible non-resonant contributions $\chi^{(2)}_{\mathrm{nr}} = \left|\chi^{(2)}_{\mathrm{nr}}\right| e^{i\xi}$ from the medium or the interface layer. The energy diagram of vibrationally resonant and non-resonant processes is illustrated in figure **2-26**. Also, the non-resonant background can interfere with the resonant part and produce distorted lineshapes, depending on the phase relation ξ between the two. This is especially prominent on metal surfaces such as gold, which shows a strong non-resonant response in the visible region.[9] Our samples, however, are on glass and we can disregard the non-resonant contribution in equation 2.165 for the most part.

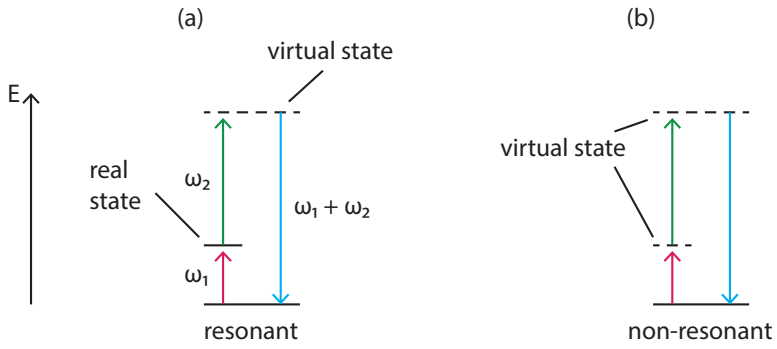

Figure **2-26**: Energy diagram of the sum-frequency processes. The infrared beam either corresponds to a vibrational level of the molecule and resonantly enhances the signal (a) or it does not and the radiation is only scattered weakly (b). Adapted from Lambert et al.[67]

In the last part of this subsection, we are finally tackling the tensor character of the susceptibility. For reasons of simplicity, we approximated the polarisation and hence the susceptibility as a scalar in the previous sections. This, however, is only accurate in isotropic materials, which are independent of direction. In general, matter can react quite differently to, say an electric field in the x-direction than in the y-direction, like the birefringent materials that we discussed in section 2.2.3. In this sense, the linear susceptibility, which is the proportionality factor between the polarisation $\mathbf{P}$ and an applied electric field $\mathbf{E}$, has $3 \times 3 = 9$ components, one for each combination of cartesian coordinates P_i and E_i with $i = (x, y, z)$. In the non-linear sum-frequency process, we are mixing two electric fields, which results in even more combinations, such that the second-order non-linear susceptibility $\chi^{(2)}$ becomes a third-rank tensor with $3 \times 3 \times 3 = 27$ possible combinations.

These 27 elements of $\chi^{(2)}$ do not, however, all contribute to the sum-frequency signal. Usually, only very few of these elements are independent and contain information. To find these elements, we need to remind ourselves why every even-order contribution to the susceptibility vanishes in centrosymmetric media. The reason is that we find both of the following equations to be true:

$$\chi^{(2)}_{ijk} = \chi^{(2)}_{-i-j-k} \tag{2.167}$$

$$\chi^{(2)}_{ijk} = -\chi^{(2)}_{-i-j-k}. \tag{2.168}$$

The first equation is the definition of a centrosymmetric medium and the second equation is due to the tensor nature of $\chi^{(2)}$ because a change in the sign of each index is the same as reversing the axis system, such that the physical information in $\chi^{(2)}$ must also reverse the sign. Both of these equations can only be true for $\chi^{(2)} = 0$, which is the non-centrosymmetric rule for even-order non-linear processes that we already discussed in subsection 2.3.4.

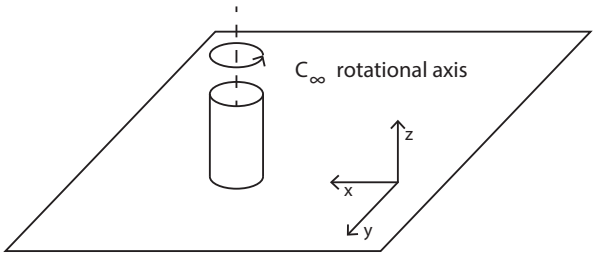

Figure **2-27**: Illustration of a planar surface that is symmetric about the surface normal. Adapted from Lambert et al.[67]

In this thesis and also most vSFS setups, the molecular sample is put on an isotropic surface and in our case, the molecules themselves are long enough to constitute their own isotropic bulk. Under these circumstances, we can generate a sum-frequency signal at the interfaces where the different media come together. These interfaces are considered to have a C_∞ rotational axis, such that they are isotropic in the xy-plane but not in the z-axis, as depicted in figure **2-27**. This C_∞ symmetry only forces the components of $\chi^{(2)}$ in the xy-plane to obey the relations in 2.167 and 2.168. Thus, one finds that all except 7 of the contributions to $\chi^{(2)}$ vanish and more specifically one can show that only the quadratic terms in x and y are nonzero, with zzz being the exception. The complete set of combinations is given by:[67]

~~xxx~~	~~xyx~~	**xzx**	~~yxx~~	~~yyx~~	~~yzx~~	**zxx**	~~zyx~~	~~zzx~~
~~xxy~~	~~xyy~~	~~xzy~~	~~yxy~~	~~yyy~~	**yzy**	~~zxy~~	**zyy**	~~zzy~~
xxz	~~xyz~~	~~xzz~~	~~yxz~~	**yyz**	~~yzz~~	~~zxz~~	~~zyz~~	**zzz**

Since the x and y contributions are equivalent in the isotropic surface, we are left with 4 independent, nonzero components $\chi^{(2)}_{ijk}$ that can generate a sum-frequency signal. These contributions are

$$\chi^{(2)}_{zxx}(=\chi^{(2)}_{zyy}), \quad \chi^{(2)}_{xzx}(=\chi^{(2)}_{yzy}), \quad \chi^{(2)}_{xxz}(=\chi^{(2)}_{yyz}) \quad \text{and} \quad \chi^{(2)}_{zzz}. \tag{2.169}$$

By carefully aligning our linearly polarised incident beams to specific polarisation combinations, we can selectively probe these contributions because the electric field vector may oscillate solely in the y-dimension or the xz-plane. Figure **2-28** shows the sketch of a common sum-frequency geometry at an interface. The reflected SF angle $\beta_{\mathrm{sf,r}}$ can be calculated, according to the phase-matching condition, with

$$n(\omega_{\mathrm{sf}})\omega_{\mathrm{sf}}\sin(\beta_{\mathrm{sf}}) = n(\omega_1)\omega_1\sin(\beta_1) + n(\omega_2)\omega_2\sin(\beta_2), \tag{2.170}$$

where $n(\omega)$ is the refractive index of the medium that the beam in consideration travels through.[67] Note that both the reflected and the refracted angle can be calculated with 2.170.

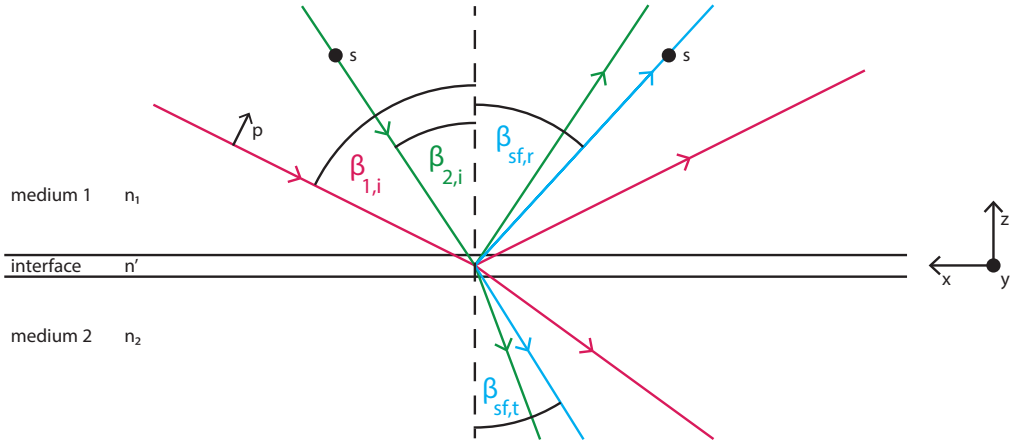

Figure **2-28**: Schematic overview of sum-frequency generation at an interface between two media with refractive indices n_1 and n_2. Shown is the *ssp* polarisation for the sum-frequency signal (blue), the visible upconversion (green) and the infrared beam (red), respectively.

In figure **2-28** we illustrated the polarisation combination *ssp*, which usually refers to the corresponding beams by decreasing frequency $\omega_{\text{sf}} > \omega_{\text{vis}} > \omega_{\text{ir}}$. The *s*-polarised beams are perpendicular (German "senkrecht") to the incident xz-plane and the p polarised beam is parallel (German "parallel") to that plane and therefore only oscillates in the y-dimension.

Specifically, four polarisation combinations correspond to nonzero components of $\chi^{(2)}$, namely *ssp*, *sps*, *pss* and *ppp*. One can show that these combinations correlate to effective susceptibilities, measured in an experiment. These effective susceptibilities are given by[93]

$$\chi^{(2)}_{\text{eff},ssp} = L_{yy}(\omega_{\text{sf}})L_{yy}(\omega_{\text{vis}})L_{zz}(\omega_{\text{ir}})\sin(\beta_{\text{ir}})\chi^{(2)}_{yyz}, \tag{2.171}$$

$$\chi^{(2)}_{\text{eff},sps} = L_{yy}(\omega_{\text{sf}})L_{zz}(\omega_{\text{vis}})L_{yy}(\omega_{\text{ir}})\sin(\beta_{\text{vis}})\chi^{(2)}_{yzy}, \tag{2.172}$$

$$\chi^{(2)}_{\text{eff},pss} = L_{zz}(\omega_{\text{sf}})L_{yy}(\omega_{\text{vis}})L_{yy}(\omega_{\text{ir}})\sin(\beta_{\text{sf}})\chi^{(2)}_{zyy}, \tag{2.173}$$

$$\begin{aligned}\chi^{(2)}_{\text{eff},ppp} = &- L_{xx}(\omega_{\text{sf}})L_{xx}(\omega_{\text{vis}})L_{zz}(\omega_{\text{ir}})\cos(\beta_{\text{sf}})\cos(\beta_{\text{vis}})\sin(\beta_{\text{vis}})\chi^{(2)}_{xxz}\\ &- L_{xx}(\omega_{\text{sf}})L_{zz}(\omega_{\text{vis}})L_{xx}(\omega_{\text{ir}})\cos(\beta_{\text{sf}})\sin(\beta_{\text{vis}})\cos(\beta_{\text{vis}})\chi^{(2)}_{xzx}\\ &+ L_{zz}(\omega_{\text{sf}})L_{xx}(\omega_{\text{vis}})L_{xx}(\omega_{\text{ir}})\sin(\beta_{\text{sf}})\cos(\beta_{\text{vis}})\cos(\beta_{\text{vis}})\chi^{(2)}_{zxx}\\ &+ L_{zz}(\omega_{\text{sf}})L_{zz}(\omega_{\text{vis}})L_{zz}(\omega_{\text{ir}})\sin(\beta_{\text{sf}})\sin(\beta_{\text{vis}})\sin(\beta_{\text{vis}})\chi^{(2)}_{zzz}.\end{aligned} \tag{2.174}$$

The β are the incident and reflected angles according to figure **2-28** and $L_{ii}(\omega)$ are the diagonal elements of $\tilde{L}(\omega)$, called the Fresnel factor at frequency ω. These Fresnel factors

are given by[93]

$$L_{xx}(\omega) = \frac{2n_1(\omega)\cos(\beta_t)}{n_1(\omega)\cos(\beta_t) + n_2(\omega)\cos(\beta_i)}, \tag{2.175}$$

$$L_{yy}(\omega) = \frac{2n_1(\omega)\cos(\beta_i)}{n_1(\omega)\cos(\beta_i) + n_2(\omega)\cos(\beta_t)}, \tag{2.176}$$

$$L_{zz}(\omega) = \frac{2n_2(\omega)\cos(\beta_i)}{n_1(\omega)\cos(\beta_t) + n_2(\omega)\cos(\beta_i)} \left(\frac{n_1(\omega)}{n'(\omega)}\right)^2. \tag{2.177}$$

According to figure **2-28**, the angles β_t and β_i are the transmitted and incident angles of the beam in consideration, respectively. The quantity $n'(\omega)$ is the refractive index of the interface between the two media, which can be quite different from either n_1 or n_2 and difficult to measure. However, the calculation of the molecular orientation is quite sensitive to n' and finding a good approximation for this value is crucial for the determination of the orientation angle.

Specifically for our samples, i.e. arachidic acid, we are mostly interested in the symmetric and antisymmetric stretching vibrations of the methyl group (CH_3). One can show that for the symmetric stretch, the hyperpolarisability tensor only has two non-vanishing independent elements β_{ccc} and $\beta_{aac} = \beta_{bbc}$ and the antisymmetric stretch spectra depend on one independent element β_{caa}.[93] Here, axis c is the principal axis of the methyl group and the ab-plane is perpendicular to that. Assuming C_{3v} symmetry for the methyl group, one can now determine the relationship between elements of the susceptibility tensor in the lab coordinate system (xyz) and the hyperpolarisabilities in the molecular coordinate system (abc).[94] For the symmetric stretch, we have

$$\chi^{(2)}_{xxz,s} = \chi^{(2)}_{yyz,s} = \frac{1}{2}N_s\beta_{ccc}\left[\cos(\theta)(1+r) - \cos^3(\theta)(1-r)\right], \tag{2.178}$$

$$\chi^{(2)}_{xzx,s} = \chi^{(2)}_{yzy,s} = \chi^{(2)}_{zxx,s} = \chi^{(2)}_{zyy,s} = \frac{1}{2}N_s\beta_{ccc}\left[\cos(\theta) - \cos^3(\theta)\right](1-r), \tag{2.179}$$

$$\chi^{(2)}_{zzz,s} = N_s\beta_{ccc}\left[r\cos(\theta) + \cos^3(\theta)(1-r)\right], \tag{2.180}$$

with the number density of molecules N_s, the relation $\beta_{aac} = r\beta_{ccc}$ and the orientational angle θ of the molecular axis c to the surface normal. For the antisymmetric stretching vibration, we have

$$\chi^{(2)}_{xxz,as} = \chi^{(2)}_{yyz,as} = -\frac{1}{2}N_s\beta_{caa}\left[\cos(\theta) - \cos^3(\theta)\right], \tag{2.181}$$

$$\chi^{(2)}_{xzx,as} = \chi^{(2)}_{yzy,as} = \chi^{(2)}_{zxx,as} = \chi^{(2)}_{zyy,as} = \frac{1}{2}N_s\beta_{caa}\cos^3(\theta), \tag{2.182}$$

$$\chi^{(2)}_{zzz,as} = N_s\beta_{caa}\left[\cos(\theta) - \cos^3(\theta)\right]. \tag{2.183}$$

From these equations, it becomes obvious how sensitive the vSF spectra are to the tilt angle θ of the methyl group. Furthermore, in this calculation, we assumed the same tilt

angle for all the molecule that generates our sum-frequency signal. In reality, however, even a well-ordered monolayer has a certain distribution of tilt angles and one needs to average over this distribution to make the calculations accurate.

This concludes not only our introduction to vibrational sum-frequency generation but also the theoretical part of this thesis altogether. In this last subsection, we learned about the important quantities that constitute the intensity of the sum-frequency signal as well as the importance of the phase-matching condition. Furthermore, we determined that a vibrational mode can only be observable in vSFS if it is both Raman and IR active, which is a strong selection rule of vSFS. Lastly, we tackled the tensor nature of the susceptibility and found that there are only four independent contributions to $\chi^{(2)}$, which can be probed with specific polarisation combinations of the three interacting beams.

Chapter 3

Experimental Aspects

The third chapter is intended to cover all experimental details that are relevant to our research. The outline of this chapter is as follows: We begin by giving a complete overview of the table setup and all components. Subsequently, we illustrate the pump-probe approach in general and specifically show how the spectroscopic information is processed. Lastly, we introduce the sample preparation and the samples themselves that we are going to investigate.

3.1 Table Setup

Our experiments are performed in a semi-controlled environment on an optical table. We say semi-controlled because even though we can regulate the airflow and climate in the laboratory to a certain degree, there are still significant fluctuations in laser power on very hot or rainy days. This has been taken into account and one can usually tell immediately if the environment is stable during a measurement or not.

On the optical table itself, we devised a novel time-resolved pump-probe vibrational spectroscopy setup that utilises a narrowband IR pulse as the pump excitation and follows up with the sum-frequency signal of a broadband IR - narrowband visible pulse pair as the probe. We call this experiment *Time-Resolved 2-Colour Vibrational Sum-Frequency Spectroscopy*. To emphasize the novelty of our setup, we decided to use the term *2-Colour Spectroscopy* as an indicator for completely independent pump and probe pulses. Most pump-probe spectroscopy setups feature a pump and a probe beam that originate from the same source, effectively resulting in coherent pulses, which is known as *2D-spectroscopy*. In theory, the novelty of our experiment allows us to pump a distant vibrational mode and observe any spectral region of interest to investigate the vibrational energy flow in the molecule.

Figure **3-1** is an illustration of our setup on the optical table. All beams are parallel to the table and meet at the entrance of the sample stage, which is illustrated in figure **3-2**.

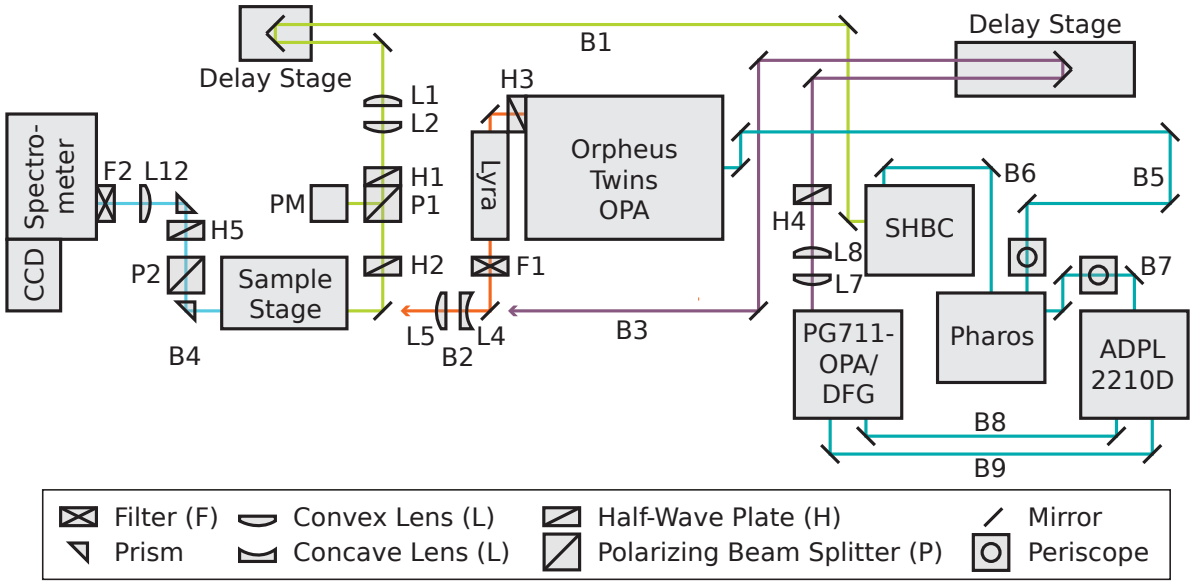

Figure **3-1**: A schematic overview of our table setup. This illustration is taken with permission from the published dissertation of my senior coworker Michael Lackner, with whom I have been working on this project.[53]

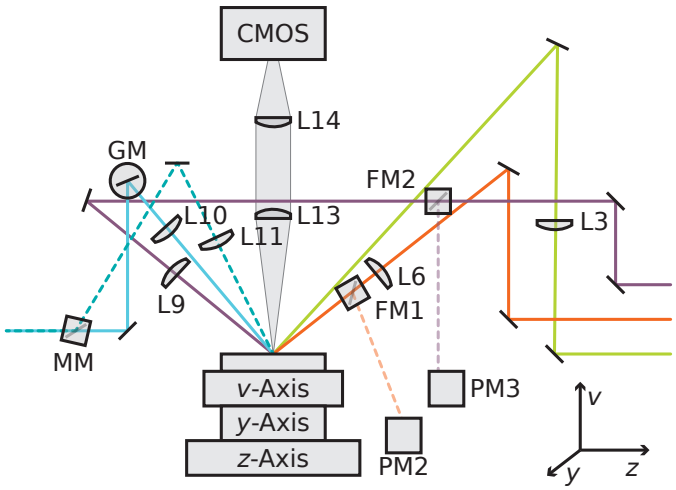

Figure **3-2**: Schematic overview and beam geometries of the sample stage. This illustration is taken with permission from the published dissertation of my senior coworker Michael Lackner, with whom I have been working on this project.[53]

The sample stage is an optical table element that is attached to the main table vertically, such that all the beams can now travel in a plane that is orthogonal to the main table. In the following subsection, we are going to take a closer look at all of the components in our setup.

3.1.1 Components

The heart of our setup (figure **3-1**) is the *Light Conversion: Pharos PH1* (Pharos) that was designed and manufactured by *Light Conversion* in Lithuania. This powerful machine generates laser pulses at 1028±5 nm with a repetition rate of 2 kHz, a pulse length of < 300 fs and pulse energies of 1.9 mJ. The output of the Pharos drives the *Light Conversion: Orpheus-Twins* (B5) and the *Light Conversion: Second Harmonic Bandwidth Compressor* (SHBC) (B6). The Pharos is also connected to the *Ekspla: APL2210D-TR* diode-pumped Nd:YAG laser (B7), which was designed and manufactured by *Ekspla* also in Lithuania. Technically speaking, the Ekspla system would also run without the Pharos, but we do need to seed the Pharos output into the Expla system to be able to synchronise our pulses.

SHBC - upconversion pulse

These three devices that are connected to the Pharos generate all of the pulses that we need to investigate our samples. First of all, we have the SHBC that generates the upconversion pulse for our sum-frequency probe (B1). This visible pulse is the second harmonic of the Pharos output with a centre wavelength of around 515 nm, a bandwidth of < 10 cm^{-1} and pulse energies of 33 μJ with a repetition rate of 2 kHz.

In the beam path, we have a movable stage (*Micos: Phytron / Micos SMC Controller*) to delay or advance the point in time when the pulse hits the sample. This delay stage is 25 mm long, which corresponds to a total delay of $\frac{2 \cdot 25\,\mathrm{mm}}{c} \approx 167$ ps and the minimal displacement is $1\,\mu$m (≈ 6.7 fs). After that, we installed a telescope (L1 and L2) to manipulate the diameter of the beam. The specifications of each of the lenses are given in table **3-1**. The next optical elements are a half-wave plate (H1) and a polarising beam splitter cube (P1). This construction serves as a simple attenuator because P1 only allows horizontally polarised light to pass and the vertical component is reflected into a Power Meter (*Thorlabs: S121C / PM100USB Controller*). This way we can attenuate the power of the transmitted beam with H1 and by measuring the residue reflected power we can calculate the approximate power that arrives at the sample at all times. The next object in the beam path is another half-wave plate to manipulate the polarisation of the attenuated beam. The beam is then directed to the sample stage (see **3-2**) and focused with a lens (L3) on the sample at a 45° angle with respect to the surface normal.

Table **3-1**: List of all lenses that are used in our setup (see figure **3-1** and **3-2** for reference).

Lense	Material	Focal Length (mm)	Location
L1	BK7	75	Telescope SHBC
L2	BK7	75	Telescope SHBC
L3	BK7	500	Sample Focus SHBC
L4	CaF_2	-40	Telescope Twin
L5	CaF_2	25	Telescope Twin
L6	CaF_2	100	Sample Focus Twin
L7	CaF_2	75	Telescope Ekspla
L8	CaF_2	75	Telescope Ekspla
L9	CaF_2	150	Sample Focus Ekspla
L10	BK7	125	Sum-Frequency Probe Collimator
L11	BK7	175	Sum-Frequency Pump Collimator
L12	BK7	150	Spectroscope Entrance
L13	BK7	75	Sample Camera
L14	BK7	75	Sample Camera

Twin - broadband IR pulse

The next device we are going to address is the Orpheus-Twins. The Twins are two independent optical parametric amplifiers that can both generate broad IR pulses with a FWHM of roughly $200\,\mathrm{cm}^{-1}$ and a pulse length of about 300 fs at a repetition rate of 2 kHz. The wavelength of the twins can be tuned from 1300 nm up to 19500 nm with the help of an additional DFG unit (*Light Conversion: Lyra*) and reach pulse energies ranging from $100\,\mu$J to $0.1\,\mu$J. In our spectral region of interest about 3400 nm we usually expect pulse energies of roughly $25\,\mu$J. In our experiment, we are only using one arm of the twins to generate the broad IR pulse for our sum-frequency probe (B2).

The first optional optical element in the beam path is a half-wave plate (H3). The problem we need to circumvent with this wave plate is the following: For all of our experiments, we need the broad IR pulse to be *p*-polarised, which is the default configuration of the output of the twins. However, to probe low energy regimes (wavelength of approx $>$ 3800 nm) the system requires the use of the Lyra unit, which switches the default output polarisation to *s*. To avoid the need to put a half-wave plate into the broad IR pulse, which not only needs to be adjusted for different wavelengths but also absorbs quite a lot of the pulse energy, we decided to rotate the Lyra by 90° and adjust the polarisation of idler and signal output of the twin with H3.

Attached to the Lyra is an interchangeable filter that is necessary to filter any unwanted residue idler/signal output. The next optical element is a telescope with lenses L4 and

L5 to manipulate the beam diameter, which is a surprisingly powerful tool to optimise the effective overlap of our pulses. The reason for the use of a concave lens is plainly the limitation of space on the optical table. In the sample stage, the beam is focused on the sample with lens L6 at a 60° angle to the surface normal. Down the path, there is an optional motorised flip-mirror (*Thorlabs: MFF101* (FM1)) that directs the beam onto a Power Meter (*Thorlabs: TD10XP / National Instruments PCIe-6321 DAQ-Board* (PM2)) to obtain an approximate measure of the pulse energy that arrives at the sample. Usually, the Twin pulses lose about half of their energy due to absorption in optical elements and the atmosphere, which puts them at around 13 μJ.

Ekspla - narrowband IR pulse

The last device that we need to introduce is the Ekspla system, which generates our narrowband IR pump pulses (B3). As we mentioned before, the Ekspla system can run on its own but is seeded by the Pharos to ensure the synchronisation of our pulses. The first box (*Ekspla: APL2210D-TR*) generates pulses of 1064 nm at a repetition rate of 1 kHz, which is half the rate of the Pharos. These pulses (B8 and B9) power the *Ekspla: PG711-DFG* unit that generates pulses ranging from 1540 nm to 16000 nm with a bandwidth of $< 10\,\mathrm{cm}^{-1}$ and respective energies of 560 μJ to 3 μJ. Unfortunately, the Ekspla system switches to the DFG regime at 3440 nm, which not only changes the polarisation of the output from vertically to horizontally but also slightly changes the beam pathing. We have yet to find a reliable solution to this problem, which is why most of our scanning experiments stop at a pump wavelength of 3439 nm.

The first optical element in the beam path is a telescope with lenses L7 and L8 for the option of manipulating the beam diameter. After that, we have an optional half-wave plate (H3) to be able to change the polarisation. The next element in the beam path is a movable stage (*Micos: LS-180 / MoCo DC Controller*) for delaying or advancing the pump pulse in time. The total displacement covered by the stage is 30.5 cm, which corresponds to a delay of $\frac{2 \cdot 30.5\,\mathrm{cm}}{c} \approx 2$ ns and the minimal displacement is 2.46 μm ($\approx$ 16.4 fs). The beam is then directed to the sample stage and with another flip-mirror (*Thorlabs: MFF101* (FM2)) it is possible to measure the pump power on a power meter (*Thorlabs: TD10XP / National Instruments PCIe-6321 DAQ-Board* (PM3)) to approximate the energy of the pulses when they arrive at the sample. The pump beam is then focussed onto the sample via lens L9 at an angle of 60° to the surface normal but opposite to the other two beams.

We chose this geometry because the pump pulse can also interact with the upconversion pulse and generate quite a strong sum-frequency signal itself. According to equation 2.170, the angle of the reflected sum-frequency beam does not change much for different IR angles. Also, in a co-propagating geometry, the pump-SF signal usually also hits the spectrometer as unwanted stray light. With our counter-propagating geometry, we

significantly alter the angle of the reflected pump-SF signal and block most of it from entering the spectrometer. However, we also have the option to observe the pump-SF signal, which is first collimated by lens L11 and directed onto an optional mirror with a magnetic mount (MM). This way, the pump-SF signal is directed onto the camera and the probe-SF signal is blocked. Observing the pump-SF signal is useful to find the temporal and spatial overlap of all three pulses and also to gain spectral information about the pump pulse.

The last beam we have to cover is the generated sum-frequency probe pulse (B4) that originates in the sample. The first optical element in the SF-beam path is a lens (L10) to collimate the diverging beam. The pulse is then directed onto a Galvanometer mirror (*Cambridge Technology: 6240H* (GM)), whose function is discussed in greater detail in the next section. The next optical element is a prism, which we use here instead of mirrors to minimise the losses in beam power. Going further, we have a Glan-Thompson polariser (*Thorlabs: GTH10M-A*) to choose what polarisation we want to resolve in a given experiment. After the Glen-Thompson, we do, however, need to make sure that the residual beam is p-polarised because the optical grating in the spectrometer is optimised for p-polarised light. We achieve this with another half-wave plate in the beam path (H5). The pulse is then focussed on the optical grating of the spectrometer with lens L12. The last optical element in front of the spectrometer's slit is a short pass filter (*Thorlabs: FESH0500* (F2)). This filter is necessary because the reflection angle of the upconversion pulse B1 is very close to that of the sum-frequency beam, which is why we detect a significant amount of stray light without the filter. The cutoff wavelength of the filter is 500 nm so that the upconversion pulse at $\approx$ 515 nm is mostly blocked and our sum-frequency signal at around 447 nm is transmitted.

The beam then enters our spectrometer (*Acton: SpectraPro-300i*), which has a focal length of 300 mm and features a holographic grating (*Princeton Instruments*). This optical grating is optimised for the visible spectral range and has a groove density of 2400 gr/mm. Attached to the exit of the spectrometer is an electron-multiplying charged coupled device camera (*Andor: iXon Ultra 897* (CCD)). This camera has a resolution of 512×512 pixels and each of these pixels has an edge length of 16 μm. Together with the groove density and length of the spectrometer, this corresponds to a spectral resolution of 0.74 cm^{-1} per pixel and a total spectral range of $\approx 380\,\mathrm{cm}^{-1}$.

At last, we need to cover the elements on the table that are not in any beam paths. For one, we have the motorised table that our samples are put on, which is a combination of two movable linear stages *Micos: Phytron / Micos SMC Controller* and one vertical stage *Standa: 8MVT40-13-1 / Standa 8SMC5-USB-B8-1 Controller*. This sample table is adjustable in all three spatial directions. For arbitrary reasons, we define the yz-plane as being parallel to the optical table and the v-axis changes the height of the sample table. This way, we can choose to irradiate a different spot on the same sample or switch to

another sample by moving the table in the yz-plane. For samples of different heights, on the other hand, we need to adjust the v-position of the table. To find the correct height for different samples such that our beam geometry is still aligned, we chose to observe the magnified, visible spot of our upconversion beam with a CMOS camera and two lenses L13 and L14 attached right above the sample table. Also, by removing the optical filters in front of the CMOS sensor, we can see some residual IR radiation from our other spots as well. This way we can find the first rough spatial overlap of our beams by observing the spots on the camera screen.

The only device on the table that we have not yet introduced is a function generator (*Tektronix: AFG1062*). This function generator is necessary to synchronise the Galvanometer mirror with the laser pulses and will be explained further in a later subsection when we address the importance of the Galvanometer mirror to our system. But first, we are going to take a closer look at the optical properties of each of our laser pulses.

3.1.2 Laser Pulse Characterisation

Each of our three laser systems generates pulses that are characterised by a temporal length and a spectral width. It is important to know about these characteristics for several reasons. First of all, we want to populate a single vibrational level in our molecules and track the energy flow that originates from this single excitation. Therefore, our pump pulse has to be spectrally narrow, which necessarily results in a longer pulse duration. This temporal length, on the other hand, is the limiting factor in our ability to track the initial dynamics because when pump and probe pulses are in temporal overlap we are effectively blind to any dynamics. In this sense, we can only track dynamics on a timescale longer than the temporal length of our pump pulse. Secondly, the IR pulse of our sum-frequency probe has to be spectrally broad and temporally narrow. The broad spectrum is advantageous to observe multiple vibrational levels simultaneously by taking a single snapshot of the system after the initial pump excitation. The temporal length of our probe IR pulse governs the temporal resolution that we can achieve with our probe setup. Lastly, the upconversion pulse from the SHBC governs our spectral resolution because every vibrational level that is populated by the probe IR is broadened by the upconversion bandwidth. Therefore, we want the SHBC pulse to be spectrally narrow and temporally broad.

Because we cannot directly observe the temporal profile of the pulses, we need to resort to other means of extracting these optical properties. One commonly deployed method is called the *cross-correlation*. The cross-correlation of two continuous functions $f(x)$ and $g(x)$ is defined as

$$(f \star g)(x) = \int_{-\infty}^{\infty} f(\tau) g(x - \tau) \, \mathrm{d}\tau \,, \tag{3.1}$$

which simply implies a shift of one signal to the other. In our case, we can generate a cross-correlation for example by observing the SHBC-Twin sum-frequency spectrum, while delaying the SHBC beam with respect to the IR beam from the Twins in time. This sum-frequency spectrum, however, cannot feature any resonances and should overall not vary in the spectral range of interest in order to properly mirror the intensity distribution of the pulses. We can achieve this for example by generating a sum-frequency signal utilising the non-resonant background from a gold surface. Furthermore, we need to make sure that the coherence time of the sum-frequency excitation is shorter than the convoluted pulse length, otherwise, we artificially stretch the pulse in time. This, however, is also given for a gold surface.

From this convoluted sum-frequency signal, we can then learn about the spectral and temporal properties of each of the single pulses, as we will see in the following. We assume that our pulses are Gaussian shaped, such that

$$f(x) = \mathrm{e}^{-\frac{x^2}{2\sigma_f^2}} \quad \text{and} \tag{3.2}$$

$$g(x) = \mathrm{e}^{-\frac{x^2}{2\sigma_g^2}}, \tag{3.3}$$

with standard deviations σ_i, widths $\mathrm{FWHM}_i = 2\sqrt{2\ln 2}\sigma_i$ and in our case the variable x can either represent time or wavenumber. Further, we set the height of each function to unity and centred the curves around the origin, for reasons of simplicity. With that, we can express the cross-correlation of our two functions as

$$\begin{aligned}
(f \star g)(x) &= \int_{-\infty}^{\infty} \mathrm{e}^{-\frac{\tau^2}{2\sigma_f^2}} \mathrm{e}^{-\frac{(x-\tau)^2}{2\sigma_g^2}} \,\mathrm{d}\tau \\
&= \mathrm{e}^{-bx^2} \int_{-\infty}^{\infty} \mathrm{e}^{-(a+b)\tau^2+2bx\tau} \,\mathrm{d}\tau \quad \text{with} \quad a = \frac{1}{2\sigma_f^2}, b = \frac{1}{2\sigma_g^2} \\
&= \mathrm{e}^{-bx^2} \mathrm{e}^{\frac{b^2x^2}{a+b}} \int_{-\infty}^{\infty} \mathrm{e}^{-\frac{b^2x^2}{a+b}} \mathrm{e}^{-(a+b)\tau^2+2bx\tau} \,\mathrm{d}\tau \\
&= \mathrm{e}^{-bx^2+\frac{b^2x^2}{a+b}} \int_{-\infty}^{\infty} \mathrm{e}^{-(\sqrt{a+b}\tau-\frac{bx}{\sqrt{a+b}})^2} \,\mathrm{d}\tau \\
&= \mathrm{e}^{-\frac{abx^2}{a+b}} \underbrace{\int_{-\infty}^{\infty} \mathrm{e}^{-(a+b)(\tau-\frac{bx}{a+b})^2} \,\mathrm{d}\tau}_{\sqrt{\frac{\pi}{a+b}}} \\
&= A\mathrm{e}^{-\frac{x^2}{2(\sigma_g^2+\sigma_f^2)}}.
\end{aligned} \tag{3.4}$$

Comparing this result to our Gaussian functions, we find that the cross-correlation of two Gaussian-shaped pulses is also Gaussian and their widths are related by

$$\mathrm{FWHM}_{f\star g}^2 = \mathrm{FWHM}_f^2 + \mathrm{FWHM}_g^2. \tag{3.5}$$

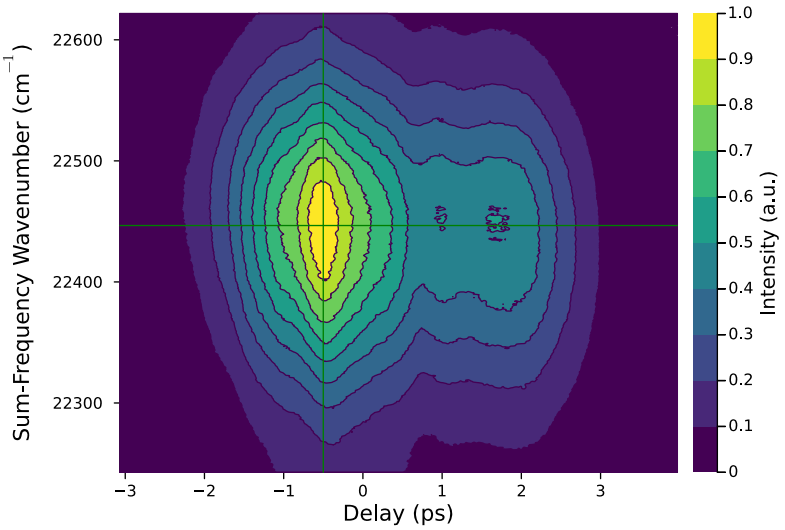

Figure **3-3**: Cross-correlation of SHBC and Twin output. This data represents the sum-frequency signal from a gold surface of the upconversion pulse with the broadband IR pulse for different delay times of the upconversion pulse. The colour scale indicates the normalised intensity of the sum-frequency signal and the green lines depict slices through the data. The data points of the horizontal slices are plotted in figure **3-4** (a) and the ones of the vertical slices are plotted in subplot (b).

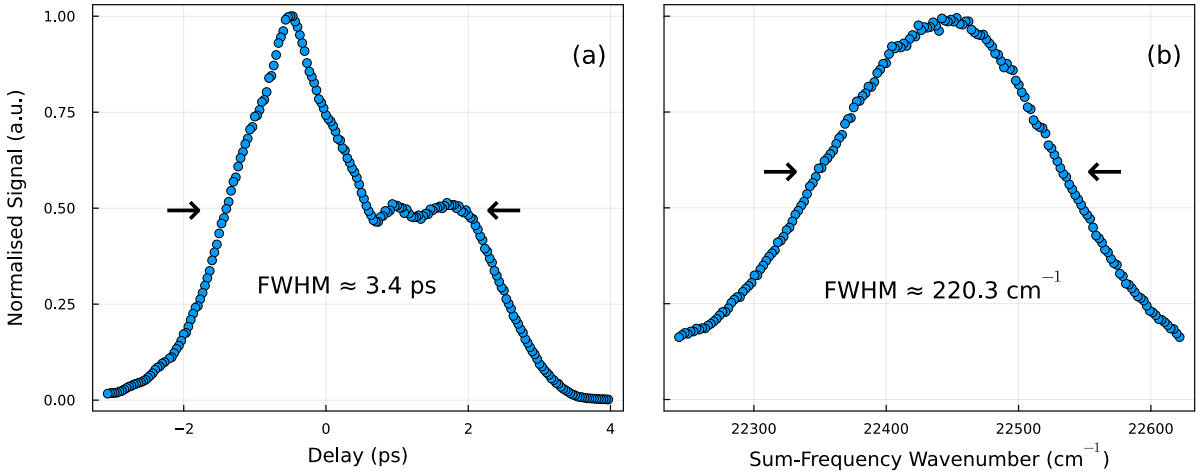

Figure **3-4**: Subplot (a) shows the temporal profile of the cross-correlation of the SHBC and Twin output. The data points are taken from figure **3-3**, illustrated by the green horizontal line. Subplot (b) shows the spectral profile of the same cross-correlation, which is visualised as the green vertical line in figure **3-3**

With our spectrometer, we can observe the sum-frequency signal of the SHBC-Twin pulse pair but also the sum-frequency signal of the SHBC and Ekspla output. First, we are going to take a look at the cross-correlation of the SHBC-Twin pulse pair. In figure **3-3** we can see a three-dimensional plot of the non-resonant sum-frequency signal of the SHBC and Twin output for different SHBC delays. Each vertical set of data points represents a sum-frequency spectrum with the relative intensity indicated by the colour scale. The x-axis represents the delay in time of the SHBC pulse with respect to the Twin pulse.

We can now extract the spectral and temporal profile of our convoluted pulses by taking different sets of data points from the cross-correlation. This is indicated by the horizontal and vertical green lines going through the spectrum in figure **3-3**. The data set of the horizontal slice is plotted in figure **3-4** (a) and represents the temporal profile of our SHBC-Twin cross-correlation with a FWHM of $\approx 3.4\,\mathrm{ps}$. Depending on daily external conditions, the Pharos slightly changes the form of this temporal profile but the data that are shown here do represent a profile that we usually observe. In the last subsection, we gave the approximate optical characteristics that were given by the manufacturer. From this, we know the Twin output is roughly $\Delta t_{\mathrm{Twin}} \approx 300$ fs long and the SHBC spectrally compresses the Pharos pulse to generate a narrowband signal, which necessarily results in a stretched pulse in time. We can, therefore, expect the upconversion pulse to be at least one order of magnitude longer than our broadband IR pulse. This, on the other hand, lets us disregard the width of the broadband IR in equation 3.5 and we find the length of the upconversion pulse to be $\Delta t_{\mathrm{SHBC}} \approx 3.4\,\mathrm{ps}$.

The data set indicated by the vertical slice in figure **3-3** is plotted in figure **3-4** (b) and represents the spectral profile of the SHBC-Twin cross-correlation with a FWHM of $\approx 220.3\,\mathrm{cm}^{-1}$. The spectral width of the SHBC output was measured by one of the service technicians during a service visit in August 2019 to be $\Delta\nu_{\mathrm{SHBC}} \approx 8.6\,\mathrm{cm}^{-1}$ and we expect the Twin output to be at least one order of magnitude broader than this value. With the same arguments as before, we can therefore disregard the smaller length in equation 3.5 again and find the spectral width of the broadband IR pulse to be $\Delta\nu_{\mathrm{Twin}} \approx 220.3\,\mathrm{cm}^{-1}$.

With the magnetic mirror mount (MM in figure **3-2**) that we mentioned in the last subsection, we can block the Twin-SHBC sum-frequency signal and instead focus the Ekspla-SHBC SF signal into the spectrometer. This way we can observe the cross-correlation of pump and upconversion pulses by changing the upconversion delay accordingly. This three-dimensional plot is shown in figure **3-5**. Same as before, the x-axis represents the delay in time of the SHBC pulse to the pump pulse, the y-axis shows the spectral information and the colour scale indicates the relative intensity of the sum-frequency signal.

Again, we begin by extracting the temporal profile from the data set indicated by the horizontal green line in figure **3-5**, which is plotted in figure **3-6** (a). Here, however, we are convoluting two pulses with similar temporal widths so we cannot just disregard the smaller quantity in equation 3.5 as we did before. Instead, we use the results from the

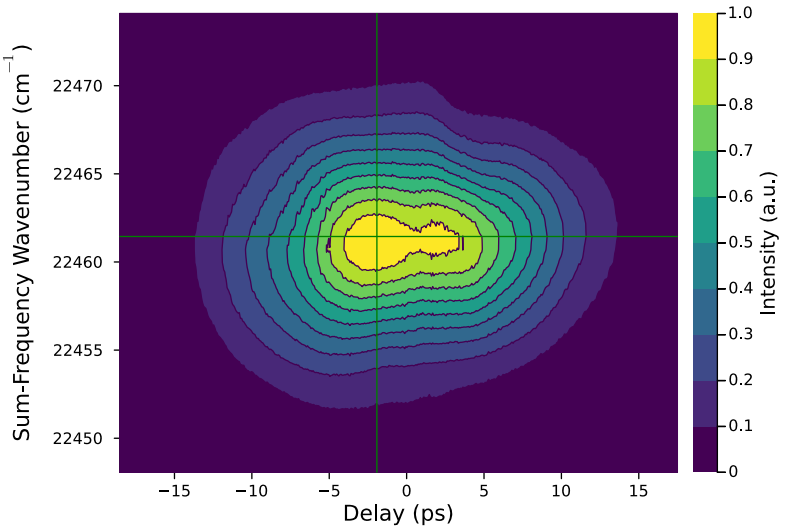

Figure **3-5**: Cross-correlation of SHBC and Ekspla output. This data represents the sum-frequency signal from a gold surface of the upconversion pulse with the narrowband IR pulse for different delay times of the upconversion pulse. The colour scale indicates the normalised intensity of the sum-frequency signal and the green lines depict different sets of data. The data points of the horizontal slices are plotted in figure **3-6** (a) and the ones of the vertical slices are plotted in subplot (b).

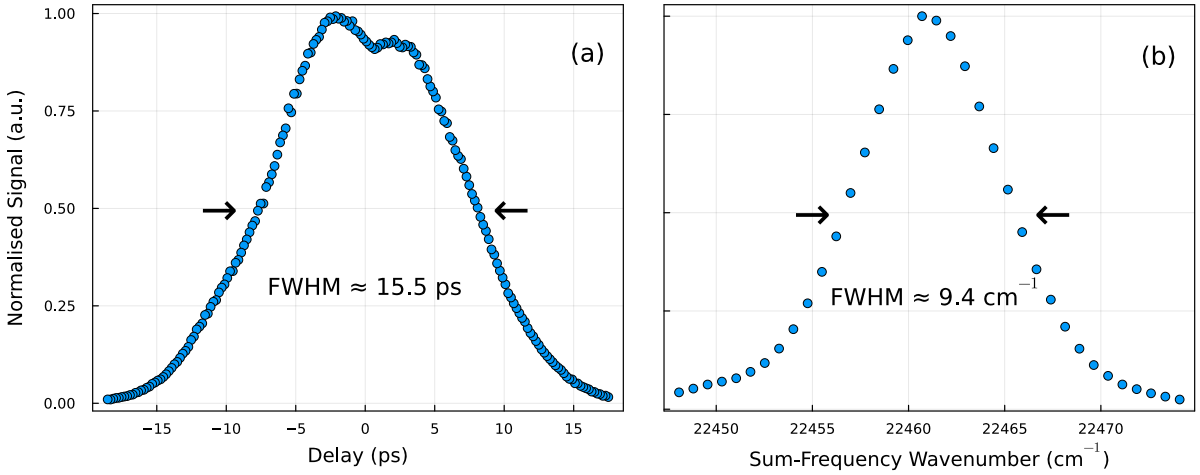

Figure **3-6**: Subplot (a) shows the temporal profile of the cross-correlation of the SHBC and Ekspla output. The data points are taken from figure **3-5**, illustrated by the green horizontal line. Subplot (b) shows the spectral profile of the same cross-correlation, which is visualised as the green vertical line in figure **3-5**

Table **3-2**: Collection of the spectral and temporal widths of our pulses that were extracted from cross-correlation measurement. All values are approximated by the FWHM of a Gaussian profile. The FWHM of the SHBC output $\Delta\nu_{\mathrm{SHBC}}$ is taken from a service report measurement in August 2019.

FWHM	SHBC	Twin	Ekspla
Δt (ps)	3.4	0.30	15.1
$\Delta\nu$ (cm^{-1})	8.6	220.3	3.8

last paragraphs to calculate the temporal width of the pump pulse as

$$\begin{aligned}\Delta t_{\mathrm{Ekspla}} &= \sqrt{\Delta t^2_{\mathrm{Ekspla\text{-}SHBC}} - \Delta t^2_{\mathrm{SHBC}}} \\ &\approx \sqrt{15.5\,\mathrm{ps}^2 - 3.4\,\mathrm{ps}^2} = 15.1\,\mathrm{ps}. \end{aligned} \tag{3.6}$$

Similarly, we can extract the spectral width of the pump pulse from the spectral profile that is plotted in figure **3-6** (b) from the vertical data points in figure **3-5**. Here, we find

$$\begin{aligned}\Delta\nu_{\mathrm{Ekspla}} &= \sqrt{\Delta\nu^2_{\mathrm{Ekspla\text{-}SHBC}} - \Delta\nu^2_{\mathrm{SHBC}}} \\ &\approx \sqrt{9.4\,\mathrm{cm}^{-1\,2} - 8.6\,\mathrm{cm}^{-1}} = 3.8\,\mathrm{cm}^{-1}. \end{aligned} \tag{3.7}$$

Table **3-2** is an overview of the optical properties that we extracted from the cross-correlation measurement except for the spectral width of the SHBC, which is taken from a service report measurement. Note, that these values represent approximations since our pulses are subjective to daily fluctuations and do not mirror a "clean" Gaussian profile. However, we can still expect the "true" values to be at least of the same order of magnitude.

With that, we can link back to the introductory paragraph of this subsection by reviewing the demands on our laser system. First of all, the spectral width of our pump laser $\Delta\nu_{\mathrm{Ekspla}} \approx 3.8\,\mathrm{cm}^{-1}$ is narrow enough to excite a single vibrational mode and the corresponding temporal width $\Delta t_{\mathrm{Ekspla}} \approx 15.1\,\mathrm{ps}$ prohibits the tracking of dynamics of significantly faster timescales. Secondly, we can track vibrational modes with a single shot in a spectral area of $\Delta\nu_{\mathrm{Twin}} \approx 220.3\,\mathrm{cm}^{-1}$ and the temporal width of our probe IR pulse $\Delta t_{\mathrm{Twin}} \approx 300\,\mathrm{fs}$ represents the temporal resolution that we can achieve in our experiments. Lastly, the resonances in our spectrum are broadened by the spectral width of the upconversion pulse $\Delta\nu_{\mathrm{SHBC}} \approx 8.6\,\mathrm{cm}^{-1}$, which dominates the spectral resolution in our experiments.

3.2 Pump-Probe Spectroscopy

In previous sections, when we talked about our pump-probe approach we did so in a superficial manner, without getting into much detail. Our setup, however, was carefully planned and built with a specific idea in mind and this section aims to convey this idea to the reader. The general pump-probe approach that we are using to track the vibrational energy transfer is sketched in the first subsection. Subsequently, we present the collected raw data and specifically show how insight into the vibrational dynamics is gained.

3.2.1 The Idea

The overall goal of our experiments is to track the vibrational energy flow in our molecular monolayer. To this end, we hit the sample with our narrowband IR pump pulse and transition the system into a non-equilibrium state, which is illustrated in figure **3-7** (a). Usually, we expect an order of 10% of molecules that are excited in the beam spot with every pulse. These molecules then populate a high energetic vibrational level, corresponding to the photon energy of the pump pulse.

In section 2.3.2 we explained how the vibrational energy is not 'trapped' in a state forever but is instead transferred to other degrees of freedom through anharmonic coupling mechanisms that depend on the system. It is, therefore, safe to assume that our molecules will also experience some sort of gradual population decay of the initially excited mode by transferring the vibrational energy into other degrees of freedom. One way of tracking this energy flow is to observe all vibrational levels of the system at different points in time, effectively mapping the population of states of the system. This idea is illustrated in figure **3-7** (b).

Now, to get the information about the population of different states in the monolayer we need the probing part of our setup. With the tunable broadband IR - upconversion pulse pair we can generate a sum-frequency spectrum in a region that contains multiple vibrational levels to take a 'snapshot' of the intensities of these resonances at different points in time. By comparing the intensities of this spectrum with one of the same systems in equilibrium, we can extract information about the population of that particular state at a specific time. This is because the molecules that are already in an excited state become transparent to photons of the energy that corresponds to the excitation of this particular state, which necessarily reduces the intensity of the sum-frequency signal.

With that, we can compare the sum-frequency signal at various points in time with the unpumped reference spectrum to observe the pump effect on a specific vibrational mode, called the *bleach*. This is schematically illustrated in figure **3-8** in the case of a singular observed resonance. From the recovery time of the bleach of this particular resonance, we learn about the timescales of the population decay. Also, by probing different vibrational modes we can track through which pathways the energy flows in the system.

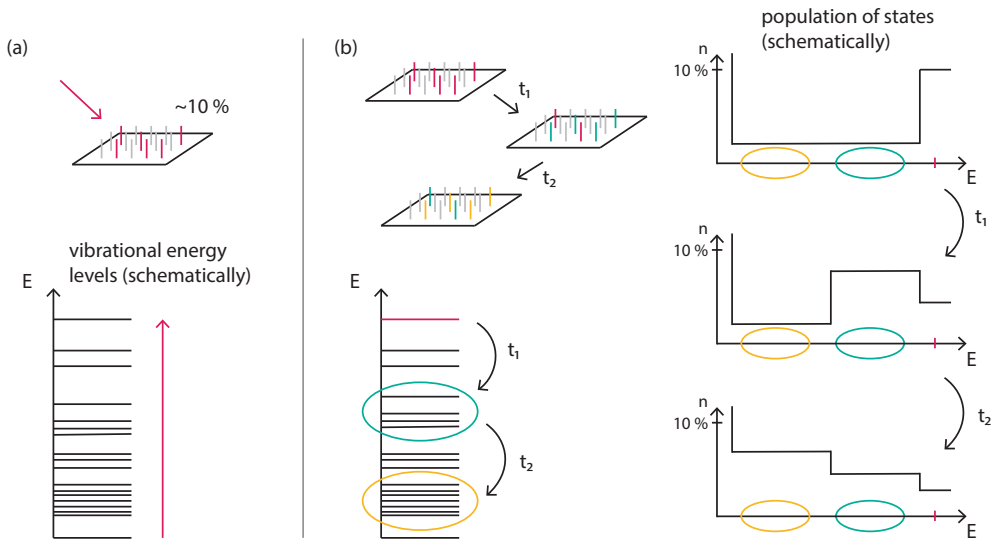

Figure **3-7**: (a) The narrowband pump IR pulse excites ≈ 10% of the irradiated molecules to a high vibrational level. (b) Through anharmonic coupling we expect this vibrational energy to be transferred into other degrees of freedom on different timescales. This is illustrated on the right, which shows the population of states at different times.

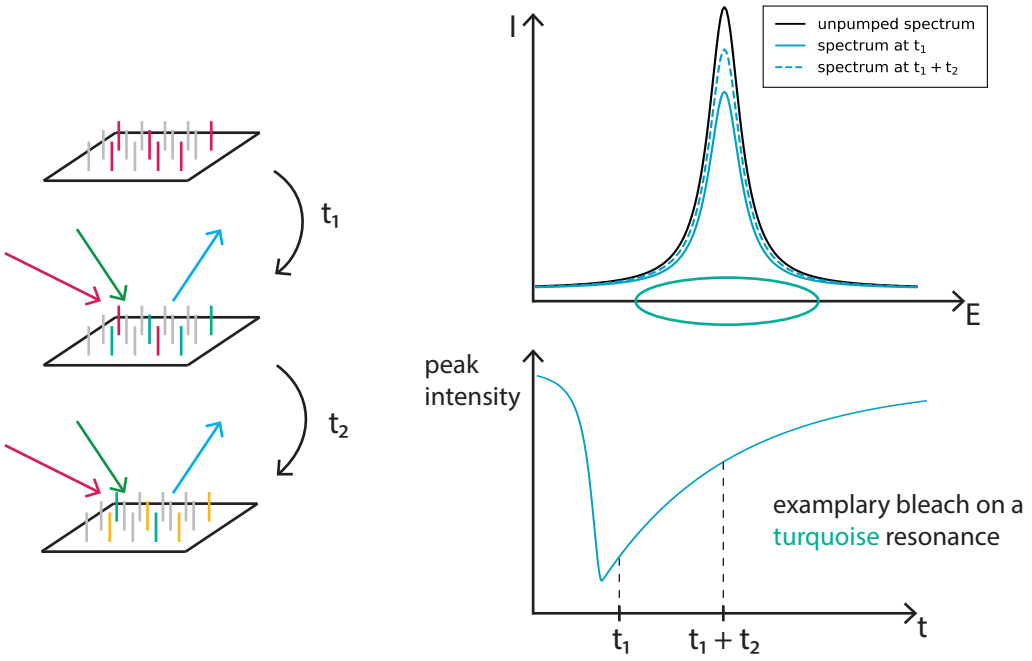

Figure **3-8**: With our sum-frequency probe, we can monitor selected resonances at different times. Comparing the sum-frequency spectra with the unpumped reference then allows us to calculate the transient bleach on these resonances and obtain information about the population decay of excited levels.

Naturally, for this to work, every sum-frequency spectrum that our camera captures needs to be accompanied by an unpumped reference spectrum to accurately determine the bleach. This is where the Galvanometer mirror (GM in figure **3-2**) comes into play. A Galvanometer mirror changes its angle in dependence on an applied voltage, which is in our case given by the function generator that we mentioned in section 3.1.1. So when we apply a sinusoidal voltage with a frequency of 1 kHz, the mirror will oscillate with that same frequency. Our IR-upconversion pulse pair has a repetition rate of 2 kHz, which means that if the phase shift of the Galvanometer is just right, the probing sum-frequency signal will hit the mirror exactly in the extrema of the amplitude. If this amplitude is very small, the path of the sum-frequency signal does not change much and we effectively get two separate signals that hit the camera. This separation distance can be changed by manipulating the amplitude with the function generator.

Now it becomes obvious why we chose the pump system to operate at a repetition rate of 1 kHz. With half the repetition rate of the probing pulses, only every other spectrum is pumped such that the two separated spectra on the camera screen are indeed the spectra of a pumped monolayer and an unpumped reference. On a side note, we can also see how our experiments are limited to systems that are in complete equilibrium again by the time the next pulse arrives, which is after 500 μs. This, however, was always fulfilled and we will even show in the next chapter that our systems recover on a timescale of nanoseconds.

3.2.2 Handling the Data

Now that we established the basic idea of our pump-probe experiments we are going to introduce how the spectroscopic data are handled specifically. Before that, however, we provide some general information about the environment of our data handling. Most of the data processing is done with a fairly new programming language called *julia*. The core code of our analysis tools was written by my senior PhD colleague Michael Lackner, with some adjustments made by me. Collecting the raw data of the CCD camera is handled by *LabView*, which we also use to operate most of our equipment on the optical table.

Raw data

When we talk about raw data, we usually refer to the picture that our CCD camera takes at a specific exposure time, which we call a single *frame*. As we mentioned earlier, this frame contains 512×512 pixels and each one of these pixels can accumulate charge that is generated by the incident radiation. In our case, the sum-frequency signal hits the optical grating in the spectrometer in such a way that it is spread out horizontally onto the CCD screen. Therefore, each pixel in a horizontal line corresponds to a different wavenumber and all the pixels in one column correspond to roughly the same wavenumber. We say

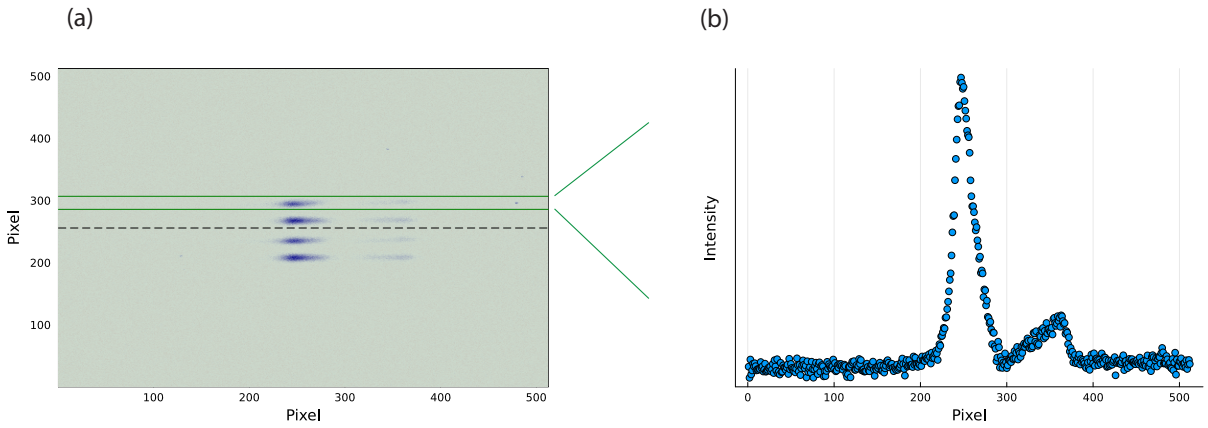

Figure **3-9**: (a) Illustration of a possible CCD image with no binning. The signals are separated at the centre (dashed line) because of the Galvanometer mirror. Each signal also has a reflection from the back of our transparent glass samples, resulting in a total of 4 visible signals on the screen. (b) Averaging multiple pixel rows that contain a signal (horizontal green lines) reveals the spectrum of the investigated molecules. The pixels can then be transformed to wavelength or wavenumber by taking the position of the optical grating in the spectrometer into account.

roughly because there might be a 'tilt' in the signal on screen if the sum-frequency pulse enters the spectrometer at a slight angle. In figure **3-9** (a) we can see a possible image of the CCD sensor with no *binning*. Binning is the ability of a CCD to selectively combine the charge of multiple pixels into a single charge packet via a special charge readout mode that reduces the signal-to-noise ratio.[95] Normally, we use a full vertical binning (all vertical pixels in a column are treated as a single pixel) for simple spectra or a 256 pixel vertical binning (the top and bottom 256 pixels in a column are treated as a single pixel each) for pump-probe experiments. Here, we have two signals that are separated by the Galvanometer mirror to hit the top and bottom parts of the CCD screen. Also, due to the nature of our samples which we will address in the next section, we get a second reflection from the back of our transparent glass slides, resulting in a total of four visible signals. If we specifically take the average of multiple pixel rows that contain a signal (green lines in figure **3-9** (a)), we can plot the intensity of each vertical pixel as is illustrated in figure **3-9** (b). The pixel axis, in turn, can then be transformed into the corresponding wavenumber, given by the position of the optical grating. This is the general idea of how we obtain our spectra.

Event removal

There are, however, several reasons why this spectrum needs to be refined to accurately describe the vibrational information in our samples. For one, we need to remove strong

isolated intensity peaks in single or multiple pixels of the CCD camera that do not correlate to photons from our experiment. These 'jumps' in intensity are liberally labelled as *Cosmic Ray Events* because they are caused by high-energy particles that originate from supernovae and pulsars.[96] However, radioactive decay can also contribute to this phenomenon.[97] The algorithm that we devised to remove these events is the following:

1. Take any 1-dimensional array that represents the intensity data on the CCD screen and calculate the difference between every array element and its subsequent neighbour.

2. Check if any of these differences are greater than a threshold, which we base on the standard deviation of the data points.

3. For all values that are above the threshold, check if any of the next values in a certain interval are below the negative threshold. The width of this interval can be altered to catch events that encompass multiple pixels.

4. If the above holds, we expect the jump in intensity at these pixels to be caused by a spurious event. In such a case, we remove the affected data points and replace them with interpolated data.

Dark data

Secondly, the CCD sensor might accumulate charge even without the presence of photons from our probe pulse, which is what we call *dark counts*. These dark counts have multiple sources:

1. Stray light from our laser pulses but also the environment can hit the CCD sensor and generate an unwanted background signal. Even though we put an appropriate filter in front of the spectrometer, the upconversion pulse is still the biggest source of stray light in our setup. This kind of contribution to the dark counts increases linearly with the exposure time of the CCD.

2. Even though the CCD sensor is cooled thermoelectrically to $-100\,^{\circ}\mathrm{C}$ there are still pixels that accumulate charge due to heat that contribute significantly to a background signal. These dark counts due to heat also increase linearly with the exposure time of the CCD.[98]

To measure these dark counts, we block the broadband IR beam such that no sum-frequency signal is generated and take multiple pictures with the same exposure time as that of the experiment, which we call *dark frames*. These frames are then averaged to ensure that roughly the same amount of stray light and heat charge accumulates in the dark frame as in the actual spectrum. The exception here is the missing stray photons

from the broadband IR pulse in the dark frame, which, however, do not contribute much to the dark counts because of the insensitivity of the CCD to infrared radiation. To rid the raw spectrum of the dark counts is as simple as subtracting the dark frame from the spectral frames.

Frame-by-frame acquisition

The next step is less of a refinement but comes about because of our limited width of the broadband IR pulse. Even with our broadband setup, we still cannot cover the whole CCD screen with a single Gaussian profile of the probe laser. This becomes relevant in the next step when normalising the spectra to the probe IR spectral profile. Here, we get huge experimental artefacts when there is little signal on the edges of the screen. To compensate for this, we usually take 3 or 4 frames with different central wavelengths to cover the edges of the screen as well as the middle part. We then simply sum up all of these frames to produce a single frame with a more evenly distributed IR intensity. Naturally, we cannot achieve a perfectly constant IR distribution across the whole screen for any finite number of frames, which is something that we have to tackle as well in the next step.

Flat data

Due to the Gaussian-shaped spectral profile of our broadband IR pulse, the resonances in our sample are necessarily not all excited equally. Furthermore, depending on the spectral range of the broadband IR pulse we might hit strong absorption bands of the air molecules, which also results in fewer photons that arrive at the monolayer. To compensate for this, we need to enhance the spectrum according to the intensity profile of our pulse. We can approximate this intensity distribution by generating a non-resonant background signal on a metallic surface that we call a *flat frame*. We use gold for this because it gives a strong non-resonant signal that is roughly constant over our spectral range. Since we only need a normalised intensity spectrum it does not matter at which exposure time the flat frame is taken as long as there is a decent signal. On the other hand, we do need to take a dark frame for the flat spectrum as well to get the accurate Gaussian-shaped intensity profile of the broadband IR pulse. Also, we need to take a flat frame for all of the different central wavelengths in our frame-by-frame acquisition. We then enhance the resonances in our spectrum by dividing each data point according to the data points of the normalised flat frame.

Baseline correction

At this point, we expect the spectral data to be zero in areas of no resonance and only deviate from zero when there is resonance. This, however, is not always the case as we,

more often than not, observe some kind of 'tilt' in the baseline. There are multiple reasons for this behaviour, like a fluctuating laser intensity for example. Also, when we take our flat frame on a gold surface, we not only have to move the sample stage to the gold sample but also adjust the height to find the correct laser geometry again. This process, however, is often tricky and the sum-frequency signal of the flat might enter the spectrometer at a slightly different angle than the spectrum signal, which can result in a tilted baseline. We remedy this by fitting a curve through some of the data points at the edges of the screen, far away from any resonance and subtracting this curve from the data. Usually, a second-order polynomial is enough to level the baseline appropriately.

Pump-probe experiments

With the above steps, we have a fully refined spectrum that we can analyse for its vibrational information. This, however, does not give us any insights into the dynamics of the system, yet. The pump-probe part of our experiments comes into play when we compare the refined spectra in the top and bottom part of the CCD screen (see figure **3-9** (a)). In case we find the appropriate temporal and spatial overlap of our three laser spots on the sample and the observed resonances are susceptible to the pump wavelength, we will find a significant deviation in the peak intensities of the two spectra. The difference in peak intensity of the unpumped and the pumped spectra then is evidence for what we call a *pump effect*. Now, we can either scan through different pump wavelengths to investigate what resonances are susceptible to which energies or we can fix the pump wavelength and change the timing of the pump pulse to observe a transient bleach of the resonances. The former is what we call a *wavelength scan* while the latter is called a *delay scan*. Both of these experiments are necessary to gain meaningful insights into the dynamics of our molecular samples.

These measurements can take up to several hours, depending on the number of scans that we take and the necessary exposure time of the CCD for decent spectra. It is very difficult to keep the system completely stable over such a long period of time as there might be a change in ambient temperature, fluctuations in laser power or even deterioration of our samples. To counter these problems, we integrated certain measures into our setup. For one, when we take a delay scan, the positions on the delay stage are approached in random order. This ensures that a transient effect due to environmental circumstances does not show up in the spectra as such but instead, the noise in the spectra will increase over time. The downside is a slightly increased runtime of the whole experiment because the delay stage occasionally needs to move long distances when the positions are chosen randomly. In addition, we can choose to measure the broadband IR power before every spectrum at the cost of an increased runtime. For the wavelength scans, we devised a procedure that allows us to measure and regulate the pump IR power before every spectrum, which ensures that we always pump with the same strength.

Even though we have taken these measures, there might still be some fluctuation in the intensities of each spectrum. Since we find the pump effect in any spectrum by subtracting the reference, the absolute difference will necessarily be smaller in spectra with less intensity. We tackle this problem by finding some sort of master reference that all spectra are then adjusted to. For this, we devised the following algorithm:

1. Find a master reference spectrum by averaging all reference spectra, which usually gives a decent signal-to-noise ratio.

2. Divide each reference spectrum by the master reference. This results in an array of 512 values (one for each horizontal pixel) for every reference spectrum. These values are what we call *reference factors* because they represent the factors by which each pixel in a spectrum has to be adjusted to match the master reference.

3. Multiply the values of each pixel in every spectrum by their respective reference factors to adjust all spectra to the master reference.

This is the last step in refining the pump-probe spectra, which brings us to a point where we minimised the experimental error and can extract the information about the vibrational dynamics in the monolayer.

3.3 Sample Preparation

This section aims to provide information about the samples that we are going to investigate in the scope of this thesis. First, the Langmuir-Blodgett technique is introduced, which we utilise to attach our molecules of interest to a glass slide. Furthermore, we take a closer look at the density of these monolayers and illustrate how to manipulate this quantity. Our actual molecules are introduced in the second subsection. Here, we show what we expect the molecular layers to look like and we also give an in-depth look at the spectral fingerprint of this rather well-known system.

3.3.1 Langmuir-Blodgett Technique

Our samples are prepared using the *Langmuir-Blodgett technique*, which is named after the pioneering work of Irving Langmuir and Katharine Blodgett in the late 1930s.[99] By now, the LB technique is a well-established method of depositing single or successive layers of molecules on a solid surface. And our setup specifically has been described in earlier works.[100] Here, we illustrate the general idea and give details regarding our sample preparation. In figure **3-10** we can see the illustration of a so-called *Langmuir trough*, which we use to coat a glass slide with a single layer of long-chained amphiphile molecules. These molecules are deposited onto a liquid subphase and pushed together by two moving

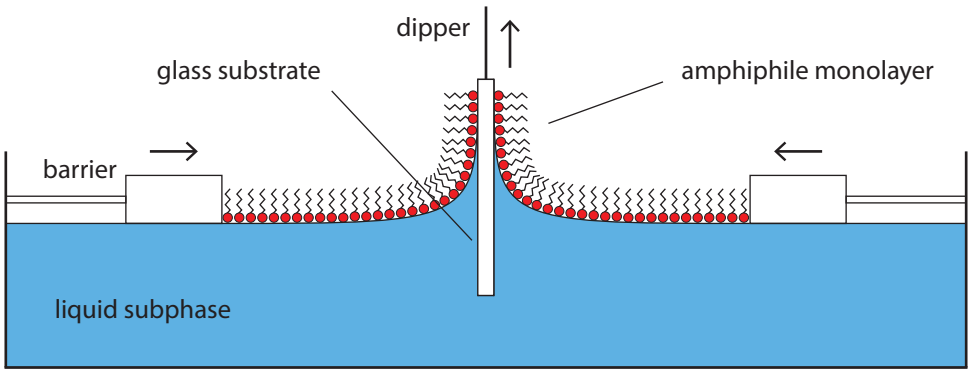

Figure **3-10**: Illustration of the Langmuir-Blodgett technique. A glass substrate is slowly pulled out of a liquid subphase, while two barriers simultaneously push an amphiphile monolayer together to maintain a constant surface pressure. This allows the monolayer to coat both sides of the glass substrate.

barriers to create pressure on the surface. If this pressure is sufficiently high, the long chains of the amphiphile molecules align horizontally and form a well-ordered monolayer on the liquid subphase.[99] A previously lowered glass slide is now slowly pulled out of the liquid subphase while the barriers simultaneously push the surface molecules together to maintain a constant pressure. This way, the molecules attach to both sides of the glass substrate, forming a thin film.

Our setup utilises a Teflon-coated Langmuir trough from the company *Riegler and Kirstein GmbH* equipped with a lift for our glass substrates ($1 \times 1\,\mathrm{cm}^2$, 0.5 mm thickness, *Plano GmbH* microscope coverslip). A Wilhelmy balance with an automated feedback system is used to guarantee constant surface pressure when the substrate is pulled out of the liquid. As the subphase, we use a solution of 5 mM $CaCl_2$ in deionized water (Millipore system, resistivity > 18 MΩ/cm). The pH value of this subphase was adjusted to 9.5 by adding a saturated solution of $Ca(OH)_2$, which is shown to have a stabilising effect on the monolayer.[100,101] About 70 μL of a 1 mM solution of our molecules in chloroform are then spread onto the liquid subphase. There are two systems that we are going to investigate in this thesis. The first one is arachidic acid, also known as eicosanoic acid ($CH_3(CH_2)_{18}COOH$, analytical grade, *Sigma Aldrich*) and the second system is a deuterated version of the same molecule: arachidic-17,17,18,18-d4 acid ($CH_3CH_2(CD_2)_2(CH_2)_{15}COOH$, *Deutero*).

Isotherms

Depending on the surface pressure, the temperature of the subphase and the density of the monolayer, multiple phases can occur in any amphiphile film. Typically, one measures the surface pressure in the Langmuir trough (usually expressed as π in millinewton per meter) while monitoring the compressed surface area (usually expressed as A in area per

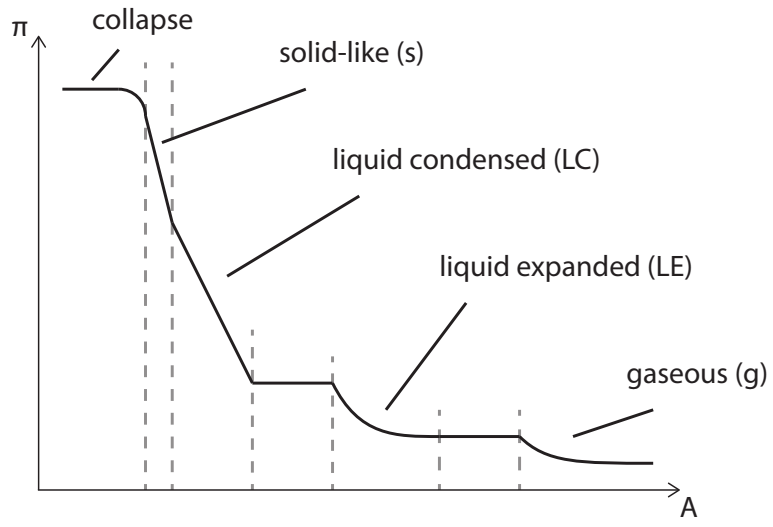

Figure **3-11**: Schematic illustration of commonly observed phases in amphiphile monolayers. The graph shows the surface pressure π vs the area per molecule A. Adapted from the book by Butt, Graf and Kappl.[102]

molecule) to get a phase diagram of the two-dimensional monolayer. This is done at a fixed subphase temperature, which is why these graphs are called *isotherms*. Figure **3-11** shows a schematic isotherm of an arbitrary amphiphile monolayer. This figure and the paragraph itself are mainly based on the book by Butt, Graf and Kappl and the article by Kaganer et al.[102,103]

Similar to any three-dimensional material, a two-dimensional Langmuir film undergoes phase transitions from gaseous over liquid to even solid-like phases. When the area per molecule is much larger than the molecule itself, there is virtually no interaction between the molecules, which is known as the *gaseous phase* (g). Here, the surface pressure is usually so small that it is nearly undetectable. Compressing a gaseous monolayer, there can be a phase transition to a liquid state, which is characterised by a significant interaction between the molecules. Most authors describe at least two types of liquid phases: a *liquid-expanded phase* (usually called LE or L1) and a *liquid-condensed phase* (usually called LC or L2).

In the LE phase, the area per molecule is still larger than the actual molecule. However, the amphiphiles do touch each other and there is interaction but no lateral order. In the further compressed LC phase, the monolayer becomes relatively stiff as the molecules align to form a somewhat ordered film. There is, however, still water present between the headgroups and the molecules are tilted to the surface normal. Here, the pressure-area isotherms become more linear. Compressing the liquid phases even further, one finds the monolayer in a *solid-like phase* (s), indicating a stiff film with largely dehydrated headgroups. The isotherms are linear and extrapolation to zero film pressure results in

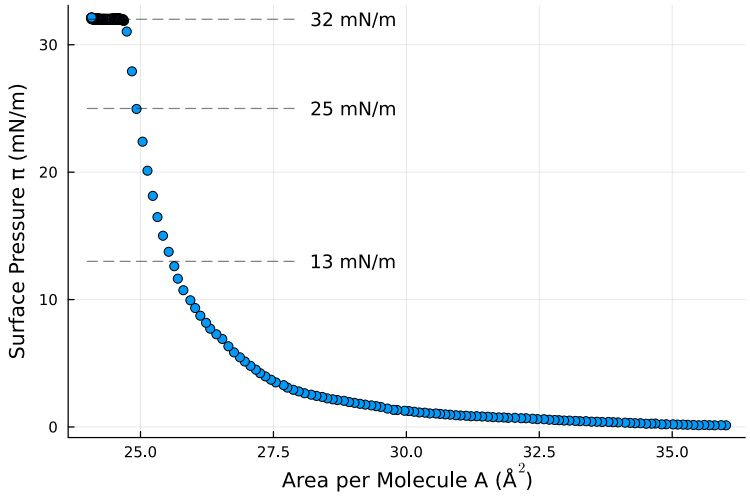

Figure **3-12**: Area vs surface pressure isotherm of calcium arachidate on a subphase at pH $\approx$ 9.5, a solution of 5 mM $CaCl_2$ and a constant temperature of 295.15 K. Shown is the sample that was prepared at a transfer pressure of 32 mN/m (millinewton per meter). The dashed horizontal lines indicate the transfer pressures of our other samples.

an area per molecule that is comparable to the cross-section of the molecule.

All of these phases can occur but for most amphiphiles, not all phases are observed. Furthermore, some systems exhibit an even greater variety of phases. Especially for long-chain fatty acids, including our arachidic acid, the phase diagram is quite complex and it is now believed that the phase of high compressibility is not the solid-like phase but a so-called *superliquid phase* (LS).[104,105] This LS phase is well-ordered and densely packed, providing an excellent film for investigation.[106]

In the scope of this thesis, we prepared our samples at three different surface pressures, which are indicated by the dashed lines in the isotherm of figure **3-12**. Naturally, each transfer pressure requires a fresh sample and a unique isotherm but in our case, plots of different transfer pressures are sufficiently similar, allowing us to show all of them in a single diagram. The 32 mN/m (millinewton per meter) and 25 mN/m pressures guarantee that the calcium arachidate monolayer is in the stable LS phase during deployment.[107] This was chosen to investigate the influence of different transfer pressures on the vibrational dynamics of our molecules. Furthermore, in earlier works of our group, it was found that in our system (calcium arachidate, subphase temperature of 295.15 K and pH of 9.5) the phase transition from the LC to the LS phase is around 15 mN/m.[106] Therefore, we chose our third transfer pressure at 13 mN/m to investigate how different phases during deployment influence our pump-probe experiments.

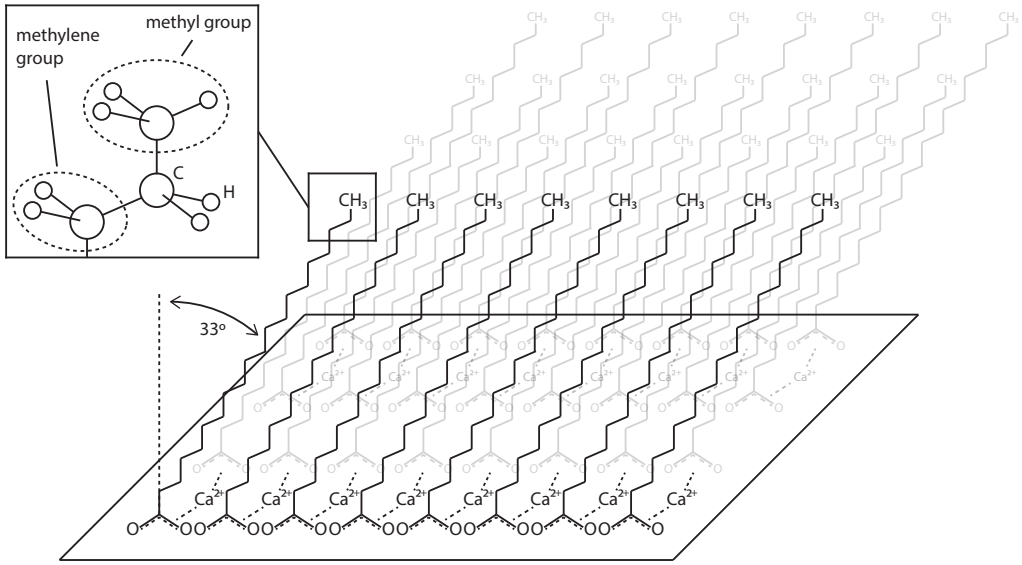

Figure **3-13**: Illustration of an ideal calcium arachidate Langmuir-Blodgett monolayer on glass. Two arachidate ions coordinate to one calcium ion and the saturated fatty acid chains are tilted at an angle of $\approx 33°$ to the surface normal.

3.3.2 Calcium Arachidate Monolayer

As previously mentioned, the molecules that we are going to investigate in this thesis are long-chain saturated fatty acids called arachidic acid. This system and fatty acids in general have been studied thoroughly in the literature and their properties are rather well-known.[108,109] In our case, we spread arachidate ions ($C_{20}H_{39}O_2{}^-$) onto a subphase of calcium ions ($Ca_2{}^+$), which is known to have an overall stabilising effect on the monolayer.[101] Figure **3-13** illustrates such a well-ordered Langmuir-Blodgett monolayer. Here, we can see how the arachidate ion consists of 18 methylene (CH_2) groups and the ends of the chain are terminated with a methyl (CH_3) and a carboxylate (COO^-) group, respectively. According to Outka et al., the zig-zag chains on a Si(111) surface are not vertical even in the highly stable LS phase but interlocked in a $33° \pm 5°$ tilt angle to the surface normal.[110] This, on the other hand, results in an almost vertically aligned methyl group ($0° \pm 5°$ tilt to the surface normal) due to the C-C-C bond angle of $\approx 115°$. Furthermore, two carboxylate groups coordinate to one calcium ion of the subphase, which is also illustrated in figure **3-13**. We expect the deuterated versions of the arachidate ion to behave in a sufficiently similar way.

Gauche Defects

In figure **3-13** we illustrated the monolayer in such a way that all of the 'kinks' in the chains are in the same plane, which is known as the anti- or all-*trans*- conformation. More

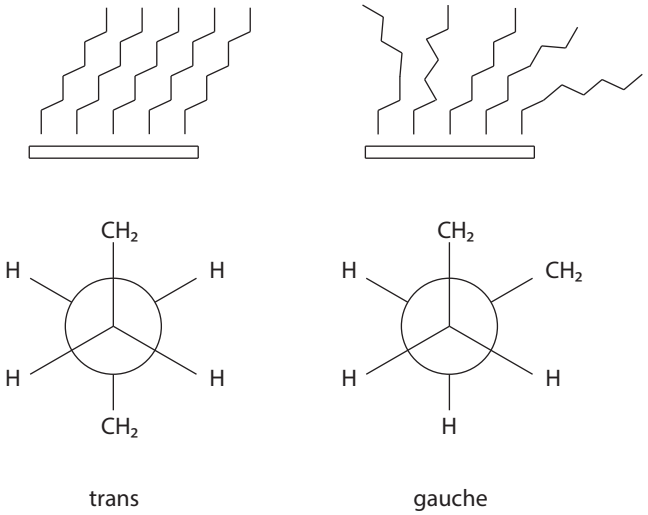

Figure **3-14**: In the lower half of the figure is the schematic illustration of a bird's-eye view of alkyl chains in the trans- and gauche conformation. The trans conformation consists of adjacent methylene groups that are rotated by 180° such that all C atoms lie in the same plane. In the gauche conformation, some CH_2 groups are rotated by $\pm 60°$, which destroys the symmetric order in a Langmuir-Blodgett monolayer. This is illustrated in the top half of the figure. Adapted from Lackner.[53]

precisely, every methylene group is rotated by 180° to their neighbours and this conformation is the thermodynamically preferred state of every molecule in the monolayer.[100] There are, however, energetically higher-lying metastable states that correlate to conformations where adjacent methylene groups are rotated by 60° in either direction. This is illustrated in figure **3-14** and such an arrangement is called a *gauche* conformation. When single or multiple chains form such gauche conformations, the symmetric order of the monolayer is locally broken, which is known as a *gauche defect*.

During our experiments, which are done at room temperature, a small amount of these gauche defects is already present in our calcium arachidate monolayers.[111] To significantly alter the symmetric order in the monolayer, however, temperatures higher than 340 K are necessary, which was shown in earlier works from our group.[100,106]

Knowledge about gauche defects is relevant to our experiment for several reasons. First of all, a gauche defect necessarily forces a change in the tilt angle of the molecule. The average tilt angle of our molecules, on the other hand, strongly influences the susceptibility of the methyl group, as we have seen at the end of section 2.3.5. Thus, with an increasing amount of gauche defects, our overall sum-frequency signal will decrease accordingly. Secondly, the methylene groups in a well-ordered monolayer form an isotropic bulk that prohibits the generation of a sum-frequency signal, as we have learned in section 2.3.4. This bulk symmetry, however, is locally broken in the vicinity of a gauche defect such that the methylene groups become SFG active. Therefore, one can derive a direct relationship

between the number of gauche defects in the monolayer and the intensity of the methylene groups' vibrational modes.[112,113] This is very important because we now have a tool to rule out if a decrease in signal intensity comes about because of accumulated heat and the consequential increase of gauche defects in the sample. We will necessarily heat our sample by inducing energy with our lasers, which is something that needs to be taken into account. Therefore, the absence of significant CH_2 bands in the spectrum strongly supports a signal decrease due to vibrational redistribution.

With this brief overview of our knowledge about calcium arachidate monolayers, we conclude the experimental chapter. Here, we learned about the structure of a densely packed film as well as the orientation of the ordered chains. Equally important, we mentioned how gauche defects are revealed in the vSF spectrum and how they can be used to monitor heat in the monolayer. With this knowledge, we are now ready to tackle the main part of this thesis, which is the analysis of sum-frequency spectra and the tracking of vibrational dynamics.

Chapter 4

Results

Chapter 4 constitutes the main part of this thesis. Here, we present the results that we have gathered from investigating calcium arachidate Langmuir-Blodgett films using pump-probe vibrational sum-frequency spectroscopy. This chapter is structured as follows: First, we take a look at the information that we can extract from the vibrational spectra of our monolayers. Specifically, we focus on the prominent stretching vibrations of the methyl and methylene groups and compare the visible modes in IR and Raman spectra to the sum-frequency results. Secondly, we present and elucidate the results of our pump-probe experiments. After that, we introduce a reservoir model in an attempt to explain the observed dynamics. Lastly, we extend our molecular system to further explore the intra- and intermolecular energy redistribution mechanism. By decreasing the density in the monolayer we hope to gain insights into the coupling mechanism between adjacent alkyl chains. Additionally, we investigate how deuteration in the chains influences the vibrational energy redistribution.

4.1 Vibrational Spectra of CaAra

As we already mentioned before, arachidic acid and alkyl chains in general have been the focus of study in many scientific works. For this reason, the spectral fingerprint of the methylene and methyl groups is well known.[114] This subsection provides infrared, Raman and sum-frequency spectra of arachidic acid and our deuterated version. Further, we compare our results with the literature and assign the prominent peaks to their respective vibrational modes, accordingly. Here, we follow the established norm of many authors and denote the vibrational modes of the methyl group with r and the ones belonging to the methylene group with d.

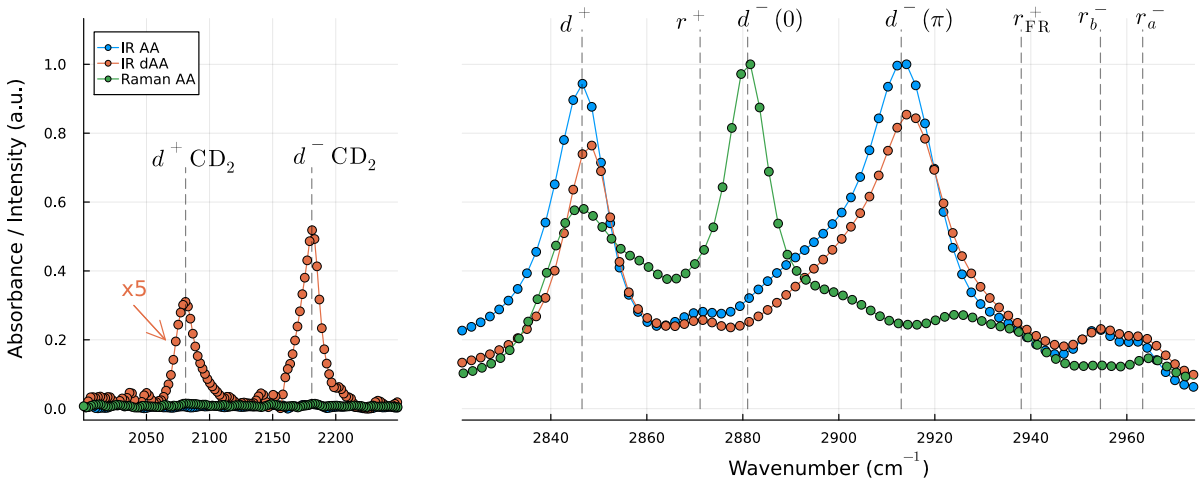

Figure **4-1**: Normalised IR absorbance and Raman intensity spectra of crystalline arachidic acid (AA) and deuterated arachidic acid-d_4 (dAA). The dashed lines indicate the most prominent peaks and their associated vibrational modes. The 2100 cm^{-1} region of the deuterated infrared spectrum on the left is enhanced by a factor of 5 with respect to the right side.

4.1.1 Infrared and Raman Spectra

Figure **4-1** shows the infrared and Raman spectra of crystalline arachidic acid (AA) and the deuterated version (dAA) in the CH stretching region around 2900 cm^{-1}.

The methyl group has been extensively studied in bulk alkanes and reportedly features a symmetric stretch (r^+) at $\approx 2875\,cm^{-1}$, to which a change in the dipole moment along the symmetry (z-) axis of the CH_3 group corresponds. Furthermore, there are two nearly degenerated antisymmetric modes at $\approx 2962\,cm^{-1}$ and $\approx 2954\,cm^{-1}$, corresponding to a change of the dipole moment in (r^-_a) and out (r^-_b) of the plane of the chain, respectively.[115] Interestingly, the r^-_a mode seems to be more Raman active than the other r^- mode. Since the sum-frequency intensity depends on both the IR and Raman transition dipole moment, as we have stated in the theory chapter in equation 2.164, we should expect a larger peak in the sum-frequency spectrum at $2962\,cm^{-1}$. Additionally, one usually finds another peak near $2935\,cm^{-1}$ that is attributed to a Fermi resonance (r^+_{FR}) of the symmetric stretch with the overtone of the methyl bending modes. These values are in good agreement with the spectroscopic data of our IR and Raman spectra.

The discussion of the more prominent methylene group is a little more tricky. According to Tasumi et al., the phase difference ϕ between the oscillating motion of a CH_2 group and its adjacent neighbour is important for the mode to be IR or Raman active.[116] This is reasonable because, as we have seen in equation 2.115 and 2.122 of the theory chapter, either the dipole moment or the polarisability has to change during the oscillation for the mode to become IR or Raman active. If we recall how the CH_2 links in a fatty acid

molecule point in opposite directions alternatingly as shown in figure **3-13**, it now becomes obvious that the combined motion of the symmetric stretching of all CH_2 links does not change the net dipole moment when all oscillators are in-phase and the superposition is therefore not IR active. On the other hand, if we have a phase shift of $\phi = \pi$ between adjacent links, we do get a net dipole moment change. A similar argument can be made about the Raman activity: When adjacent links are in-phase, the expanse of the combined symmetric stretch gets larger during the motion, resulting in a changing polarisability of the system and a Raman active mode. When the adjacent links are again shifted in phase by π, the expanse stays the same and the mode becomes Raman inactive.

Snyder et al. assigned the most intense peaks at $\approx 2850\,\mathrm{cm}^{-1}$ and $\approx 2920\,\mathrm{cm}^{-1}$ in the infrared spectrum to the symmetric ($d^+(\pi)$) and antisymmetric ($d^-(\pi)$) stretching of the CH_2 group that have a phase shift of $\phi = \pi$ to their adjacent neighbours.[117] In the Raman spectrum, on the other hand, the modes that are in-phase with their neighbours ($\phi = 0$) become visible. Here, we find the symmetric CH_2 stretch ($d^+(0)$) at the same wavenumber $\approx 2850\,\mathrm{cm}^{-1}$ but the antisymmetric stretch ($d^-(0)$) is shifted to $\approx 2880\,\mathrm{cm}^{-1}$. These values were observed for the extended polymethylene chain and are only roughly comparable to our arachidic acid spectra in figure **4-1**. There are, however, works that investigate palmitic acid ($C_{16}H_{32}O_2$), which report values much closer to our system.[118] A comparison of multiple systems from different sources is shown further below in table **4-1**.

The infrared spectrum of the deuterated molecule does not differ much from the undeuterated species. Blaudez et al. report the symmetric stretch of the CD_2 group (d^+CD_2) at $\approx 2089\,\mathrm{cm}^{-1}$ and the antisymmetric stretch (d^-CD_2) at $\approx 2194\,\mathrm{cm}^{-1}$ for fully deuterated crystalline cadmium arachidate.[119] These values are comparable to the peaks in the $2100\,\mathrm{cm}^{-1}$ region of the deuterated infrared spectrum. Interestingly, one finds a slight blue shift of the CH_2 modes in the deuterated molecule against the natural molecule that is not observable for the CH_3 modes. It stands to reason if this small shift comes about due to the partially deuterated chain or is an experimental artefact.

4.1.2 Sum-Frequency Spectrum

Figure **4-2** shows a typical sum-frequency spectrum of a calcium arachidate Langmuir-Blodgett film, taken with our setup in the *ssp* and *ppp* polarisation combinations. As mentioned in section 2.3.4, the methylene groups are mostly invisible here because of the centrosymmetric rule for even-order susceptibilities. Therefore, we find the most prominent peaks originating from the methyl modes. Guyot-Sionnest et al. report for a system similar to ours, strong resonances at $\approx 2875\,\mathrm{cm}^{-1}$ and $\approx 2940\,\mathrm{cm}^{-1}$ for the *ssp* sum-frequency spectrum, which they identify with the symmetric stretch r^+ and the Fermi resonance r^+_{FR}, respectively.[115] Furthermore, the *ppp* spectrum reveals a strong band at $\approx 2960\,\mathrm{cm}^{-1}$, associated with the r^- mode and a weaker r^+-feature. These values are in

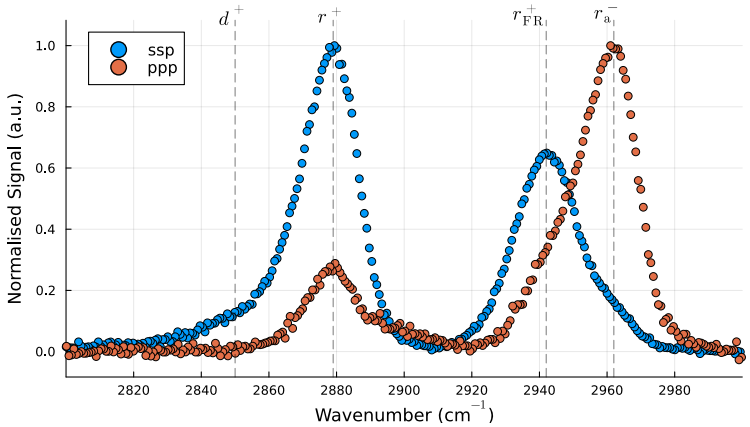

Figure **4-2**: Vibrational sum-frequency spectrum of a calcium arachidate Langmuir-Blodgett film. Shown is the *ssp* polarisation combination in blue and the *ppp* polarisation combination in orange. The important features are indicated with black dashed lines.

good agreement with our spectra. However, even though some authors observe a splitting of the r^- mode, we cannot resolve by eye the in-plane (r^-_{b}) vibration in our sum-frequency spectra.[120,121]

As previously mentioned, we perform our experiments at room temperature and expect some gauche defects to be present in our samples. Therefore, we can attribute the weak shoulder at $\approx 2850\,\mathrm{cm}^{-1}$ in the *ssp* polarisation spectrum to the symmetric stretch (d^+) of the methylene group, which is also found by Guyot-Sionnest et al.[115] The broad background around $2900\,\mathrm{cm}^{-1}$ in the *ppp* polarisation spectrum can also be attributed to CH_2 stretches.[115] More specifically, some authors attribute a feature at $\approx 2900\,\mathrm{cm}^{-1}$ in the vSF spectra of alkyl chains to the antisymmetric stretching of the CH_2 group that is adjacent to the CH_3 group (d^-_ω).[120] A comparison of different systems and their respective mode assignments is shown in table **4-1**.

Comparing our sum-frequency spectrum with the literature, it is reasonable to assume our peak assignment in figure **4-2** is correct. A list of all prominent modes and their wavenumbers is given in table **4-2**. With that, we have a good idea about the different vibrational modes that are visible in our sum-frequency spectra and we can now tackle the pump-probe experiments.

4.2 Pump-Probe Experiments

This section presents the results of our pump-probe experiments. We begin by showing the data of our wavelength scans, which provide the necessary insight as to how susceptible the monolayer is to specific pump wavenumbers. Building up on that, we then fix the pump photon energy to a specific resonance and observe the transient bleach. These

Table **4-1**: List of observable modes and their respective wavenumbers (cm^{-1}) in similar molecular systems. The investigated samples are pentadecanoic acid (PDA, $CH_3(CH_2)_{13}COOH$), octadecylsiloxane (ODS, $CH_3(CH_2)_{17}SiOH$), docosanethiol (DT, $CH_3(CH_2)_{21}SH$), palmittic acid (PA, $CH_3(CH_2)_{14}COOH$), fully deuterated arachidic acid (dAA, $CD_3(CD_2)_{18}COOD$) and our arachidic acid (AA, $CH_3(CH_2)_{18}COOH$). Bracketed values indicate Raman data and the mode assignment from Hill et al. is supported and extended by Snyder et al.[117]

Source	Guyot-Sionnest et al.[115]	Chow et al.[120]	Himmelhaus et al.[121]	Hill et al.[118]	Blaudez et al.[119]	This work
System	PDA on water	ODS on glass	DT on gold	PA in KBr pellet	dAA in KCl pellet	AA in KBr pellet
Spectrum	vSF	vSF	vSF	IR (Raman)	IR	IR (Raman)
Mode						
r_a^-		2964	2968	2961 (2964)		2963 (2964)
r^-	2960					
r_b^-		2958	2954	2953 (2955)		2953 (2954)
r_{FR}^+	2940	2941	2940	2938 (2938)		2937 (2939)
d^-		2920	2916		2925	
$d^-(\pi)$				2917		2913
d_ω^-		2905				
$d^-(0)$				(2880)		(2881)
r^+	2875	2877	2880	2871 (2871)		2871
d^+	2850	2850	2855	2848 (2846)	2852	2847 (2846)
d^-CD_2					2194	2181 [dAA]
d^+CD_2					2089	2081 [dAA]

delay scan spectra allow us to obtain information about the vibrational dynamics of our molecular system. Lastly, we conclude this section with a summary of our findings.

4.2.1 Wavelength Scans

We begin the presentation of our results by showing the wavelength scan data, even though the chronology of events during the project was quite different. In reality, we found the first pump effects more or less by chance, pumping different modes and looking for any kind of change in the transient delay scans. However, we feel like introducing the wavelength scans first and presenting how susceptible the molecules are to different pump energies paints a more coherent picture.

Figure **4-3** shows the two-dimensional wavelength scan of a calcium arachidate monolayer. As mentioned previously in section 3.2.1, our setup allows for self-referencing because of the Galvanometer mirror, such that the top and bottom parts of the CCD

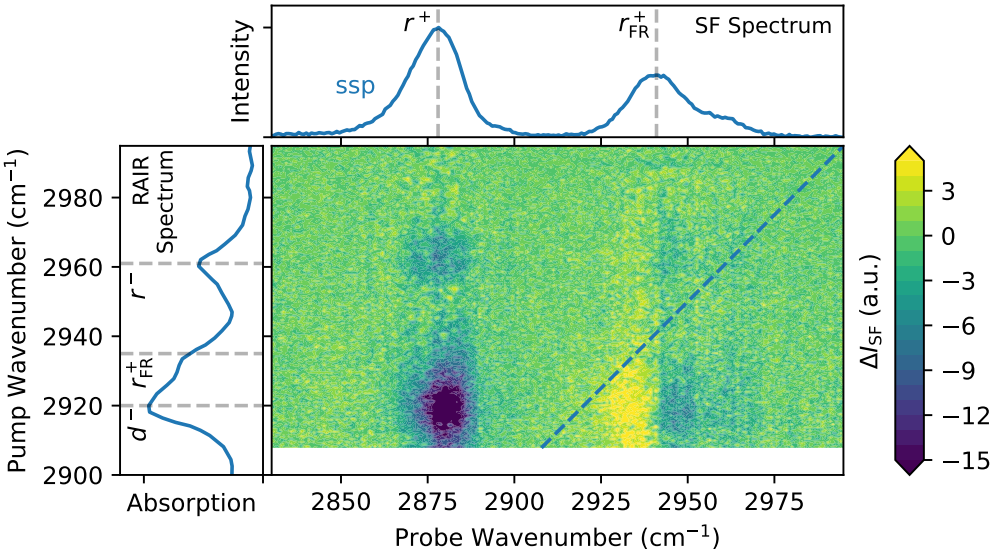

Figure **4-3**: Two-dimensional plot showing the difference between pumped and reference spectra for different pump wavenumbers. The sum-frequency spectra are taken in the *ssp* polarisation combination and a single of these spectra is displayed in the top part of the figure. The left panel shows the RAIR spectrum that indicates how much of the pump-IR energy is absorbed at what wavenumbers. Dashed lines either indicate notable vibrational modes or show where the pump and probe wavenumbers are identical.

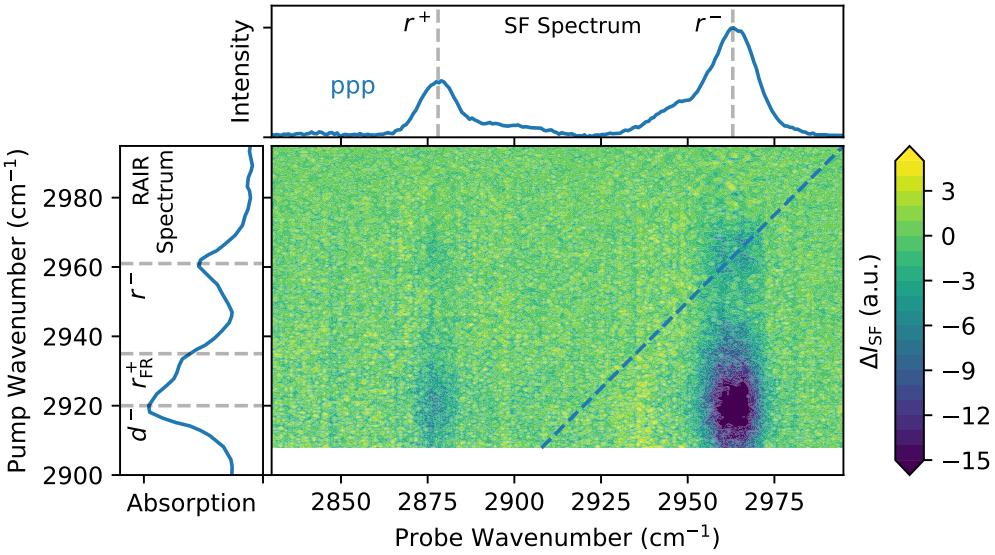

Figure **4-4**: Same plot as in figure **4-3** but in *ppp* polarisation.

Table **4-2**: A list of visible resonances and their mode assignment in the *ssp* and *ppp* sum-frequency spectrum of calcium arachidate (figure **4-2**).

Mode	*ssp*	*ppp*
r^-	shoulder	2962
r^+_{FR}	2942	shoulder
r^+	2879	2879
d^+	shoulder	

correspond to a pumped spectrum and an unpumped reference. What is shown in figure **4-3** is the difference in intensity between the pumped sum-frequency spectra and their references

$$\Delta I_{\mathrm{SF}} = I_{\mathrm{SF,pump}} - I_{\mathrm{SF,ref}}. \tag{4.1}$$

Furthermore, every row in the two-dimensional plot corresponds to a different pump wavenumber and we put all three pulses in temporal overlap to achieve a strong pump effect. Due to the non-coherence of our pump and probe IR beams we do not need to worry about any unwanted interference phenomena arising from the overlapping of all three pulses. The spectra are taken in the *ssp* polarisation combination and a single of these sum-frequency spectra is shown in the top part of this figure. On the left side is the reflection absorption infrared (RAIR) spectrum of a similar system (stearic acid) on a gold surface, which was provided by Yujin Tong as part of a collaboration with the group of R. Kramer Campen. Even though our samples are on glass, we expect the absorption spectra of our arachidic acid to not deviate too much from the RAIR spectrum. The dashed line in the two-dimensional plot indicates where the pump and probe wavenumber are equal.

This quite complex figure reveals some interesting facts about our calcium arachidate monolayers. The most evident feature appears in the more prominent r^+ mode but in the Fermi resonance r^+_{FR} we can see some features as well. The RAIR spectrum on the left was taken in a similar beam geometry to our setup, which is why we can expect this graph to roughly approximate the amount of pump IR energy that is absorbed by our monolayer. Interestingly enough, the pump effect seems to mirror the RAIR spectrum quite well, which raises the question of whether the features in the difference spectrum are primarily due to heat.

In section 3.3.2 we introduced gauche defects and discussed how they appear in the monolayer with increasing temperature. Therefore, we should expect a decent amount of sum-frequency active methylene groups to be present in the monolayer if we significantly heat the sample with our pump laser. According to table **4-1** of the last section, we would expect the d^+ and the d^- mode to appear around $\approx 2850\,\mathrm{cm}^{-1}$ and $\approx 2920\,\mathrm{cm}^{-1}$,

respectively. However, at neither of these values do we find prominent features in the SF spectrum or the difference spectrum. Assuming a Boltzmann distribution, a temperature far above 1000 K is necessary to explain our peak bleach of roughly 17 %. Consequently, we can safely rule out a signal decrease due to heat.

The next thing that might pique the reader's interest is the change in intensity in the red flank of r^+_{FR}. Here, the difference spectrum shows a signal *increase* for pump wavenumbers near d^- as opposed to the expected decrease. This curious behaviour can have various causes. For one, the Fermi resonance is known to be quite sensitive to its environment, according to Guyot-Sionnest et al.[115] So it is possible that r^+_{FR} slightly shifts to lower frequencies in the pumped spectra, which would result in a signal increase in the difference spectra. This is illustrated on the left side of figure **4-5** with simulated sum-frequency data, according to

$$I_{\mathrm{SF}} = \left| \sum_k \frac{a_k A_k}{\omega_{0,k} - \omega + i\Gamma_k} \right|^2 . \tag{4.2}$$

This equation is very similar to the one we derived in 2.166, except for a neglected non-resonant background contribution and an additional factor a_k, which we call the *attenuation coefficient*. This coefficient attenuates the line strength A_k and represents a measure of how many available oscillators there are for a single resonance in comparison to the unpumped equilibrium state. Also, equation 4.2 is only a valid representation of our data if all resonances are in-phase, such that $\phi = 0$ or anti-phase, such that $\phi = \pm\pi$. In the latter case, the A_k are negative. Otherwise, we would need an additional phase factor $\mathrm{e}^{i\phi}$ for every resonance. For calcium arachidate monolayers, however, we expect this to be the case and we can hide the phase factor in the sign of A_k.

Coming back to figure **4-5**, the top left part shows simulated sum-frequency spectra with a resonance ω_0 that is shifted with respect to the one in the reference spectrum ω_{ref}. Illustrated in the bottom left panel is the difference between pumped and reference spectra. This difference is also calculated by equation 4.2 and in this case, we set the attenuation coefficient for all spectra to $a_k = 1$. Here, we can see a significant increase in the difference signal, the more the resonance of the pumped spectrum is shifted.

Secondly, when there are two resonances close together, they form a convoluted sum-frequency signal, which is shown in the top right part of figure **4-5**. If these resonances have opposite phases, one can also observe an increase in the difference spectrum even though the population in both modes decreases. This is illustrated in the bottom right part of figure **4-5**. The phases of r^+_{FR} and r^- fit such a case, which has been resolved by Ji et al. for octadecyltrichlorosilane monolayers on glass.[122] The shown sum-frequency spectrum is a simulation of two convoluted modes that roughly resemble r^+_{FR} and r^-. The spectra are simulated with equation 4.2 and the exact parameters are given in the caption of figure **4-5**. It is hard to say at this point, whether the increase in the difference

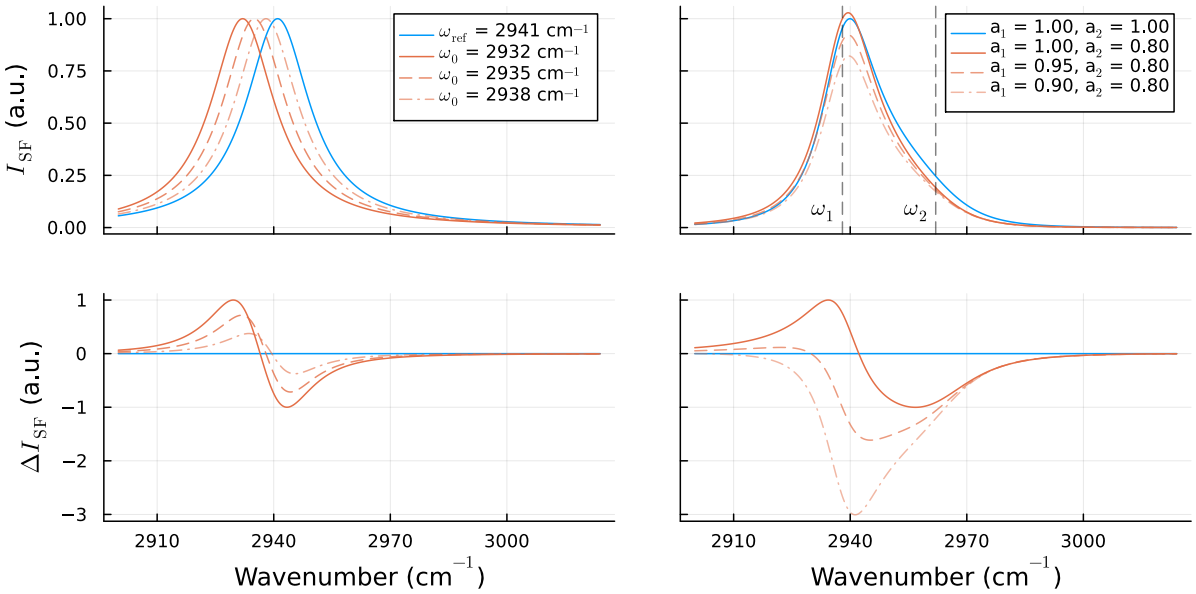

Figure **4-5**: Simulated sum-frequency data to illustrate the possibility of a signal increase in the two-dimensional difference plot in figure **4-3**. The top row of this figure shows the sum-frequency spectra and the bottom row reveals the resulting signal difference. The plots on the left side illustrate spectra of a single resonance ω_0 that is slightly shifted to the reference spectrum ω_{ref}. On the right side is the sum-frequency spectrum of two convoluted modes that resemble r^{+}_{FR} and r^{-}. Here, the effect of different attenuation coefficients a_k, according to equation 4.2 is shown. Parameters for the spectra on the left side are $A = 1$, $\Gamma = 10\,\text{cm}^{-1}$ and $a = 1.0$. Parameters for the convoluted spectra on the right are $A_1 = 7$, $A_2 = -6$, $\omega_1 = 2938\,\text{cm}^{-1}$, $\omega_2 = 2962\,\text{cm}^{-1}$, $\Gamma_1 = 9\,\text{cm}^{-1}$ and $\Gamma_2 = 17\,\text{cm}^{-1}$.

spectrum of figure **4-3** comes about due to a shift of the resonances, a convolution of modes or something else but both mentioned scenarios might play a significant role here.

The final aspect we need to address is the white area in the two-dimensional difference plot. As we previously mentioned in section 3.1.1, the Ekspla system that generates our pump pulses switches to the DFG regime at 3440 nm and significantly alters the beam path and power. We could not get around this problem, which is why our pump-probe experiments, unfortunately, are limited to stopping at around $2908\,\text{cm}^{-1}$.

Figure **4-4** shows a similar two-dimensional difference plot as in figure **4-3**. Here, we are looking at the *ppp* spectra and the most intense modes are r^{+} and r^{-}. The strongest pump effect is now visible in the r^{-} mode, which makes sense because it is the most intense mode in the sum-frequency spectrum. However, it is noteworthy that this correlates to a strong pump effect in a vibrational mode that is significantly *higher* in energy ($r^{-} \approx 2960\,\text{cm}^{-1}$) than the excited mode ($d^{-} \approx 2920\,\text{cm}^{-1}$). Naturally, this is only possible if there is energy

flow not only from the initially excited mode but from multiple lower modes as well. Even so, it is difficult to say what modes contribute to this mechanism, at this point.

We can, however, explore this phenomenon a little further by looking at the product of the Boltzmann constant and the temperature kT, which is basically an estimate for an energy level that is significantly populated at the temperature T. In our case, we need to compensate for an energy mismatch of $\Delta\nu \approx 40\,\mathrm{cm}^{-1}$ between r^- and d^-. This energy corresponds to a temperature of

$$T = 10^2 hc\Delta\nu/k \tag{4.3}$$

$$\approx 60\,\mathrm{K}, \tag{4.4}$$

with h and c being the Planck constant and the speed of light in vacuum, respectively. Since we operate at room temperature, where kT corresponds to $\approx 200\,\mathrm{cm}^{-1}$, we should expect that there is always a low energy vibration available to compensate for the energy mismatch $\Delta\nu$ by either creating of annihilating an excitation. We will tackle this point again later on when we model the data.

At first glance, the strong pump effects in areas of significant IR absorption seem to be reproducible in the *ppp* spectra, which is especially clear to see in the r^- mode. Nevertheless, it is hard to discern by eye if we can observe a signal increase in the red flank of r^+_{FR}, similar to the *ssp* spectra. This is something that we have to take a closer look at in the following.

Taking a Closer Look at the Data

Now that we have taken a first look at the two-dimensional wavelength scan data, we are interested in a more discerning view. Figure **4-6** shows vertical slices through the two-dimensional difference spectra in the *ssp* (figure **4-3**) and *ppp* (figure **4-4**) polarisation combination. The slices are centred at the most prominent modes r^+ and r^- at $2879\,\mathrm{cm}^{-1}$ and $2962\,\mathrm{cm}^{-1}$, respectively. Furthermore, the data are averaged over a range of $\approx 10\,\mathrm{cm}^{-1}$ in probe wavenumbers to include most of the dominant pump effects. Additionally, the RAIR spectrum is shown as well for a more detailed comparison.

First of all, we should note that the *ssp* and *ppp* datasets in figure **4-3** and **4-4** are normalised to the most intense peaks, such that ΔI_{SF} roughly represents the intensity decrease in per cent for the most prominent peaks. In figure **4-6** only the RAIR data are scaled, which means that we have a surprisingly good reproducibility of the pump effects in the most prominent modes of two experiments on different days. Secondly, the data points do roughly follow the RAIR spectrum except in the region of r^+_{FR} around $2935\,\mathrm{cm}^{-1}$. Here, we find a significant shoulder in the RAIR spectrum that is not observed in the datasets.

Furthermore, as we mentioned previously, it is hard to distinguish between the in- and out-of-plane vibrations (r^-_{b} and r^-_{a}) of the antisymmetric methyl stretch in our sum-

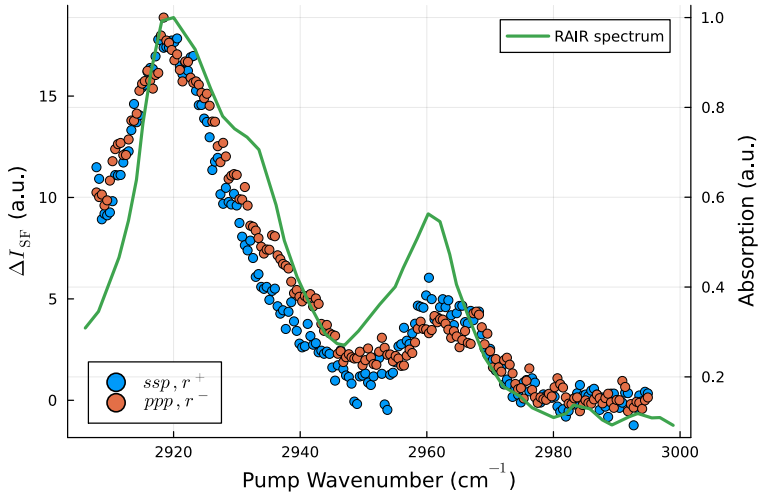

Figure **4-6**: The data points show vertical slices through the two-dimensional difference spectra of figures **4-3** and **4-4**. The blue dots represent a vertical slice at the position of r^+ (2879 cm^{-1}) in the *ssp* spectra and the orange dots represent a vertical slice through r^- (2962 cm^{-1}) in the *ppp* spectra. Both datasets are averaged over a range of 10 cm^{-1} and their values are displayed on the left axis. The right axis shows the IR absorption values of the RAIR spectrum that is also taken from figure **4-3**.

frequency spectra (figure **4-2**). In the RAIR spectrum, on the other hand, we find a significant peak at $\approx$ 2962 cm^{-1} and a prominent shoulder around $\approx$ 2954 cm^{-1}, which correspond quite well to r_a^- and r_b^-, according to table **4-1**. Interestingly enough, the pump effect seems to only be significant when pumping the out-of-plane vibration r_a^-.

Now, let us take a closer look at the pump effect along the probe IR axis. Figure **4-7** shows horizontal slices through the difference spectra of figure **4-3** and **4-4** that are centred at d^- ($\approx$ 2920 cm^{-1}) and averaged over a range of 10 cm^{-1} to include most of the prominent pump effect. As we have already seen in the two-dimensional spectra, we find that the pump effect mostly mimics the intensity in the sum-frequency spectra. There is a strong signal decrease in the r^+ mode around 2879 cm^{-1} and a very weak effect in the region of the r^- mode around 2962 cm^{-1} for the *ssp* polarisation combination and vice versa for the *ppp* spectra.

It becomes more interesting near the Fermi resonance r_{FR}^+ at 2942 cm^{-1}. Here, we can see the signal *increase* in the difference spectra very clearly. Also, the steep decline on the right side of the peak resembles the effect that we simulated on the left side of figure **4-5**. We can, therefore, assume that a shift in the resonance frequency plays a significant role in the shape of the difference spectra. Equally important, there seems to be a very slight signal increase in the *ppp* spectra as well, which was not visible in the two-dimensional plots. This does, however, correlate quite well with the fact that the Fermi resonance is also visible in the *ppp* spectra as we can see in the red shoulder of r^- in figure **4-2**. On

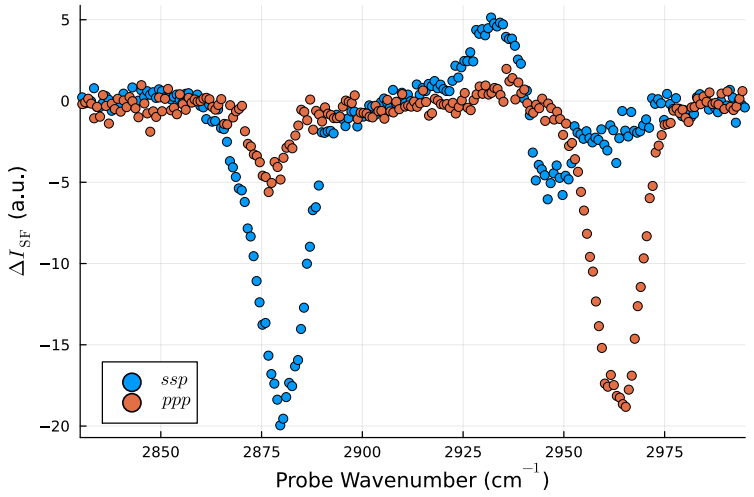

Figure **4-7**: The data points show horizontal slices through the two-dimensional difference spectra of figures **4-3** and **4-4**. Both datasets are horizontal slices, centred at d^- ($2920\,\mathrm{cm}^{-1}$) and averaged over a range of $10\,\mathrm{cm}^{-1}$. The blue dots represent the *ssp* data and the orange dots represent the *ppp* data.

the other hand, it is very hard to discern if there is a similarly steep decline in the *ppp* spectra as there is in the *ssp* polarisation combination.

This is as much information as we can extract from the wavelength scan data at this moment. To gain further insights into the underlying energy transfer mechanism, we need to find a model that simulates the data sufficiently well. This is something that we are going to tackle in section 4.3. First, however, we will introduce the transients derived from the delay scan data.

4.2.2 Transients

Now that we have taken a sophisticated view of the static wavelength scan data from our pump-probe experiments, we will direct our focus on the transients. By transients, we mean experiments in which we fix the pump photon energy to a certain value that induces a strong response in the monolayer and observe the dynamics. From the last subsection, we know that we can expect such a strong response if we tune the pump laser to the d^- and the r^- mode at $\approx 2920\,\mathrm{cm}^{-1}$ and $\approx 2960\,\mathrm{cm}^{-1}$, respectively. With the pump wavelength fixed, we then change the timing between the arrival of the pump pulse and the sum-frequency probe (broadband IR - upconversion pulse pair) on the sample, the result of which is what we call a *delay scan*. These delay scans then reveal how long the energy is stored in a specific mode and give insight into the timescales of the vibrational energy redistribution mechanism. On a side note, we will use the terms 'transient' and 'bleach' interchangeably in this thesis.

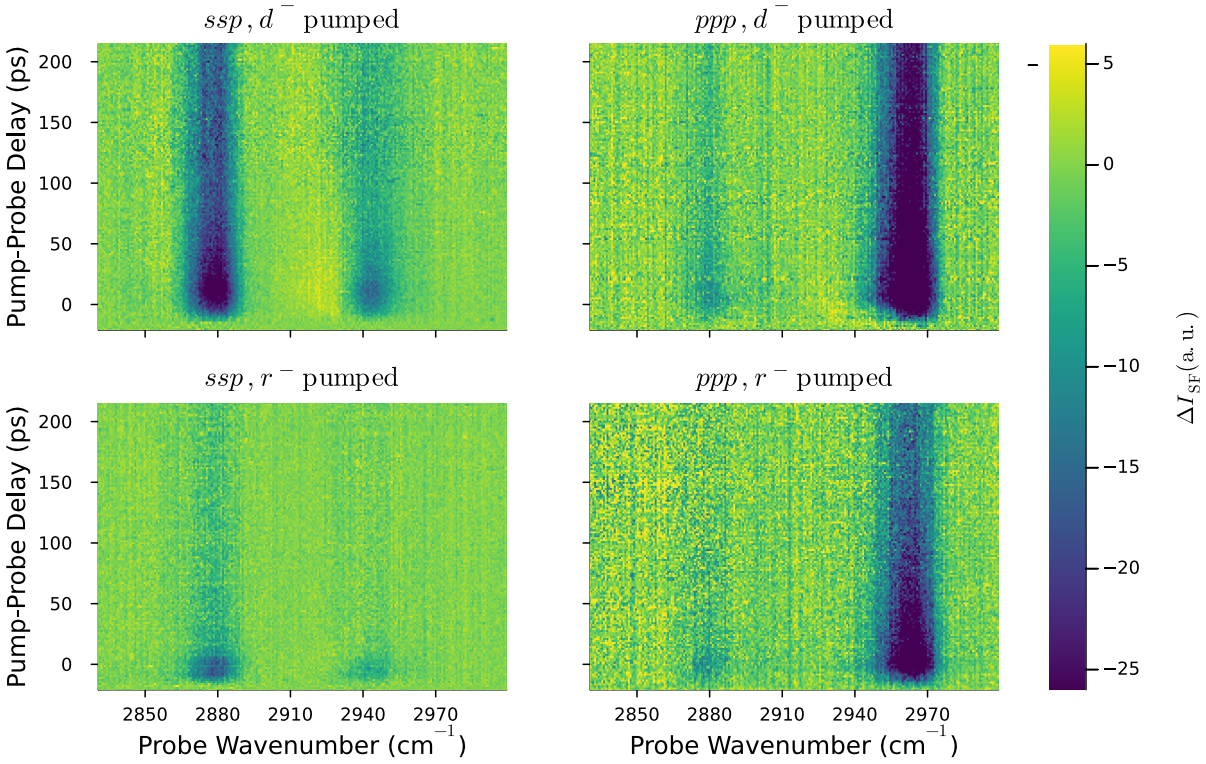

Figure **4-8**: Two-dimensional transient difference spectra for the *ssp* and *ppp* polarisation combination experiments. The pump laser is set to either 2915 cm^{-1} or 2962 cm^{-1}, corresponding to the d^- and the r^- band, respectively. The left axes show the delay between the arrival of the pump pulse and the broad IR - upconversion pair on the sample. The bottom axes indicate the broadband IR wavenumber.

Figure **4-8** shows the two-dimensional transient difference spectra of our delay scan experiments. On the left side are *ssp* spectra with either the d^- mode or the r^- mode pumped and the right side shows the *ppp* polarisation combination. The colour bar indicates the difference between the pumped spectra and their references just like in figure **4-3** and **4-4**.

There are several things that we can learn from a first glance at our delay scan data. First of all, we can see a signal decrease in all visible modes, which is not surprising since we have seen similar behaviour in the wavelength scan data. We did, however, not learn from the previous experiments that there is a visible signal change on a timescale of picoseconds. This is a first impression of the order of magnitude that we can expect for the energy redistribution mechanism. Secondly, the signal decrease occurs as soon as the pump pulse hits the sample around a delay of 0 ps in all four plots. This is reasonable because as soon as we depopulate the ground state with the pump pulse, we should immediately observe an effect on the other modes in the spectrum as well. It stands to reason, however, if we also populate the CH_3 modes at the same time when pumping d^-

or if the decrease in signal comes about solely due to the depopulated ground state.

Next, the form of the transients is very similar in that there seems to be a spike when the pump pulse arrives and a very slow recovery that extends beyond the scanning range. However, the *ssp* polarised, r^- pumped data stand out because here, the transition from spike to slow recovery seems to be much faster than in the other experiments. This is something that we should also keep in mind. Lastly, the top left plot in figure **4-8** shows a signal increase in the red flank of r^+_{FR}, which we explained earlier by either a shift in frequency or a convoluted mode. Unfortunately, the data is too noisy to clearly show if this signal increase transitions into a similarly slow decay as the other modes but it does seem to be shorter-lived.

Taking a Closer Look at the Data

This is about as much as we can glean from a first glance. To extract more information from the transient data, we are going to take vertical slices through the prominent modes, as we did with the wavelength scan data in the last subsection. Figure **4-9** shows these vertical slices through the two-dimensional difference spectra of figure **4-8**. The plots are arranged in the same fashion in both figures such that the *ssp* polarised data are on the left and the *ppp* polarised data are on the right. The *ssp* experiments show slices through the r^+ mode and the blue flank of r^+_{FR} to circumvent the increasing signal for now. The *ppp* experiments show slices through the r^+ and the r^- modes. All data points represent an average over a range of $\approx 10\,\mathrm{cm}^{-1}$ to encompass most of the signal change and reduce overall noise.

Further, the black lines represent exponential fits to the data between 50 and 230 ps, according to

$$I_{\mathrm{bleach}}(t) \propto 1 - 4\,\delta N \mathrm{e}^{-t/\tau}. \tag{4.5}$$

Here, δN is the fractional population that is transferred from the ground to the excited state and τ is the population lifetime T_1 that we already introduced in section 2.3.2. This equation is derived in detail by Han et al. and is, strictly speaking, only valid for a two-level system and small transfer rates δN.[123] Also, the factor of 4 comes about because we take a fraction, let's say x, of the molecules out of the ground state and push them into the excited level. This results in a population difference between the two states of $2x$, which is then squared to get the intensity. When we pump the d^- mode, however, we can only be sure to depopulate the ground state but we do not know if the r modes are populated as well, which would invalidate the prefactor. Nevertheless, this provides us with a reasonable approximation of the timescales at which our dynamics occur.

The first thing to note is that we will not address every mode specifically but rather list similarities and differences between the experiments. Also, we now normalised every mode to itself, which gives us the fractional signal in every mode. Therefore, the transients of a

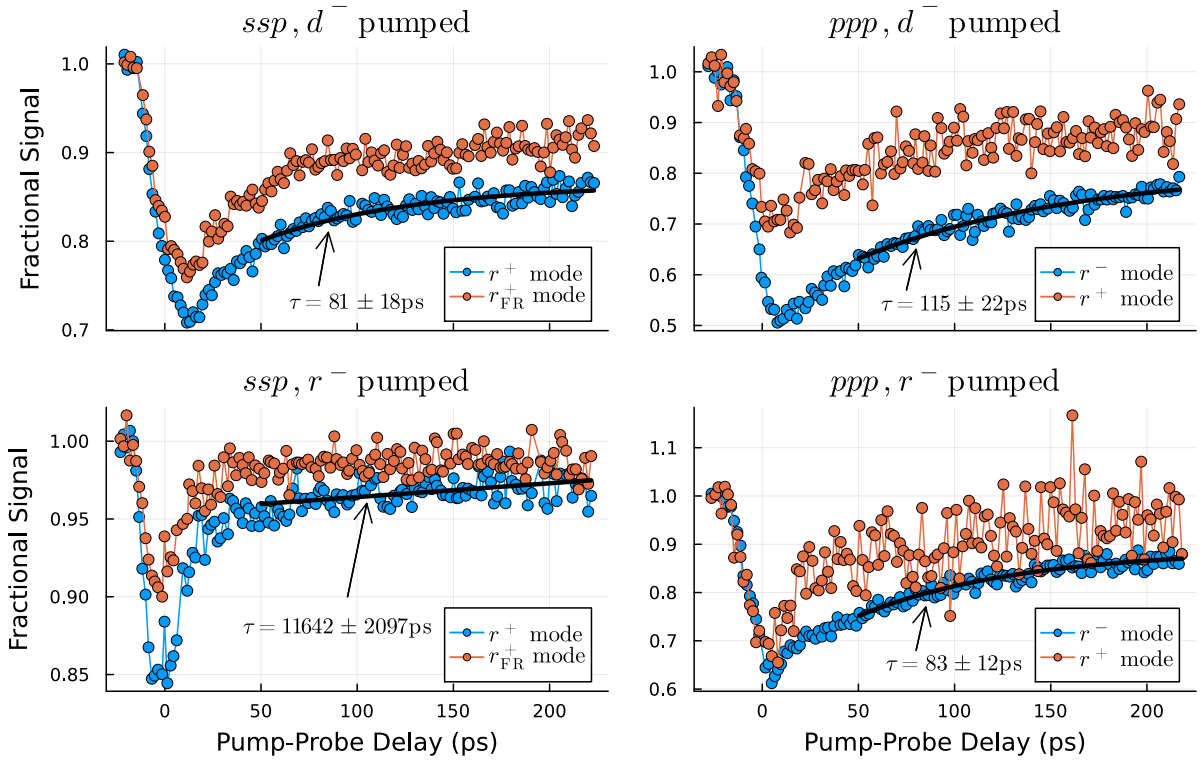

Figure **4-9**: The data points show vertical slices through the two-dimensional transient difference spectra of figure **4-8**. The slices are centred at the prominent modes around 2879 cm^{-1}, 2945 cm^{-1} and 2962 cm^{-1}, corresponding to the r^+ band, the blue flank of r^+_{FR} and the r^- band, respectively. Shown is the average intensity over a range of $\approx 10\,\mathrm{cm}^{-1}$. The left axes indicate the fractional signal of each mode and the solid black lines show the fitted lifetime according to equation 4.5.

single experiment can be compared with one another. Comparing transients of different experiments is a little more tricky, however, because multiple factors influence the strength of the pump effect:

1. Assuming the intensity of the sum-frequency spectra does not change (same spatial and temporal overlap for broadband IR and upconversion pulse) we can get significantly different pump strengths depending on how well we align the pump pulse with the others.

2. Even though we can control the intensity of the pump laser to a certain degree, environmental changes like spiking humidity can lead to more IR absorption in the air and significantly reduce the number of photons that arrive at the sample.

3. Some modes might be inherently more susceptible to the initial pump energy and act more as a catalyst for the energy flow than others.

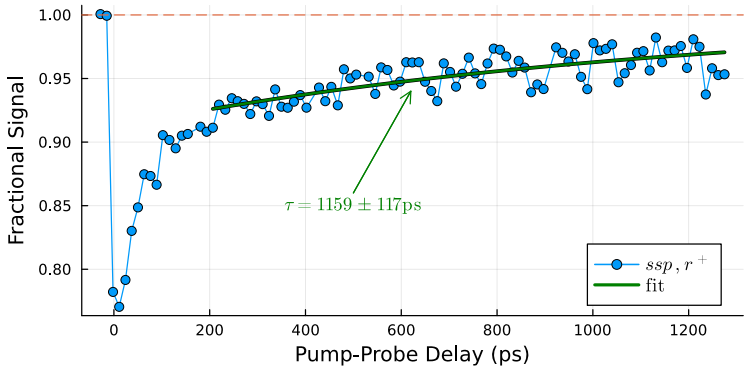

Figure **4-10**: Repetition of the experiment in the top left of figure **4-9** with a total delay of up to 1.2 ns. The green line is an exponential fit of the slow component in the transients. The dashed line indicates equilibrium.

These are important aspects that we should keep in mind for future reference.

Secondly, most if not all transients show a biexponential pattern such that a faster decay with a time constant of roughly ≈ 100 ps transitions into a much slower component that kind of plateaus and does not reach equilibrium on the timescale that is shown. The only exception is the ssp, r^- pumped spectra in the bottom left. Here, the system transitions into the plateau level immediately after the pump pulse has passed and we find a time constant in the nanosecond regime.

To investigate this behaviour further, we repeated the experiment in the top left of figure **4-9** but utilised the full length of our delay stage. The resulting transient is shown in figure **4-10**. Here, we can see how the recovery still does not reach the equilibrium level that is indicated by the dashed line and an exponential fit of the plateau with equation 4.5 suggests a lifetime of > 1 ns. To find an upper limit, we can manipulate the Pharos such that another earlier pulse is seeded into the pump laser system. The internal Pharos oscillator runs at 76 MHz, which puts the timing between these pulses at around ≈ 13.2 ns. Doing that, we found that the signal is completely recovered after 13 ns, which supports a lifetime in the magnitude of nanoseconds.

Having covered the limit of very long delays, we will now focus on the limit of small delays, which is essentially the moment when the pump pulse is in temporal overlap with the other pulses. In our experiments, we find this point zero by first overlapping the broadband IR with the upconversion pulse to generate our sum-frequency probe signal. We then block the broadband IR and adjust the narrowband IR pump pulse to generate a sum-frequency signal with the upconversion pulse. In theory, this guarantees a spatial and temporal overlap of all three pulses and we can set the point of zero delay, accordingly. Naturally, this adjustment is prone to error but we estimate the error to be no more than a few picoseconds.

That being said, we can observe some interesting elements in the transients. Almost

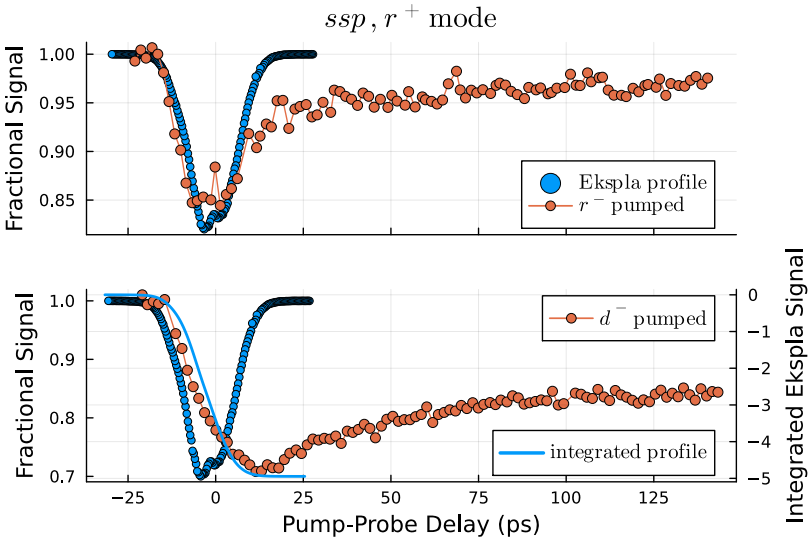

Figure **4-11**: Comparison of the transient delay scan data with the temporal shape of the pump pulse. The top part shows the r^+ mode in *ssp* polarisation with the r^- mode pumped, which is taken from the bottom left of figure **4-9**. The bottom part also shows the r^+ mode in *ssp* polarisation but with the d^- mode pumped, taken from the top left part of figure **4-9**. The blue dots represent the Ekspla time profile according to our cross-correlation experiments in figure **3-6** and the blue line indicates the numerically integrated signal of the Ekspla pulse, shown on the right axis.

all trends show how the maximal signal decrease occurs roughly $10-20$ ps after the pump pulse hits the sample. The only exception is the *ssp* polarised, r^- pumped delay scan in the bottom left of figure **4-9**, which features a minimum at around zero delay. The r^+ mode in the bottom right of the same figure might show a similar trend, even though the data are very noisy. In these plots, it looks as if the signal change mirrors the Gaussian shape of the pump pulse when it hits the sample.

This idea is further investigated in the top part of figure **4-11**. Here, the plot shows the transient data of the r^+ mode in the bottom left experiment of figure **4-9** and the approximate time profile of our pump pulse, taken from the cross-correlation measurements of figure **3-6**.

We should note here, that we only scaled the intensity of the pump pulse profile to compare the data and left the position on the time axis untouched. Even though the two datasets were taken on different days they fit surprisingly well together. Looking at the bottom part of figure **4-11**, we see the same comparison as before but with the pump laser set to the d^- mode. Evidently, in this case, the time profile does not fit the transient data at all. However, if we instead look at the integrated signal from the pump pulse we find a curve that fits the data much better.

As we have mentioned before, this does indeed suggest a very rapid decay in the *ssp*

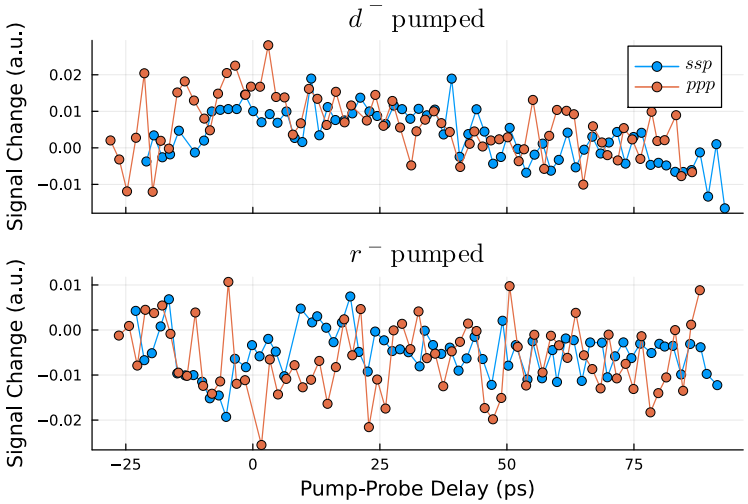

Figure **4-12**: The data points show vertical slices through the two-dimensional transient difference spectra of figure **4-8**. All slices are centred at $\approx 2928\,\mathrm{cm}^{-1}$ and averaged over $\approx 10\,\mathrm{cm}^{-1}$ to include the signal increase in the red flank of r^+_{FR}. The top part shows the *ssp* and *ppp* experiments with the pump laser set to d^- and the bottom part shows the same experiments with r^- pumped.

polarised, r^- pumped transients such that the system stays only excited as long as the pump pulse is present and immediately transitions into the plateau level. In the other experiments, the energy of the pump pulse seems to be stored longer and only dissipates on a timescale of ≈ 100 picoseconds into the plateau.

Finally, we want to illuminate the signal increase in the red flank of r^+_{FR} that we observed in the top left part of figure **4-8**. To this end, we take slices through the two-dimensional difference spectra again, as we did in figure **4-9**. This time, however, the slices are all centred at $\approx 2928\,\mathrm{cm}^{-1}$ and again averaged over $10\,\mathrm{cm}^{-1}$ to include the left flank of the r^+_{FR} mode. This is shown in figure **4-12**.

Even though the signals are very noisy, we can make out a similar signal increase in the *ppp* spectra as well. This was hard to pick up in the two-dimensional difference spectra. Interestingly enough, this feature seems to only be present when pumping the d^- mode, as the bottom part of figure **4-12** suggests. Setting the pump laser to r^- either does not affect the red flank of r^+_{FR} or even decreases the band intensity. Unfortunately, we are unable to extract any finer details from the datasets because of the background noise.

4.2.3 Summary

We conclude this section with a summary of the most important insights that we have gained from our pump-probe experiments. First, we will focus on the results from the wavelength scan data in subsection 4.2.1 and afterwards we are going to summarise the

results of the delay scan experiments in subsection 4.2.2.

Wavelength Scan

For the wavelength scan data, we put all three of our pulses in temporal and spatial overlap to achieve a strong pump response, while sequentially scanning through different pump photon energies. Analysing the resulting difference spectra, we found some very interesting characteristics of our calcium arachidate monolayers:

1. We observed the strongest response to the pump pulse when the pump photon energy was set to the d^- and the r^- modes at around $2920\,\mathrm{cm}^{-1}$ and $2962\,\mathrm{cm}^{-1}$, respectively. Interestingly, these photon energies correspond to strong IR absorption bands, according to the RAIR spectrum of a similar system. We did, however, rule out a signal decrease due to heat because there was no evidence of gauche defects.

2. Comparison to the RAIR spectrum also revealed that pumping the Fermi resonance r^+_{FR} around $2935\,\mathrm{cm}^{-1}$ does not contribute to the pump effect even though there is strong absorption in the monolayer. Furthermore, in the r^- region, the pump effect seemed to be more prominent when pumping the out-of-plane vibration r^-_{a}.

3. Surprisingly, we observed a signal *increase* rather than the expected decrease in the red flank of the Fermi resonance. As we later confirmed in the delay scan experiments, this increase is roughly equally strong in the *ssp* and *ppp* polarisation combination but seems to only be present when pumping the d^- mode. We illustrated how a shift in the resonance frequency or a pump effect in multiple convoluted modes can result in such a signal increase.

4. Lastly, the *ppp* polarised experiments featured a strong pump response in the r^- mode around $2962\,\mathrm{cm}^{-1}$ when we pumped the energetically lower lying d^- mode. Naturally, this is only possible if there is energy exchange not only between the excited modes but a contribution from lower modes as well.

Delay Scan

After we wrapped up the fixed-delay wavelength scan data, we transitioned to the delay scan experiments that gave insight into the dynamics of the system. Our delay scans are characterised by fixing the pump photon energy, while solely increasing the time delay between the arrival of the pump pulse and the sum-frequency probe pulse pair. This allowed us to take snapshots of the system at different stages in the energy decay process. By analysing this transient evolution we gained important knowledge about the vibrational energy redistribution mechanism in our molecules:

1. The first thing to note is that our temporal resolution is limited by the width of our Twin's pulse, which is roughly 0.3 ps and usually, our experiments encompass a range of ≈ 200 ps. On this timescale, we were able to observe multiple components of the energy decay process.

2. All experiments eventually transitioned into a very slow component, which we refer to as the plateau level that extended beyond our usual scanning range. By utilising the full length of our delay stage and manipulating the pulse seeding of the Pharos, we found that the system recovers to equilibrium on a timescale of a few nanoseconds.

3. Most experiments indicated an at least biexponential decay such that there was an initial spike in the difference spectra, which transitioned into a faster decay before plateauing out into the slow component. The exception was the experiments with the pump laser set to r^- in *ssp* polarisation and to a lesser extent the r^+ mode in *ppp* polarisation. Here, the data did not show an exponential decay but mirrored the temporal shape of our pump laser. This suggests a mechanism on the timescale of a few picoseconds, limited by the temporal width of the pump laser since we are blind to any dynamics that occur during the arrival of the pump pulse.

4. Comparing the pump pulse profile with the other experiments, we found that here, the data does not fit the temporal shape but rather the numerically integrated profile. This further supports how, in these experiments, the energy is stored in the respective modes for a longer time before decaying on a timescale in the magnitude of 100 ps into the plateau level.

5. Finally, we found virtually no delay between the arrival of the pump pulse and the signal change in all experiments. This suggests a very rapid first internal energy redistribution between the methylene and the methyl groups because we observed an immediate effect in the r modes regardless of pumping the d or r modes.

This concludes the illustration of our pump-probe experiments and the presentation of our results. The next step in understanding the underlying mechanism that dictates the energy flow in our molecules is finding a suitable model that can explain our observations. We will tackle this problem in the next section.

4.3 Temperature Model

Building upon the previous section, this section introduces a three-temperature model in an attempt to explain the observations from our pump-probe experiments. The structure is as follows: First, we will validate our experimental data from the last section to find

what trends are reproducible. After that, we will motivate a three-temperature model and introduce the corresponding reservoirs. Next follows a mathematical description of our model and we conclude this section by comparing experimental and simulated data.

4.3.1 Validation of the Data

Before we introduce a suitable model to our observations, we will attempt to validate the experimental data of the pump-probe experiments from the last section. Naturally, it is impossible to exactly reproduce an experiment due to the amount of optimisation that goes along with each setup. However, it is still important to repeat the experiments mainly because of two questions:

1. Is the shape or trend of the data points reproducible?

2. How strongly does the bleach intensity vary in different measurements?

To this end, we repeated the experiments in figure **4-9** of the last section roughly half a year later. Figure **4-13** displays a comparison between the earlier presented pump-probe data and the repeated experiments. Shown are only the most prominent modes, i.e. r^+ in *ssp* and r^- in *ppp* but the weaker modes are reproducible in the same manner. The orange dots illustrate the experimental data from the last section and the blue dots represent the repetition of the same experiments.

The first to note when looking at the plots is that we can reproduce the trends of all experiments surprisingly well. However, to achieve this we had to shift the orange data points in the top and bottom left plots by -5 ps and $+5$ ps, respectively. Such a shift seems reasonable because the approximate time profile of our pump laser in figure **3-6** (a) features two small peaks that are roughly 5 ps apart. Therefore, when looking for the zero delay position, we may not always optimise the signal to the same peak and accidentally create a shift of 5 ps between different measurements.

Secondly, we find strong variation in the intensity of the bleaches. We had to scale the data points by factors of 1.1 to 1.7 to overlap the different datasets. Such surprisingly strong deviation can only be attributed to two things: The power of the pump laser during measurement and the spatial overlap of the pump laser with the other beams. Every other alignment in the experimental setup only affects the intensity of the sum-frequency spectra and not the bleach.

To investigate the influence of the pump pulse energy, we measured the maximum bleach intensity of a single mode and sequentially decreased the power of the pump pulse. The data points in figure **4-14** show the maximum bleach intensity of the r^+ mode in *ssp* when pumping the d^- mode as a function of the applied pump power. As expected, the initial data points seem to go linearly with the pump pulse energy. More surprisingly is the fact that the bleach intensity seems to saturate at around 30 mW, which might lead

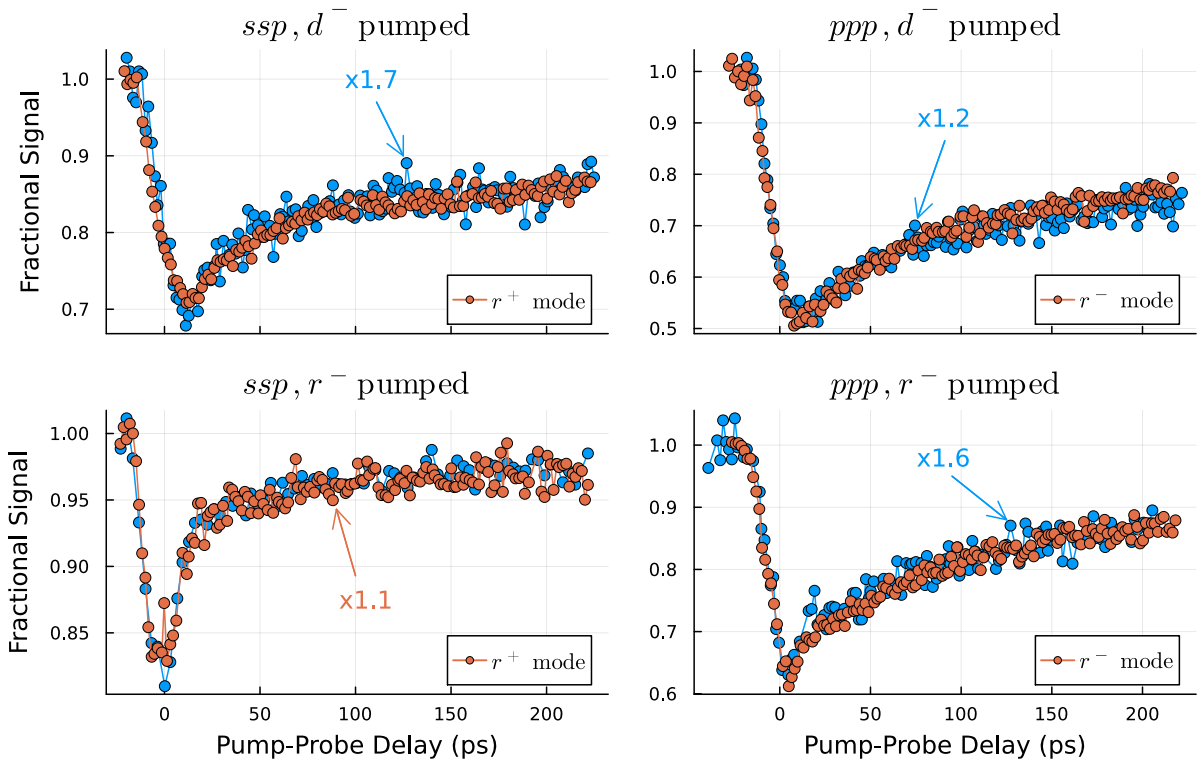

Figure **4-13**: This figure shows the bleaches in figure **4-9** and a repetition of the same experiments roughly half a year later. The blue dots represent the most prominent modes of figure **4-9** and the orange dots are the same modes of the repeated experiments. The coloured arrows indicate which dataset is enhanced by what factor to overlap both experiments. Additionally, the orange dots in the top left and bottom left are shifted by -5 ps and $+5$ ps, respectively.

to problematic effects in our pump-probe measurements. However, since the maximum bleach that we observed in our experiments is roughly 50 %, which correlates to a population shift of $(1 - \sqrt{0.5})/2 \approx 15\,\%$ for a simple two-level system, we should be safe in that regard. The saturation effect that we observe in figure **4-14** might just be due to experimental factors that arise when manipulating the attenuation of the pump laser. On the upside, however, a fluctuation in the pump power during measurement should only have a minute effect on the observed bleach intensity. On the other hand, if we follow this line of thought, we necessarily have to assume that the variation in bleach intensity in figure **4-13** cannot be attributed to the pump power but has to significantly rely on the spatial alignment of the pump pulse.

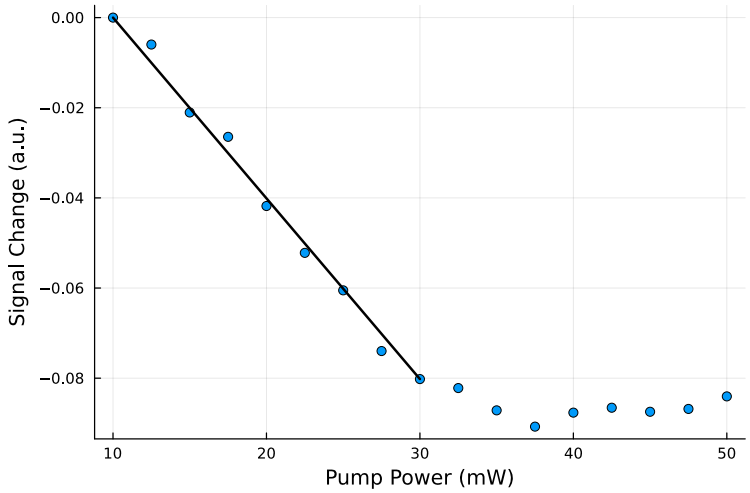

Figure **4-14**: The data points show the bleach on the r^+ mode in *ssp* polarisation when pumping the d^- mode as a function of the approximate pump IR power at the sample. The black line indicates the linear part of the data.

Bleach Comparison

Now that we made sure the shape of the transient data is reproducible, we are going to compare the bleaches of different experiments with one another. It is reasonable to look for similarities between different experiments with the same pump laser parameters. Figure **4-15** shows the bleaches on the r^+ and r^- modes in the *ssp* and *ppp* polarisation combinations. The left part shows the experiments with the pump laser set to d^- and the r^- pumped spectra are on the right. We decided to drop the bleach on the Fermi resonance r^+_{FR} because it is strongly convoluted and its frequency might be shifting, as we have seen in section 4.2.1.

We begin with the top left plot in figure **4-15**. Here, we can see the bleach on the r^+ mode in the *ssp* and *ppp* experiments with the pump laser set to d^-. Since the polarisation combinations are essentially just two different ways of looking at the same thing, we should expect the bleach on the same mode to also be the same. This gives us a powerful tool to determine a scaling factor between two different experiments. Surprisingly, here, in the top left plot, we find that the datasets are very similar even though we did not enhance any of them. Unfortunately, the data points of the *ppp* measurement are very noisy because the mode is very weak but the two datasets show a very similar trend, nonetheless.

Coming to the bottom left plot of figure **4-15**, we are now comparing the most prominent modes in *ssp* and *ppp*. Here, we find that the bleach on the r^- mode is much stronger and we had to enhance the r^+ mode by a factor of 1.75 to match the other dataset. This seems to be an inherent characteristic of the system because the pump laser alignment should be comparable in both experiments as we have seen in the plot above. This be-

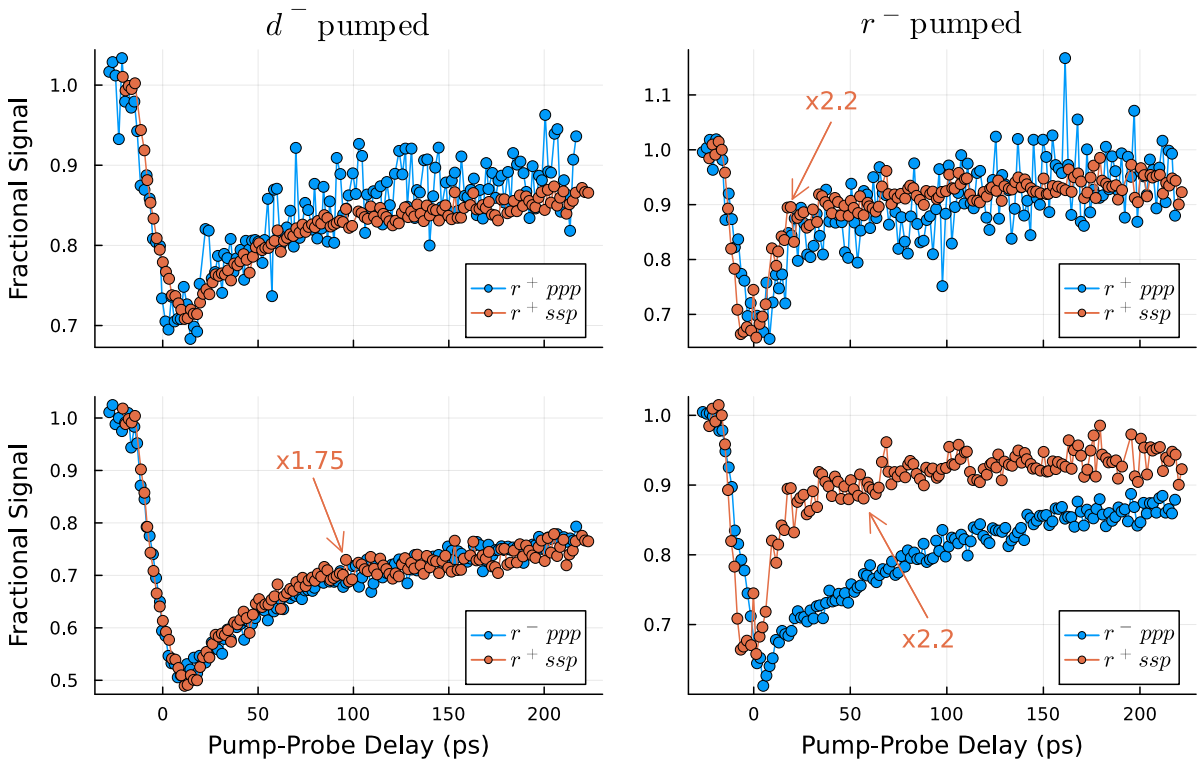

Figure **4-15**: This figure compares the bleaches of different experiments. The left part shows the measurements with the pump laser set to d^- and the right part shows the r^- pumped spectra. The coloured arrows indicate how much a certain dataset is enhanced.

haviour is quite puzzling because r^- is roughly $80\,\mathrm{cm}^{-1}$ higher in energy than r^+ and about $40\,\mathrm{cm}^{-1}$ higher than the pumped d^- mode. This seems counter-intuitive since most of the energy is flowing into the energetically higher mode. Apart from this scaling factor, however, the temporal evolution of the bleaches on r^+ and r^- appear to be very similar.

Now we take a closer look at the r^- pumped experiments. The top right plot of figure **4-15** compares the r^+ mode in both polarisation combinations again. Surprisingly, here we find the *ppp* measurement more than twice as intense as the *ssp* measurement. Since we ruled out a significant effect of the pump power, we have to assume this discrepancy in bleach intensity is due to the alignment of the spatial overlap of the pump laser. With this huge enhancement factor, the two datasets do seem to show similar behaviour as far as we can tell with the noisy *ppp* measurement.

The bottom right plot in figure **4-15** is where it gets interesting. We enhanced the *ssp* measurement by the factor from the plot above to make both experiments comparable. Clearly, the datasets show very different trends even though the intensity of the maximum bleach is comparable after the enhancement. The bleach trend that follows the time profile of the pump laser seems to be reproducible only in the r^+ mode but when observing the same mode that is pumped, we see a unique trend. Initially, the peak bleach seems to

decay similarly fast to the other r^- pumped measurements but instead of following the pump laser profile the redistribution mechanism then transitions to a much slower decay similar to the one in the d^- pumped experiments. We should keep this peculiar behaviour in mind.

Now that we have verified the data and taken a closer look at the transients we are going to propose a model that reproduces our observations.

4.3.2 Reservoirs

Apart from the puzzling r^- resonance when the mode itself is pumped, there seems to be a clear trend in the transients of figure **4-15**: If the d^- mode is pumped, we observe a slower decay into the plateau level. When the pump laser is set to r^-, however, the redistribution mechanism is faster than we can resolve such that the bleach mirrors the temporal profile of our pump laser before plateauing out.

A reasonable explanation for such a behaviour might lie in the amount of CH_2 groups in the molecule. We could define energy reservoirs, that represent the energy contained in the vibrational stretching modes. Since there are 18 methylene groups and just one methyl group, the reservoir for the CH_2 modes necessarily has to be much larger and longer-lasting than the one for the CH_3 modes. So when pumping the d^- mode, we first fill up a larger reservoir and observe a slower recovery than in the r^- pumped case.

To investigate this idea further, we propose a three-temperature model with three energy reservoirs, representing the methyl stretching vibrations, the methylene stretches and a bath that contains the low-frequency deformation modes. These energy reservoirs are illustrated in figure **4-16** (a) with an approximate scale of how large each reservoir is in comparison to one another. According to table **4-1** in section 4.1, we can attribute four stretching vibrations to the methyl reservoir, which we will call R. The methylene groups only feature two stretching vibrations but with the amount of CH_2 modes, we get a total of $2 \cdot 18 = 36$ vibrational modes that are contained in the larger reservoir D. The even larger heat bath is a little more tricky to define because it is hard to say what modes contribute to this reservoir. We can approximate this number, however, by taking all vibrational modes of the methylene groups $3N - 6 = 156$ and subtracting the modes of the D reservoir to get $156 - 36 = 120$. We assume this number is a reasonable approximation to the actual amount of deformation modes that are contained in reservoir B.

Naturally, these reservoirs need to be coupled to exchange energy and exhibit transient change. We decided to go with three distinct coupling parameters a_{RD}, a_{DR} and a_B that represent the energy flow from R $\rightarrow$ D, D $\rightarrow$ R and R/D $\leftrightarrow$ B, respectively. Usually, the more complex a model becomes the more permutations of different parameters lead to the same behaviour. Therefore, our approach is to find a model in a simple, physically reasonable frame and try to fit the simulations to our data within that frame.

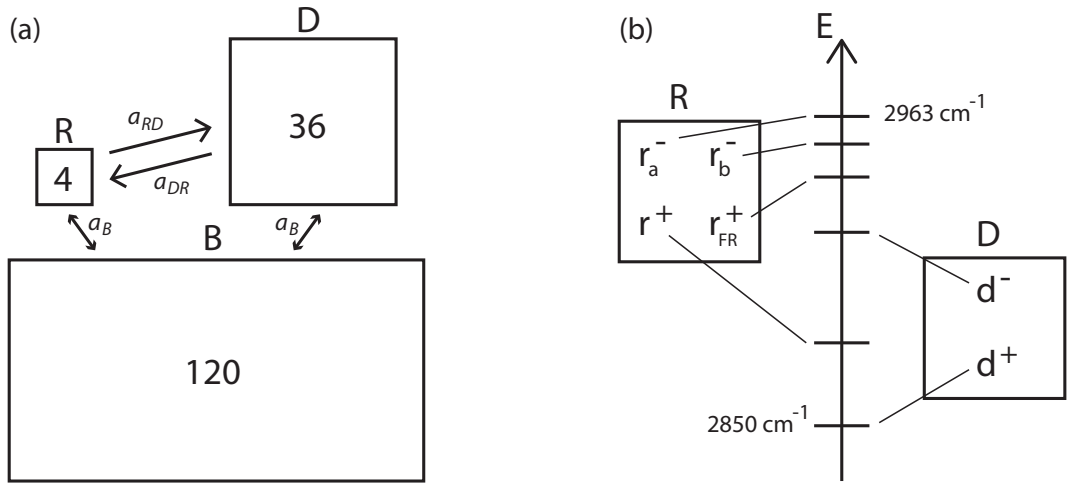

Figure **4-16**: Illustration of the energy reservoirs. Part (a) shows how big the single reservoirs are in comparison to one another due to the number of vibrational modes that are contained within and also their coupling parameters. Part (b) indicates the average vibrational energy of the modes in R and D.

Also, the vibrational modes in R are on average roughly $80\,\mathrm{cm}^{-1}$ higher in energy than the modes in D. This is illustrated in part (b) of figure **4-16**, which shows the vibrational energy level of each mode in the R and D reservoir. The boxes are located at the average vibrational energy of the contained modes. Here, we assumed that the energy flow from R to D is favoured, such that $a_{RD} > a_{DR}$.

Earlier, in section 4.2.1, we claimed that at room temperature there is always a low-energy vibrational available to compensate for the energy mismatch between r^- and d^-. However, this does not seem to hold anymore because it is important to distinguish between a_{RD} and a_{DR} to accurately model the data.

The coupling to the deformation mode, on the other hand, influences the transition into the plateau level and we expect this parameter to be much smaller than the coupling between R and D. Further, even though the coupling of R $\rightarrow$ B and D $\rightarrow$ B is surely not equal, we assume the difference to be sufficiently small such that it can be neglected.

Rationale

With this reservoir model, we are able the explain our observations in the following way:

When pumping the r^- mode, the energy quickly equilibrates between the stretching vibrations of the methyl and methylene groups on a time scale that we cannot resolve. Subsequently, the R and D reservoirs are drained by coupling to the deformation modes. Presumably, this whole process occurs during the arrival of our pump pulse, such that after the pulse is passed there is very little energy left in any single mode and we only observe the plateau level of the heat bath.

When pumping the d^- mode, on the other hand, we fill a much larger reservoir with roughly twice the amount of energy than in the r^- pumped case, according to our RAIR spectrum. There is now an equally fast energy redistribution process between the R and D reservoirs. This time, however, the huge, filled D reservoir dissipates its energy with a $\approx 100\,\mathrm{ps}$ time constant and constantly 'feeds' the R reservoir. This explains the observed slow recovery into the plateau level even after the pump pulse is passed.

4.3.3 Mathematical Defintion

Now that we have introduced our model qualitatively, we will provide a mathematical definition. In the previous subsection, we declared three reservoirs R, D and B that represent the methyl, methylene and deformation modes. We can represent the energy in these reservoirs by

$$E_i = c_i T_i \quad (i = R, D, B), \tag{4.6}$$

with c_i being the heat capacity and T_i being the temperature of the corresponding reservoir. With the heat capacities, we can manipulate how much energy is needed to balance a temperature difference between the reservoirs. Therefore, the heat capacities represent how large each reservoir is and should reflect the number of vibrational modes according to figure **4-16** (a). Consequently, we expect the heat capacities to not deviate much from the ratio $4 : 36 : 120$ for the reservoirs R : D : B.

We further introduced a simple set of coupling parameters a_{RD}, a_{DR} and a_B, according to figure **4-16** (a) that represent the rate constant of the energy flow from R $\rightarrow$ D, D $\rightarrow$ R and R/D $\leftrightarrow$ B. With this setup, we can formulate a set of differential equations that govern the energy flow in our system as

$$\frac{\mathrm{d}T_R}{\mathrm{d}t} = \frac{1}{c_R}\left[-a_{RD}(T_R - T_D) - a_B(T_R - T_B)\right] \tag{4.7}$$

$$\frac{\mathrm{d}T_D}{\mathrm{d}t} = \frac{1}{c_D}\left[2f_{\mathrm{pump}}(t) - a_{DR}(T_D - T_R) - a_B(T_D - T_B)\right] \tag{4.8}$$

$$\frac{\mathrm{d}T_B}{\mathrm{d}t} = \frac{1}{c_B}\left[-a_B(T_D - T_B) - a_B(T_R - T_B)\right] \tag{4.9}$$

for the d^- pumped case and as

$$\frac{\mathrm{d}T_R}{\mathrm{d}t} = \frac{1}{c_R}\left[f_{\mathrm{pump}}(t) - a_{RD}(T_R - T_D) - a_B(T_R - T_B)\right] \tag{4.10}$$

$$\frac{\mathrm{d}T_D}{\mathrm{d}t} = \frac{1}{c_D}\left[-a_{DR}(T_D - T_R) - a_B(T_D - T_B)\right] \tag{4.11}$$

$$\frac{\mathrm{d}T_B}{\mathrm{d}t} = \frac{1}{c_B}\left[-a_B(T_D - T_B) - a_B(T_R - T_B)\right] \tag{4.12}$$

for the r^- pumped case. Note that we enhanced the pump laser input by a factor of 2 in the d^- pumped case because the IR absorption is roughly twice as strong for d^- than it is for r^-, according to the RAIR spectrum of figure **4-6**.

We modelled the pump laser input with a Gaussian temporal profile, such that

$$f_{\mathrm{pump}} = \mathrm{e}^{-\frac{(t-t_0)^2}{\sigma^2}} \quad \text{and} \tag{4.13}$$

$$\sigma = \frac{\mathrm{FWHM}}{2\sqrt{2\ln 2}}. \tag{4.14}$$

Further, we approximated the full width at half maximum of our pump laser by FWHM = 15 ps, according to table **3-2** of section 3.1.2. The offset t_0 represents the point in time when the pump pulse reaches its maximum intensity.

Integrating these differential equations reveals the temperature transients and, hence, the energy content of each reservoir as a function of time. To extract the bleach on r^+ and r^-, we need to figure out how to convert these temperatures to population differences. Naturally, this is where the Boltzmann function comes into play. However, with our simple approach, we only consider a handful of energy levels and disregard most of the lower-frequency skeletal modes. In this abstract system, it is a reasonable approximation to convert the temperatures linearly to populations of the first vibrationally excited levels.

Next, we need to consider how the bleach is inferred from a change in the population of the respective energy levels. The bleach intensity of the R reservoir for example is proportional to the square of the population difference between the ground state and the R state. In other words, the number of available oscillators in the ground state but also the population in the observed state contribute to the bleach signal.

Let us consider a simple three-level system, like the one in figure **4-17**. If we now push a fraction Δ of the oscillators from the ground state into the R state and another part Σ into D, the bleach on R becomes

$$I_{\mathrm{bleach},R} \propto (1 - 2\Delta - \Sigma)^2. \tag{4.15}$$

Note here that Δ contributes twice because the ground state is drained and the R state is populated by Δ at the same time.

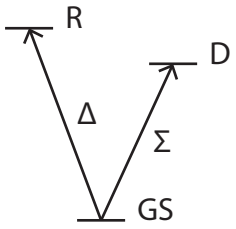

Figure **4-17**: Illustration of an abstract three-level system. The symbols Δ and Σ indicate how much population is transferred from the ground state (GS) to either the R or D level.

With this reasoning, we can now define the bleach on R in terms of the reservoir temperatures, as

$$I_{\text{bleach},R} \propto (1 - k_{\text{vib}}(2T_R + T_D))^2. \tag{4.16}$$

The temperatures T_R and T_D are solutions to the differential equations above in either the d^- or r^- pumped case. For the sake of completeness, we can also calculate the bleach on the D reservoir, such that

$$I_{\text{bleach},D} \propto (1 - k_{\text{vib}}(T_R + 2T_D))^2. \tag{4.17}$$

However, since we are unable to observe the methylene modes properly, we cannot compare this simulation with experimental data.

The experimental constant k_{vib} contains a lot of different information like the inherent characteristics of the vibrational mode but also experimental aspects like pump power and spatial pump pulse alignment. For this reason, k_{vib} can vary strongly between measurements. However, we decided to fix this constant in the d^- and r^- pumped simulations and instead scale the bleach afterwards to fit different datasets. As we have seen in section 4.3.1, this scaling factor can range from 1.1 up to 2.2, depending on the spatial overlap of the pump pulse.

With these tools, we can now find suitable coupling parameters by fitting the simulated data points to our experimental observations. We will tackle this in the next subsection.

4.3.4 Simulation of the Data

Following up on the last subsection, our goal is now to solve the differential equations in 4.7 such that the resulting bleach on the R reservoir, which we defined in equation 4.16 fits the transient trends of the r^+ and r^- modes in our delay scans. We decided to fit the simulations to our *ssp* datasets with the least squares method and then compare the results with the *ppp* spectra.

The final fit parameters are displayed in table **4-3**. Our ambition in this endeavour was to find a good fit to our data with a model that has few but reasonable parameters.

Table **4-3**: Parameters that were used to solve the differential equations in 4.7 such that the extracted bleaches fit the dynamics shown in figure **4-18**. Values in brackets were fixed and not fitted.

Parameter	Value
c_R	$[2\,\mathrm{JK}^{-1}]$
c_D	$[18\,\mathrm{JK}^{-1}]$
c_B	$50\,\mathrm{JK}^{-1}$
a_{DR}	$0.5\,\mathrm{J(K\cdot ps)}^{-1}$
a_{RD}	$0.9\,\mathrm{J(K\cdot ps)}^{-1}$
a_B	$0.2\,\mathrm{J(K\cdot ps)}^{-1}$
k_{vib}	$0.0415\,\mathrm{K}^{-1}$
t_0	$-5\,\mathrm{ps}$

Therefore, we fixed the heat capacities c_R and c_D as 2 J/K and 18 J/K to represent the size of the reservoirs, according to figure **4-16** (a). However, since we cannot be sure about how large the heat bath is, we allowed c_B to deviate slightly from the expected value of 60 J/K. Further, the offset t_0 only shifts the transients along the delay axis but does not influence the shape of the curve. Similarly, the parameter k_{vib} mainly scales the intensity of the bleach and has no significant impact on the dynamics. This leaves us with the three coupling parameters a_{DR}, a_{RD} and a_B that primarily dictate the shape of our curves.

The simulated data are shown in figure **4-18**. The top part shows the temperature of each reservoir R, D and B as a function of the delay between the pump and probe pulse. Across the whole figure, the blue colouring indicates d^- pumped data and orange represents the r^- pumped case. When pumping the smaller R reservoir, we observe a steep incline in R and the energy equilibrates between D and R, such that after the pump pulse is gone, only very little energy remains in any single oscillator. Pumping the larger D reservoir, indicated by the blue curves, we observe a similar but slightly delayed steep incline in the D reservoir. This time, however, energy continues to accumulate in D even after the pump pulse maximum passes because of the slower redistribution mechanism. For the same reason, the R reservoir is constantly fueled by D, such that the dynamics seem much slower than they inherently are.

With these temperature functions, we are now able to calculate the bleach on a single reservoir with equation 4.16. This is illustrated in the middle and bottom parts of figure **4-18**. The middle part shows the transients of the r^+ mode in *ssp* polarisation and the solid lines indicate the simulated bleaches. As mentioned earlier, we decided to keep the parameter k_{vib} fixed in all simulations even though it can vary between measurements. We offset this fluctuation by enhancing the curves afterwards to fit the experimental data.

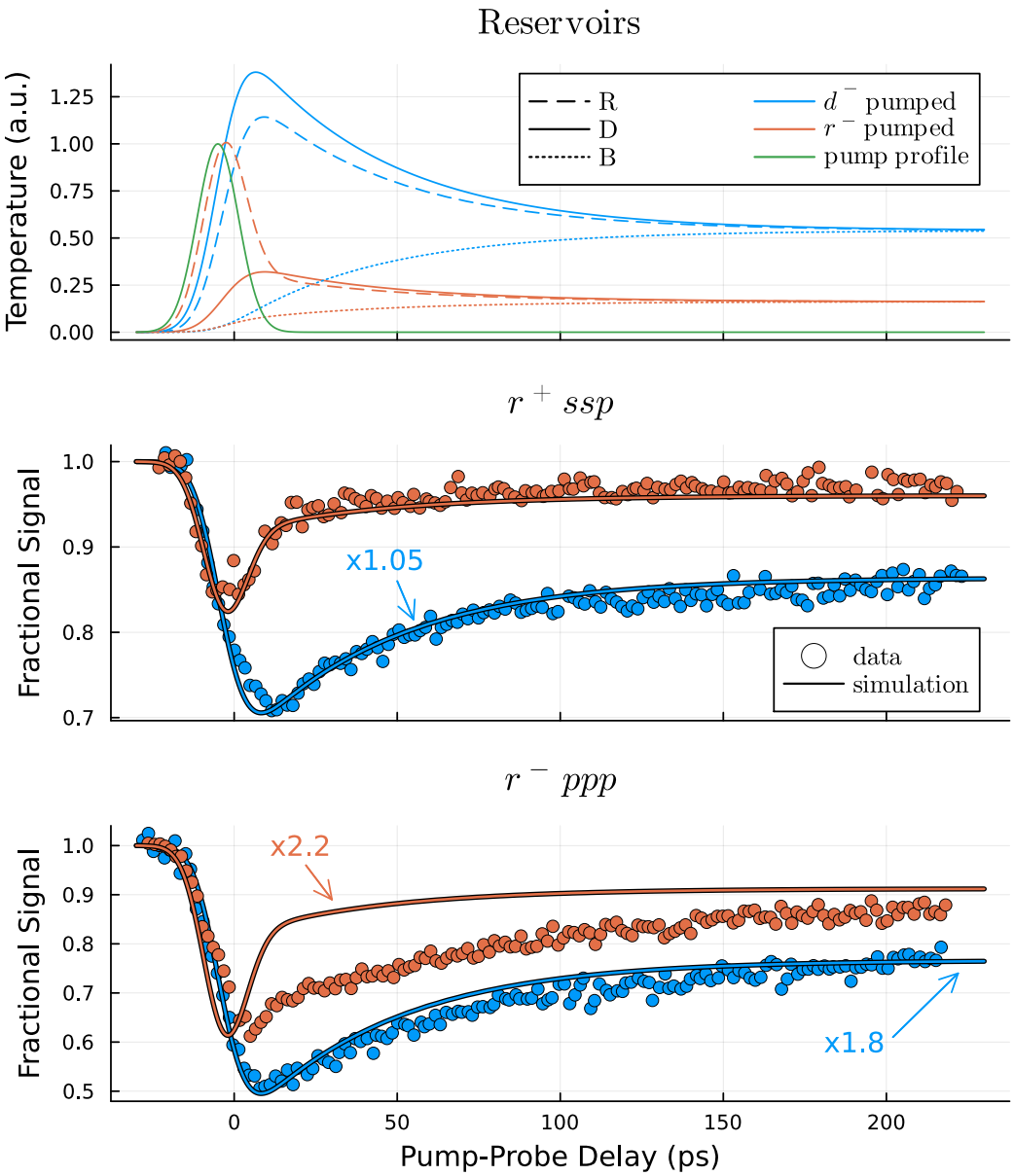

Figure **4-18**: Simulation of the energy flow in the reservoir model. The top part shows the solution of the differential equations in 4.7 with the parameters taken from table **4-3**. The blue and orange colouring indicates d^- and r^- pumped datasets, respectively, across the whole figure. The middle part compares the r^+ mode in *ssp* with the simulated bleaches and the bottom panel shows the same but with the r^- mode in *ppp*. All circles are experimental data and the solid/dotted/dashed lines represent simulations. The arrows show by what factor a simulated bleach is enhanced.

Surprisingly, the model fits very well considering we only fitted more or less three parameters in our simple model that significantly altered the shape of the curves. Furthermore, we previously only had the option to compare two measurements with the same pump wavelength settings. With our model, however, we can now compare a d^- pumped with a r^- pumped measurement and take the enhancement factor as an indicator of how similar the alignment was.

With a small factor of 1.05 in the middle part of figure **4-18**, we can then assume the setup to be almost equal during the measurements. This is interesting because both the maximum intensity and the plateau levels are roughly twice as large for the blue curve than for the orange one. So we can assume that twice as much energy is stored in the system when pumping d^-. This fits very well because the absorption measured in the RAIR spectrum in section 4.2 is also roughly twice as strong for d^-, which strongly supports the temperature model.

The bottom part of figure **4-18** shows the transients of the r^- mode in the *ppp* polarisation experiments. As we have seen before, the trend of the transients when pumping d^- is similar for the r^+ and r^- modes but the intensity is almost twice as strong in r^-. The only aspect our model cannot explain is the puzzling behaviour of the r^- mode when the mode itself is pumped. We enhanced the bleach by the factor taken from figure **4-15**, which does help the peak intensity to approach the maximum in the data. However, the shape of the transient data is clearly not represented by our simulation.

Our model is based on the assumption that there is energy flow from R to D, which is expressed in the coupling parameter a_{RD}. Since the simulation does not fit for r^- when r^- is pumped, the energy exchange necessary has to be different here.

Even though we are not able to explain the peculiar behaviour of the r^- mode, we decided to adhere to the basic idea of our model because it fits the rest of the data very well. We will note, however, that the model is quite obviously not perfect and should be extended in future works in order to better explain the energy flow through the r^- channel.

4.3.5 Summary

We learned many interesting things in this important and quite complex section. To recap, we first validated the trends of our delay scan experiments by comparing the already presented data with a repetition of the same experiments roughly half a year later. Secondly, we introduced a three-temperature model in an attempt to explain the energy flow dynamics in our system. We then fitted the parameters in our simulation to match the observed transients. Finally, we will summarise the most important insights we gained in each of these steps to conclude this section.

Validation of the data

1. Comparing the already presented delay scans with a repetition of the same experiments we were able to reproduce the trend of each bleach surprisingly well.

2. The maximum bleach intensity, on the other hand, could vary between measurements up to almost twice the amount.

3. We further found that this huge difference in pump strengths significantly depends on the spatial alignments of the pump pulse and the pump power only played a subordinate role in that regard.

4. Lastly, we confirmed how the shape of the bleach on the same mode in *ssp* and *ppp* is similar if the pump laser settings are comparable.

Introducing Reservoirs

1. We introduced a three-temperature model with the reservoirs R, D and B, which represent all of the methyl, methylene and lower-frequency deformation modes, respectively.

2. Further, we set the heat capacities to values that correspond to the number of vibrational modes in each reservoir to manipulate how large each reservoir is.

3. As a final step, we then formulated a set of differential equations for the d^- pumped case and one for the r^- pumped case that dictates the transient temperature change in each reservoir. Solving these equations with the proper parameters will then reveal the energy flow dynamics in our system.

Simulation of the Data

1. We chose to simulate our data with a simple model that depends on very few variables. This approach is reasonable because a very complex model might fit the data better but can also lead to multiple sets of parameters that all fit the data similarly well. Therefore, if we can explain our data with a simple model, we can be sure to understand the underlying, fundamental physical mechanism.

2. For this reason, we fixed the heat capacities $c_R = 2$ and $c_D = 18$, according to the number of vibrational modes in the corresponding reservoir. Because we were not sure about the size of the heat bath, however, we allowed c_B to vary slightly from the expected value of 60.

3. Apart from the slight variation of c_B, the only parameters that significantly change the shape of the transients are the coupling parameters a_{DR}, a_{RD} and a_B.

4. We found suitable coupling parameters by solving the differential equations, extracting the bleach on the R reservoir from the resulting temperatures and fitting these simulations to our experimental data. These parameters are: $a_{DR} = 0.5\,\mathrm{J(K \cdot ps)^{-1}}$, $a_{RD} = 0.9\,\mathrm{J(K \cdot ps)^{-1}}$ and $a_B = 0.2\,\mathrm{J(K \cdot ps)^{-1}}$. All parameters are listed in table **4-3**.

5. With our simple model of more or less three significant parameters we found a surprisingly good fit for the *ssp* polarised experiments. In *ppp*, however, only the d^- pumped transients could be explained with the simulation. The r^- mode, when the mode itself is pumped shows a very puzzling transient that we were not able to explain.

This concludes the introduction of the three-temperature model and its significance to our experimental data. As a next step, we will now extend the analysis of our molecular systems by studying one with a different monolayer density and we also deuterate a number of the CH_2 groups. With this, we hope that the energy flow in the monolayer is significantly altered, allowing us to learn even more about the properties of our molecules. We will tackle this question in the next section.

4.4 Extending the System

With the temperature model, we now have a good idea about the general energy flow in our molecular system. However, we still want to learn more about the actual anharmonic coupling mechanism. Specifically, the role of intermolecular energy exchange is still mostly unknown. To this end, we decided to prepare the Langmuir-Blodgett films with different surface pressures, according to the isotherm plot in figure **3-12**. By reducing the surface pressure and forcing the monolayer into different phases, we hope to significantly alter the intermolecular coupling and learn more about how the energy is redistributed. The results are shown in the first subsection. In the second subsection, we investigate a deuterated version of our calcium arachidate molecules. Specifically, by deuterating two of the CH_2 links, we aim to hinder the energy exchange between the R to the D reservoir and reveal more information about the intramolecular coupling. In the third subsection, we will combine the two approaches by preparing a deuterated calcium arachidate film with low surface pressure. The last subsection summarises our findings.

4.4.1 Monolayer Density

In this subsection, we will investigate a slightly different version of our calcium arachidate films. Up till now, we have only investigated films that were prepared with the specific surface pressure of 32 mN/m (millinewton per meter) to ensure that we have a well-ordered monolayer. By reducing the surface pressure in the Langmuir-Blodgett trough

during deployment, we necessarily end up with a less dense monolayer. Furthermore, if we decrease the surface pressure sufficiently the film even undergoes a phase transition to a less ordered state, as we have explained in section 3.3.1.

Therefore, we decided to investigate two scenarios:

1. We will decrease the surface pressure slightly to 25 mN/m. This guarantees that the monolayer is still in the highly stable LS phase but is less dense.

2. We reduce the pressure to 13 mN/m during deployment, which forces the monolayer into the less ordered LC phase.

Even though we deem it necessary to consider the reproducibility of our data, we want to restrict this section to the relevant plots. For this reason, we decided to simply claim at this point that the data are reproducible and refer the reader to figure **A-1** and **A-2** in appendix A. Furthermore, because there was no visible change in the wavelength scan spectra for different densities, we decided to forego the presentation of the static experiments and focus on the transient data.

25 mN/m Films

We begin by presenting the results for the 25 mN/m films. Figure **4-19** shows the bleach on the most prominent modes in *ssp* and *ppp* spectra for the d^- and r^- pumped case for the 25 mN/m films. The transients we see here are very similar to the 32 mN/m case presented in figure **4-9** of section 4.2.2. Unfortunately, the exponential fit with equation 4.5 reveals lifetimes that, taking the experimental error into account, indicate the same dynamics as in the denser monolayer. If there is a difference in the energy flow due to the density of the monolayer, it is smaller than the experimental error allows us to resolve.

More interesting are the plots in figure **4-20**. Here, we compare the bleaches of different experiments but with the same molecular system, like we did in figure **4-15**. As expected, the transient trend of the r^+ modes in *ssp* and *ppp* is reproducible here as well. Comparing the r^+ and the r^- mode, however, yields a different result as in the 32 mN/m pressure films. For the r^- pumped case in the bottom right plot, the transients differ significantly, which is something that we have also seen before. But now the d^- pumped spectra also show very different shapes. This is the first indicator of significant change in the dynamics and we will investigate this further after we present the 13 mN/m results.

Taking a closer look at the strength of the pump effect, we found the bleach on r^- to be stronger by a factor of 1.75 than on r^+, when pumping the d^- mode in the 32 mN/m films. This seems to be reproducible here, as we find a factor of $1.5 \cdot 1.2 = 1.8$ when comparing the top and bottom left plots of figure **4-20**. Note, that the bleach on r^+ should be equal in *ssp* and *ppp*, so the scaling factor of 1.5 in the top left plot comes about due to experimental alignment differences.

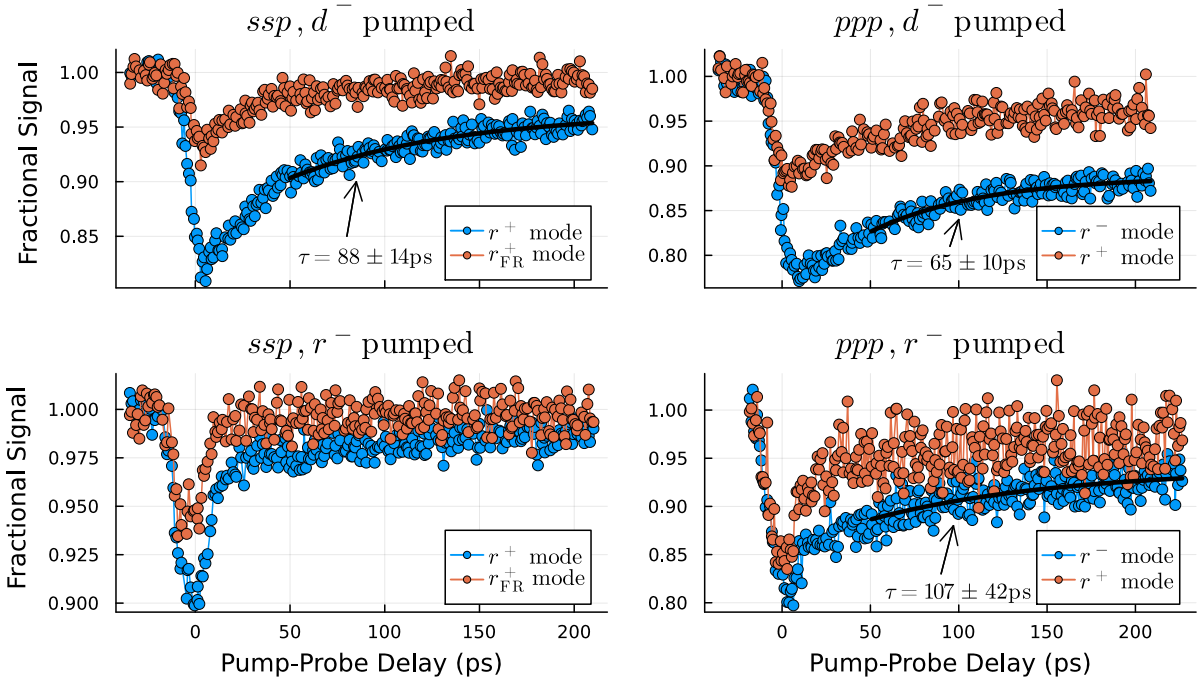

Figure **4-19**: Similarly to figure **4-9**, this figure shows the bleach on the most prominent modes in *ssp* and *ppp* with d^- and r^- pumped but for a 25 mN/m film sample. The black lines indicate lifetime fits to the data, according to equation 4.5.

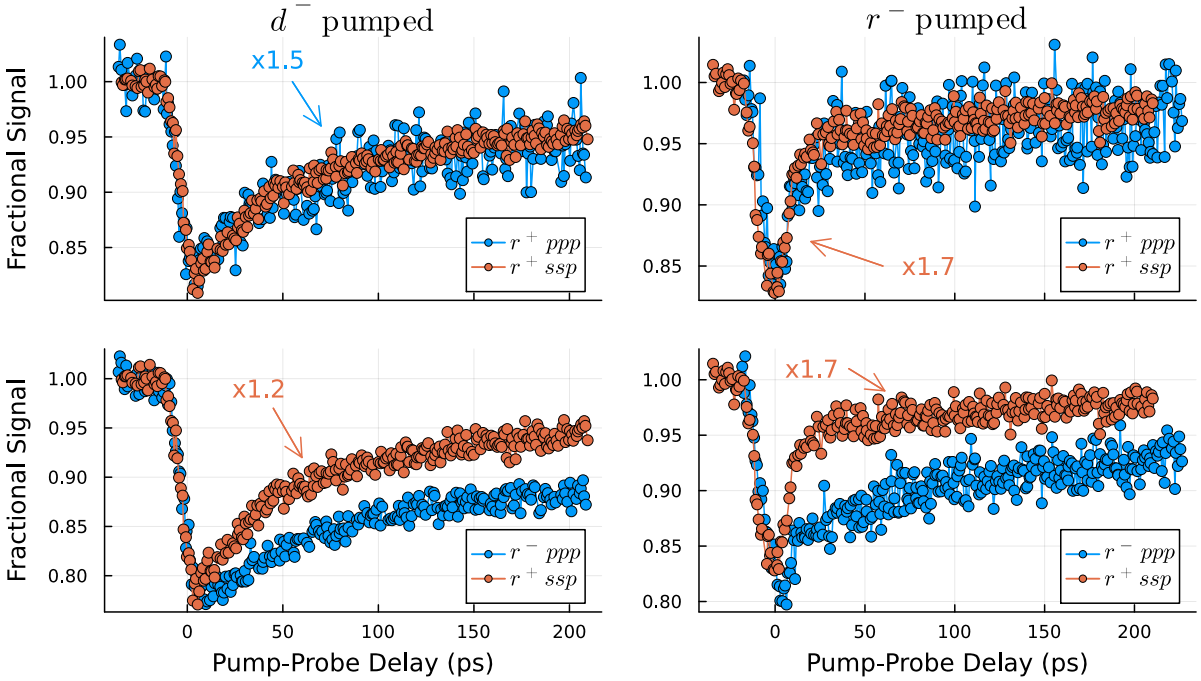

Figure **4-20**: This figure compares the transients of different experiments of the same molecular system, similarly to figure **4-15** but for 25 mN/m surface pressure monolayers.

13 mN/m Films

Turning our attention to the less-ordered 13 mN/m films, we will briefly cover the same plots as for the 25 mN/m case above. Figure **4-21** shows bleaches on the most prominent modes and, again, the exponential fits suggest very similar lifetimes as the denser monolayers. Unfortunately, it seems like we are unable to significantly alter the population decay from the R/D reservoir into the skeletal modes or at least are unable to resolve it properly. However, taking a closer look at the bottom right plot, the puzzling behaviour of the r^- mode when it is itself pumped seems to also be visible in the r^+ mode. Even though the r^+ data are quite noisy, there is a clear trend that we did not observe in the denser films and we will investigate this further at the end of this subsection.

Before we come to that, however, we are going to complete the introduction of the 13 mN/m films by comparing the bleaches of different experiments and the same density with one another. These are compiled in figure **4-22**. Looking at the top left plot, we can properly match the bleach on r^+ in the *ssp* and *ppp* experiments by enhancing the *ppp* measurement, which is something that should always be possible. More puzzling then is the plot in the top right, which seems to show different transients for the r^+ mode in *ssp* and *ppp*, when pumping r^-. Needless to say, the *ppp* data are quite noisy but even then we can hardly argue for similar dynamics in both experiments. Furthermore, the bottom left plot shows a similar discrepancy as in the 25 mN/m case above.

Comparing the bleach strengths again, we find that it is stronger on r^- by a factor of $1.2 \cdot 1.6 = 1.92$ than on r^+ for the 13 mN/m films. This aligns quite well with the other factors of 1.75 and 1.8 for the 32 mN/m and 25 mN/m films, respectively. It is, however, difficult to say if the increasing factor does in fact correlate with the density or comes about due to experimental error. Nevertheless, the general magnitude of roughly twice the bleach intensity in r^- compared to r^+ is reproducible.

Density Comparison

Now that we have introduced the results for our 25 mN/m and 13 mN/m films separately, we are going to compare all three systems to one another. Figure **4-23** shows the bleaches on the most prominent mode in each experiment for every investigated monolayer density.

Surprisingly, the transients of the r^- pumped experiments in the bottom part seem to not change at all with decreasing monolayer density. There is, of course, some variation in the data but this can likely be attributed to experimental error. The only significant differences are visible in the transients of the r^+ mode when pumping d^-. Interestingly, this behaviour seems to be exclusive to the r^+ mode as we cannot observe a similar trend for the r^- mode in the *ppp* experiments.

To investigate this aspect further, we will take a closer look at the r^+ mode when pumping d^- in both *ssp* and *ppp*. This is illustrated in figure **4-24**. The left part shows the r^+ mode observed in *ssp* and on the right are the much noisier *ppp* measurements

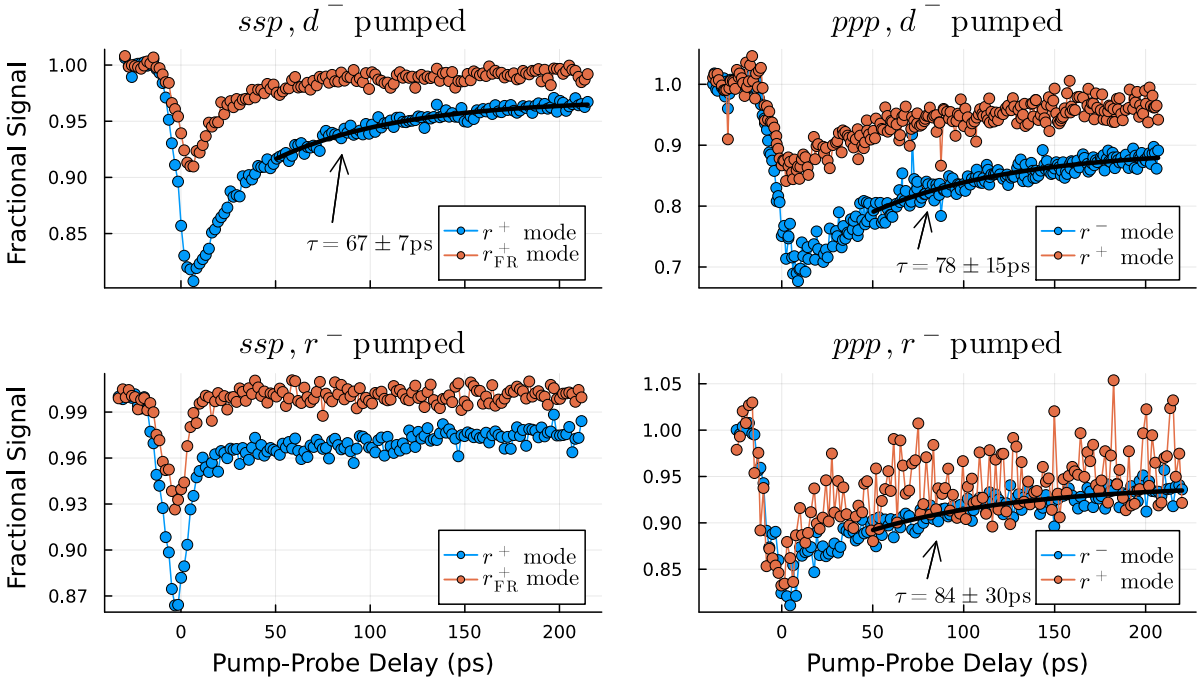

Figure **4-21**: Like the experiments in **4-19**, this figure also shows the bleach on the most prominent modes in *ssp* and *ppp* with d^- and r^- pumped but with the less-ordered 13 mN/m films.

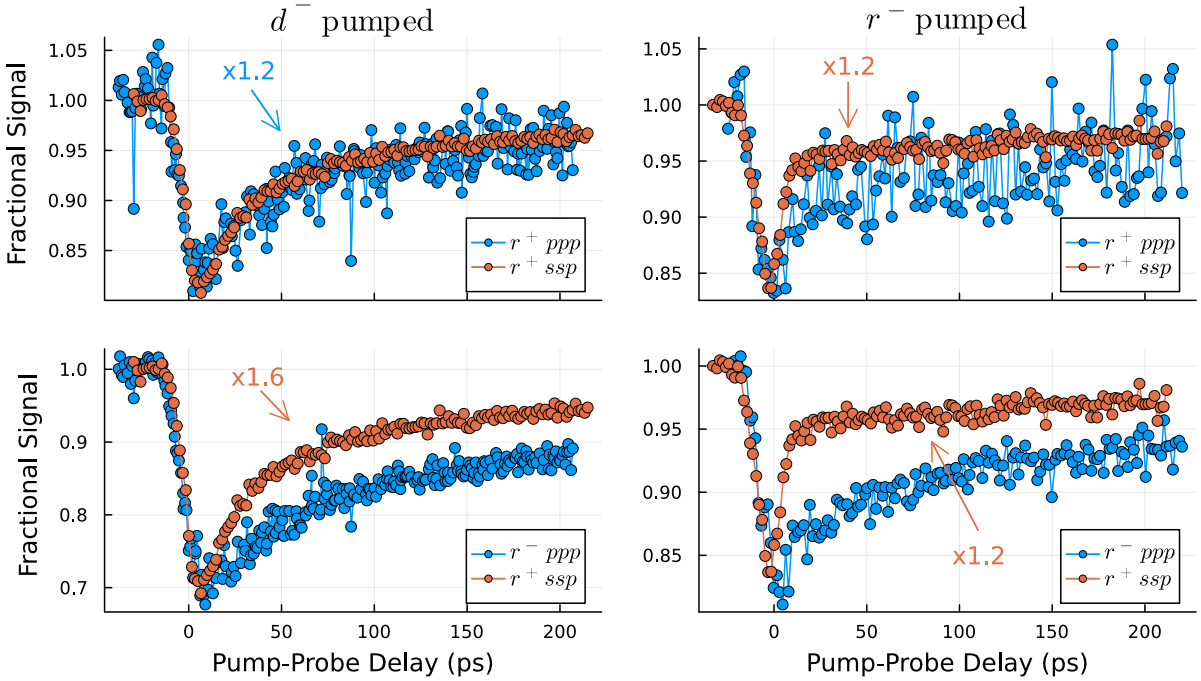

Figure **4-22**: Like the experiments in **4-20**, this figure compares the transients of different experiments of the same molecular system but with the less-ordered 13 mN/m films.

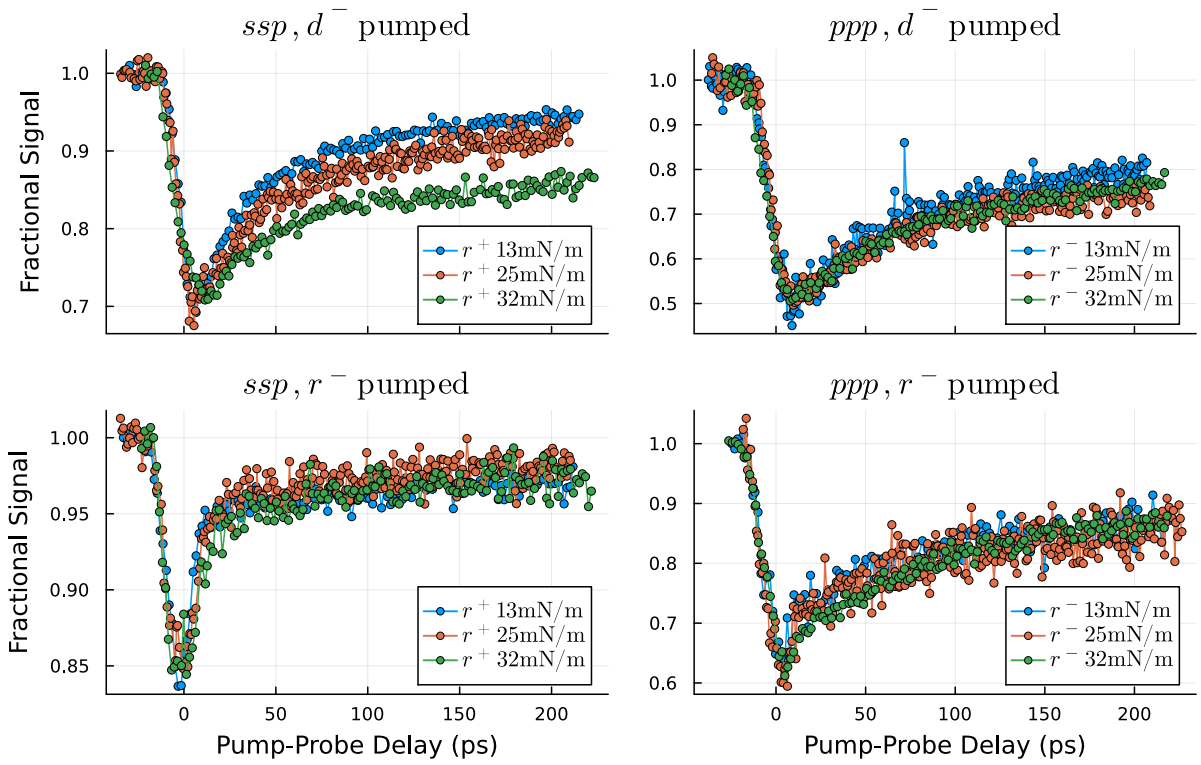

Figure **4-23**: This figure shows the bleach on the most prominent mode in every experimental setup for different film pressures during deployment. On the left are the transients of the r^+ mode and r^- is displayed on the right.

presented. In an attempt to improve the noisy *ppp* measurement, we reduced the number of data points by averaging every three points. Even though this helps to a certain degree, the effect that we observed on the left side is barely reproducible here. We could argue that the trend is similar, i.e. transients of the less dense monolayers show a plateau level that corresponds to smaller bleaches, but the effect is certainly much weaker in the *ppp* measurement.

Several possible scenarios can explain the trends in the left plot of figure **4-24**. For example, the orientation of the alkyl chain is presumably slightly altered in the less dense monolayers. Consequently, the dipole moment of the CH_2 links is also slightly different and might not align quite as well anymore with the polarisation of the pump beam. This will necessarily reduce the overall energy that the monolayer can absorb, thus explaining the lower plateau level in the films with less density.

On the other hand, this argumentation should also lead to a reduced maximum bleach intensity, which is hard to track because of experimental alignment. Another possible explanation that is independent of the maximum bleach intensity but explains the different plateau levels is the following:

In the denser monolayers, the alkyl chains are pressed together very tightly such that

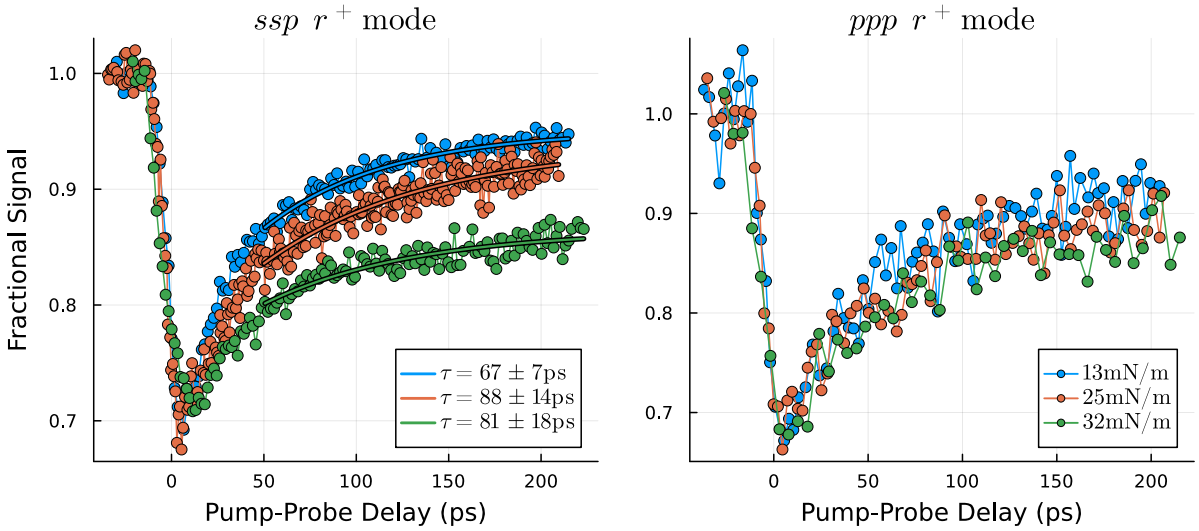

Figure **4-24**: The left part shows the bleach on the r^+ mode observed in *ssp* polarisation for different monolayer densities. The solid lines indicate lifetime fits according to equation 4.5. On the right are the transients of the r^+ mode observed in the *ppp* polarisation combination. And every three data points are averaged to reduce noise. All plots show experiments with the pump laser tuned to d^-. Both legends apply to both plots.

the skeletal modes have very little freedom. When we reduce the surface pressure during deployment of the other films, we increase this freedom such that it becomes 'easier' for the energy to flow into these lower deformation modes. This would fit quite well with the left plot of figure **4-24** because in the denser films, the plateau level of the slow component is higher such that more of the energy is stuck in the r^+ mode.

However, neither the orientation of the alkyl chains nor the increased freedom of the skeletal modes are limited to the *ssp* polarisation experiments. With these arguments, we should then be able to reproduce the transients in the left plot of figure **4-24** also on the right side, which we do not. Therefore, we have to assume that these ideas are only part of the truth at best and that the real mechanism is more complex. We have not yet found an answer to this curious behaviour but we have to presume a process that is not only exclusive to the r^+ mode but to the *ssp* polarisation combination as well.

4.4.2 Isotopologues

In this subsection, we will investigate the effects of deuteration in our arachidate chains. To this end, we prepared another batch of samples with an arachidate isotopologue, namely arachidic-17,17,18,18-d4 acid ($CH_3CH_2(CD_2)_2(CH_2)_{15}COOH$). Deuteration is the process of exchanging a hydrogen atom with a deuterium atom in a molecule. A deuterium atom has a single electron and proton, just like the hydrogen atom but also an additional

neutron in its nucleus. Because the number of electrons stays the same, most of the chemical reactivity is unchanged when deuterating a molecule. However, since the nucleus is now twice as heavy, the resonance frequencies are much lower than in the original system ($\propto \frac{1}{\sqrt{2}}$), as we have already seen in the IR spectra in figure **4-1**.

Additionally, the IR spectrum of the deuterated species in figure **4-1** shows how the resonance frequencies of the methyl and methylene groups stay roughly the same. So we can expect the sum-frequency spectrum of the deuterated monolayers to also not deviate much from the original one. The intramolecular energy flow, on the other hand, is something that we expect to change. By introducing a sort of 'anchor' into the chain due to the deuteration, we anticipate the energy exchange between the CH_3 and CH_2 modes to be slowed down.

As in the previous subsection, we are going to claim here that the presented transients of the deuterated molecules are reproducible and refer to figure **A-3** in appendix A. Furthermore, we will primarily focus on the transient data for the deuterated molecules, as well.

Continuing the approach of the previous section, we will briefly show slices through the two-dimensional difference spectrum centred at the most prominent modes of each experiment. After that, we compare the bleaches of different experiments with one another and finally evaluate similarities and differences between the data for the deuterated molecules and the original ones. We begin with the bleaches on the most prominent modes in each experimental setup.

Figure **4-25** shows slices through the two-dimensional delay scan data of the deuterated 32 mN/m monolayers, centred at the most prominent modes of each experiment and averaged over a range of $\approx 10\,\mathrm{cm}^{-1}$. In addition, the transients are fitted with equation 4.5 between $50 - 230$ ps to encompass the transition into the plateau niveau. At first glance, the data seem to show no surprising or special trends. Unfortunately, the lifetime fits all show the same dynamics within their respective errors and do not deviate much from the lifetimes that we found in earlier sections. Hence, there does not seem to be a significant effect on the energy flow in our molecules due to the deuteration or at least we are not sensitive enough to observe it.

Moving on from the evaluation of every experiment separately, we will now compare the transients of different experiments with one another, as we have done in the previous sections. The top part of figure **4-26** shows the bleach on the r^+ mode in both *ssp* and *ppp* with both pump laser settings. The bottom plots of the same figure then compare the transients of r^+ and r^-.

Similar to the other experiments, we can reproduce the shape of the bleach on r^+ quite well in both the *ssp* and *ppp* polarisation combinations. Looking at the bottom part of figure **4-26**, however, we find a significant discrepancy between the bleach on r^+ and r^- when pumping d^-. This is something that was not visible in the 32 mN/m film with our original arachidate molecules but rather a feature of the 25 mN/m and 13 mN/m films.

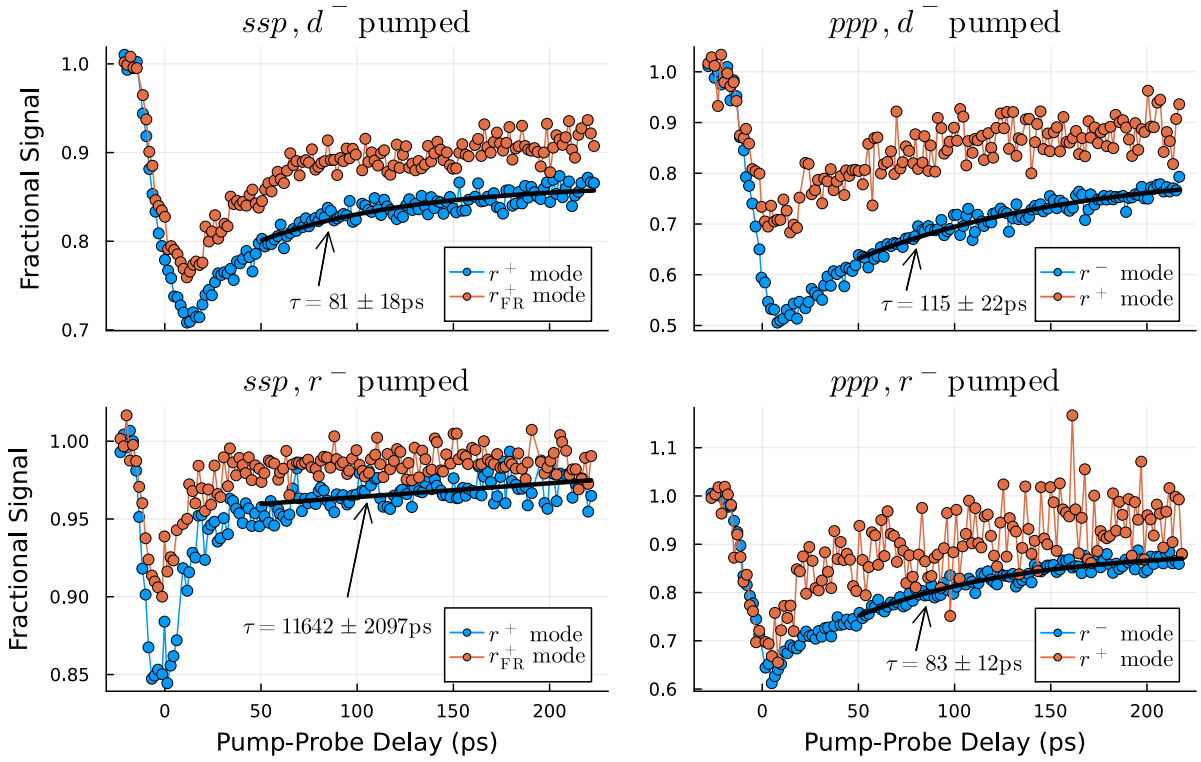

Figure **4-25**: Similar to figures **4-21** and **4-19** of the previous subsection, this figure shows the bleach on the most prominent modes in *ssp* and *ppp* with d^- and r^- pumped but for a deuterated 32 mN/m monolayer.

We should note here, however, that the transients in the *ppp*, d^- pumped spectra were tricky to reproduce and show a slightly different trend in the repeated experiments (see figure **A-3** in appendix A). So we should keep the bottom left plot of figure **4-26** in mind but treat it with caution.

Furthermore, in the previous sections, we found that the bleach on r^- is almost twice as strong as on r^+ when pumping the d^- mode. For the deuterated molecules, we find a factor of 1.95 in the bottom left plot. However, both experiments did not have a similar alignment as we can see in the factor of 1.35 in the top left plot. So evidently, we have to divide 1.95 by the experimental alignment factor 1.35. Finally, we find that the bleach on r^- is stronger by $1.95/1.35 = 1.45$ than on r^+ when pumping d^-. This quite significant difference from ≈ 2 seems to be a result of the deuteration.

Isotopologue Comparison

Finally, figure **4-27** shows the most prominent mode in every experiment for the 32 mN/m films of the original arachidate molecule and its deuterated isotopologue. As we have seen earlier, the population lifetimes are very similar for the deuterated species so we do expect

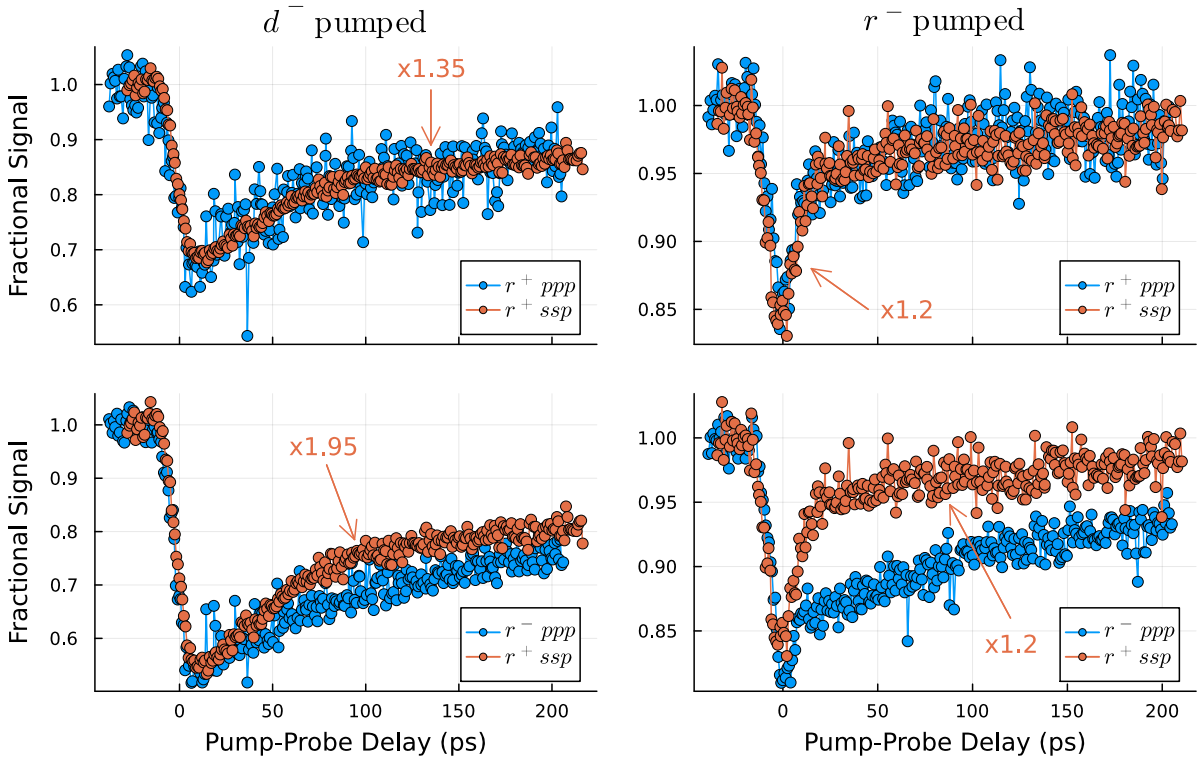

Figure **4-26**: Similar to figures **4-20** and **4-22** of the previous subsection, this figure compares the transients of different experiments of the same molecular system but for the deuterated 32 mN/m films.

very similar shapes of the transient data. Looking at the comparison between the original and the deuterated molecules, this is evidently the case. Unfortunately, this also means that the effect of the deuteration on the energy flow is not as significant as we had hoped.

However, there is one thing we can learn here. Taking a closer look at the 'lift-off' point, i.e. the delay position at which the system leaves equilibrium, we see a different trend for the d^- pumped case than for r^-. In the top plots of figure **4-27** the blue curves seem to lift off a little later than the orange ones, which is not observed in the r^- pumped plots at the bottom. This is interesting because if we indeed slow down the coupling between the R and D modes with the deuteration, we should expect a different behaviour when pumping d^- or r^-. However, the lift-off point should stay the same, because we immediately deplete the ground state when the pump pulse hits. It is the maximum bleach that should instead shift to longer delays when we hinder the coupling mechanism. Surprisingly, we do not observe such a shift in the maximum bleach here.

Although the effect is quite small with a shift of roughly ≈ 3 ps, it does seem to be attributed to the deuterated links. One could argue that the deuteration experiments were performed on a different day and the experimental setup might have been slightly off, resulting in a shorter pump pulse. This could explain the observed shift but it would

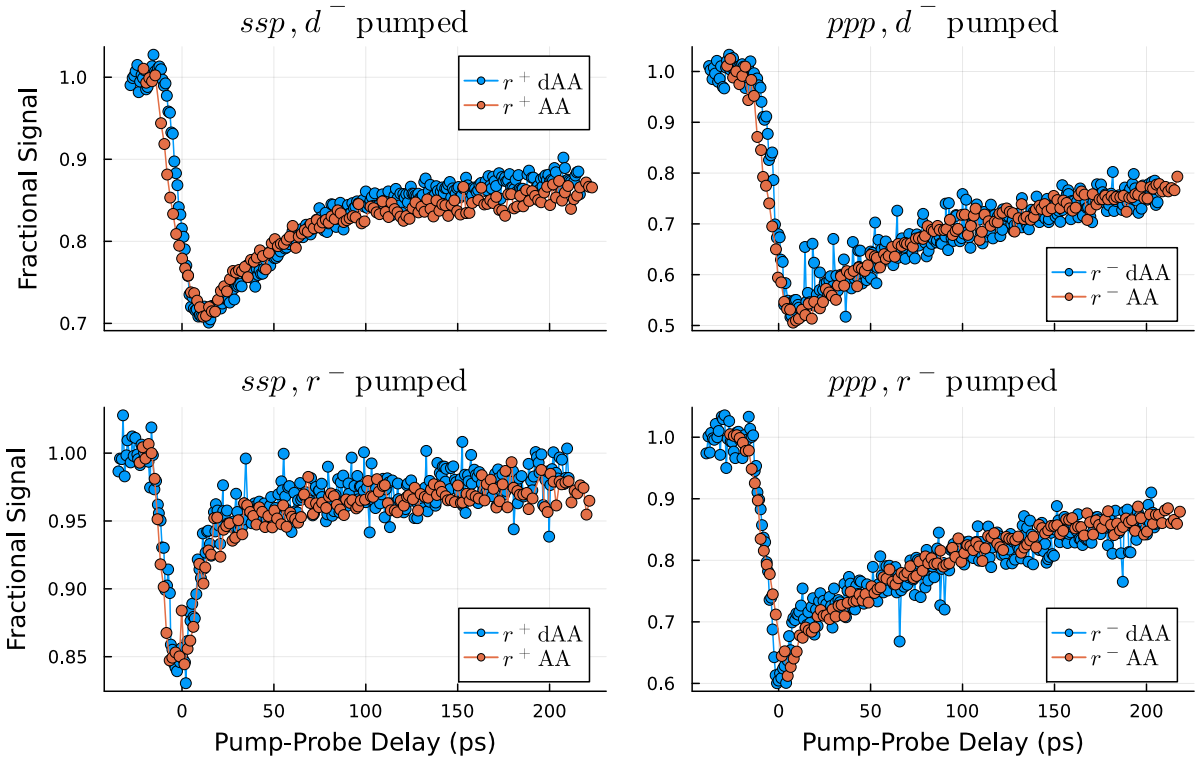

Figure **4-27**: This figure shows the bleaches on the most prominent mode in every experiment of the original arachidic acid (AA) monolayers and the deuterated version (dAA).

not explain why we only observe this phenomenon for the d^- pumped spectra.

4.4.3 Combining Both Approaches

Unfortunately, neither the monolayer density nor a partial deuteration of the arachidate chains yielded a sufficiently strong effect on the energy redistribution mechanism of our monolayers. In a last attempt, we are going to investigate if a combination of the two approaches gives rise to additional features in the transient data. Therefore, the last system that we will introduce in this thesis is a deuterated arachidate monolayer at a surface pressure of 13 mN/m during deployment.

Contrary to the other experiments, we were not able to make enough decent measurements of this molecular system to validate the shape of the transients. This is partly because of the time frame in the last stages of the PhD work. Mainly, however, it was very difficult to generate decent data because the 13 mN/m films are less ordered in general and keeping a good overlap for several hours was a little more tricky. We are confident, however, that the data we are going to present can be trusted to a sufficient degree.

As per usual, we begin with the inspection of every experiment separately. Figure **4-28** shows the most prominent modes of every experimental setup and lifetime fits according

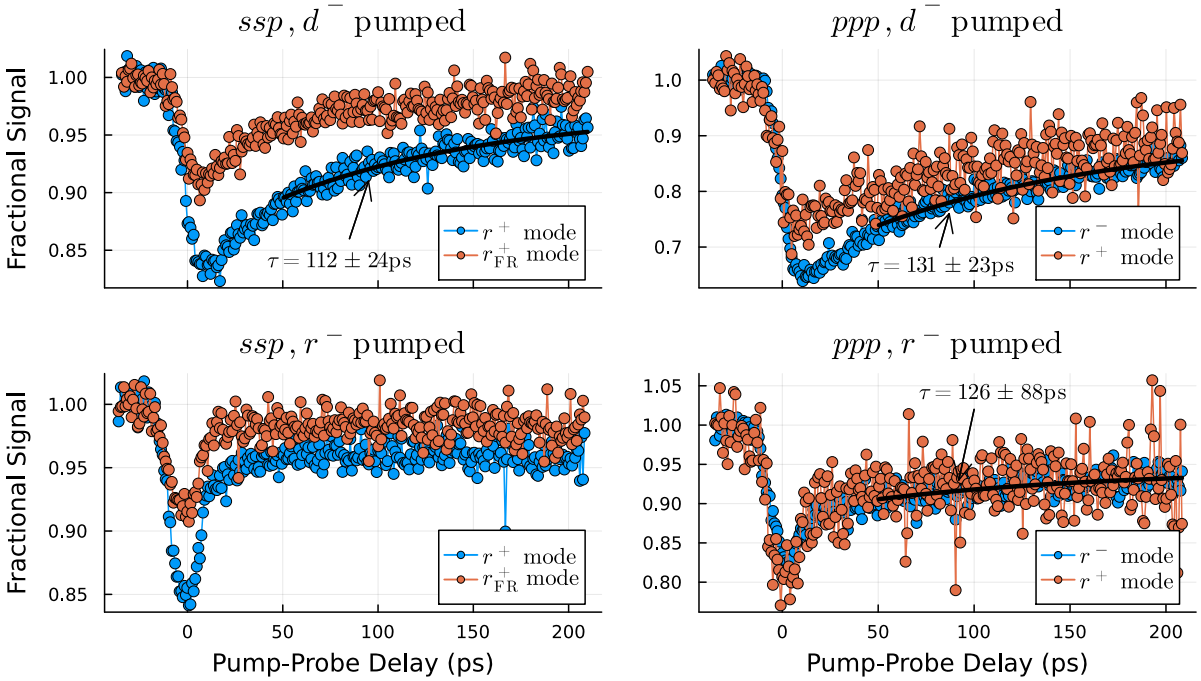

Figure **4-28**: Similar to figure **4-25** of the previous subsection, this figure shows the bleach on the most prominent modes in *ssp* and *ppp* with d^- and r^- pumped but for a deuterated 13 mN/m monolayer.

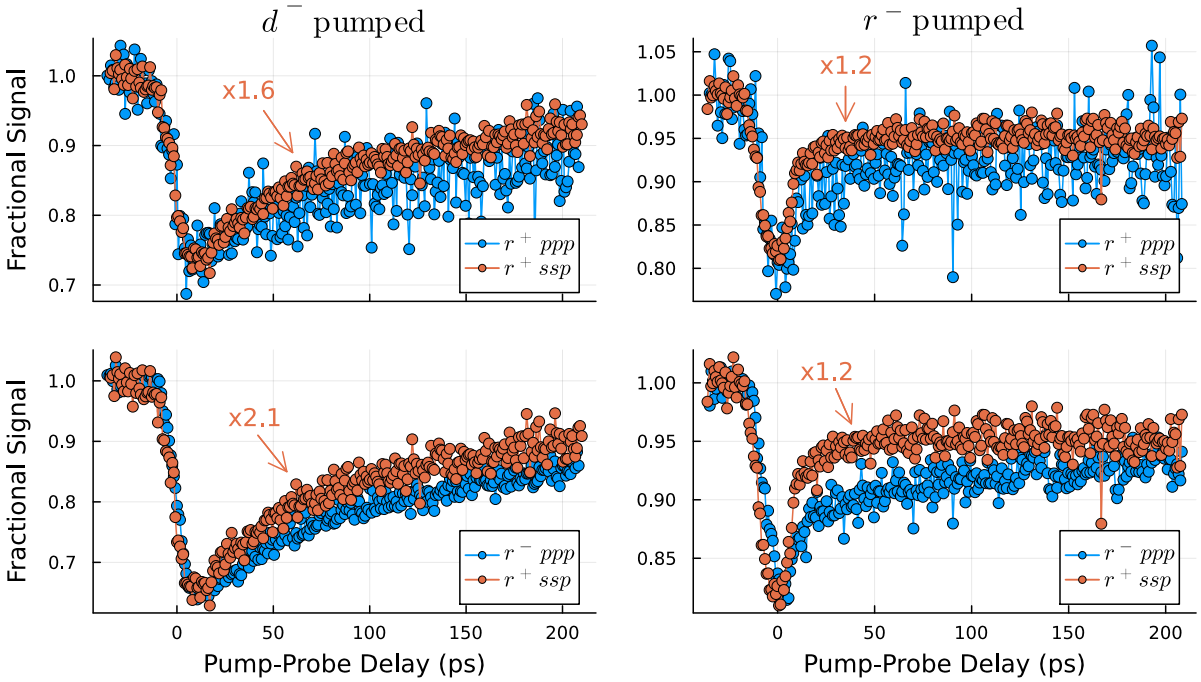

Figure **4-29**: Similar to figure **4-26**, this figure compares the transients of different experiments of the same molecular system but for the deuterated 13 mN/m films.

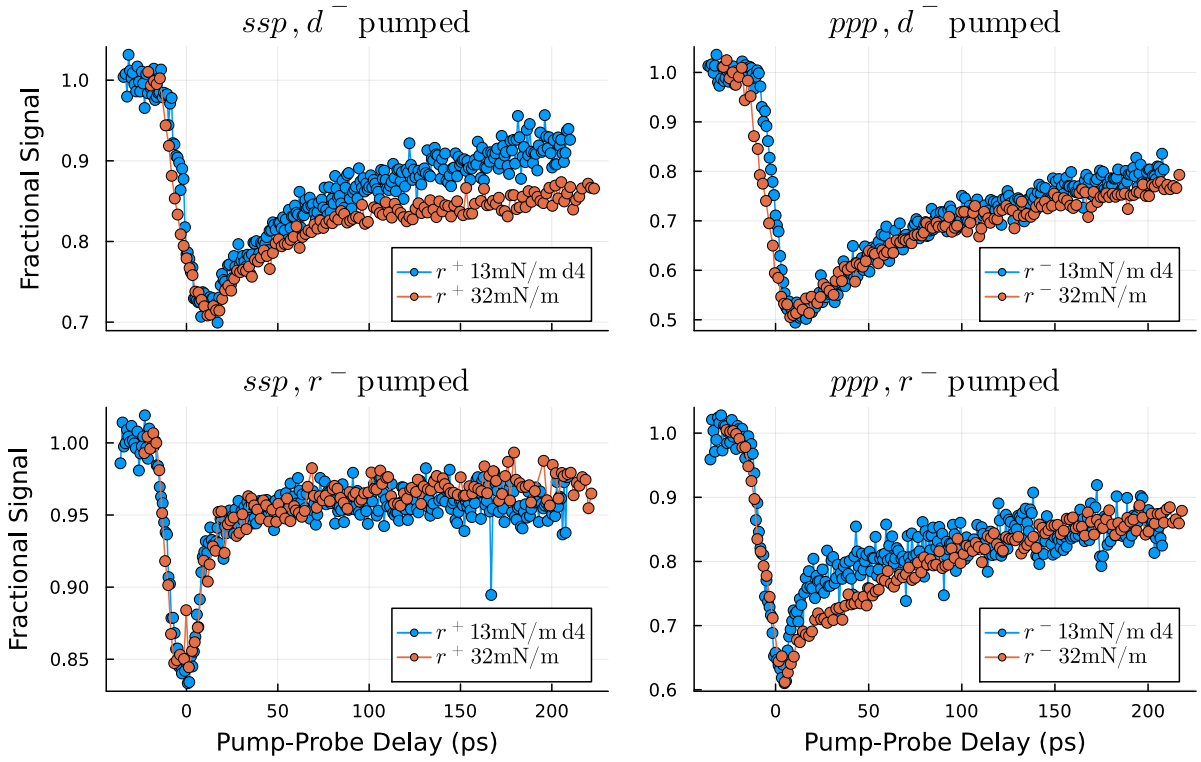

Figure **4-30**: This figure shows the most prominent mode in each experiment and compares the original 32 mN/m films with the deuterated and less dense 13 mN/m monolayers.

to equation 4.5. Interestingly, the lifetimes here indicate a slower redistribution with all fits resulting in values > 100 ps. The experimental error, however, is also significantly larger than in the experiments of other sections due to the more noisy measurements in general. So even though we should treat this result with caution, this is the first strong indicator of a significant change in the dynamics of our monolayers.

Coming to the comparison of different experiments of the same system to one another, figure **4-29** shows the transients of the 13 mN/m films with the deuterated molecules. The bleach on the r^+ mode is more or less reproducible, even though the *ppp* measurements are quite noisy. The bottom left plot also shows an offset in the plateau level, similar to the previous measurements with less dense monolayers. Furthermore, we found that the bleach on r^- is stronger than on r^+ by a factor of 1.45 for the deuterated 32 mN/m. Here, we find a similar small factor of $2.1/1.6 = 1.3$ compared to the factor of ≈ 2 for the original molecules. Hence, we have another indicator that the relative bleach strength on r^+ and r^- when pumping d^- is indeed influenced by the deuteration.

Lastly, figure **4-30** compares the transients of the original 32 mN/m films with the deuterated 13 mN/m monolayers. Here, we find some interesting things. First of all, the slight delay shift in the d^- pumped spectra for the deuterated molecules is evident here as well. This is a strong indicator that this effect can indeed be attributed to the

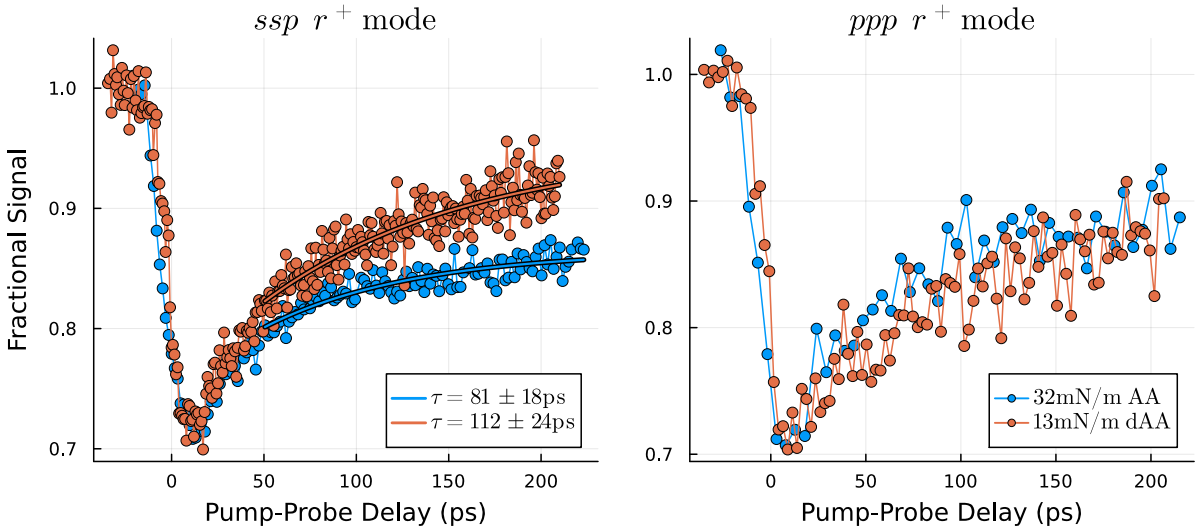

Figure **4-31**: The left part shows the bleach on the r^+ mode in *ssp* for the original 32 mN/m films and the deuterated 13 mN/m monolayers. The solid lines indicate lifetime fits according to equation 4.5. On the right are the transients of the r^+ mode in the *ppp* polarisation combination and every three data points are averaged to reduce noise. All plots show experiments with the pump laser set to d^-.

deuteration. Secondly, the top left plot shows a relaxation to a different plateau level for the deuterated 13 mN/m films. We saw a similar effect in subsection 4.4.1 and attributed this plateau shift to the density of the monolayer.

These are all features that we already saw in the previous subsections and they seem to be reproducible. There is, however, one aspect that we did not pick up earlier. The plot in the bottom right does not show the same behaviour for both experiments. Observing the bleach on the r^- mode, when pumping the mode itself, we can see the usual trend for the original 32 mN/m films. The deuterated 13 mN/m monolayers, however, show a much more pronounced 'kink' in the data points, meaning the bleach follows the pump profile much longer before transitioning into a slower component.

We were not able to explain the biexponential curve of the bleach on the r^- mode with our model in section 4.3 and we still do not know what mechanism causes this trend. With the results from figure **4-30**, however, we might learn something new about the underlying physics. We should also keep in mind, though, that we were not able to reproduce the data of our deuterated 13 mN/m films and proceed with caution.

Taking a glance at figure **4-27** of the previous subsection, we find no clear indication of a similar effect in the isotopologue comparison. The density comparison in figure **4-23**, on the other hand, does seem to indicate a less pronounced but visible 'kink' in the less dense monolayers, as well. It is quite interesting then, that we find such a strong effect when combining both deuteration and monolayer density.

Unfortunately, since we do not know the underlying energy redistribution mechanism that governs the bleach on r^- it is difficult to explain this new phenomenon. However, the goal of our experimentation with different samples was to weaken the inter- and intramolecular anharmonic coupling and in this regard, we can argue to have been successful. For some reason, there is a transition from the extremely fast redistribution such that we can only observe a bleach that mirrors the pump profile to a much slower component and this transition seems to be delayed in the deuterated 13 mN/m monolayers.

In figure **4-24** of subsection 4.4.1, we found a puzzling behaviour of the r^+ mode. The shift of the plateau niveau for the less dense films was not reproducible in the *ppp* spectra when pumping d^- or at least much weaker. Figure **4-31** shows the same experiments for the original 32 mN/m films and their deuterated 13 mN/m counterpart. Evidently, we observe a very similar trend here: the different transients on the left are not reproducible in the *ppp* setup on the right.

4.4.4 Summary

Our goal in this section was to alter our molecular films in such a way that the intra- and intermolecular energy redistribution rates change significantly. To this end, we prepared samples at smaller surface pressures during deployment, making the molecular films less dense. Additionally, we prepared another batch of samples with a deuterated isotopologue, namely arachidic-17,17,18,18-d4 acid. Finally, we combined both approaches by preparing a deuterated Langmuir-Blodgett film at a surface pressure of 13 mN/m.

Overall, it was very difficult to significantly change the dynamics in the molecular films, as most experiments showed the same transients. Even though this is a clear indicator that we can reproduce our findings very well, we were hoping for interesting deviations that reveal more insight into our system's dynamics. Albeit few, we did find some variation in the data, which we will cover in the following.

1. Fits to the data of the transition into the plateau level yielded results that are all very similar and feature time constants around 80 ps. Only the deuterated 13 mN/m films featured lifetimes larger then 100 ps. In these systems, however, the error margin was much larger because there was a lot of noise in the measurements.

2. We found the bleach on r^- stronger than on r^+ by a factor of ≈ 1.75 when pumping d^-. This is close to the values for the 25 mN/m films (≈ 1.8) and for 13 mN/m films (≈ 1.92) as well. The deuterated molecules, on the other hand, show factors of ≈ 1.45 for the 32 mN/m films and ≈ 1.3 for the 13 mN/m films. This significant gap can likely be attributed to the deuteration even though we did not yet find a convincing explanation for the underlying principle.

3. The only significant change in the density experiments was visible in the r^+ mode

in *ssp* when pumping d^-. Here, the bleach transitioned into a lower plateau level for the less dense monolayers. Surprisingly, this was not reproducible for the r^+ mode in the *ppp* spectra. We did, however, get the same results for the deuterated 13 mN/m films. In an attempt to explain the shifting plateau level, we proposed two ideas. First, we suggested that the molecular orientation angle distribution is slightly altered in the different films, such that less energy is absorbed by the d^- modes. Secondly, we presented how the skeletal modes might have more freedom in the less dense monolayers, resulting in more of the population of r^+ decaying into the lower deformation modes. Both approaches, however, are not limited to the r^+ mode or the *ssp* polarisation combination. So the true fundamental behaviour is likely more complex.

4. The deuterated samples all show a slightly delayed lift-off point when the pump laser was set to d^-. This is unexpected because we would assume that the maximum bleach position is shifted to longer delays instead of the lift-off point. Nevertheless, we observed this behaviour multiple times and only for the deuterated d^- pumped case so it is likely a feature and not an experimental artifact.

5. When combining both density and isotopologue features, we found a stronger 'kink' in the r^- mode when pumping the mode itself in the deuterated 13 mN/m samples, compared to the original 32 mN/m films. This seems to indicate that the transients follow the temporal shape of the pump laser (similarly to the behaviour on the r^+ mode) for much longer before transitioning into a slower component. Even though we do not know what causes the behaviour of the r^- mode, the deuteration and thinning of our films presumably resulted in a delay of this unknown process.

Chapter 5

Conclusion

This chapter is intended as a summary of the most important research aspects that are presented in this thesis. Further, we are going to link back to the introductory chapter and review if and how the initial goals are achieved. Lastly, we will give a brief outlook with suggestions of how the research could be continued.

5.1 Summary

The accomplishments covered in this thesis can be roughly put into three categories:

1. Experimental setup with proof of principle.
2. Pump-probe experiments of calcium arachidate monolayers and a subsequent attempt to explain the observations with a three-temperature model.
3. Extending the molecular system to investigate the significance of intra- and intermolecular coupling.

In the following, we will take a closer at each of these categories and summarise the core aspects.

Experimental Setup

In the scope of the PhD work that is the foundation for this thesis, we were able to produce a time-resolved non-coherent pump-probe sum-frequency spectroscopy experiment. We had to adjust the setup multiple times to improve the odds of finding evidence of a pump effect. Roughly two years after the initiation of the project we found proof of principle in the form of a transient bleach on the methyl modes when pumping the methylene modes of a calcium arachidate sample. We have also shown in multiple figures how the transient data is reproducible to a high degree, effectively allowing us to track vibrational dynamics reliably.

Calcium Arachidate Results

In the next leg of this journey, we utilised our pump-probe setup to investigate calcium arachidate Langmuir-Blodgett films. While focusing on the methyl stretching modes (r^+ at $2879\,\mathrm{cm}^{-1}$ and r^- at $2962\,\mathrm{cm}^{-1}$) we found evidence of a strong pump effect in spectral areas that correspond to high absorption. Specifically pumping the antisymmetric methylene and methyl modes at $2920\,\mathrm{cm}^{-1}$ (d^-) and at $2962\,\mathrm{cm}^{-1}$ (r^-) correlated to strong drops in the intensity of the prominent modes in the sum-frequency spectrum. We did, however, rule out a signal decrease due to an overall temperature increase because there was no evidence of gauche defects in our spectra.

The fixed-delay wavelength experiments were followed up by the scanning-delay experiments to reveal the transient bleaches. Here, we were able to reproduce a certain trend in the transient data. We found that the dynamic regime consists of multiple components:

- All transients show an initial spike when the pump pulse comes into temporal overlap with the other pulses, which is reasonable because the ground state gets depopulated as soon as the pump pulse hits.

- The trends for the first $\approx 20\,\mathrm{ps}$ after the initial spikes depend on the pumped mode:

  - Pumping r^-, the bleach mirrors the temporal profile of the pump laser, which suggests a rapid decay with a time constant of a few picoseconds, limited by the temporal width of our pump pulse.

  - Pumping d^-, the bleach mirrors the integral of the temporal profile, which suggests a slower decay with a time constant larger than the temporal width of our pump pulse.

- Eventually, all transients transition into a very slow component that we refer to as the plateau level. This decay features a time constant of a few nanoseconds and is presumably the energy redistribution into the substrate. There are, however, differences according to the pumped mode:

  - Pumping r^-, the bleach immediately enters the plateau level after the pump pulse passes.

  - Pumping d^-, we find two components before entering the plateau:

    * Faster component (roughly between delay of $20 - 50\,\mathrm{ps}$) that we were not able to categorise nor could we find a reproducible time constant.

    * Slower component (roughly between delay of $50 - 200\,\mathrm{ps}$), which presumably is the energy redistribution into the lower deformation modes with a population decay time constant of roughly $100\,\mathrm{ps}$.

- The only measurement that deviated from this behaviour, albeit reproducibly, is the bleach on r^- in *ppp* when pumping r^-. Here, the transient mirrors the temporal profile of the pump like the r^- pumped spectra but then transitions into a slow decay similar to the d^- pumped case. Unfortunately, we were not able to provide a satisfactory explanation here.

In an attempt to understand the underlying mechanism that governs the energy flow in our samples, we devised a three-temperature model approach. The three temperature reservoirs R, D and B correlate to the methyl and methylene stretching modes and the heat bath that contains the lower deformation modes, respectively. We tied the heat capacities of each reservoir to the number of vibrational modes such that the ratio of R:D:B is roughly 4:36:120 to reflect how large each reservoir is in comparison to the others. We then defined a set of coupled differential equations to describe the energy flow between these reservoirs. Further, we decided to describe the system with as little as three coupling parameters: a_{DR}, a_{RD} and a_B for the transition from R $\rightarrow$ D, D $\rightarrow$ R and R/D $\leftrightarrow$ B, respectively. This approach is reasonable because we can simulate our observations sufficiently well with this simple model even though our model neglects a lot of finer details. It is, therefore, likely that we have grasped the fundamental principle.

We then had to solve the differential equations, transform the temperatures to populations and compare the population difference of the R reservoir to our transient data. In doing so, we found parameters that fit the *ssp* spectra very well. The coupling parameters are: $a_{DR} = 0.5\,\mathrm{J(K \cdot ps)^{-1}}$, $a_{RD} = 0.9\,\mathrm{J(K \cdot ps)^{-1}}$ and $a_B = 0.2\,\mathrm{J(K \cdot ps)^{-1}}$. All parameters are listed in table **4-3**. Comparing the simulation to the *ppp* spectra, we found good alignment with the d^- pumped measurements but we were not able to reproduce the puzzling behaviour of the r^- mode when the same mode is pumped. Regardless of these shortcomings, we are confident that the fundamental idea is correct and the trends of the transients are caused by the much larger methylene reservoir, which takes longer to drain and constantly fuels the R reservoir when pumping d^-. Pumping r^-, on the other hand, fills up a much smaller reservoir that is quickly drained into the lower deformation modes. We will note, however, that this model needs to be expanded to fully reflect the vibrational dynamics of our samples.

Extension of Sytems Studied

In an attempt to learn more about the intra- and intermolecular coupling mechanism, we decided to investigate samples that are slightly altered. First, we changed the surface pressure during deployment of the Langmuir-Blodgett films such that the molecular monolayer is less dense or even in a different phase. The samples that we investigated so far were prepared at a surface pressure of 32 mN/m (millinewton per meter) and the new samples are deployed at 25 mN/m and 13 mN/m. By modifying the density of the films, we were hoping to weaken the exchange between adjacent molecules to draw conclusions

about the intermolecular coupling mechanism. Secondly, we introduced deuterium into our molecules to make them heavier and push the resonant frequency far below the natural one. By deuterating two of the CH_2 links we were hoping to significantly delay the energy redistribution between the methyl and methylene modes and gain more insight into the intramolecular coupling mechanism. Lastly, we combined both approaches by preparing deuterated samples with less density.

We begin by summarising the density approach. Overall, the effect of the surface pressure during deployment of the film was surprisingly weak. Almost all transients showed very little deviation that could likely be attributed to limits in reproducibility due to day-to-day differences in the setup. The only significant change was visible in the transients of the r^+ mode in *ssp* when pumping d^-. Here, the plateau level of the slow component featured a smaller bleach with decreasing density of the films. This suggests that the amount of vibrational energy that is contained in the symmetric methyl stretch for longer times is larger in the denser films. We illustrated some scenarios that could explain such behaviour but ultimately none of these explanations were exclusive to this specific experiment. However, we have been able to reproduce this behaviour in the deuterated films with smaller density as well.

Next, we discuss the investigation of the arachidate isotopologues. The transients show very little deviation from the ones we found for the original molecular layers and the time constants are also equal within their experimental errors. There is, however, one aspect that we picked up. The transients of the deuterated samples featured a slightly delayed 'lift-off' point for the initial spike when pumping d^-. This is unexpected because we would assume that the maximum bleach position is shifted to longer delays instead of the lift-off point if we weaken the coupling between the methylene and methyl modes. Nevertheless, we observed this behaviour multiple times and only for the deuterated d^- pumped case so it is likely a feature and not an experimental artifact.

5.2 Review

Even though the density and isotopologue experiments did not yield the surprising results we had hoped for, the overall research is considered a success. We established a novel setup that allows for time-resolved pump-probe measurements, revealing the vibrational energy flow in our samples. Linking back to the introductory chapter, we specifically motivated our research with the following questions in mind:

1. How does the system react or evolve in time after it has been brought into a non-equilibrium state?

2. How does the coupling to different degrees of freedom work?

3. How long does a 'hot' adsorbate exist on the surface after an initial chemical reaction step?

Regarding the first question, we found evidence of strong anharmonic coupling when pumping specific resonance frequencies. In the non-equilibrium state, the system transfers the vibrational energy through different channels into the substrate until equilibrium is reached. With our model, we were able to map the transient energy content in different vibrational modes and found specific time constants for the energy exchange.

We answered the second question by investigating the pump-probe spectra of calcium arachidate. Here, we found a very strong anharmonic coupling between the methyl and methylene stretches. This is reasonable because of similar symmetries in the oscillatory motion and because of the close spectral vicinity. Further, we found that by deuterating some of the CH_2 links, for which the natural frequencies of the methylene stretches are smaller, the coupling mechanism is weakened. With a three-temperature model, we then proposed how the methyl and methylene stretches are slightly weaker coupled to the lower deformation modes before relaxing all of their vibrational energy to the substrate. We did not find evidence of strong intermolecular coupling with our density experiments.

The third question was not answered specifically. We did, however, find concrete numbers for the lifetime of certain vibrational modes in calcium arachidate. This is proof of principle and shows that our experimental setup lays the foundation to investigate a tailored chemical reaction and target a specific 'hot' adsorbate.

5.3 Outlook

The research presented in this thesis still left a lot of open questions. The three-temperature model approach for example fits most of our data very well except for a single *ppp* measurement. To further investigate this approach, future works could focus on two things:

First, being able to observe the CH_2 stretches directly would help tremendously. This could be made possible by purposely inducing gauche defects in our samples, thus breaking the bulk symmetry and revealing the methylene modes in the sum-frequency spectra. Secondly, the plateau level that all transients transition into eventually, is assumed to represent the coupling to the lower deformation modes. Being able to probe these skeletal modes could provide a more detailed view of the complex coupling mechanisms. This, however, is difficult to realise because the skeletal modes lie in spectral regions of strong absorption bands in atmospheric water. One would have to cover the probe IR beam path in dry air to reduce the absorption in the atmosphere and produce satisfactory spectra.

Further, the isotopologue and density experiments yielded only very little new information. In the deuterated samples, the 'lift-off' point of the initial bleach spike was slightly delayed when pumping the methylene modes. It would be interesting to see if this trend becomes more prominent when more than two of the CH_2 links are deuterated. This could

provide the means of tailoring the coupling strength between the methylene and methyl modes in long-chain fatty acid molecules.

The only significant feature in the density experiments was a shifted plateau level in the *ssp* spectra when pumping d^-. We were unable to explain this phenomenon but observing the skeletal modes directly, as previously mentioned, could illuminate this behaviour as well. Another approach to investigate the intermolecular coupling mechanism is to dilute the monolayer instead of just reducing the surface pressure. Adding additional molecules into the monolayer, like fully deuterated arachidate for example, should strongly influence the energy exchange between adjacent molecules.

Finally, we hope that this novel pump-probe setup encourages future work groups to dive into the exotic world of non-equilibrium dynamics and uncover more of the fascinating phenomena that are yet to be found.

Appendix A

Data Validation

Figure **A-1** and **A-2** shows two delay scans, taken on different days, for each experimental setup in the 25 mN/m and the 13 mN/m case, respectively.

Figure **A-3** also shows a repetition of the same experiments but for the deuterated arachidate monolayers with a surface pressure of 32 mN/m during deployment.

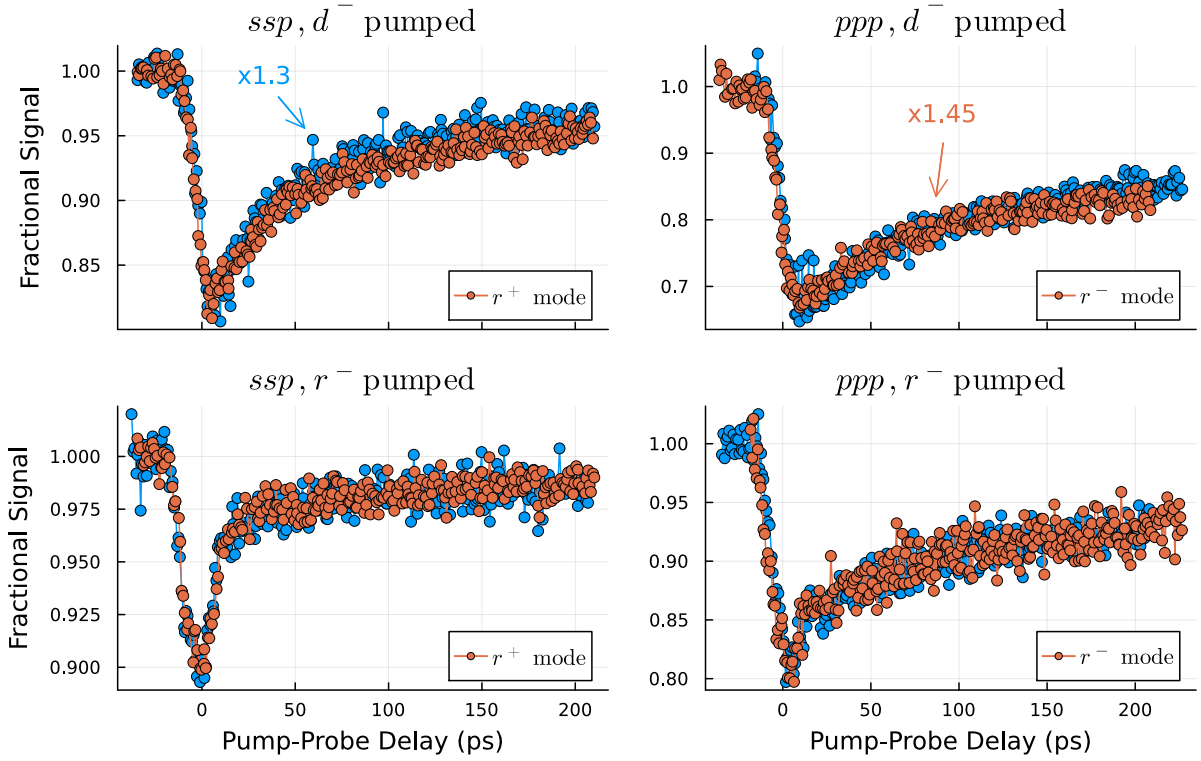

Figure **A-1**: Similar to figure **4-13**, this figure validates the reproducibility of our data. All orange data points indicate experiments with 25 mN/m surface pressure, which are investigated in section 4.4.1. The blue dots represent a repetition of the same experiments on a different day. The coloured arrows show the scaling factor necessary to match the datasets.

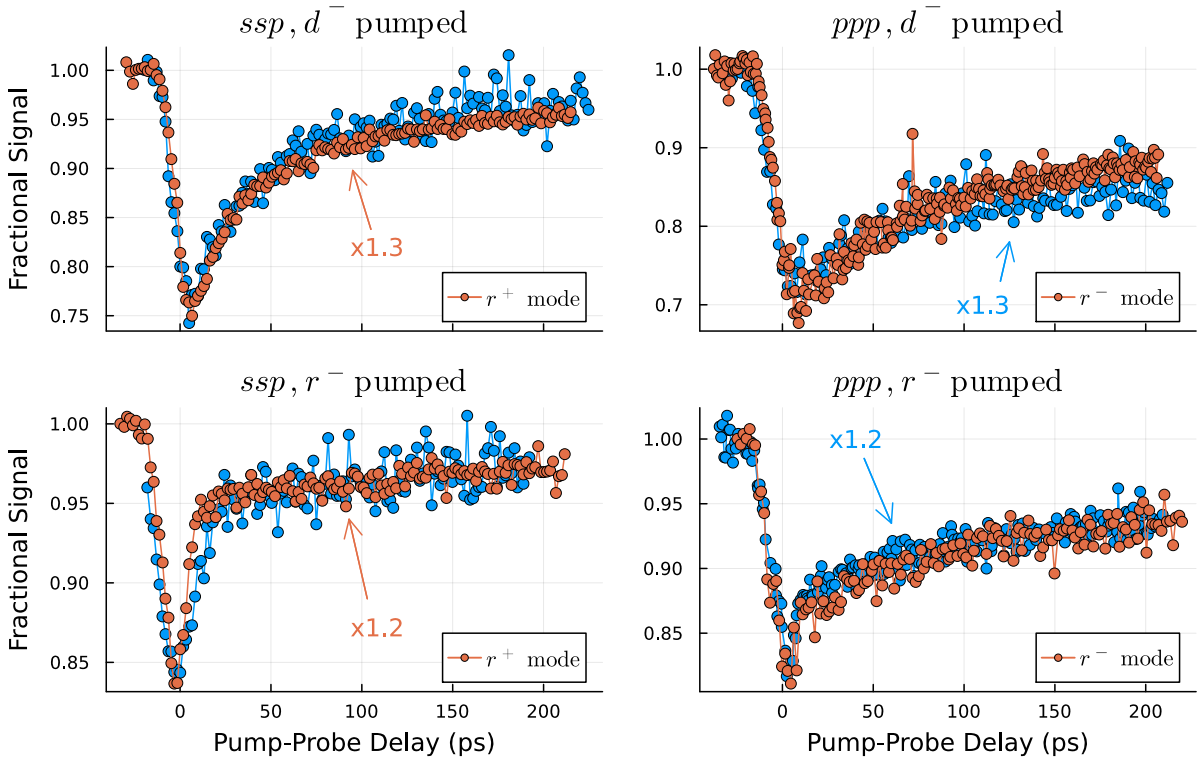

Figure **A-2**: This figure shows the same as **A-1** but with monolayers at a surface pressure of 13 mN/m during deployment.

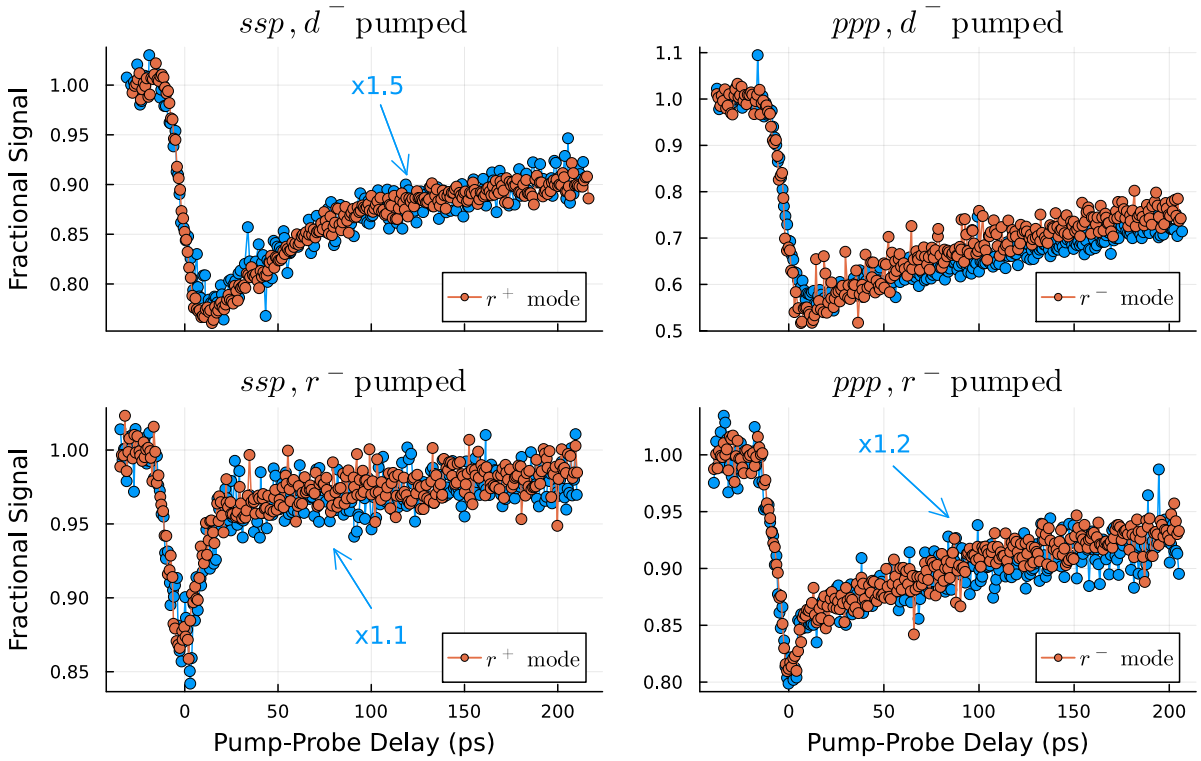

Figure **A-3**: This figure shows the same as **A-1** but with monolayers of deuterated CaAra at a surface pressure of 32 mN/m during deployment.

Bibliography

[1] Albert Einstein. The Meaning of Relativity. pages 54–75, 1922. ↑1

[2] R. P. Feynman, R. B. Leighton, and M. L. Sands. *The Feynman lectures on physics - Volume I.* Addison-Wesley Pub. Co., 1963. ↑1 , ↑9 , ↑11 , ↑15 , ↑18 , ↑23 , ↑26 , ↑30 , ↑33 , ↑34

[3] Tadao Nagatsuma. Terahertz technologies: present and future. *IEICE Electronics Express*, 8(14):1127–1142, 2011. ↑2

[4] Sven Grundmann, Daniel Trabert, Kilian Fehre, Nico Strenger, Andreas Pier, Leon Kaiser, Max Kircher, Miriam Weller, Sebastian Eckart, and Lothar Ph H Schmidt. Zeptosecond birth time delay in molecular photoionization. *Science*, 370(6514):339–341, 2020. ↑2

[5] A L Harris and N J Levinos. Vibrational energy relaxation in a molecular monolayer at a metal surface. *The Journal of Chemical Physics*, 90(7):3878–3879, 1989. ↑3

[6] A L. Harris and N. J. Levinos. Vibrational Energy Relaxation In A Molecular Monolayer Measured By Picosecond Sum Spectroscopy. *Photochemistry in Thin Films*, pages 66–72, 1989. ↑3

[7] A. L. Harris, L. Rothberg, L. H. Dubois, N. J. Levinos, and L. Dhar. Molecular vibrational energy relaxation at a metal surface: Methyl thiolate on Ag(111). *Physical Review Letters*, 64(17):2086–2089, 1990. ↑3

[8] Martin T Zanni and Robin M Hochstrasser. Two-dimensional infrared spectroscopy: a promising new method for the time resolution of structures. *Current Opinion in Structural Biology*, 11(5):516–522, 2001. ↑4

[9] Franck Vidal and Abderrahmane Tadjeddine. Sum-frequency generation spectroscopy of interfaces. *Reports on Progress in Physics*, 68(5):1095, 2005. ↑4 , ↑69

[10] Wei Xiong, Jennifer E. Laaser, Randy D. Mehlenbacher, and Martin T. Zanni. Adding a dimension to the infrared spectra of interfaces using heterodyne detected

2D sum-frequency generation (HD 2D SFG) spectroscopy. *Proceedings of the National Academy of Sciences*, 108(52):20902–20907, 2011. ↑4

[11] Heike Arnolds and Mischa Bonn. Ultrafast surface vibrational dynamics. *Surface Science Reports*, 65(2):45–66, 2010. ↑4

[12] Zhen Zhang, Lukasz Piatkowski, Huib J. Bakker, and Mischa Bonn. Ultrafast vibrational energy transfer at the water/air interface revealed by two-dimensional surface vibrational spectroscopy. *Nature Chemistry*, 3(11):888–893, 2011. ↑4

[13] Nils Huse, Satoshi Ashihara, Erik T.J. Nibbering, and Thomas Elsaesser. Ultrafast vibrational relaxation of O–H bending and librational excitations in liquid H2O. *Chemical Physics Letters*, 404(4-6):389–393, 2005. ↑4

[14] Zhaohui Wang, Jeffrey A Carter, Alexei Lagutchev, Yee Koh, Nak-Hyun Seong, David G Cahill, and Dana D Dlott. Ultrafast flash thermal conductance of molecular chains. *Science*, 317(5839), 2007. ↑4

[15] B. N. J. Persson and R. Ryberg. Vibrational interaction between molecules adsorbed on a metal surface: The dipole-dipole interaction. *Physical Review B*, 24(12):6954–6970, 1981. ↑4

[16] J D Beckerle, R R Cavanagh, M P Casassa, E J Heilweil, and J C Stephenson. Subpicosecond transient infrared spectroscopy of adsorbates. Vibrational dynamics of CO/Pt(111). *The Journal of Chemical Physics*, 95(7):5403–5418, 1991. ↑5

[17] Mischa Bonn, Christian Hess, and Martin Wolf. The dynamics of vibrational excitations on surfaces: CO on Ru(001). *The Journal of Chemical Physics*, 115(16):7725–7735, 2001. ↑5

[18] P. Jakob. Dynamics of the C-O Stretch Overtone Vibration of CO/Ru(001). *Physical Review Letters*, 77(20):4229–4232, 1996. ↑5

[19] David C. Lindberg. *Theories of Vision from Al-kindi to Kepler*. University of Chicago Press, 1981. ↑8

[20] Evangelos Papadopoulos. Distinguished Figures in Mechanism and Machine Science, Their Contributions and Legacies Part 1. *History of Mechanism and Machine Science*, pages 217–245, 2007. ↑8

[21] D. B. Ion and M. L. D. Ion. Principle of Minimum Distance in Space of States as New Principle in Quantum Physics. *arXiv*, 2007. ↑8

[22] David C Lindberg. *The beginnings of Western science: The European scientific tradition in philosophical, religious, and institutional context, prehistory to AD 1450.* University of Chicago Press, 2010. ↑8

[23] Roshdi Rashed. A Pioneer in Anaclastics: Ibn Sahl on Burning Mirrors and Lenses. *Isis*, 81(3):464–491, 1990. ↑8

[24] K. B. Wolf and G. Krotzsch. Geometry and dynamics in refracting systems. *European Journal of Physics*, 16(1):14–20, 1995. ↑8

[25] Alistair Kwan, John Dudley, and Eric Lantz. Who really discovered Snell's law? *Physics World*, 15(4):64–64, 2002. ↑8

[26] W. B. Joyce and Alice Joyce. Descartes, Newton, and Snell's law. *Journal of the Optical Society of America*, 66(1):1, 1976. ↑8

[27] Fokko Jan Dijksterhuis. Once Snell Breaks Down: From Geometrical to Physical Optics in the Seventeenth Century. *Annals of Science*, 61(2):165–185, 2004. ↑8

[28] Max Born and Emil Wolf. *Principles of Optics: 60th Anniversary Edition.* Cambridge University Press, Cambridge, 7 edition, 2019. ↑9 , ↑32

[29] Z. Néda and S. Volkán-Kacsó. Flatness of the setting Sun. *American Journal of Physics*, 71(4):379–385, 2003. ↑10

[30] From *Feynman Lectures on Physics, Vol. I* by Richard Feynman, copyright © 2011. Reprinted by permission of Basic Books, an imprint of Hachette Book Group, Inc. ↑12 , ↑38 , ↑41

[31] H. Hertz. Ueber einen Einfluss des ultravioletten Lichtes auf die electrische Entladung. *Annalen der Physik*, 267(8):983–1000, 1887. ↑12

[32] Albert Einstein. Über einem die Erzeugung und Verwandlung des Lichtes betreffenden heuristischen Gesichtspunkt. *Annalen der Physik*, 4, 1905. ↑13

[33] Morris H. Shamos. *Great experiments in physics: firsthand accounts from Galileo to Einstein.* Courier Corporation, 1987. ↑13

[34] Roger Bach, Damian Pope, Sy-Hwang Liou, and Herman Batelaan. Controlled double-slit electron diffraction. *New Journal of Physics*, 15(3):033018, 2013. ↑17

[35] Claus Jönsson. Elektroneninterferenzen an mehreren kuenstlich hergestellten Feinspalten. *Zeitschrift für Physik*, 161(4):454–474, 1961. ↑16

[36] W. Heisenberg. Über den anschaulichen Inhalt der quantentheoretischen Kinematik und Mechanik. *Zeitschrift für Physik*, 43(3-4):172–198, 1927. ↑17

[37] Louis De Broglie. Recherches sur la théorie des Quanta. *Annales de Physique*, 10(3):22–128, 1925. ↑18

[38] E. H. Kennard. Zur Quantenmechanik einfacher Bewegungstypen. *Zeitschrift für Physik*, 44(4-5):326–352, 1927. ↑18

[39] C. Stewart, Gillmor. *Coulomb and the Evolution of Physics and Engineering in Eighteenth-Century France*. Princeton University Press, 2017. ↑19

[40] Massimo Mitolo, Rodolfo Araneo, and Barry C. Brusso. A Brief History of Electromagnetism. *IEEE Industry Applications Magazine*, 25(2):7–11, 2019. ↑19

[41] Fawwaz T., Ulaby and Ravaioli Umberto. *Fundamentals of applied electromagnetics*. Pearson, Boston [u.a.], 7. ed., global ed. edition, 2015. ↑19

[42] James Clerk, Maxwell. *A treatise on electricity and magnetism*, volume 1. Clarendon press, 1873. ↑20

[43] Christopher Donaghy-Spargo and Alex Yakovlev. Oliver Heaviside's electromagnetic theory. *Philosophical Transactions of the Royal Society A: Mathematical, Physical and Engineering Sciences*, 376(2134):20180229, 2018. ↑20

[44] J.D. Jackson. *Classical Electrodynamics*. Wiley, 1999. ↑22

[45] E. Schrödinger. An Undulatory Theory of the Mechanics of Atoms and Molecules. *Physical Review*, 28(6):1049–1070, 1926. ↑24

[46] Paul Adrien Maurice Dirac. The quantum theory of the electron. *Proceedings of the Royal Society of London. Series A, Containing Papers of a Mathematical and Physical Character*, 117(778):610–624, 1928. ↑25

[47] Ricardo Karam. Schrödinger's original struggles with a complex wave function. *American Journal of Physics*, 88(6):433–438, 2020. ↑25

[48] GREGORY J GBUR. *Falling Felines and Fundamental Physics*. Yale University Press, 2019. ↑25

[49] Max Born. Zur Quantenmechanik der Stoßvorgänge. *Zeitschrift für Physik*, 37(12):863–867, 1926. ↑25

[50] Hooke R. *Lectures de Potentia Restitutiva, Or of Spring Explaining the Power of Springing Bodies*. John Martyn, 1678. ↑27

[51] Stephen M Stigler. *Statistics on the table: The history of statistical concepts and methods*. Harvard University Press, 2002. ↑28

[52] Demtröder Wolfgang. *Laser spectroscopy: basic concepts and instrumentation.* Springer Science and Business Media, 2013. ↑28 , ↑35

[53] Michael Lackner. *Tracking Vibrational Dynamics.* PhD thesis, University of Duisburg-Essen, 2021. ↑28 , ↑44 , ↑53 , ↑76 , ↑99

[54] Anne Myers, Kelley. *Condensed-phase molecular spectroscopy and photophysics.* John Wiley & Sons, 2012. ↑28

[55] Jan Hilgevoord. The uncertainty principle for energy and time. *American Journal of Physics*, 64(12):1451–1456, 1996. ↑29

[56] Michael Kotlarchyk. Encyclopedia of Spectroscopy and Spectrometry. pages 2074–2084, 1999. ↑31

[57] Meschede Dieter. *Optics, light and lasers: the practical approach to modern aspects of photonics and laser physics.* John Wiley and Sons, 2017. ↑31

[58] Haken Hermann and Wolf Hans Christoph. *The physics of atoms and quanta: introduction to experiments and theory*, volume 1439. Springer Science and Business Media, 2005. ↑31

[59] Lorenzo J, Curtis. *Atomic structure and lifetimes: a conceptual approach.* Cambridge University Press, 2003. ↑31

[60] V. Canuto, J. Lodenquai, and M. Ruderman. Thomson Scattering in a Strong Magnetic Field. *Physical Review D*, 3(10):2303–2308, 1971. ↑31

[61] Max Born. *Optik: ein Lehrbuch der elektromagnetischen Lichttheorie.* Springer-Verlag, 2013. ↑31

[62] A. Kramida, Yu. Ralchenko, J. Reader, and NIST ASD Team. NIST Atomic Spectra Database (ver. 5.9), [Online]. Available: `https://physics.nist.gov/asd` [2022, April 29]. National Institute of Standards and Technology, Gaithersburg, MD., 2021. ↑31

[63] Milton Kerker. *The scattering of light and other electromagnetic radiation: physical chemistry: a series of monographs*, volume 16. Academic press, 2013. ↑32

[64] R. P. Feynman, R. B. Leighton, and M. L. Sands. *The Feynman lectures on physics - Volume II.* Addison-Wesley Pub. Co., 1963. ↑33 , ↑37

[65] José A, Bittencourt. *Fundamentals of plasma physics.* Springer Science & Business Media, 2004. ↑36

[66] From *Feynman Lectures on Physics, Vol. II* by Richard Feynman, copyright © 2015. Reprinted by permission of Basic Books, an imprint of Hachette Book Group, Inc. ↑36

[67] Alex G. Lambert, Paul B. Davies, and David J. Neivandt. Implementing the Theory of Sum Frequency Generation Vibrational Spectroscopy: A Tutorial Review. *Applied Spectroscopy Reviews*, 40(2):103–145, 2005. ↑37 , ↑63 , ↑68 , ↑70 , ↑71

[68] Charles Kittel and Paul McEuen. *Kittel's Introduction to Solid State Physics*. John Wiley & Sons, 2018. ↑40

[69] Brillouin Léon. *Wave propagation and group velocity*, volume 8. Academic press, 2013. ↑41

[70] Ingolf V. Hertel and C.-P. Schulz. *Atome, Moleküle und optische Physik 2, Moleküle und Photonen - Spektroskopie und Streuphysik*. 2010. ↑43 , ↑45 , ↑46 , ↑47 , ↑48 , ↑53 , ↑56

[71] M. Born and R. Oppenheimer. Zur Quantentheorie der Molekeln. *Annalen der Physik*, 389(20):457–484, 1927. ↑45

[72] A V Mitin. Analytical solution of the Schrödinger equation for the hydrogen molecular ion H_2^+. *arXiv*, 2015. ↑45

[73] Demtröder Wolfgang. *Experimentalphysik 3: Atome, Moleküle und Festkörper*. Springer-Verlag, 2016. ↑46 , ↑48 , ↑53

[74] Henry E. Fleming and K. Narahari Rao. A simple numerical evaluation of the Rydberg-Klein-Rees integrals: Application to $X^1\Sigma^+$ state of $^{12}C^{16}O$. *Journal of Molecular Spectroscopy*, 44(1):189–193, 1972. ↑47

[75] Dean Boyall and Katharine L. Reid. Modern studies of intramolecular vibrational energy redistribution. *Chemical Society Reviews*, 26(3):223–232, 1997. ↑50 , ↑51 , ↑53

[76] Katharine L., Reid. Picosecond time-resolved photoelectron spectroscopy as a means of gaining insight into mechanisms of intramolecular vibrational energy redistribution in excited states. *International Reviews in Physical Chemistry*, 27(4):607–628, 10 2008. ↑51

[77] Peter M Felker and Ahmed H Zewail. Dynamics of intramolecular vibrational-energy redistribution (IVR). I. Coherence effects. *The Journal of Chemical Physics*, 82(7):2961–2974, 1985. ↑51

[78] K. K. Lehmann, B. H. Pate, and G. Scoles. Intramolecular vibrational redistribution on the nanosecond time scale: v_1 and $2v_1$ spectra of substituted acetylene compounds. In J. Jortner, R. D. Levine, and B. Pullman, editors, *Mode Selective Chemistry*, pages 17–23, Dordrecht, 1991. Springer Netherlands. ↑51

[79] Heike Arnolds. Vibrational dynamics of adsorbates – Quo vadis? *Progress in Surface Science*, 86(1-2):1–40, 2011. ↑51 , ↑52

[80] Jeffrey R Hill, Eric L Chronister, Ta-Chau Chang, Hackjin Kim, Jay C Postlewaite, and Dana D Dlott. Vibrational relaxation and vibrational cooling in low temperature molecular crystals. *The Journal of Chemical Physics*, 88(2):949–967, 1988. ↑51

[81] Velsko So and Hochstrasser RM. Studies of vibrational relaxation in low-temperature molecular crystals using coherent Raman spectroscopy. *The Journal of Physical Chemistry*, 89(11):2240–2253, 1985. ↑51

[82] J.W. Gadzuk and A.C. Luntz. On vibrational lineshapes of adsorbed molecules. *Surface Science*, 144(2-3):429–450, 1984. ↑52

[83] H. Ueba. Vibrational relaxation and pump-probe spectroscopies of adsorbates on solid surfaces. *Progress in Surface Science*, 55(2):115–179, 1997. ↑52

[84] Daniel C, Harris and Michael D, Bertolucci. *Symmetry and spectroscopy: an introduction to vibrational and electronic spectroscopy*. Courier Corporation, 1989. ↑53

[85] J. C. D., Brand. The Discovery of the Raman Effect. *Notes and Records of the Royal Society of London*, 43(1):1, 1989. ↑53

[86] Robert W. Boyd. *Nonlinear Optics*. Academic Press, 2020. ↑57 , ↑58 , ↑59 , ↑61 , ↑62 , ↑63 , ↑64 , ↑66 , ↑68

[87] Richard L, Keiter. Spectroscopically silent fundamental vibrations. *Journal of Chemical Education*, 60(8):625, 1983. ↑58

[88] P. A. Franken, A. E. Hill, C. W. Peters, and G. Weinreich. Generation of Optical Harmonics. *Physical Review Letters*, 7(4):118–119, 1961. ↑58

[89] Robert W., Boyd. Order-of-magnitude estimates of the nonlinear optical susceptibility. *Journal of Modern Optics*, 46(3):367–378, 1999. ↑59

[90] Shen Yuen-Ron. Principles of nonlinear optics. 1984. ↑59

[91] J.H. Hunt, P. Guyot-Sionnest, and Y.R. Shen. Observation of C-H stretch vibrations of monolayers of molecules optical sum-frequency generation. *Chemical Physics Letters*, 133(3):189–192, 1987. ↑69

[92] M Buck and M Himmelhaus. Vibrational spectroscopy of interfaces by infrared–visible sum frequency generation. *Journal of Vacuum Science & Technology A: Vacuum, Surfaces, and Films*, 19(6):2717, 2001. ↑69

[93] X. Zhuang, P. B. Miranda, D. Kim, and Y. R. Shen. Mapping molecular orientation and conformation at interfaces by surface nonlinear optics. *Physical Review B*, 59(19):12632–12640, 1998. ↑72 , ↑73

[94] Jie Wang, Chunyan Chen, Sarah M. Buck, and Zhan Chen. Molecular Chemical Structure on Poly(methyl methacrylate) (PMMA) Surface Studied by Sum Frequency Generation (SFG) Vibrational Spectroscopy. *The Journal of Physical Chemistry B*, 105(48):12118–12125, 2001. ↑73

[95] Patrick M Epperson and M Bonner Denton. Binning spectral images in a charge-coupled device. *Analytical Chemistry*, 61(14):1513–1519, 1989. ↑90

[96] Luke O'C. Drury. Origin of cosmic rays. *Astroparticle Physics*, 39:52–60, 2012. ↑91

[97] Ralph Florentin-Nielsen, Michael I Andersen, and Sven P Nielsen. Cosmic Ray Events and Natural Radioactivity in CCD Cryostats. *Symposium - International Astronomical Union*, 167:207–211, 1995. ↑91

[98] James R Janesick, Tom Elliott, Stewart Collins, Morley M Blouke, and Jack Freeman. Scientific charge-coupled devices. *Optical Engineering*, 26(8):692–714, 1987. ↑91

[99] Katharine B. Blodgett and Irving Langmuir. Built-Up Films of Barium Stearate and Their Optical Properties. *Physical Review*, 51(11):964–982, 1937. ↑94 , ↑95

[100] Jan Weber, Andre Beier, Eckart Hasselbrink, and Thorsten Balgar. Thermally induced conformational changes of Ca-arachidate Langmuir-Blodgett Films at different compression. *The Journal of Chemical Physics*, 141(4):044912, 2014. ↑94 , ↑95 , ↑99

[101] Gareth Roberts. *Langmuir-blodgett films*. Springer Science & Business Media, 2013. ↑95 , ↑98

[102] Hans-Jürgen Butt, Karlheinz Graf, and Michael Kappl. *Physics and chemistry of interfaces*. John Wiley & Sons, 2013. ↑96

[103] Vladimir M. Kaganer, Helmuth Möhwald, and Pulak Dutta. Structure and phase transitions in Langmuir monolayers. *Reviews of Modern Physics*, 71(3):779–819, 1999. ↑96

[104] William D Harkins and L E Copeland. A Superliquid in Two Dimensions and a First-Order Change in a Condensed Monolayer I. Energy, Compressibility, and Order of Phase Transformations. *The Journal of Chemical Physics*, 10(5):272–286, 1942. ↑97

[105] Anna M. Bibo and Ian R. Peterson. Phase diagrams of monolayers of the long chain fatty acids. *Advanced Materials*, 2(6-7):309–311, 1990. ↑97

[106] Jan Weber. *Temperature induced change in aliphatic monolayers observed by vibrational sum-frequency generation spectroscopy.* PhD thesis, University of Duisburg-Essen, 2014. ↑97 , ↑99

[107] M. L. Kurnaz and D. K. Schwartz. Morphology of Microphase Separation in Arachidic Acid/Cadmium Arachidate Langmuir-Blodgett Multilayers. *The Journal of Physical Chemistry*, 100(26):11113–11119, 1996. ↑97

[108] J.B Peng, G.T Barnes, and I.R Gentle. The structures of Langmuir–Blodgett films of fatty acids and their salts. *Advances in Colloid and Interface Science*, 91(2):163–219, 2001. ↑98

[109] C M Knobler and R C Desai. Phase Transitions in Monolayers. *Annual Review of Physical Chemistry*, 43(1):207–236, 1992. ↑98

[110] D. A. Outka, J. Stöhr, J. Rabe, J. D. Swalen, and H. H. Rotermund. Orientation of arachidate chains in Langmuir-Blodgett monolayers on Si(111). *Physical Review Letters*, 59(12):1321–1324, 1987. ↑98

[111] M Kinzler, A Schertel, G Hähner, Ch Wöll, M Grunze, H Albrecht, G Holzhüter, and Th Gerber. Structure of mono- and multilayer Langmuir–Blodgett films from Cd arachidate and Ca arachidate. *The Journal of Chemical Physics*, 100(10):7722–7735, 1994. ↑99

[112] Andre Beier-Hannweg, Damian Firla, and Eckart Hasselbrink. Order and melting stability of calcium arachidate Langmuir-Blodgett monolayers prepared at different pH. *Thin Solid Films*, 642:1–7, 2017. ↑100

[113] Jan Weber, Thorsten Balgar, and Eckart Hasselbrink. Conformational disorder in alkylsiloxane monolayers at elevated temperatures. *The Journal of Chemical Physics*, 139(24):244902, 2013. ↑100

[114] LJFC Bellamy. *The infra-red spectra of complex molecules*. Springer Science & Business Media, 2013. ↑101

[115] P. Guyot-Sionnest, J. H. Hunt, and Y. R. Shen. Sum-frequency vibrational spectroscopy of a Langmuir film: Study of molecular orientation of a two-dimensional system. *Physical Review Letters*, 59(14):1597–1600, 1987. ↑102 , ↑103 , ↑104 , ↑105 , ↑108

[116] M Tasumi and T Shimanouchi. Crystal Vibrations and Intermolecular Forces of Polymethylene Crystals. *The Journal of Chemical Physics*, 43(4):1245–1258, 1965. ↑102

[117] R.G. Snyder, S.L. Hsu, and S. Krimm. Vibrational spectra in the C-H stretching region and the structure of the polymethylene chain. *Spectrochimica Acta Part A: Molecular Spectroscopy*, 34(4):395–406, 1978. ↑103 , ↑105

[118] Ian R Hill and Ira W Levin. Vibrational spectra and carbon–hydrogen stretching mode assignments for a series of n-alkyl carboxylic acids. *The Journal of Chemical Physics*, 70(2):842, 1979. ↑103 , ↑105

[119] D Blaudez, T Buffeteau, N Castaings, B Desbat, and J -M Turlet. Organization in pure and alternate deuterated cadmium arachidate monolayers on solid substrates and at the air/water interface studied by conventional and differential Fourier transform infrared spectroscopies. *The Journal of Chemical Physics*, 104(24):9983–9993, 1996. ↑103 , ↑105

[120] B.C. Chow, T.T. Ehler, and T.E. Furtak. High-resolution sum-frequency generation from alkylsiloxane monolayers. *Applied Physics B*, 74(4):395–399, 2002. ↑104 , ↑105

[121] M Himmelhaus, F Eisert, M Buck, and M Grunze. Self-Assembly of n -Alkanethiol Monolayers. A Study by IR-Visible Sum Frequency Spectroscopy (SFG). *The Journal of Physical Chemistry B*, 104(3):576–584, 2000. ↑104 , ↑105

[122] Na Ji, Victor Ostroverkhov, Chao-Yuan Chen, and Yuen-Ron Shen. Phase-Sensitive Sum-Frequency Vibrational Spectroscopy and Its Application to Studies of Interfacial Alkyl Chains. *Journal of the American Chemical Society*, 129(33):10056–10057, 2007. ↑108

[123] Xu Han, Thorsten Balgar, and Eckart Hasselbrink. Vibrational dynamics of hydrogen on Ge surfaces. *The Journal of Chemical Physics*, 130(13):134701, 2009. ↑114